Iron oxide- Indocyanine green based magneto-optical nanocomposites for potential multi-modal applications in cancer therapeutics

by

Nisha Lamichhane

A thesis submitted in partial fulfilment for the requirements for the degree of Doctor of Philosophy at the University of Central Lancashire

July 14, 2022

RESEARCH STUDENT DECLARATION FORM

Type of Award _____**PhD (*via* MPhil)** _____

School _____**Natural Sciences**_____

1. Concurrent registration for two or more academic awards

*I declare that while registered as a candidate for the research degree, I have not been a registered candidate or enrolled student for another award of the University or other academic or professional institution

2. Material submitted for another award

*****I declare that no material contained in the thesis has been used in any other submission for an academic award and is solely my own work

3. Collaboration

Where a candidate's research programme is part of a collaborative project, the thesis must indicate in addition clearly the candidate's individual contribution and the extent of the collaboration. Please state below:

_____

4. Use of a Proof-reader

*No proof-reading service was used in the compilation of this thesis.

Nisha

Signature of Candidate: _____

Print name: _____**NISHA LAMICHHANE**_____

ABSTRACT:

Magneto-optical nanocomposites possess properties of both magnetic and optical components as novel nanomedicines and demonstrate an immense potential in cancer therapeutics under the application of external stimuli such as alternating magnetic field (AMF) and near-infrared (NIR) laser irradiation. In this thesis, two different hydrophilic and one hydrophobic iron oxide nanoparticles (IONPs) types synthesised by modified co-precipitation methods, acted as a magnetic component. Synthesised IONPs cores (IO1, IO2 and IO3) were further coated with mesoporous silica shell using hexadecyl trimethyl ammonium bromide (CTAB) as a surface directing agent. Upon removal of CTAB from the mesopores by acidic ethanolic washing, the resultant magnetic silica (MS) nanocomposites (MS1, MS2 and MS3) were utilised for loading indocyanine green (ICG), acting as an optical component. The resultant ICG loaded magnetic silica nanocomposites (MSICG) nanocomposites (MS1ICG, MS2ICG and MS3ICG) were novel magneto-optical nanocomposites. Synthesised IONPs, MS and MSICG nanocomposites were extensively characterised and tested for their performance in magnetic hyperthermia therapy (MHT), photothermal therapy (PTT) and photodynamic therapy (PDT) *in-vitro* using commercial MCF7 breast cancer cell lines.

All the synthesised IONPs were spherical in morphology with superparamagnetic properties. Hydrophilic IONPs (IO1 and IO2) exhibited higher saturation magnetisation of 63.6 emu/g and 59.4 emu/g compared to hydrophobic IONPs (IO3) of 49.3 emu/g. Zeta potential measurements indicated that the surface of the IONPs were positively charged. The distinct XRD patterns corresponds to iron oxides. All IONPs showed a distinct Fe-O bond vibration at 550 cm^{-1} from FTIR analysis due to magnetite phase. In addition, hydrophobic IONPs showed peaks at 2925 and 2852 cm^{-1}, corresponding to -CH_2 stretching vibrations due to the presence of oleic acid. Following silica coating, the MS nanocomposites were nearly spherical with increased average size. The MS nanocomposites with hydrophobic IONPs had average size of 38 nm from TEM analysis and showed a thin layer of silica coating around magnetic core. Upon silica coating, the surface charge of the MS nanocomposites reversed from positive (around +19 mV for IONPs) to negative (around -23 mV) charge confirming the formation of core-shell nanocomposites. The presence of a silica shell around magnetic core was further confirmed with characteristic bond vibrations at 1080 and 795 cm^{-1} equivalent to Si-O-Si stretching by FTIR. The mesoporous silica shell dramatically enhanced the surface area of magnetic core due to the internal porosity in the nanocomposites. MS1 nanocomposites had the highest value of BET surface area 965 m^2g^{-1} with mesopores

diameter of around 3 nm. The saturation magnetisation values reduced significantly in MS nanocomposites when hydrophilic IONPs were used as cores. Whereas MS3 nanocomposites containing hydrophobic magnetic core showed relatively high saturation magnetisation value of 44.51 emu/g. Furthermore, ICG loading efficiency was dependent on surface area and showed higher loading in MS1ICG nanocomposites with encapsulation efficiency of 68.6% compared to MS2ICG (23.4%) and MS3ICG (32.2%)., The presence of encapsulated ICG in MSICG nanocomposites was confirmed by FTIR (a small peak at 1409 cm^{-1} due to N-H bending) and TGA weight loss of about 1.55% equivalent to calculated loading value from UV-vis spectrophotometer.

IO2 nanoparticles showed better heating efficiency by reaching the maximum set temperature of 42 ℃ within 88 seconds compared to IO1 at 196 seconds with SPA values of IO1- 35.8 W/g and IO2- 94.1 W/g under an AMF. Similarly, the MS2 nanocomposites showed better heating efficiency by reaching 42 ℃ within 129 seconds with SPA values of 58.1 W/g compared to MS1 (6.8 W/g) and MS3 (25.2 W/g). The results indicated the materials ability to magnetic hyperthermia therapy (MHT) as potential cancer therapeutics. Similarly, the MSICG showed heating efficiency under NIR laser irradiation (wavelength- 808 nm, power density- 1.2 W/cm^2). An increase in temperature of up to 22 ℃ in 6 minutes for MS3ICG when compared with MS1ICG (19 ℃) and MS2ICG (13 ℃). The results indicated the presence of ICG as a photosensitiser increased the materials ability for PDT/PTT. Therefore, application of both AMF and laser as external stimuli can be considered as multimodal routes in cancer therapeutics.

Furthermore, MS2ICG and MS3ICG nanocomposites were systematically studied for their therapeutic efficiency *in-vitro* using a commercial breast cancer cell line, MCF7. Cultured MCF7 cells treated with MS2ICG and MS3ICG nanocomposites in the presence of AMF and laser irradiation showed higher cancer cell killing efficiency with potential for dual cancer therapeutics. Further evaluation of MCF7 cells treated with laser irradiation alone showed effective dose and time dependent cancer cells killing efficiency. Further investigation of endocytosis using different endocytic inhibitors suggested the nanocomposites internalisation was an active energy dependent pathway followed by multiple other pathways, mainly clathrin-mediated endocytosis.

Furthermore, the assessment of oxidative stress in MCF7 cells upon treatment with nanocomposites in the absence and presence of external stimuli (laser irradiation) using cellular integrity markers and oxidative stress markers showed the presence of different reactive oxygen species (ROS) and reactive nitrogen species (RNS), responsible for cellular damage. The elevated value of lactase dehydrogenase (LDH) and lipid peroxidation (LPO) suggested the cellular damage caused due to the ROS

generation. The DCFDA (2',7'-dichlorodihydrofluorescein diacetate) assay provided further evidence of ROS generation *via* higher fluorescence in cells treated with MSICG nanocomposites. Finally, both MSICG nanocomposites tested for apoptotic gene expression by RTPCR showed the elevated pro-apoptotic genes such as p53, Bax and a decrease in anti-apoptotic gene Bcl-2.

In conclusion, the synthesised magneto-optical nanocomposites (MSICG) exhibited efficient MHT/PDT/PTT effects due to the presence of both magnetic and optical components and opened an avenue for further investigation *in-vivo* with potential for cancer therapeutics.

TABLE OF CONTENTS:

ACKNOWLEDGEMENT

I would like to extend my gratitude to everyone who supported, guided, or contributed over the course of my PhD. Firstly, I am extremely grateful to my Director of Studies (DoS) Dr Tapas Sen for welcoming me in his laboratory. I am very thankful for his guidance, patience, constant encouragement, and opportunities provided within and beyond my PhD journey. I sincerely thank Professor Kamalinder K Singh, my second supervisor, who encouraged me to join this project and shared her incredible expertise on nanoparticle formulation and cell culture. I am grateful to Professor Indrajit Roy for his support during my short visit in his lab, University of Delhi and providing guidance on experimentation with optical probes and laser irradiation. I am always grateful to Professor Anita Kamra Verma for her guidance and supporting me during my visit in Kirori Mal College, University of Delhi, which has helped me to successfully complete *in-vitro* and oxidative stress studies. I am grateful to Dr Tim Mercer for sharing his expertise in magnetic nanoparticles and performing magnetisation studies. Without their guidance, the thesis work would be impossible to complete.

There are many people I am grateful for sharing their words of motivation when I needed the most and teaching me techniques when I was a novice. Thank you to Dr Yogita Patil Sen for being kind and sharing her expertise in synthesising iron oxide nanoparticles and guiding me to conduct *in-vitro* experiments. I am grateful to Dr Runjie Mao for his support in TGA and BET experiments. I am very much thankful to Dr Andrea Julie Burrow for providing training and guidance *in-vitro* research and Dr Sarah Rachel Dennison for her support as lab manager.

I must thank my friends, especially Monika Yadav and Largee Biswas for supporting me to conduct *in-vitro* research and data analysis, and all the friends from Professor Roy's and Verma's lab, who welcomed me wholeheartedly and made my stay in India one of the greatest experiences that I will always look back with joy. I would also like to thank my colleagues, Dr Abdullah Alakalabi, Dr Naif and Dr Joseph Owede Adoghe for their encouragement and support for making this journey a pleasant one.

I would like to acknowledge University of Central Lancashire for providing me a great research environment and also supporting me financially, mainly at the time of Covid-19 pandemic. I would like to thank UKEIRI (IND/Cont/G 16-17/62) for partially funding my project. I would like to thank all the staff and lab technicians who have supported me in this journey, to name few, Clare Altham, Khalil Ahmed Patel, Tamar Garcia Sorribes, Dr Peter Bentley and Sameera Mahroof.

Lastly, a special thank you to Mum, Dad, my husband, my sister, and brother-in-law for supporting and encouraging me in every step and holding me steady when times were tough. This journey would not have been possible without the support of my family. Lots of love to my nephews. Thank you!

LIST OF TABLES:

LIST OF FIGURES:

ABBREVIATION LIST

$^1O_2$	Singlet oxygen	DNA	deoxyribonucleic acid
ABMDMA	9,10-anthracenediyl-bis (methylene) dimalonic acid	DPBS	Dulbecco's Phosphate Buffered Saline
AMF	Alternating magnetic field	DPX	Dibutyl phthalate Plasticizer Xylene
ATCC	American Type Culture Collection	DTNB	5,5'-Dithiobis (2-nitrobenzoic acid)
Bax	Bcl2-Associated X Protein	EDTA	ethylenediaminetetraacetic acid
Bcl-2	Antiapoptotic B cell leukemia/lymphoma 2	EE	Encapsulation efficiency
BET	Brunauer-Emmett-Teller surface area analysis	EPR	Enhanced Permeability and Retention
BSA	Bovine serum albumin	FBS	Fetal Bovine Serum
		Fe^{2+}	Ferrous ion
Cas9	Caspase9	Fe^{3+}	Ferric ion
cDNA	Complementary deoxyribonucleic acid	FTIR	Fourier Transform Infrared Spectroscopy
CDNB	1-chloro-2,4-dinitrobenzene	GAPDH	Glyceraldehyde-3-Phosphate Dehydrogenase
CDT	Chemodynamic therapy	GPx	Glutathione Peroxidase
CFE	Cell free extract	GR	Glutathione reductase
CO_2	Carbon dioxide	GSH	Reduced Glutathione
CTAB	Cetyltrimethylammonium bromide	GAPDH	Glyceraldehyde-3-Phosphate Dehydrogenase
DAPI	4′,6-diamidino-2-phenylindole	GSSG	Glutathione disulfide
DCF	Dichloro fluorescein	H_2O_2	Hydrogen peroxide
DCFDA	2',7'-dichlorodihydrofluorescein diacetate	HCl	Hydrochloric acid
DLC	Drug loading capacity	HEPES	(4-(2-hydroxyethyl)-1-piperazineethanesulfonic acid
DLS	Dynamic Light Scattering	ICG	Indocyanine Green
DMEM	Dulbecco's Modified Eagle Medium	ILP	Intrinsic Loss Power
DMF	N, N-dimethylformamide	IO	Iron oxide
DMSO	Dimethyl sulphoxide	IONPs	Iron oxide nanoparticles

IR	Infrared
LDH	Lactate dehydrogenase
LPO	Lipid peroxidation
MEM	Minimum Essential Medium
MS	Magnetic core silica shell nanocomposites
MSICG	Magnetic silica indocyanine green nanocomposites
MTT	3-(4,5-dimethylthiazol-2-yl)-2,5-diphenyl tetrazolium bromide
MWCO	Molecular weight cut-off
NaOH	Sodium hydroxide
NBT	Nitro blue tetrazolium
NEDD	*N*-1-napthylethyldiamine dihydrochloride
NEEA	Non-essential amino acids
NIR	Near infrared
NO	Nitric oxide
OA	Oleic acid
OD	Optical density
p53	Tumour protein p53 gene
PBS	Phosphate buffered saline
PCR	Polymerase chain reaction
PDT	Photodynamic therapy
PMS	Phenazine methosulphate
PTT	Photothermal therapy
RNA	Ribonucleic acid
ROS	Reactive oxygen species
RT	Room temperature
RT-PCR	Real time polymerase chain reaction
SD	Standard deviation
SDS	Sodium dodecyl sulphate
SEM	Scanning Electron Microscope
SOD	Superoxide dismutase
SPA	Specific Power Absorption
SPL	Specific Power Loss
TBA	Thiobarbituric acid
TBHP	Tert-Butyl Hydrogen Peroxide
TCA	Trichloroacetic acid
TEM	Transmission Electron Microscope
TEOS	Tetraethyl orthosilicate
TGA	Thermogravimetric Analysis
VSM	Vibrating sample magnetometry
XRD	X-ray diffraction
βNADH	β-Nicotinamide adenine dinucleotide
βNADPH	β-Nicotinamide adenine dinucleotide 2′-phosphate reduced tetrasodium salt

UNITS AND SYMBOLS

a.u.	arbitrary unit
Å	ångström or angstrom = 1×10^{-10} m
A/m	Ampere/metre
B	Magnetic field
C_{np}	Specific heat of nanoparticles
C_s	Specific heat of solvent
℃	degree Celsius
cm	centimetre
d	diameter
D_C	critical diameter
emu	electromagnetic units
f	frequency
g	gram
H	Field intensity amplitude
Hz	Hertz
J/g	Joules/gram
J/sec	Joules/seconds
K	degree Kelvin
kD	kilodalton
kHz	Kilohertz
kOe	kilooersted (1×10^{3} Oe)
kV	kilovolt (1×10^{3} V)
m	metre
M	molar (moles per litre)
M_s	Saturation magnetisation
mg	milligram (1×10^{-3} g)
min	minutes
ml	millilitre (1×10^{-3} L)
mm	millimetre (1×10^{-3} m)
mmol	millimoles (1×10^{-3} moles)
mV	millivolt
mW	milliwatt
nH	nanoHenry
nm	nanometre (1×10^{-9} m)
pH	potential of hydrogen
rpm	revolutions per minute
sec	seconds
T	Temperature
t	Time
v/v	volume per volume
W/kg	Watt/kilogram
w/v	weight per volume
µg	microgram (1×10^{-6} g)
µl	microlitre (1×10^{-6} L)
µM	micromolar
µmol	micromoles (1×10^{-6} moles)
%	Percentage
λ	wavelength

PROJECT MOTIVATION

In recent years, the search for externally targeted cancer therapy has been in the forefront of cancer research due to the limitation of current cancer therapeutics such as surgery, chemotherapy and radiotherapy involving invasive procedures, use of toxic chemicals and unspecific drug delivery causing life threatening acute or chronic side effects. The current challenges have driven towards the development of alternative cancer therapeutics such as nanomedicine. Nanomedicine involves the study of nanoscale materials (nanoparticles), which has escalated in its scope and complexity with the potential of a revolution in cancer therapeutics. As a recent trend on nanomedicine research, innovative ideas have emerged for monitoring, control, prevention, diagnosis, and treatment of diseases like cancer (Tinkle *et al.*, 2014; Soares *et al.*, 2018).

An exciting innovation in nanomedicine, idealised as “smart” multifunctional nanoparticles represents a combination of nanomaterials employing additional modalities that strategically improves cancer diagnosis and treatment (Dutta Chowdhury *et al.*, 2018). The multifunctional nanoparticles within a single platform possess multifunctional properties with encouraging outcomes in cancer research (Curry *et al.*, 2014). In this context, magnetic nanoparticles have been extensively used as magnetic contrasting agents in MRI, controlled drug delivery to the target sites under the influence of an external magnetic field and localised heating under an alternating magnetic field (AMF) as magnetic hyperthermia treatment (MHT). Similarly, optical nanoparticles such as quantum dots have evolved as potential bioimaging agents, however clinically proven to be highly toxic. Several organic dyes have been commonly used as bioimaging agents and have their own limitations due to low quantum yield and rapid photobleaching. In addition, most of the organic dyes have emission in the fluorescence region which has limited penetration depth. Therefore, near infrared dyes (NIR) have emerged as a new class of organic photosensitizers for bioimaging with potential therapeutic effect due to their ability to heat upon exposure of NIR light, named as photothermal therapy (PTT). In addition, they can also create reactive oxygen species (ROS) upon exposure of laser, which is responsible for cellular death, named as photodynamic therapy (PDT).

Therefore, a combination of magnetic and optical properties together on a single matrix as a new class of nanocomposites, named “Magneto-optical nanocomposites” are worth exploring as multi-modal cancer therapeutics.

CHAPTER 1

INTRODUCTION

1.1 Overview of Cancer

Cancer is a serious clinical challenge and a leading cause of death worldwide. In 2020, an estimated 19.3 million new cases of cancer and almost 10 million deaths from cancer were reported worldwide (Ferlay *et al.*, 2021). Despite substantial actions from the past and current research, scientific community is struggling to develop a universal route to cancer treatment. The ongoing Covid-19 pandemic halting or limiting the cancer research activity could further impact on the progression of the field (Fox *et al.*, 2021). As the cancer burden continues to grow globally, significant response and commitment of experts in cancer is vital.

Cancer is a disease involving uncontrolled growth of abnormal cells along with the potential to invade or spread to other parts of the body. The abnormality in cells is due to a defect in regulatory circuits that would otherwise govern normal cell proliferation and homeostasis. In 2000, Hanahan and Weinberg distinguished the alteration in cell physiology that governed the malignant growth of cells as hallmarks of cancer (Hanahan and Weinberg, 2000). With continuous conceptual progress on the study of cancer, in 2022, Hanahan has provided a new dimension on hallmarks of cancer such as, self-sufficiency in growth signals, insensitivity to growth-inhibitory signals, evasion of programmed cell death (apoptosis), limitless replicative potential, sustained angiogenesis, tissue invasion and metastasis, tumour-promoting inflammation, genome instability and mutation, unlocking phenotypic plasticity, non-mutational epigenetic reprogramming, polymorphic microbiomes, and senescent cells (Hanahan, 2022).

Researchers continuously study the hallmarks of cancer for the strategic development of cancer treatment. However, frequent mutation on cancer cells along with the complexities of treatment leads to development of resistance on the treatment over time. More than one hundred distinct cancer types with other cancer subtypes further increases the complexity. Current cancer treatments used worldwide includes surgery, chemotherapy, radiation therapy, immunotherapy, photodynamic therapy, hyperthermia and gene therapy (Arruebo *et al.*, 2011). The shortcomings of each of these treatments are associated with acute or chronic side effects. Other limitations include invasive procedures, pain, use of toxic chemicals and radiation, development of resistance to the chemical agents, restricted specificity on cancer type and late-stage diagnosis. Major drawbacks of these treatment procedures are their poor bioavailability, dose related toxicity and non-specific targeting that effects healthy tissues leading to elevated levels of side effects. To overcome these drawbacks, development of novel strategies with highly specific targeted delivery, enhanced bioavailability and biocompatibility, and precision therapy based on external stimuli (such as light, ultrasound or magnetic field)

should be the part of next mode of cancer treatment. To achieve the goal of specific cancer targeted therapy, scientists have sought the use of multifunctional treatment agents, particularly nanoparticles with lower toxicity that are stimulated or triggered from outside (external stimuli) and targeted towards specific tumour region.

1.2 Nanomedicine for Cancer Therapeutics

1.2.1 Definition of Terms Related to Nanomedicine

For the purpose of this thesis, some of the terms used to understand nanomedicine will be defined below as recommended by The International Organisation for Standardisation (ISO) (ISO/TR 10993-22:2017, 2017) or The European Commission (The European Commission, 2011) :

'Nanomedicine' is the use of nanoscale materials called nanomaterials designed for medical application.

'Nanoscale' is defined as a size range approximately from 1-100 nm (nanometre).

'Nanomaterial' is the material in an unbound state or as an aggregate or as an agglomerate with at least 50% or more particles in number size distribution and one or more external dimension in nanoscale (The European Commission, 2011) without significant difference on the axes and having internal or surface structure in the nanoscale (ISO/TR 10993-22:2017, 2017). This generic term is inclusive of nanoform or nano-object or nanoparticle.

'Aggregate' also termed as 'secondary particles' is strongly bonded or fused particles with significantly smaller external surface area compared to the sum of individual components surface area.

'Agglomerate' also termed as 'secondary particles' is the collection of weakly bound particles or aggregates or mixtures of the two with significantly smaller external surface area compared to the sum of individual components surface area.

'Colloid' is the heterogenous substance in a dispersion medium in which nanoscale particles uniformly suspend by their electrical charge.

1.2.2 Introduction of Nanomedicine for Cancer Therapeutics

Advances in materials science and nanotechnology have contributed to various interesting novel nanoscale materials with specific functions. The increase in number of nanomaterials containing products for therapeutics and diagnostics provides an innovative medical solution for the benefit of patients. Therefore, the European Union has recognised the use of nanotechnology as a 'Key Enabling Technology' to address unmet medical needs (Pita, Ehmann and Papaluca, 2016). The application of

nanotechnology has revolutionized modern medicine and a perfect example is the approval of Covid-19 nano vaccines at the time of the pandemic (Friedrichs and Bowman, 2021). In connection with cancer, clinical trials on various application of nanomaterials are being investigated such as enhanced drug delivery, early detection of diseases, bioimaging, targeted biopsy, and enhanced radiation and tracer agents (Kemp and Kwon, 2021).

Over the traditional cancer diagnostics and therapeutics (known altogether as theranostics) applications, nanomedicine has potential for improved early detection, improved treatment efficacy, and early diagnosis of cancer (Peer *et al.*, 2007). For the treatment of solid tumours, the main limitation of traditional approach is to achieve effective localised drug doses while avoiding healthy tissues. To overcome such limitations of the chemotherapeutic drug, particularly doxorubicin (Dox), FDA approved liposomal doxorubicin (Doxil), known as the first nanomedicine to be clinically approved (Shi *et al.*, 2017). Doxil demonstrates favourable toxicity profile without compromising the efficacy making it a favourable choice over the conventional drug with better cardiac safety and less side effects (Patel, 1996). The major timeline in development of cancer nanomedicine is provided by Shi *et al.* (2017 as shown in Figure 1-1. The major events such as discovery of liposomes, sustained delivery of low molecular weight compounds and controlled release polymeric system led to huge progress in cancer nanomedicine.

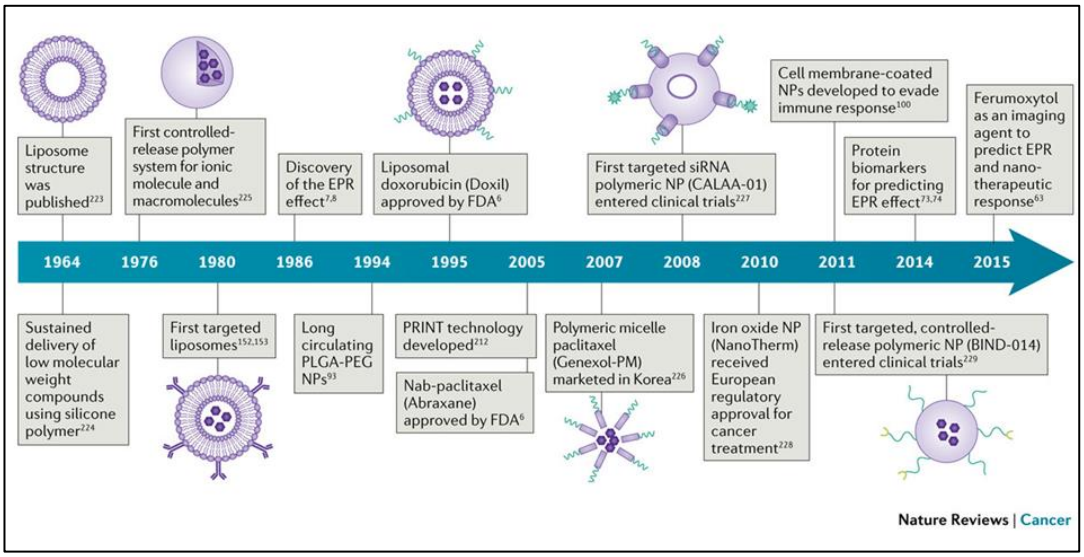

Figure 1-1: Major timeline in development of cancer nanomedicine. Reproduced from Shi *et al.* (2017)

Furthermore, with an advent of a key mechanism behind selective accumulation of nanomaterials into the tumour site, known as enhanced permeability and retention (EPR) effect (Matsumura and Maeda, 1986), the progress of cancer nanomedicine increased rapidly making it a better candidate for cancer therapeutic applications

(Maeda, Nakamura and Fang, 2013). The EPR effect is thought to be hyperpermeability of the tumour vasculature with poor lymphatic drainage leading to leakage of products to the solid tumour site and referred as passive tumour diffusion or passive targeting. The malformed structure of tumour vessels differs from normal healthy tissues having irregular shaped, dilated and leaky blood vessels, misaligned endothelial cells with large fenestration, wide lumen, and abnormal basement membranes (Iyer *et al.*, 2006). Thus, the systemic delivery of nanoparticles is enhanced in tumours. Many studies validating the effectiveness of EPR effect range from animal tumour models to clinical applications (Maeda, Tsukigawa and Fang, 2016; Golombek *et al.*, 2018).

However, the dependence on EPR only is questionable as there are multiple biological steps in the systemic delivery of nanoparticles that influence the EPR effect, such as nanoparticle-protein interaction, blood circulation, extravasation and interaction with tumour microenvironment, tissue penetration and cell internalisation (Shi *et al.*, 2017). Similarly, inadequate EPR effect of nanomedicines is observed in large solid tumours identified as 'heterogeneity of EPR effect', requiring further improvement in formulation of nanomedicines that use EPR effective therapeutic application (Fang, Islam and Maeda, 2020). In addition, the biological processes are influenced by the properties of nanoparticles, thus threatening the EPR effect and therapeutic outcomes. Some key factors that must be taken into consideration during nanomaterials design comprise physicochemical properties such as particle size, shape, surface charge, elasticity, stiffness, porosity, composition, targeting ligands and stability; interaction of nanoparticles with tumour and tumour microenvironment; and interaction of nanoparticles with the bio-compounds (i.e., biomolecules, proximal fluids, etc.) (Auría-Soro *et al.*, 2019). The targeting ability can be enhanced through active targeting using specific biomolecules or biomarkers so that the nanoparticles are actively diffused to specific organs/tissues/cells.

Although the first cancer nanomedicine has been in clinical practice for decades, eventually only few nanomaterial products are approved for cancer treatment in US and Europe (**Error! Reference source not found.**). Some of those cancer nanomedicines are based on organic and inorganic nanoparticles such as liposomes, albumin, micelles, iron oxides or hafnium oxides (Kemp and Kwon, 2021). Doxil was the first approved liposomal Dox cancer nanomedicine as mentioned earlier. However, in an attempt to reduce additional toxicity, improve biodistribution to the tumour site, increase potential of dual functionality as therapeutics and diagnostic agents, the encapsulation of Dox using different organic or inorganic nanomaterials is being thoroughly investigated (Dutta Chowdhury *et al.*, 2018). Similarly, a number of clinical trials are in progress utilising

various approaches to target tumour for cancer therapy (Fan and Zhang, 2013; Kenchegowda *et al.*, 2021).

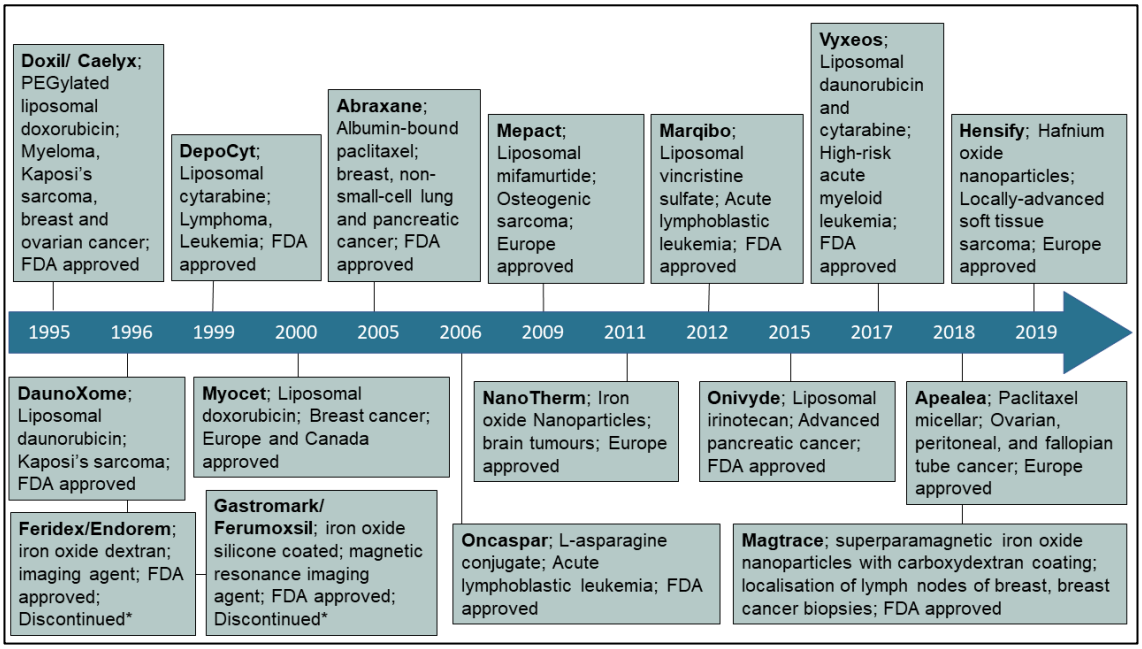

Figure 1-2: Clinically approved cancer nanomedicines. Nano-formulated cancer therapeutics clinically approved by US and Europe. *Discontinued: iron oxide nanoparticles were discontinued in 2012. Adapted from Kemp and Kwon (2021)

The strategies to improve the performance of nanomedicines using nanoparticulate systems is considered to be novel research as the distinct physicochemical properties of certain nanomaterials enhance the imaging of tumour, decrease radiation exposure time, lower toxicity, circumvent drug resistance, and facilitate multifunctional treatment modalities (Kemp and Kwon, 2021). An exciting innovation in nanomedicine, idealised as "smart" multifunctional nanoparticles represents a combination of nanomaterials employing additional treatment modalities that strategically improves cancer therapeutics and diagnostics (Chowdhury et al., 2018). Multifunctional nanoparticles hold the promise of accurately targeted cancer treatment with successful outcome within a single platform (Curry et al., 2014). These modalities enrich the controlled drug release to specific tumour sites and minimal release in normal cells with low drug doses. It reduces the cytotoxic effects of chemotherapeutic drugs to normal tissues with enhanced performance on killing cancer cells. A unique platform of multifunctional nanoparticles with magnetic and optical properties holds advantage of additional cancer therapeutics which will be discussed further as the main work of the thesis.

1.3 Magnetic Materials and Iron Oxide Nanoparticles

The revolution in applications of nanoscale magnetic materials extends from magnetically driven toxic metal ions separation from polluted water to many biomedical applications such as magnetic bead based separation of biomolecules, catalytic support, biomolecular testing, magnetically targeted drug delivery, early detection, therapeutic treatment by heating under an alternating magnetic field (AMF), contrast agents for magnetic resonance imaging (MRI), magnetic levitation for disease diagnostics, etc (Sen, Sebastianelli and Bruce, 2006; Sen, Bruce and Mercer, 2010; Mahmoudi *et al.*, 2011; Sen *et al.*, 2012; Bakhtiary *et al.*, 2016; Ashkarran and Mahmoudi, 2021). Magnetic nanoparticles (MNPs) have attracted huge attention of cancer researchers as a promising agent for theranostic approaches (Xu and Zhu, 2016).

In magnetic materials, magnetism arises from the movement of electrons within atoms. A magnetic field is created by the spin and orbital motion of unpaired electrons and their resultant magnetic moments. Since orbital moment in solids is often quenched due to coulombic crystal field, the moment per atom or ions is due to the spin of unpaired electrons. These unpaired electron spins determine the classification and behaviour of different magnetic materials as summarised in Table 1-1. In all the cases except diamagnetic materials and weak paramagnetic materials, below its Curie temperature, the atoms and unpaired electrons energetically align in a lower net energy state leading to a spontaneous magnetisation throughout the material. However, on application of an external magnetic field, the magnetic moments are aligned to create a net magnetic moment. Above the Curie temperature, materials become paramagnetic due to energy of thermal agitation as moments flip randomly in the thermal field.

Table 1-1: Summary of distinct magnetic behaviours and their characteristics. Reproduced from Lamichhane *et al.* (2022)

Type of Magnetism	Characteristics	Direction of spins state
Ferromagnetic	Atoms hold parallel aligned magnetic moments due to exchange interaction between adjacent unpaired electrons. Ferromagnetic materials possess a permanent magnetic field.	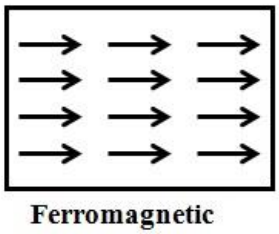 Ferromagnetic
Paramagnetic	Atoms possess randomly angled magnetic moments due to thermal agitation. Under the influence of a magnetic field the magnetic moments align to create a low magnetisation with direction similar to that of the field.	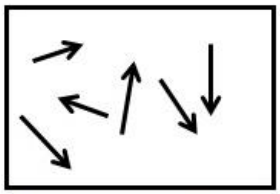 Paramagnetic
Antiferromagnetic	Atoms hold antiparallel aligned magnetic moments. The magnetic fields counteract, and the material behaves like a paramagnetic material above the Néel Temperature.	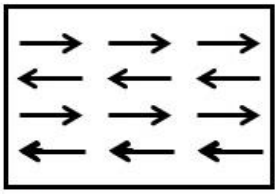 Antiferromagnetic
Ferrimagnetic	Atoms possess mixed parallel and antiparallel aligned magnetic moments of direction-dependent magnitude. Here the 'up' moment is greater than the 'down' moment and so results in an overall magnetisation in the 'up' direction (pointing to the right in the schematic). Hence these materials behave like ferromagnetic materials but with lower saturation magnetisations.	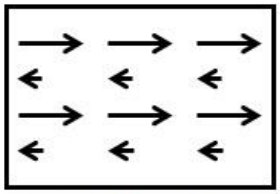 Ferrimagnetic
Diamagnetic	Atoms have no net magnetic moment in zero field. In the presence of an externally applied field a small negative magnetisation is apparent, i.e., in the opposite direction to that of the applied field	No unpaired spins

Among many MNPs, iron oxide nanoparticles (IONPs) have attracted interest due to their availability, low environmental impact (as naturally occurring minerals) and can be readily synthesised in the laboratory. Common IONPs for clinical studies include magnetite (Fe_3O_4) and maghemite (γ-Fe_2O_3) which can be oriented by an external magnetic field with special characteristic of superparamagnetism (Mahmoudi *et al.*,

2011). Each of these iron oxides possess unique magnetic, catalytic, and biochemical properties with suitability for specific biomedical applications. The crystalline structure of various IONPs is shown in **Error! Reference source not found.**. Hematite is the most stable iron oxide and also used as a starting material to synthesise magnetite and maghemite (Wu *et al.*, 2010). Hematite structure is composed of Fe^{3+} ions occupying two-thirds of the octahedral sites with hexagonal close-packed O lattice as shown in **Error! Reference source not found.**. Magnetite has a cubic inverse spinel structure consisting of 32 O^{2-} ions in cubic closed packed array with all Fe^{2+} occupying half of the octahedral structure while Fe^{3+} split evenly across remaining octahedral and tetrahedral sites. Maghemite is cubic structured with each unit containing 32 O^{2-} ions giving rise to a cubic array with 8 Fe^{3+} ions distributed over tetrahedral sites.

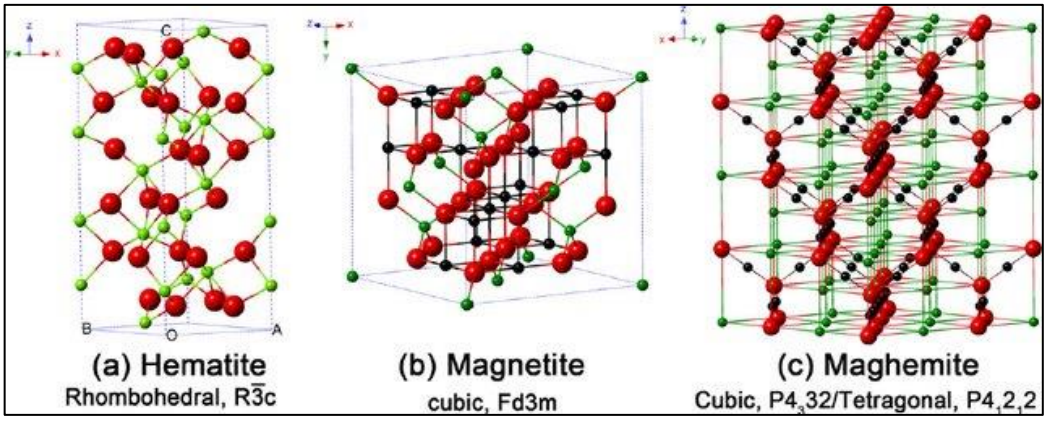

Figure 1-3: Crystallographic data and crystal structure of hematite, magnetite and maghemite. Black ball is Fe^{2+}, green ball is Fe^{3+} and red ball is O^{2-}. Open access for Creative Common: Wu *et al.* (2015)

1.3.1 An Overview of Synthesis of Iron Oxide Nanoparticles

IONPs are prepared by various methods such as dry processing, wet chemical, microbiological, or green chemistry. Mainly, these are differentiated as physical, chemical, and biological methods. Physical methods such as pulsed laser deposition or sputtering are used to grow spinel ferrites (Sun *et al.*, 2014). However, the main limitation of this method is an inability to control size of particles in nanometre size range (Ali *et al.*, 2016). Chemical methods consist of a wide range of methods that are convenient, efficient, and managed in terms of size, shape, and composition of nanoparticles. The methods are adopted by researchers due to their low production cost, narrow size distribution and high yield. Biological methods mainly comprise of bacteria, fungi, plant, protein, or animal mediated synthesis. A detailed comparison of most common synthesis methods is given in Table 1-2. As this thesis work is focused on chemical synthesis of iron oxide nanoparticles using the co-precipitation method, it will be further discussed in brief.

Table 1-2: Comparison of most common iron oxide nanoparticle synthesis methods.

Methods	Summary of synthesis method	Frequently used Iron Precursors	Reaction Temp. (℃)/ Reaction Period	Size distribution/ Shape Control	Reference
Co-precipitation	Very simple and convenient, use aqueous iron salt solution with base solution, performed under inert atmosphere, hydrophilic NPs	$FeCl_3.6H_2O$, $FeCl_2.4H_2O$, $FeSO_4$	20-150/ Hours-Days	Relatively narrow/ Polydisperse nanoparticles	(Sen *et al.*, 2006, 2012)
Thermal decomposition	Simple, organometallic compounds decomposed with stabilisers in organic solvents, performed under pressurised inert atmosphere, insoluble in water with limitation for nanomedicine application requiring surface engineering after synthesis	$Fe(acac)_3$, $Fe(oleate)_3$, $FeO(OH)$	150-220/ Hours-days	Very narrow/ Exceptionally good	(Lassenberger *et al.*, 2017)
Sonochemical	Quite simple, uses high intensity/ high energy ultrasonication and pressure of over 1800 kPa	$Fe(OH)_2$, $FeCl_3$, $FeSO_4$, $Fe(CO)_5$, $Fe(OAc)_2$	20-80/ Minutes	Narrow/ Inconsistence	(Fuentes-García *et al.*, 2020)
Microemulsion	Little complicated, uses nanosized water droplets in oil phase condition in presence of surfactant or cosurfactant molecules. Usually needs several washing processes and further stabilization treatments	$FeCl_3.6H_2O$, $FeCl_2.4H_2O$	20-80/ Hours	Narrow/ Good	(Vidal-Vidal, Rivas and López-Quintela, 2006; Wu, He and Jiang, 2008)
Sol-gel	Complicated, multi-step reaction, Particle size controlled by annealing temperature under vacuum, high purity	$C_{15}H_{12}FeO_6$, $FeCl_3.6H_2O$	200-400/ Hours	Narrow/ Good homogeneity	(Qi, Yan and Li, 2010; Lemine *et al.*, 2012)
Electrochemical reduction	Very Simple, cathodic electrodeposition from a nitrate bath in presence of stabilisers, can effectively control the composition, crystallinity, purity, particle size and deposit properties	$Fe(NO_3)_3 \cdot 9H_2O$ $FeCl_2 \cdot 4H_2O$, $(NH_4)_2Fe(SO_4) \cdot 6H_2O$	20-150/ Minutes	Relatively narrow/ Not good	(Starowicz *et al.*, 2011)
Hydrothermal	General phase transfer, multi-step, forced hydrolysis of the reactants, performed under high pressure	$FeCl_3.6H_2O$, $FeCl_2.4H_2O$, $FeSO_4$	100-220/ Hours-days	Relatively narrow/ Good	(Cai *et al.*, 2013)
Microwave assisted	Use of electromagnetic radiation, homogenous heating of reaction solution, advantage of rapid volumetric heating, high reaction rate, low cost.	$FeSO_4$, $Fe_2(SO4)_3$ $FeCl_3$, $Fe(acac)_3$	30-200/ Minutes-Hours	Relatively narrow/ Good	(Fernández-Barahona, Muñoz-Hernando and Herranz, 2019)
Biomimetic	Produced by magnetotactic bacteria, species specific synthesis, mineralisation processing to form uniform NPs	-	-	Relatively narrow/ Good	(Klem, Young and Douglas, 2005)
Green synthesis	Complicated, uses organic matter from plant or animal extracts, reduction reaction of ferric and ferrous chlorides	$FeCl_3$	RT -55/ Hours-Days	Narrow/ Inconsistence	(Lakshminarayanan *et al.*, 2021)

In general, iron oxides such as magnetite are synthesised by co-precipitation by adding 1:2 molar ratio of Fe^{2+} and Fe^{3+} ions in a basic aqueous solution, resulting in a black coloured precipitate. The overall reaction is written as:

$$\boldsymbol{Fe^{2+} + 2Fe^{3+} + 8OH^{-} \rightarrow Fe_3O_4 + 4\,H_2O} \qquad \text{(Equation 1-1)}$$

The particle size as well as polydispersity of the nanoparticles can be somewhat controlled by tailoring the associated factors such as Fe^{2+}/Fe^{3+} ratio, base solution used (NaOH, NH_4OH, and CH_3NH_2), ionic strength ($CH_3NH_3^+$,$(CH_3)_4N^+$, NH_4^+, Na^+, K^+), temperature (RT to 80 ℃), rate of mixing, agitation, inert gas used and pH (Ali *et al.*, 2016). The main limitations of IONPs synthesised by co-precipitation are their broad size distribution, aggregation, oxidation, and purity. The nanoparticles aggregate mainly due to their large surface area to volume ratio. To reduce the surface energy, the nanoparticles tend to come in close contact resulting in the formation of larger aggregates which are difficult to dissociate. It is however established that a short burst of nucleation and subsequent slow controlled growth produces monodisperse nanoparticles (Lu, Salabas and Schüth, 2007). Furthermore, nanoparticles such as magnetite tends to oxidise in air losing its form to become maghemite. To avoid the oxidation of Fe^{2+} into Fe^{3+} during synthesis, normally an inert gas atmospheric arrangement is used (Mascolo, Pei and Ring, 2013). However, boiling condition to remove dissolved oxygen can also be used to synthesis magnetite (Bandhu *et al.*, 2009). In many cases, starting mixture of the nanoparticles are polydisperse requiring additional processing to maintain narrow size distribution. For instance, researchers have used sequential centrifugation to obtain monodispersed iron oxides from a polydisperse suspension (Dadfar *et al.*, 2020). Significant measures have been taken by researchers in preparing magnetite nanoparticles *via* co-precipitation method to reduce these limitations, which will be discussed later in this chapter.

1.3.2 Properties of Iron Oxide Nanoparticles and Their Therapeutic Applications

IONPs have attracted considerable interest in cancer treatment due to their properties such as superparamagnetism, magnetic hyperthermia under AMF and Fenton reaction mediated catalytic activity. Each of these properties will be discussed below in accordance with their importance in cancer therapeutic application.

1.3.2.a Superparamagnetic Properties

As illustrated earlier in Table 1-1, both ferromagnetic and ferrimagnetic materials possess spontaneous magnetisation. Until and unless effort is made to magnetise the materials, they do not show their magnetic properties. The reason for this apparent lack

of magnetisation can be explained by the term “domain”. In magnetic materials, the magnetic moments are aligned within a region called domain separated by a barrier called domain wall. Each of these domains have their own spontaneous magnetisation and on application of external magnetic field, multiple domains align to be fully magnetised to the direction of the magnetic field and saturate the magnetisation. This magnetisation is called saturation magnetisation (M_s). When the applied magnetic field is removed, ferromagnets retain the memory of applied field called remanence (M_r). The magnetisation of the materials is reduced to zero by applying coercive force (H_c). The magnetic response of these magnetic materials under the external magnetic field can be studied using a hysteresis cycle as presented in **Error! Reference source not found.** B. The hysteresis cycle is described by variation of degree of magnetisation (M) with intensity of magnetic field (H), commonly referred as magnetisation curve. As shown in **Error! Reference source not found.** B, ferrimagnetic nanoparticles show a hysteresis where area of hysteresis loop indicates the energy dissipation upon reversal of magnetic field. The magnetic materials of larger hysteresis loop with high remanence and coercivity are desirable for permanent magnets which are known as hard magnets. But for clinical studies, the magnetic materials which can be easily magnetised and demagnetised at low magnetic field with low coercivity (H_c) are sought after which are known as soft magnets.

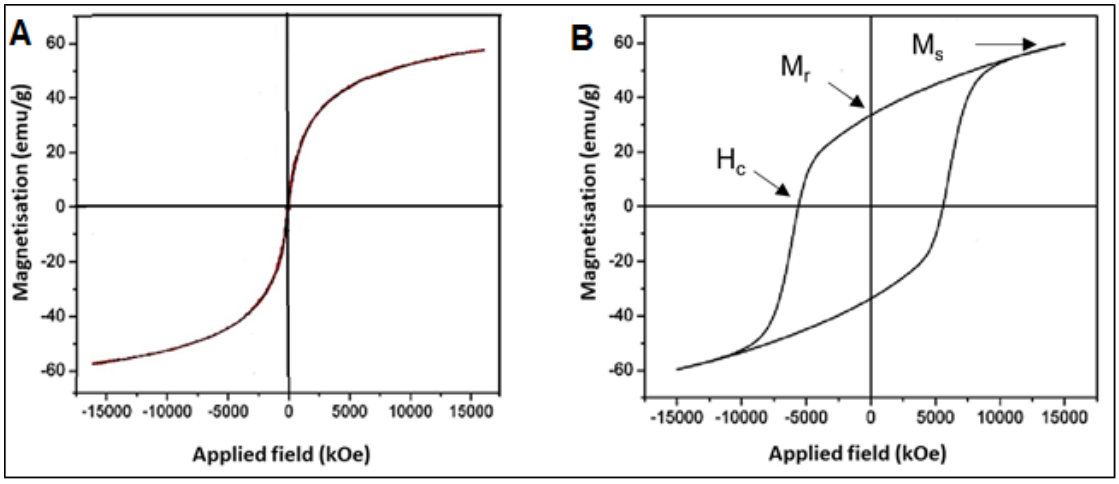

Figure 1-4: A typical hysteresis loop obtained from superparamagnetic (A) and ferromagnetic (B) materials- magnetisation vs applied magnetic field. M_s: Magnetic saturation, M_r: Remanent magnetisation, H_c: Coercivity

When the size of these magnetic materials is reduced to sub-micron scale i.e., around few nanometres, the decrease in size equates to a single domain structure. For example, critical single-domain size of spherical magnetite and maghemite occurs at around diameter (d) 128 nm and 166 nm, respectively (Leslie-Pelecky and Rieke, 1996). Thus, a decrease in size, creating single domain MNPs, creates a new property known

as superparamagnetism. Superparamagnetism is a phenomenon that allows the nanoparticles to avoid permanent magnetic moment (as ferromagnetic nanoparticles) but attracted by the influence of an external magnetic field. Such individual nanoparticles have a fast response to applied magnetic field (H) with negligible remanence (M_r) and coercivity (H_c) and represents a closed or zero hysteresis loop (**Error! Reference source not found.** A).

This property is especially useful as site-specific drug or diagnostic agent delivery since no permanent magnetic moment is achieved until an external magnetic field is applied. Many researchers have worked on these iron oxides and are commonly known as superparamagnetic iron oxide nanoparticles (SPIONs). M_s values for SPIONs are generally reported to be in the range of 30-60 emu/g compared to 100 and 80 emu/g, respectively for bulk magnetite and maghemite at 5 K and 30 KOe (Dadfar *et al.*, 2020). Mostly, biocompatible SPIONs with a diameter smaller than 100 nm shows the property of superparamagnetism. The superparamagnetic property is dependent on the particle size, shape, and surface coatings of magnetic materials and these are key factors in engineering nanoparticles for clinical application. According to Kim *et al.* (2009), when nano cubes in the range of 20-160 nm were measured in accordance with their coercivity, the particle size of ~20 nm showed the superparamagnetic property.

1.3.2.b Hyperthermia

Another significant property of MNPs is the increase in heating efficiency under an applied alternating magnetic field (AMF) known as “magnetic hyperthermia”. The heat induced by MNPs in a carrier fluid is generally due to three independent mechanisms, namely, hysteresis loss, Néel relaxation and Brownian relaxation (Figure 1-5, top left) (Suriyanto, Ng and Kumar, 2017). Hysteresis loss is the energy loss associated with shifting domains in multi-domain MNPs while reversing the magnetization of the material. The hysteresis loss is calculated from the area enclosed by the hysteresis loop (**Error! Reference source not found.** B). As superparamagnetic nanoparticles have negligible coercivity and remanence with near zero hysteresis loop, the hysteresis loss is insignificant compared to other two mechanisms of heat induction.

The relaxation losses in single domain MNPs under AMF is caused by the gradual alignment of magnetic moments during magnetisation. When the particles are assumed to be physically constrained, the only mechanism of relaxation considered would be the reorientation of magnetisation vector within the particles in order for them to stay aligned in the changing field direction known as Néel relaxation (Figure 1-5, top left). Néel relaxation time (t_N) is represented as:

$$t_N = t_0 e^{\frac{KV}{kT}}$$ (Equation 1-2)

where, t_0 = 10^{-9} sec, K = anisotropy constant, V = volume of magnetic nanoparticles, k = Boltzmann constant and T = temperature.

In a ferrofluid, the MNPs rotate themselves resulting in friction and consequently loss in energy known as Brownian relaxation (Figure 1-5, top left). Brownian relaxation is more significant in ferrofluid upon AMF and the major reason for heat generation. The Brownian relaxation time (t_B) is represented as:

$$t_B = \frac{3\eta V_B}{kT}$$ (Equation 1-3)

where, η = viscosity of carrier liquid, V_B = hydrodynamic volume of particle, k = Boltzmann constant, T = temperature.

Upon the removal of magnetic field, the magnetisation relaxes back to zero by both Néel and Brownian relaxation working in parallel. The effective relaxation time (t) is given as:

$$t = \frac{t_N t_B}{t_N + t_B}$$ (Equation 1-4)

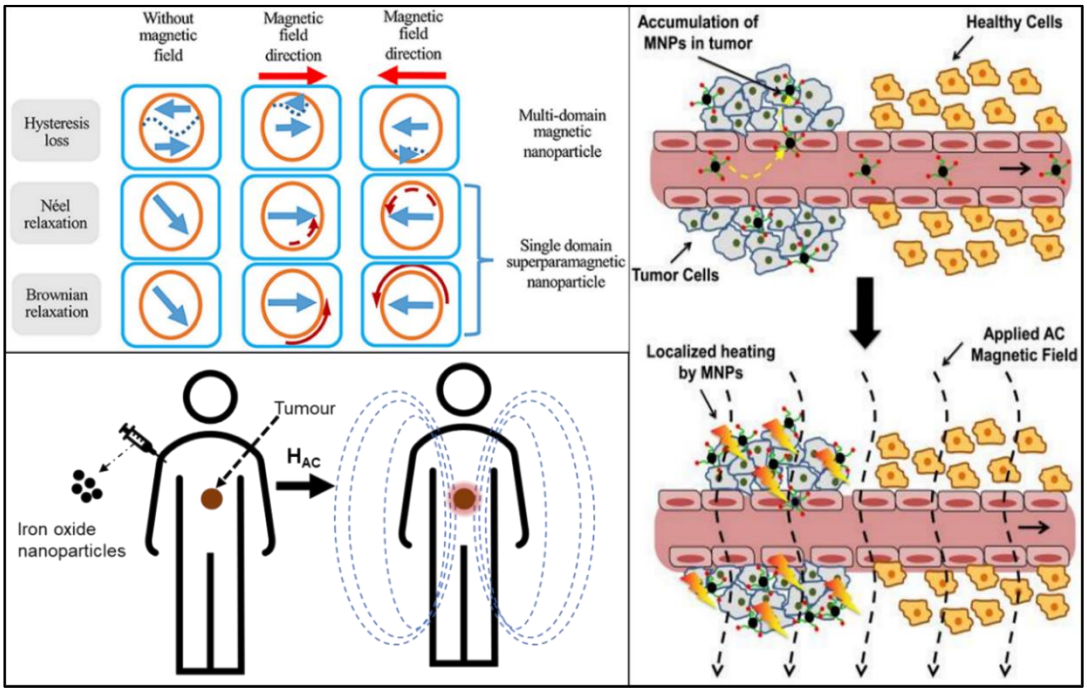

Figure 1-5: Principles of Magnetic Hyperthermia Therapy (MHT) under alternating magnetic field (AMF). Top left: Mechanism of heat generation. Orange circles: iron oxide nanoparticles, short straight arrows: magnetic field direction, solid curved arrow: the movement, dashed curved arrow: change in magnetic moment direction, and dashed lines: domain boundaries in multi-domain particles. Adapted from Suriyanto, Ng and Kumar (2017) Bottom left: Schematic representation of MHT in tumour patients, Right: Targeted magnetic nanoparticles delivery and MHT. Adapted from Cole, Yang and David (2011).

MNPs can be extensively used as seeds for cancer hyperthermia therapy (Figure 1-5, right). The concept of magnetically induced hyperthermia using magnetic materials was first introduced by Gilchrist and colleagues (Gilchrist *et al.*, 1957), and later advanced with introduction of magnetic nanoparticles. According to Sanz *et al.* (2017), magnetic hyperthermia therapy (MHT) or thermotherapy is the delivery of heat to the tumour cells by using MNPs also called 'nano-heaters' under an alternating magnetic field (AMF). Usually, this procedure involves the introduction of MNPs in the tumour site and subsequent irradiation of high frequency AMF raising a normal body temperature of 37 ℃ to temperature range of 41-45 ℃ (Figure 1-5, bottom left) (Suriyanto, Ng and Kumar, 2017). The increase in temperature due to the magnetic hyperthermia is ideal for killing cancer cells if MNPs accumulate in tumour region with minimal damage to normal cells (Figure 1-5, right). This increase in temperature in cancer cells alters the cellular metabolism, leads to cellular damage, and induce apoptosis.

The usefulness of this procedure depends upon the accumulation of MNPs on the tumour site generating as much heat as possible, at the lowest nanoparticles content. Therefore, the MNPs are either targeted through passive (EPR effect) or active (biomarkers) targeting, or magnetically targeted to the tumour site. When the accumulation of MNPs around the tumour cells increases, under AMF, the nanoparticles absorb energy by increasing alignment with the applied magnetic field and converts this energy to heat as the particles undergo relaxation (Cole, Yang and David, 2011). Another limiting factor for the safety of MHT for clinical application is the product of magnetic field intensity and frequency, H×f, known as the Atkinson–Brezovich limit, established to be $H \times f = 4.85 \times 10^8\ Am^{-1}s^{-1}$ (Atkinson *et al.,* 1984). Patients could tolerate magnetic field intensities up to 36.3 A/m and a frequency of 13.56 MHz for extended time periods. However, the heat production depends upon the size of the exposed tissue changing the Atkinson–Brezovich safety limit. For instance, in Nanotherm® therapy, approved by FDA as MHT, patients with glioblastoma can tolerate magnetic fields up to 18 kA/m at 100 kHz ($H \times f = 1.8 \times 10^9\ Am^{-1}s^{-1}$) (Mahmoudi *et al.,* 2018). Similarly, recent *in-vivo* studies have shown H×f values up to $9.46 \times 10^9\ Am^{-1}s^{-1}$ was safe for MHT (Herrero de la Parte *et al.,* 2022).

1.3.2.c Fenton Reaction Mediated Catalytic Activity

IONPs possess intrinsic peroxidase-like activity, suggesting they are capable of catalysing the oxidation of hydrogen peroxide (H_2O_2) into hydroxyl radical (·OH). It was first discovered by Yan *et al.* in 2007 and subsequently, researchers conducted extensive investigation on IONPs to mediate the generation of reactive oxygen species (ROS) for tumour treatment (Yu *et al.*, 2021). Reactive oxygen species (ROS) describes a number

of reactive molecules and radicals derived from molecular oxygen including superoxide ($\cdot O_2^-$), peroxides ($\cdot O_2^{-2}$), hydrogen peroxide (H_2O_2), hydroxyl radical ($\cdot OH$) and singlet oxygen ($^1O_2$).

Iron is a transition metal that exists mostly in the form of heme in our body as an essential molecule to support life. Paradoxically, free iron also has the potential to become cytotoxic when electron exchange with oxygen is unrestricted and catalyses the production of ROS (Soares and Hamza, 2016). Macrophages play a significant role in establishing the delicate balance of iron in the body and additionally, in the production of ROS (Soares and Hamza, 2016). Heme-iron transports electrons across biological membranes where production of superoxide occurs *via* the following reaction:

$$O_2 + e^- \rightarrow \cdot O_2^- \qquad \text{(Equation 1-5)}$$

Then, $\cdot O_2^-$ accumulates in macrophages giving rise to other ROS, *via* reaction with hydrogen peroxide (H_2O_2). H_2O_2 level within a tumour microenvironment is elevated and over-expressed due to insufficient blood supply as compared to normal cells (Szatrowski and Nathan, 1991; Chen *et al.*, 2012). In case of increase in H_2O_2, it acts avidly with iron to generate hydroxyl radicals ($\cdot OH$) and hydroxide ions (OH^-) and hydrogen peroxide radicals ($HOO\cdot$) in acidic lysosome condition. This latter step occurs *via* two iron-catalysed reactions known as Fenton reaction (Bedard and Krause, 2007):

$$\text{(i) } Fe^{2+} + H_2O_2 \rightarrow Fe^{3+} + HO\cdot + OH^- \qquad \text{(Equation 1-6)}$$

$$\text{(ii) } Fe^{3+} + H_2O_2 \rightarrow Fe^{2+} + HOO\cdot + H^+ \qquad \text{(Equation 1-7)}$$

Thus, the peroxidase-like activity of IONPs for H_2O_2 disproportionation and corresponding production of radicals can be used in cancer treatment. The production of ROS on the tumour cells damages DNA and protein and causes lipid peroxidation, thus killing cancer cells. This approach is referred as chemodynamic therapy (CDT).

1.3.3 Possibilities and Challenges of Iron Oxide Nanoparticles for Cancer Therapeutics

The IONPs are a promising candidate for a wide range of applications in cancer theranostics such as magnetic separation of biomolecules contributing to the development of diagnostics, magnetic drug targeting (MDT), magnetofection (MF) and gene delivery, magnetic hyperthermia therapy (MHT), magnetic resonance imaging (MRI), magnetic particle imaging (MPI), generation of reactive oxygen species (ROS) under near infrared (NIR) irradiation, etc (Kudr *et al.*, 2017; Estelrich and Busquets, 2018; Dadfar *et al.*, 2020). The IONPs are widely favoured because of the ease of synthesis,

presence of reactive surface for modification with biocompatible coatings, therapeutic molecules, targeting ligands and imaging agents.

Currently, SPIONs are being investigated for many *in-vitro* and *in-vivo* experiments as well as in clinical trials or clinically approved for medical imaging or therapeutic applications, which has recently been reviewed (Lamichhane *et al.*, 2021; Montiel Schneider *et al.*, 2022). A list of IONPs either in clinical trial or already approved and used for cancer therapeutics or diagnostics is given in Table 1-3. Amongst them, Ferumoxytol is an FDA approved IONPs used to treat iron deficiency anaemia in adults with chronic kidney diseases which is also used as 'off label' contrast agent for cancer imaging. Researchers are repurposing Ferumoxytol to treat early mammary cancers, and lung cancer metastases in liver (Zanganeh *et al.*, 2016). Nanotherm is another commercial IONPs which is intracranially injected to efficiently induced hyperthermia in glioblastoma treatment (Montiel Schneider *et al.*, 2022). Recently, Nanotherm has been approved by FDA to be repurposed for treating prostate cancer (MagForce USA, 2022). All of the approved IONPs till now provide passive targeting only.

Table 1-3: Commercial IONPs based materials for therapeutic and diagnosis in cancer treatment. Adapted from Lamichhane *et al.* (2022)

Company Name	**Generic Name**	**Brand Name**	**Applications**	**Clinical Trials**	**Clinically Approved**
AMAG Pharmaceuticals www.amagpharma.com	Ferumoxtran-10	Combidex® (USA) Sinerem® (EU)	lymph node and macrophage imaging	✓	
AMAG Pharmaceuticals	Ferumoxytol	Feraheme® (USA) Rienso® (EU)	Iron deficiency anaemia (IDA), 'Off-label' imaging	✓	✓
Bayer healthcare www.Bayer.com	Ferucarbotran	Resovist® (Japan) Cliavist® (France)	Liver imaging, CNS imaging, cell labelling	✓	
Berlex Laboratories	Ferumoxide	Feridex® IV (USA), Endorem® (EU)	Liver imaging, CNS imaging, cell labelling	✓	
AMAG Pharmaceuticals	Ferumoxsil	Lumirem® (USA) GastroMARK® (EU)	Oral MRI contrast agent	✓	✓
Imagion www.imagionbiosystems.com	-	PrecisionMRX®	Cancer detection using MagSense™ technology	✓	
Endomag www.endomag.com	Magnecarbodex	Sienna^{+} or MagTRACE™	Breast cancer lesion localisation and		✓

			tracer for sentinel node biopsies using Sentimag®		
Magforce www.magforce.com	Aminosilane coated SPION	Nanotherm	Magnetic Hyperthermia		✓

Amongst many ongoing clinical trials on these commercial IONPs, a major concern is toxicity. Many IONPs such as Ferumoxsil, Ferumoxide and Ferucarbotran have been discontinued in some countries or withdrawn because of the concerns of toxicity and other side effects (see timeline in **Error! Reference source not found.**). Therefore, biocompatibility and safety issues associated with IONPs should be dealt carefully. IONPs are reported to be toxic to normal cells (Patil *et al.*, 2018). One of the reasons for increase in cytotoxicity of IONPs is their ability to induce oxidative stress. As discussed earlier, IONPs can produce reactive oxygen species (ROS) which are responsible for killing cancer cells. However, IONPs can be toxic to normal cells as well if non-specifically targeted. In addition, IONPs have exceptionally low solubility that leads to agglomeration which can even obstruct blood vessels (Patil *et al.*, 2018). The agglomerated IONPs can be rapidly eliminated by the reticuloendothelial system (RES) (Sun *et al.*, 2014). So, to avoid these issues IONPs are usually coated with a suitable biocompatible material (e.g., silica or liposomes) for increasing colloidal stability, water dispersibility and biocompatibility, while reducing toxicity and agglomeration (Veiseh, Gunn and Zhang, 2010). The size of the nanoparticles also dictates their fate. In order to avoid filtration from spleen and liver and prolong blood circulation, the IONPs should be smaller than 500-200 nm yet larger than 10 nm to evade rapid kidney filtration. Additional ambiguity on research comparing the IONPs toxicity *in-vitro* and *in-vivo* could add challenges for IONPs. Toxicity studies *in-vivo* compared to responses in different cell lines, suggest there is the possibility that individuals may be able to maintain homeostasis by storing excess iron in the body; considerably reducing the side effects of SPIONs. Therefore, researchers should work to modify their approach in *in-vitro* cytotoxicity assessment for comparable results (Mahmoudi *et al.*, 2010).

Furthermore, IONPs present limitations when used alone for cancer therapeutics. Even though IONPs demonstrate effective therapeutic efficacy *in-vitro*, their efficacy *in-vivo* is not satisfactory. For instance, when IONPs are utilised for CDT to treat cancer, the intratumoural H_2O_2 might not be abundant enough for the production of ROS. The mild acidity of tumour microenvironment (TME) and the antioxidants present in the system for scavenging ROS can limit the efficacy of Fenton reaction (Liu *et al.*, 2022). In addition, IONPs alone are inefficient to induce heating efficiency and distribution *in-vivo* (Laurent *et al.*, 2011). The slow temperature increase upon externally triggered

hyperthermia may lead to thermal tolerance in cancer cells (Tang and McGoron, 2009). These drawbacks can be removed by using multimodal systems that combine the efficacy of IONPs with other therapeutics. For instance, their therapeutic efficacy can be improved by combining with photodynamic therapy (PDT) or photothermal therapy (PTT) where absorption of specific laser irradiation is higher and the conversion of energy to heat is more efficient than individual IONPs (Estelrich and Busquets, 2018). In addition, PTT-induced hyperthermia promotes hydroxyl radial (•OH) generation and accelerates ROS based oxidation of biological molecule (Liu *et al.*, 2022). Besides, it has been suggested that some of the drugs show improved efficiency under heat activation demonstrating a synergistic effect of hyperthermia and chemotherapy over monotherapy (Yang *et al.*, 2020).

1.4 Surface Functionalisation of Iron Oxide Nanoparticles

The stabilization and protection of IONPs are intricately linked with each other and are crucial requirements for almost all of their applications. Additionally, their properties need to be enriched because of their limitations for biomedical applications as explained earlier. Therefore, it is important to develop efficient strategies to protect IONPs and add chemical and physical functions on the surface for specific biomedical application. The coating layer may stabilise the nanoparticles and provide functional groups for the conjugation of additional moieties including targeting ligands, biomolecules, drugs, dyes, etc. The coating layer can be designed to limit non-specific cell interactions, reduce the toxicity of the bare IONPs, and prolong circulation time. Furthermore, it can be tailored for drug loading and release behaviours at targeted sites.

The coating of IONPs can be performed by using organic or inorganic layers. Surface modification can be performed either during synthesis of nanoparticles or post-synthesis process. The most commonly used organic coatings are the surfactants such as oleic acid, lauric acid and alkane sulphonic acids which stabilises the IONPs and polymers such as polylactic acid (PLA), polyvinyl alcohol (PVA), polyvinyl pyrrolidine (PVP), polyacrylic acid (PAA), polyethylene glycol (PEG), polyethylene imine (PEI), etc., which stabilises the IONPs as well as improves the biocompatibility and adds specific characteristics useful for biomedical applications (Cai *et al.*, 2013; Sun *et al.*, 2014; Ali *et al.*, 2016). Surfactant mediated synthesis are normally proceeded in organic solvents during synthesis procedure. The hydrocarbon chains of the surfactant molecules form a layer around nanoparticles making them less susceptible to aggregation. However, further processing is prerequisite for such hydrophobic IONPs to be utilised for biomedical application. The polymers are normally coated post synthesis of IONPs and can be synthesised in hydrophilic solvents for ease of biomedical application. There are

a number of inorganic nanoparticles used to coat IONPs such as, silica, gold, silver, organic dye molecules, etc (Chen *et al.*, 2013). These coating materials protect the iron oxides from oxidation and hence helps maintain their characteristic properties. Among them silica coating has been used in this thesis and will be discussed briefly here.

1.4.1 Silica Coating on Iron Oxide Nanoparticles and their Application

A variety of silica coatings on IONPs exist, including amorphous silica, organically modified silica, and mesoporous silica. The silica shell surface is biocompatible as well as compatible for the conjugation of many chemicals. It protects the IONPs against oxidation and agglomeration improving its chemical stability. It is interesting that silica coated IONPs are usually stable and easily disperse in an aqueous or organic solvents, even without surfactants (Sun *et al.*, 2014). In addition, during the formation of silica shell, small molecules such as drugs and dyes can be incorporated into the silica shell or covalently attach various ligands and biomolecules to the silanol group (Si-OH) formed on the surface of the shell (Sonmez *et al.*, 2015).

Silica coating on IONPs is possible through different methods such as sol-gel method, microemulsion, surfactant structured templates and surface protecting etching. As shown in Figure 1-6 A, the Stober method uses hydrolysis and condensation of organosilane precursors, such as tetraethyl orthosilicate (TEOS) in ethanol solution in the presence of water with ammonia as a catalyst (Stöber, Fink and Bohn, 1968). Due to the high hydrolysation rate of TEOS, polydisperse nanoparticles are formed (Sonmez *et al.*, 2015). The reaction parameters such as amount and type of precursors, amount of catalyst, volume of alcohol to water, alcohol type, etc. can be modified to prepare different nanoparticles (Deng *et al.*, 2005). Microemulsion methods have also been used to coat nanoparticles with uniform layer of silica by using water/oil emulsion in presence of surfactants (Santra *et al.*, 2001). The micelles formed can act as nanoreactors to deposit a silica layer on IONPs and the size of these droplets is related to the size of the nanoparticles formed (see Figure 1-6 B).

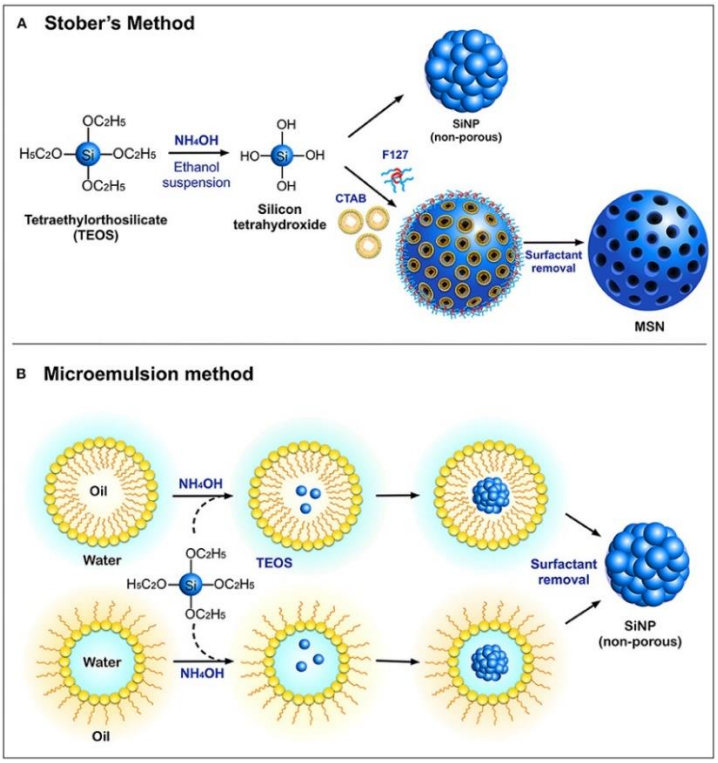

Figure 1-6: Schematic representation of synthesis of silica nanoparticles (A) Stober's method and (B) Microemulsion method. Reproduced from Selvarajan *et al.*, (2020)

Mesoporous silica is a promising material to be used as platforms for multifunctional components ranging from chemotherapeutics to optical probes. The key points to be considered while coating IONPs with mesoporous silica includes porosity and a large surface area that provides higher drug loading efficiency, ease of surface modification for targeting, biocompatibility and improved imaging compatibility (Hong and Choi, 2018). Mesoporous silica nanoparticles (MSNs) have the characteristic pore diameter, ranging between 2 to 50 nm (IUPAC nomenclature) as stated by Sen, Sebastianelli and Bruce (2006). Furthermore, reactive silanol groups (≡Si-OH) on the surface can link *via* covalent or hydrogen bonding with organic functional groups. Even the hollow space within the MSNs allows physical adsorption of different components. MSNs not only allows the assembly of versatile reagents but also improves biocompatibility and eliminates cytotoxicity (Zhang *et al.*, 2009) by manipulating pore volume, particle size, shape control and stability (Rosenholm, Sahlgren and Lindén, 2010; Kettiger *et al.*, 2015). MSNs are highly biocompatible compared to colloidal silica and should be carefully designed since its physical and chemical properties influence the biocompatibility (Lee, Yun and Kim, 2011). According to Bhavsar, Patel and Sawant (2019), MSNs synthesized using sodium silicate (an economical source of silica) was biocompatible with various cell lines. About 90% of the MSNs were excreted (urine and faeces) in the form of silicic acid within 3-4 days.

1.4.2 Optical Probes as Potential Multimodality in Cancer Therapeutics

As IONPs alone possess limitations for cancer therapeutic applications, the addition of other functionalities is sought after by the researchers. The design of these nanoparticles not only adds new functionalities but also helps in enhancing the properties of IONPs. Mainly, to enhance the properties of specific targeting cancer sites, selected biomarkers can be attached onto the nanoparticles. It is important to develop efficient strategies to protect the bare magnetic nanoparticles without losing its properties while adding further moieties.

The combination of optical probes and superparamagnetic iron oxides with or without chemotherapeutic agents is an emerging research area (Estelrich and Busquets, 2018; Lamichhane *et al.*, 2021). In this approach, the therapeutic applications of the optical probe can be added along with the properties of magnetic nanoparticles. Before going through the application of dual therapeutics, it is important to discuss about the properties of optical probes. Usually, optical probes are used in biomedical applications for imaging, however, they are efficient for therapeutic applications owing to their photothermal and photodynamic properties (Abrahamse and Hamblin, 2016). Optical probes provide non-invasive, precise, and rapid disease diagnosis and therapeutics with negligible toxicity to normal cells. Organic dyes such as Rhodamine 6G (R6G) have been widely used as a fluorescence marker for monitoring the distribution of biological molecules into the target sites by using fluorescence spectroscopy (Benton Swanson *et al.*, 2022). However, there are drawbacks when using organic dyes, such as their low quantum yield and rapid photo-bleaching. To overcome the limitations of small molecular fluorophores, different optical nanoparticles such as quantum dots, silica nanoparticles, semiconducting polymers, or conjugated polymers, etc., are developed with high quantum yield and photo-stability which are either water-soluble or water-dispersible nanoparticles/supramolecular assemblies for different theranostic applications (Jiang and Pu, 2018).

1.4.2.a Properties of Optical Probes and their Therapeutic Applications

The properties of organic optical agents are largely influenced by their molecular structures and aggregated state. The Jablonski diagram illustrates different electronic states of a molecule and the transition processes between them which elucidates a basic principle of photoexcitation designed for diagnostic or therapeutic applications. When an optical agent absorbs a photon, it can be converted into different imaging signals or therapeutic effects (Figure 1-7). When a photon is absorbed, it will be excited and change from the ground electronic state (S_0) to a singlet excited state (S_n), which subsequently

undergoes a rapid internal conversion (IC) to the lowest singlet excited state (S_1). At the singlet excited state (S_1) the energy dissipates and can undergo three different pathways. Firstly, the conversion of S_1 to S_0 results in the release of a photon with a lower energy and longer wavelength, giving a fluorescence signal. Secondly, the energy dissipated could undergo a nonradiative vibration relaxation from S_1 to S_0 which is mediated by intramolecular movements and collisions leading to heat generation. This process is referred as thermal deactivation process where the local temperature is elevated leading to the therapeutic effect known as photothermal therapy (PTT). Thirdly, the optical agents can undergo a transition known as intersystem crossing (ISC) from S_1 to lowest triplet state (T_1). Molecules could relax from T_1 state to the state of S_0 through radiative decay known as phosphorescence. The excited energy state (T_1) could also be transferred to nearby oxygen molecules generating reactive oxygen molecules (ROS) such as singlet oxygen ($^1O_2$) or radicals. This effect is known as photodynamic effect and can be used as a therapeutic application called photodynamic therapy (PDT).

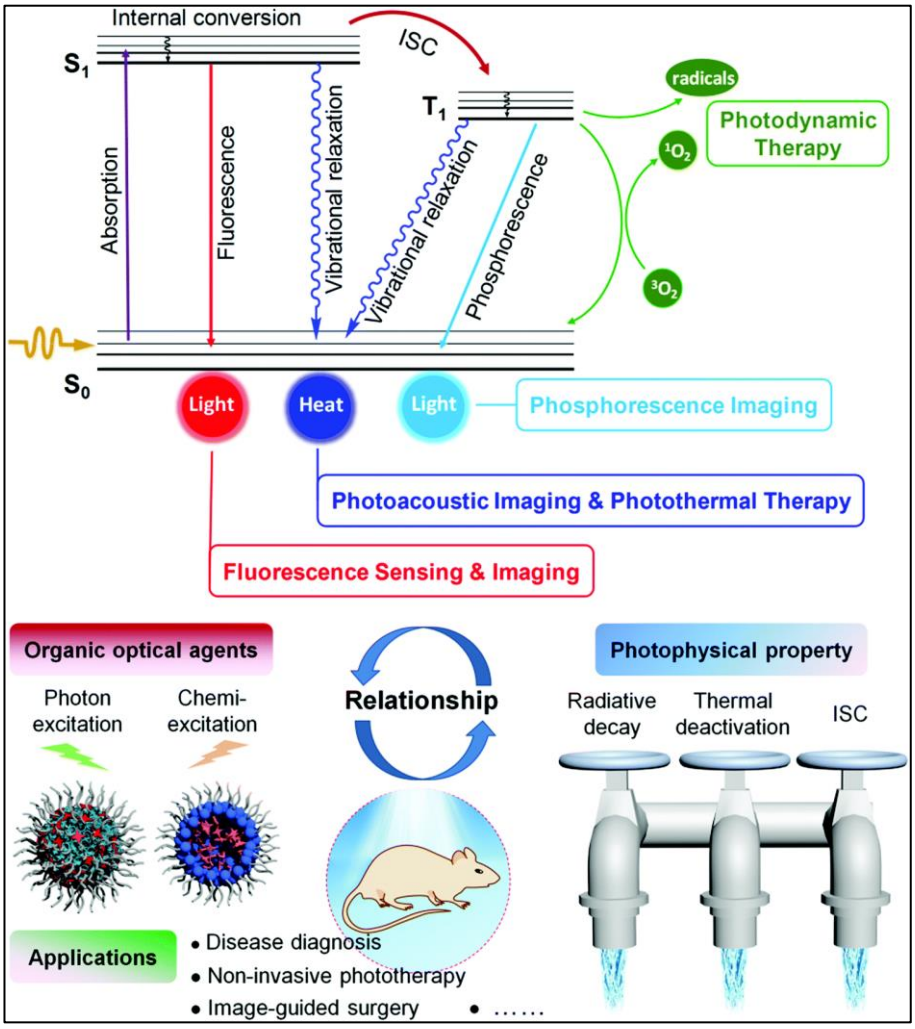

Figure 1-7: Schematic of Jablonski diagram and its role in designing optical agents with their properties. Reproduced from Feng, Zhang and Ding (2020)

Each of these three energy dissipation pathways are competitive and should be controlled to achieve different phototheranostic functions. Scientists have developed different strategies and techniques to construct various organic agents for applications of disease diagnosis, image-guided surgery, photothermal therapy (PTT) and photodynamic therapy (PDT). The florescence imaging in the near-infrared region (NIR-I, 700-1000 nm) provides opportunities for non-invasive imaging as well as improved penetration depth (Hong, Antaris and Dai, 2017; Dai *et al.*, 2021). Biological tissues/organs possess high autofluorescence in the visible region (~400 – 700 nm), causing interference in the fluorescence imaging (Li *et al.*, 2021). The NIR region- I is beyond the autofluorescence range of biological tissues, providing sharp images with low signal to background noise ratio (Li *et al.*, 2021). Further red shifting to the emission wavelength (NIR- II region, 1000- 1700 nm) can increase enhancement of the fluorescence as well as depth of penetration (Dai *et al.*, 2021). Moreover, the high value of fluorescence quantum yield (QY) significantly improves the signal-to-noise ratio with high resolution in bio-imaging. The majority of the fluorescent probes have QY of 10-20% only in serum (Rurack and Spieles, 2011). Therefore, the development of dyes with enhanced fluorescence QY is ongoing. Another important characteristic is solubility, as many fluorescence dyes are poorly soluble in water. Therefore, additional groups such as sulfonates have been substituted (e.g., in indocyanine green) to increase the solubility for *in-vivo* administration (Kohl *et al.*, 2004). However, most of the fluorescent probes eventually degrade by the exposure of light, hence, a thorough characterisation is required after the synthesis and before the administration. Lastly, for clinical application, toxicity and clearance of fluorescence dyes should be extensively studied (Hameed *et al.*, 2019).

The optical agents such as photosensitisers (PS) are capable of absorbing light and transferring that energy to adjacent oxygen molecules for the photodynamic effect to take place (Ormond and Freeman, 2013). This property is utilised in photodynamic therapy (PDT) for cancer treatment due to their non-invasive nature, minimal side effects and enhanced selectivity (Huang *et al.*, 2019). PDT is a clinically approved non-invasive treatment modality. A specific wavelength of light (non-toxic to the human body) is irradiated through the tissues and PS transfer the energy to neighbouring oxygen molecules (within a distance of 20 nm) to generate cytotoxic ROS and successively killing the tumour cells by direct cell death (necrosis or apoptosis), vascular damage (leading to tissue ischemia) or immune modulation, (Dolmans, Fukumura and Jain, 2003; Algorri *et al.*, 2021). PS do not have significant toxicity until light irradiation which helps to avoid systemic side-effects (Dolmans, Fukumura and Jain, 2003). Nevertheless, PDT

is confined to patients without distant metastases and a tumour extent of ≤3 cm in diameter (Tomizawa and Tian, 2012). A range of photosensitisers along with carbon-based nanoparticles such as graphene can be utilised for PDT/ PTT; however, they have their own limitation (low fluorescence quantum yield) and suitability in real life application due to the short penetration depth of UV light irradiation. Therefore, it is important to find a suitable photosensitiser which can be excited using NIR light to overcome this limitation of penetration depth *in-vivo*. Indocyanine green (ICG) is a suitable photosensitiser in the NIR region which has been readily used for PDT and PTT applications and will be discussed in detail related to magneto-optical nanocomposites reported in this thesis.

1.4.2.b Indocyanine Green (ICG)

Indocyanine green (ICG) is an anionic (negatively charged) and amphiphilic (having both hydrophilic and hydrophobic parts) tri-carbocyanine dye (Figure 1-8 A). It is a fluorophore molecule with a diameter of 1.2 nm, MW of 776 Da (Polom *et al.*, 2014). The presence of hydrophilic part makes this fluorophore one of the water-soluble dyes. ICG has been approved by the Food and Drug Administration (FDA) and European Medicines Agency for diagnostic aid and used to determine blood volume, cardiac output, hepatic function, liver blood flow and ophthalmic angiography (Jung, Vullev and Anvari, 2014; Kraft and Ho, 2014). ICG is a near infrared (NIR) fluorophore with peak absorption at around 778 nm with little absorption in the visible range. It is advantageous over visible fluorophores with improved tissue penetration and lower auto-fluorescence.

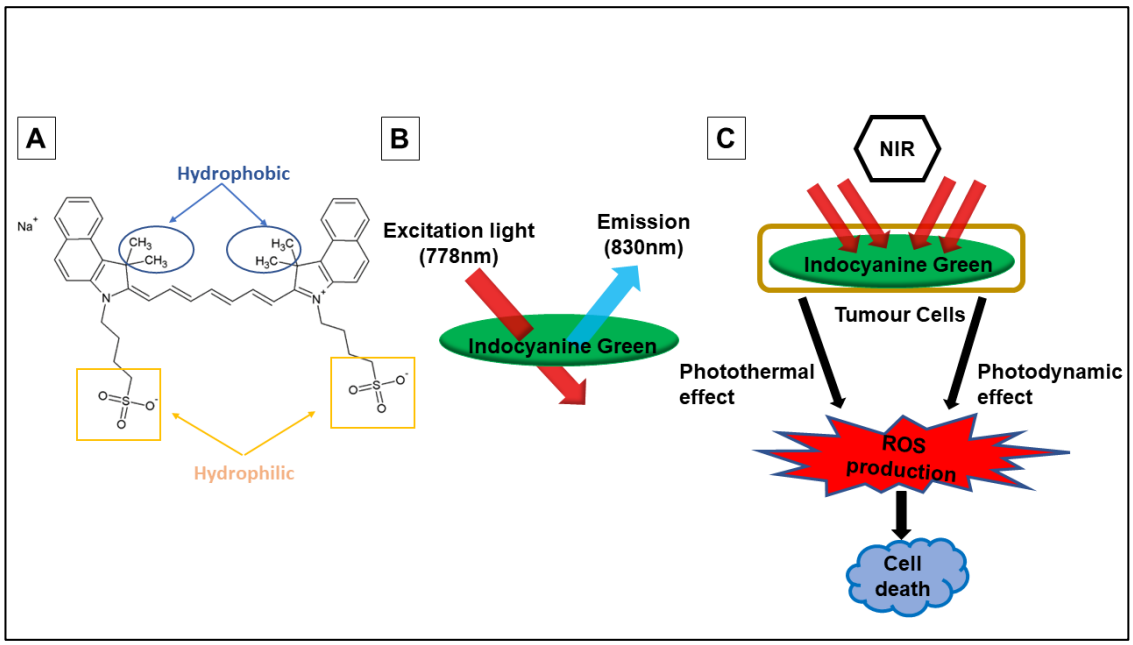

Figure 1-8: Indocyanine green for cancer therapy. A. Indocyanine green (ICG) structure, B. fluorescence properties showing emission at near-infrared (NIR)-I region upon excitation at 778nm, C. Application of ICG-NIR for cancer therapy.

ICG is used as a medical contrast agent in 'fluorescent-guided surgery' to visualise the contrast between hepatic lesions and normal liver tissue (Kokudo and Ishizawa, 2012). Normally, 0.5 mg/kg of ICG is injected intravenously where it actively binds to the protein. The protein bound ICG when illuminated with NIR light of 750-810 nm emits light at around 830 nm (Figure 1-8 B). This fluorescence is utilized in real-time surgery and *in-vivo* or *ex-vivo* imaging. However, after binding with protein, ICG dramatically loses its fluorescence intensity with time. According to Bourgeois *et al.* (2021), when ICG was injected intravenously in groups for one day before surgery and immediately before surgery, breast cancer could be detected on the later with high sensitivity. Additionally, the fluorescence is depended on the concentration of ICG, depth and location of the tumour, and tumour histological grade (Bourgeois *et al.*, 2021). Therefore, a nanoparticulate system which can increase the fluorescence of ICG as well as protect it from photobleaching, is needed.

1.4.2.c Possibilities and Challenges of Using Indocyanine Green Alone for Cancer Therapeutics

ICG is noted to be accumulated in varieties of primary tumours including hepatocarcinoma, head and neck cancers, lung cancers, brain tumours and breast cancer (Veys *et al.*, 2018; Bourgeois *et al.*, 2021). Even though the *in-vivo* kinetics of ICG uptake on tumour cells is unknown, EPR effect *via* the non-covalent reversible binding of ICG to macromolecular serum proteins, such as albumin, contribute for the accumulation in tumour tissues (Onda *et al.*, 2016). However, the low tumour specificity of ICG discourages its use alone for tumour therapy. In addition, upon systemic administration of ICG, rapid protein binding leads to degradation of ICG and fast clearance (Ferrauto *et al.*, 2017).

ICG has the properties of NIR photosensitisers (PS) generating ROS by NIR irradiation killing cancer cells. Interestingly, ICG can also be used for photothermal therapy (PTT), when irradiated with light at 750-810 nm, it emits the energy as heat, making it an ideal photothermal agent. According to Tang and McGoron (2009), ICG at just 5 µM produced a temperature of approximately 43 ℃ within a minute of laser irradiation (1 W/cm^2, 808 nm). Furthermore, when combined to chemotherapeutic agents like doxorubicin, it has synergistic effect on the ability to kill cancer cells. However, the ability of pure ICG to generate heat upon irradiation of laser is not sufficient as to be considered as single treatment modality since it does not destroy all the cells (Tang and McGoron, 2009).

The combination of PDT and PTT has also shown significant improvement in cancer therapeutic effects (Sheng *et al.*, 2014; Fang *et al.*, 2017). Sheng and colleagues

prepared human serum albumin- ICG nanoparticles which could efficiently induce ROS with change in temperature upon a single NIR laser irradiation of 808nm with a power density of 1 W/cm^2 for 5 minutes (Sheng *et al.*, 2014). However, the success of PDT or PTT highly depends on the power of incident light as well as the optimal PS dosage with the accumulation of PS in the target tissue.

Even though ICG has interesting therapeutic properties, the application of free ICG is limited due to its instability under physiological condition. ICG tends to aggregate in solution and lose its properties. Additionally, ICG has limited functional groups and the conjugation chemistry of ICG is difficult. Thereafter, researchers have tried to physically adsorb ICG on polymers or mesoporous silica to synthesise nanoplatforms stabilising ICG for biomedical application (Sheng *et al.*, 2014; Fang *et al.*, 2017; Huang *et al.*, 2019). ICG also exhibits concentration-dependent florescence quenching because of its high degree overlap between absorption and emission spectra (Kraft and Ho, 2014).

Thus, the encapsulation of ICG in nanocarriers have been tested to improve its stability and performance. ICG has been encapsulated in micelles, human serum albumin, liposomes, carbon nanotubes or silica (Ferrauto *et al.*, 2017). Typically, encapsulating ICG has shown enhanced photostability and bioavailability. Packing ICG in lipids has reduced the self-quenching, improving its physical properties (Kraft and Ho, 2014). Similarly, encapsulating ICG in silica nanoparticles protects it from degradation (Liu *et al.*, 2015). Moreover, the coating presents an ideal platform for fabrication of multimodal agents which would otherwise be difficult or alter the bio-distribution or pharmacological parameters. In the case of conjugation of fluorophores onto the surface of IONPs, the physiological properties of fluorophores could quench, reducing the therapeutic properties of nanoparticles. The modification on the surface of IONPs could also alter the biodistribution and other pharmacological parameters (Kumar, Anuradha and Roy, 2014). For that reason, encapsulation of the IONPs and fluorophores within the nanostructures would preserve the magnetic and optical properties (Kumar, Anuradha and Roy, 2014).

1.5 Application of Magneto-Optical Nanoparticles for Cancer Therapy

The application of both the magnetic and optical components in the nanocomposites form is a new multimodal system that could enhance the efficacy for cancer therapeutic application. The conjugation of IONPs with various possible optical probes for cancer theranostics has been extensively reviewed and differentiated into various classes as shown in Figure 1-9 (Lamichhane *et al.*, 2021). They have been identified as (i) molecule-based agents such as fluorophores and photosensitizers, and (ii) nanomaterial-based agents such as semiconductor nanoparticles (quantum dots),

carbon nanoparticles (graphene, carbon nanotubes), up-conversion nanoparticles, plasmonic nanomaterials, rare-earth-doped matrices (nanophosphors), dye-doped optically transparent matrices (e.g., dye/silica) and fluorescent polymers. The IONPs conjugated optical probes can be utilised for diagnostics, targeting and therapeutic application. The IONPs provide diagnostic modalities such as magnetic resonance imaging (MRI) and magnetic particle imaging (MPI); magnetic targeting; and therapeutic modality like magnetic hyperthermia therapy (MHT). Additionally, the optical probes conjugated with IONPs could enhance their effect by additional modalities such as florescence imaging (FI), optical imaging (OI), photoacoustic imaging (PA), active targeting visualised by florescent probes, photodynamic therapy (PDT) and photothermal therapy (PTT).

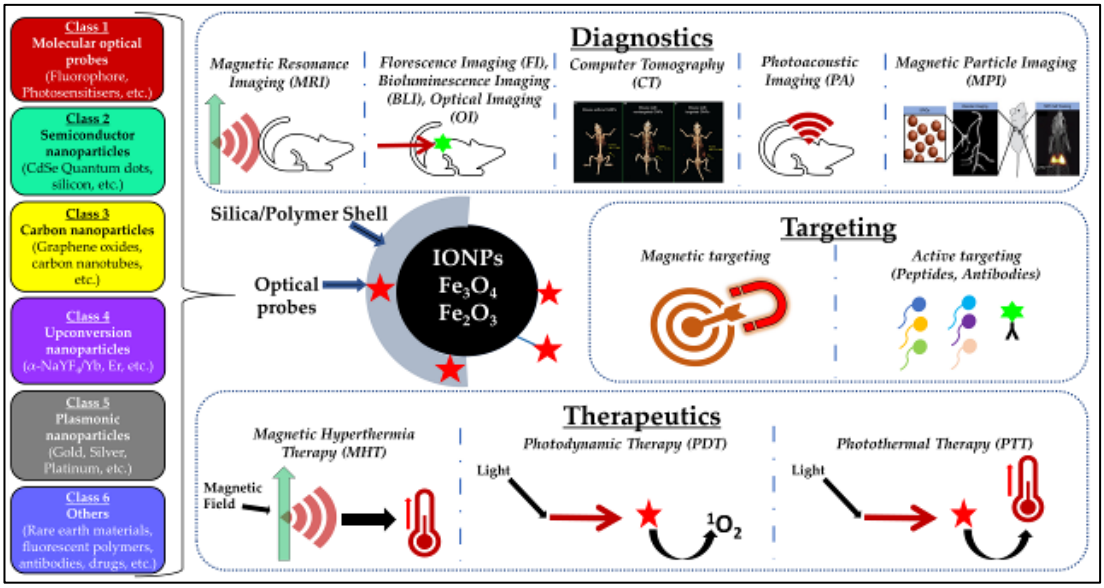

Figure 1-9: Application of Magneto-optical nanoparticles for cancer theranostics. Reproduced from Lamichhane *et al.* (2021)

Out of various optical probes conjugated with IONPs, some of the molecular agents responsible for therapeutic application has been outlined in Table 1-4. It is evident that IONPs conjugated with optical agents are utilised for imaging purposes as these agents provide excellent fluorescence properties. Similarly, the therapeutic aspects of these conjugates are also used for therapeutic applications. The enhancement of therapeutic effect such as PDT that generates singlet oxygen to damage cancerous tissues and PTT that increase the temperature of tumour cells above 42 ℃ using specific wavelength of laser irradiation in the presence of specific photosensitisers have been reported with or without conventional chemotherapeutic agents (Estelrich and Busquets, 2018). Additionally, the functionalised optical nanoparticles can be directed magnetically to the site of interest and their distribution in tumours/ other organs can be imaged.

Table 1-4: Different molecular optical probes incorporated iron oxide nanoparticles for cancer therapeutics with/without combination of diagnostics application

Optical probe	**Size of NPs TEM/ DLS (nm)**	**Surface coating or nanocarrier**	**Application**	**Reference**
Photofrin	40 -	Polyacrylamide	PDT and MRI imaging for targeted detection and treatment in mice bearing orthotropic glioma	(Reddy *et al.*, 2006)
PHPP	20 ± 5 -	Chitosan	MRI guided magnetic targeting with PDT functionalities in colon cancer xenograft mice model	(Sun *et al.*, 2009)
Ce6	7 ± 1 72	Polyethylene glycol	MRI/fluorescence imaging with targeted PDT in mice bearing gastric cancer	(Yin *et al.*, 2016)
Ce6	92	Oleic acid	MRI/optical imaging and PDT in mice bearing breast cancer	(Amirshaghaghi *et al.*, 2019)
PpIX	7 ± 1 37	PpIX coated	MRI and PDT on breast cancer cells *in-vivo*	(Yan *et al.*, 2018)
MHI-148	74 ± 15 84 ± 6	DSPE-PEG-NH_2 micelles	MRI-NIRF dual imaging with PTT	(Lee *et al.*, 2017)
m-THPC	150 200	Liposomes	PDT and MHT on epidermoid carcinoma *in-vivo*	(Di Corato *et al.*, 2015)
ICG	12 ± 4.8 121.4	Prussian blue	MHT combined with PDT and PTT in breast cancer model *in-vivo*	(Xue *et al.*, 2018)
IR820	- 212	PCLA-PEG-PCLA	magnetic field guided tumour targeting with MRI/NIR imaging, and imaging-guided photo-chemotherapy	(Liao *et al.*, 2017)
CBT	- 139 ± 24	Carboxyl-coated	MRI and PTT effect in breast cancer model *in-vivo*	(Yaguang Wang *et al.*, 2020)
PheoA	- 222 ± 5	Hyaluronic acid-coated	PDT and MHT combined with imaging modalities in melanoma bearing tumour model	(Kim *et al.*, 2016)
TCPP	95 98	Zr Metal organic framework	PDT and PTT combined with imaging modalities in immunodeficient *in-vivo* model	(Zhang *et al.*, 2017)

*Notes: PHPP: 2,7,12,18-Tetramethyl-3,8-di(1-propoxyethyl)-13,17-bis-(3-hydroxypropyl) porphyrin; Ce6: Chlorin e6; PpIX : Protoporphyrin IX; MHI-148: Heptamethine cyanine dye; m-THPC: Tetrakis(3-hydroxyphenyl)chlorin; ICG: Indocyanine green; IR820: cyanine green dye; CBT: 2-cyanobenzothiazole; PheoA: Pheophorbide A; TCPP: 5,10,15,20-tetrakis (4-carboxyphenyl) porphyrin; DSPE- PEG: 1, 2-Distearoyl-*sn*-glycero-3-phosphoethanolamine-Poly(ethylene glycol); PCLA-PEG-PCLA: Poly(ε-caprolactone-co-lactide)-b-poly(ethylene glycol)-b-poly(ε-caprolactone-co-lactide)

1.6 Targeting Regulated Cell Death (RCD) for Cancer Nanotherapy

The ongoing progress in cancer research has found unique properties of cancer cells differentiating them from normal cells (Hanahan, 2022) which is of immense importance for designing targeted therapies. The unique property of cancer cells to evade programmed cell death, also termed as regulated cell death (RCD), is one of the major fields of cancer research to establish the significance of cancer therapeutic drugs. In the field of cancer nanomedicine, the possible cytotoxic effect of nanoparticles producing reactive oxygen species (ROS) or initiating other signalling pathways can eventually lead to several types of RCD including apoptosis, autophagy, ferroptosis, pyroptosis, and necroptosis (Mohammadinejad *et al.*, 2019). Common efforts on inhibiting or inducing different RCD to restrain tumour growth or cause instant tumour cell death depends on the strategy being employed. Furthermore, the fate of RCD is based on the type of nanoparticles, doses and their physico-chemical characteristics like size, shape, surface charge and functional groups (Mohammadinejad *et al.*, 2019). In addition, the cell lines being studied and time of exposure of nanoparticles change the fate of RCD. In combination with therapeutic applications such as MDT, MHT, PDT and PTT, new interventions to sensitise the tumours might possibly propose successful outcomes (Zeng *et al.*, 2022). Here a brief comparison on distinct types of RCD based on the variations occurred in cells is presented in Table 1-5. Further, two specific RCDs, apoptosis and ferroptosis, induced by nanoparticles are discussed briefly.

Table 1-5: Comparative characteristics of Apoptosis, Autophagy, Ferroptosis, Pyroptosis and Necroptosis

	Definitions	**Morphological features**	**Biochemical features**	**Key pathways**
Apoptosis	Common RCD (Regulated Cell Death) initiated by perturbation of extracellular or intracellular microenvironment	Disrupted cell membranes, Broken cytoplasmic and nuclear skeletons, Extruded cytosol, Degradation of chromosomes, nuclear fragmentation, membrane blebbing and formation of apoptotic bodies	DNA (Deoxyribonucleic Acid) fragmentation, Release of mitochondrial intermembrane proteins, Activation of caspases	Caspase, p53, Bcl-2 mediated signalling pathways
Autophagy	Vacuole presenting RCD, a self-degradative process of its own components, balancing the sources of energy during development	degraded cellular macromolecules and organelles releasing metabolites, Autolysosome and autophagosome formation	Amplified lysosomal activity	MAPK-ERK mTOR, P13K-AKT mTOR signalling pathways
Ferroptosis	Iron dependent RCD initiated by oxidative perturbations of intracellular microenvironment constituting Gpx4, initiated by lipid peroxidation	Shrinking mitochondria and mitochondria membrane rupture	Iron and ROS accumulation in intracellular environment, inhibition of system Xc and Gpx4, decreased cysteine uptake, GSH depletion, NAPDH oxidation, lipid peroxidation	xCT, Nrf2, Gox4, MVA, LSH signalling pathways
Pyroptosis	inflammatory RCD	rapid plasma-membrane rupture and release of proinflammatory intracellular contents pore on the plasma membrane followed by cellular swelling and subsequent rupture	caspases activation or release of granzymes	Caspase-3/8-mediated pathway, Granzyme-mediated pathway
Necroptosis	Form of necrosis performs RCD, triggered due to factors outside the cell	Swelling and rupture of plasma membrane, swelling of organelle, cluster of cells	Stimulation of RIP1, RIP3, mixed lineage kinase domain-like protein (MLKL), Depletion of ATP	TNF (Tumour Necrosis Factor) α, TLR3, TRAIL, TNFR1, MAPK, FasL pathways

1.6.1 Apoptosis

Apoptosis is the most common RCD mechanism and in fact the first to be discovered and proposed as the hallmark of cancer (Hanahan and Weinberg, 2000). Distinct morphological changes in cells upon apoptotic cell death is observed such as membrane blebbing, cell shrinking, chromatin condensation, DNA fragmentation, and

formation of small vesicles called apoptotic bodies (Jayakiran, 2015). In the case of detecting apoptosis *in-vitro*, researchers use the property of phosphatidylserine flip-flop from inner layer of plasma membrane to outer layer that represents the incidence of apoptosis. Numerous studies have investigated apoptosis pathways upon exposure to specific inorganic nanoparticles, for instance, silica and iron oxides *in-vitro* for cancer therapeutics (Napierska *et al.*, 2009; Sharma *et al.*, 2015). The nanoparticles induce apoptosis *via* ROS generation, organelle dysfunction and DNA damage, along with distinct pathways involved in generation of apoptosis including extrinsic pathway relating to cell death receptors and intrinsic pathways including mitochondria, or endoplasmic reticulum (ER) (Mohammadinejad *et al.*, 2019) is shown in Figure 1-10. A cascade of signalling events takes place to promote apoptotic cell death, which is mainly regulated by either anti-apoptotic protein Bcl-2 for stimulating cell survival or pro-apoptotic Bax protein triggering intrinsic apoptotic pathways and activation of Cas9.

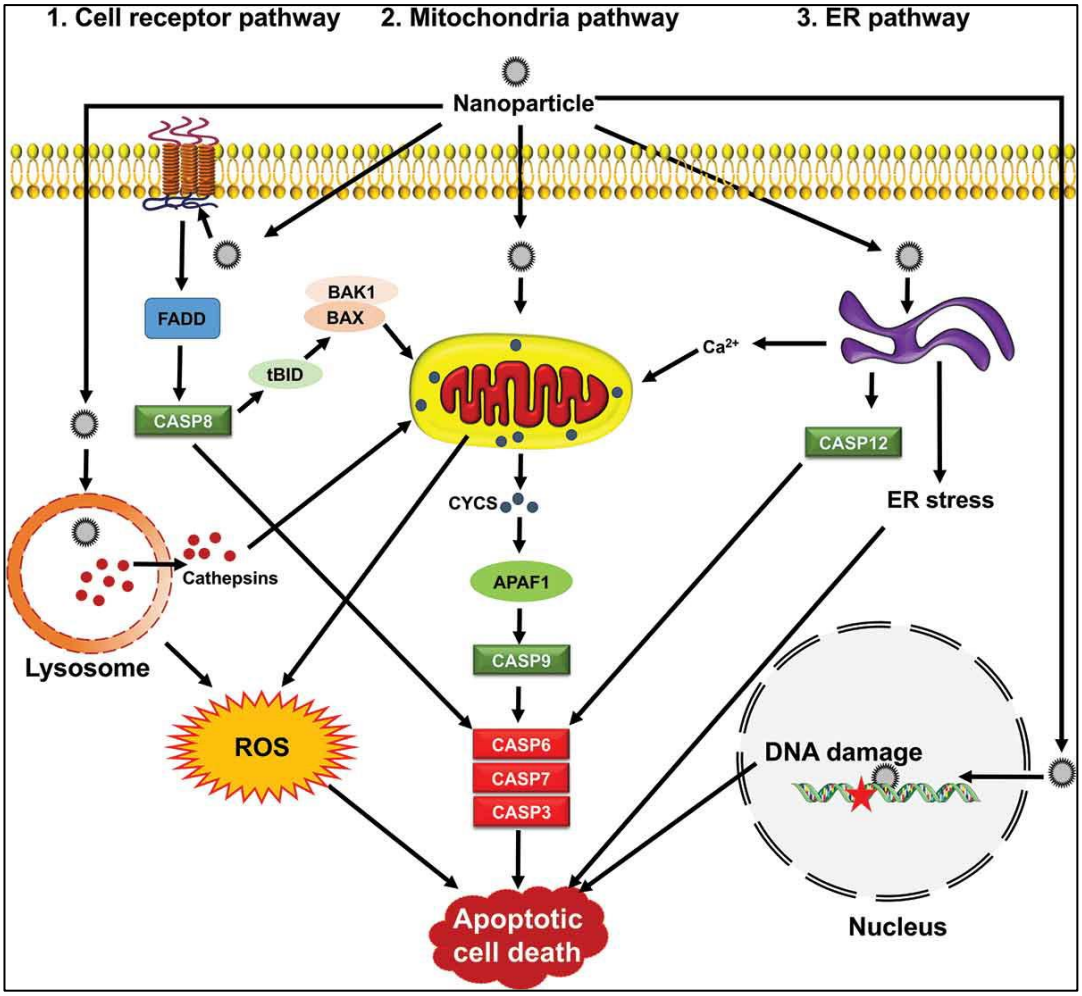

Figure 1-10: Signalling pathways involving nanoparticles induce apoptosis mediated through 3 main apoptotic pathways including cell receptor, mitochondria and endoplasmic reticulum, that trigger caspases to execute self-killing process. Reproduced from Mohammadinejad *et al.* (2019)

1.6.2 Ferroptosis

Chemotherapy generating apoptosis has been a universal mode of treatment for cancer patients, however, it faces the outcome of recurrence while some exhibit resistance to existing treatment modalities (Holohan *et al.*, 2013). Therefore, a search for new anti-tumour strategies has led to the discovery of many non-apoptotic cell death pathways, including ferroptosis.

Ferroptosis is a non-apoptotic form of RCD associated with accumulation of iron, initiating iron dependent oxidative perturbations of intracellular microenvironment that is iron-dependent and under constitutive control of glutathione peroxidase 4 (GPx4) (Galluzzi *et al.*, 2018; Hadian and Stockwell, 2020). Ferroptosis leads to a characteristic morphological and physiological changes in features, for instance, nuclei of cell remain intact, shrinking of mitochondria with mitochondrial outer membrane rupture (Galluzzi *et al.*, 2018), increase in iron content in the cells with lipid ROS formation, glutathione (GSH) inhibition and increased NADPH oxidation (Stockwell *et al.*, 2017; Han *et al.*, 2020). The main biochemical features of ferroptosis are the increase in lipid hydroperoxides (LOOH) and iron concentration as the cells experience Fenton reactions (reaction explained in Section 1.2.4.c). The polyunsaturated fatty acids (PUFAs) are oxidised by the free radicals that leads to the formation of LOOH and ROS causing ferroptosis. GPx4, an enzyme that is dependent on biosynthesis of GSH, reduces lipid peroxidation, however, is inactivated upon depletion of GSH, resulting to ferroptosis (Yang *et al.*, 2014; Shimada *et al.*, 2016).

It is however realised that ferroptosis occurs in conjunction with other cell death pathways such as apoptosis, autophagy, or necroptosis (Mou *et al.*, 2019; Liu *et al.*, 2021). For example, the signalling pathways related to apoptosis or autophagy are also related to ferroptosis. GPx4, p53 and Nrf2 are closely related signalling pathways for apoptosis, autophagy and ferroptosis. The overexpression of GPX4 inhibits autophagy as well as ferroptosis. Similarly, p53 genes, which are required for apoptosis in the transcription-dependent pathway, are also required for ferroptosis. The activation of p53 leads to ferroptotic cell death in the presence of ROS stress and is independent of cell-cycle arrest, senescence and apoptosis (Jiang *et al.*, 2015).

1.7 Aims and Objectives

The main aim of this project was to develop novel magneto-optical nanocomposites for externally stimulated cancer therapy.

The general objectives include:

1. Preparation of both hydrophilic and hydrophobic iron oxide nanoparticles (IONPs) in a fully reproducible manner with optimum physico-chemical properties

2. Fabrication of biocompatible core-shell nanocomposites involving iron oxide core and mesoporous silica shell with enhanced surface area and controlled porosity for eventual formation of magneto-optical nanocomposites by optimum loading of an NIR dye, indocyanine green (ICG) inside the mesopores.

3. Testing the performance of magneto-optical nanocomposites developed under objective 2 for localised heating under an AMF (MHT), localised heating under NIR laser irradiation (PTT) and generation of ROS (PDT).

4. Testing biocompatibility of optimum magneto-optical nanocomposites developed and tested under objectives 2 and 3 using commercially available breast cancer cell lines (MCF7) and evaluating their efficacy (cell viability, cellular uptake, and uptake mechanism) *in-vitro*

5. Testing the performance of optimum magneto-optical nanocomposites developed and tested under objectives 2 and 3 for MHT, PTT, PDT *in-vitro* cellular system under the influence of either an AMF alone, laser irradiation alone or simultaneously as external stimuli.

6. Investigating the oxidative stress markers for therapeutic effects (PDT/PTT) *in-vitro* using the laser irradiation with optimum magneto-optical nanocomposites developed

7. Finding the plausible mechanistic pathways for therapeutic effects (PDT/PTT) *in-vitro* using the laser irradiation with optimum magneto-optical nanocomposites developed.

1.8 Thesis Outlines

This thesis will be delivered in six chapters reporting on the synthesis of iron oxide core, silica shell nanocomposites loaded with indocyanine green (ICG) and their functional application in magnetic hyperthermia, photodynamic and photothermal therapy.

Chapter 1 presented a detailed literature review on magnetic iron oxide nanoparticles along with optical probes within the context of cancer therapeutics. The application of magneto-optical nanocomposites in cancer therapeutics were discussed. The research aims and specific objectives of this thesis were given along with an outline of the thesis.

Chapter 2 will demonstrate the methods of experimentation with required materials. It will provide all the methodology of experimentation that will be performed to provide the results for further chapters.

Chapter 3 will describe the preparation and characterisation of iron oxide nanoparticles, core-shell mesoporous silica coated nanocomposites and indocyanine green loaded final nanocomposite. The data were analysed and discussed following the characterisation methods such as TEM, DLS, VSM, FTIR, XRD, BET, TGA, UV-Vis spectrophotometry, florescence microscopy and hyperthermia.

Chapter 4 will describe the physicochemical properties of core nanoparticles and core-shell nanocomposites upon hyperthermia and laser irradiation to evaluate their therapeutic performance.

In Chapter 5, the characterised magneto-optical nanocomposites will be used for *in-vitro* and *ex-vivo* studies to look at their biocompatibility and nanoparticle-cell interaction. The *in-vitro* studies on MCF-7 cell lines will be discussed to check cellular viability, cellular toxicity, cellular uptake, and ROS generation demonstrating the effectiveness of the synthesised nanocomposites for cancer therapeutics.

Finally, Chapter 6 demonstrate a mechanistic aspect of nanocomposites for PDT and PTT upon laser irradiation on breast cancer cell line (MCF-7). The synthesised nanocomposites will be studied in presence or absence of laser light to show the effectiveness of externally targeted cancer therapeutics.

Finally, the thesis will be concluded with Chapter 7 containing a comprehensive conclusion to the research and future direction of the work suggested for further studies to this subject matter.

CHAPTER 2

MATERIALS AND METHODS

2.1 Materials

All the chemicals used in this project were of analytical grade and commercially available. They were used without further modification unless otherwise stated. All experiments were performed using ultrapure water distilled to 18.0 MΩ. All the cell culture experiments were performed in sterile conditions in biological safety cabinet II. Most of the experiments were performed in the University of Central Lancashire under the supervision of Dr Tapas Sen and Professor Kamalinder K Singh. A small section of the thesis work related to mechanistic pathways has been carried out in Professor Anita Verma's laboratory, the Kirori Mal College, University of Delhi under the UK-India Education & Research Initiative project (2017-2021).

2.1.1 General Chemicals and Solutions

Table 2-1: List of chemicals used for synthesis and characterisation of nanocomposites

Product	Grade, (%) Purity	CAS Number; Suppliers
Iron (III) chloride hexahydrate ($FeCl_3$. $6H_2O$)	Reagent grade, ≥98%	F2877-500G; Sigma-Aldrich, USA
Iron (II) chloride tetra hydrate ($FeCl_2$. $4H_2O$)	Puriss. p.a., ≥99%	44939-250G; Sigma-Aldrich, USA
Hexadecyl trimethyl ammonium bromide (CTAB)	BioXtra, ≥99%	H9451-100G; Sigma-Aldrich, USA
Tetraethyl orthosilicate (TEOS)	≥99%	86578-1L; Sigma-Aldrich, USA
Ammonium hydroxide (NH_4OH)	ACS reagent, 28-30%	S221228-2-5L-A; Sigma-Aldrich, USA
Hydrochloric acid (HCl)	Analytical reagent grade, 32%	Fisher Scientific, UK
Sodium hydroxide (NaOH)	Laboratory reagent grade	1310-73-2; Fisher Scientific, UK
Ethanol (C_2H_5OH)	Analytical reagent grade, ≥99.8%	64-17-5; Fisher Scientific, UK
Oleic acid (OA)	Technical grade, 90%	112-80-1; Sigma-Aldrich, USA
Nitric acid	Trace analysis grade, >68%	Fisher Scientific, UK
Hexane	Analytical reagent grade, 95%	110-54-3; Fisher Scientific, UK
Acetone [$(CH_3)_2CO$]	Analytical reagent grade, 99.98%	67-64-1; Fisher Scientific, UK
Indocyanine green (ICG)	United States Pharmacopeia (USP) Reference Standard	3599-32-4; Sigma-Aldrich, USA

Table 2-2: Solution for detection of singlet oxygen

Product	Supplier	Solution	Storage
9,10-anthracenediyl-bis (methylene) dimalonic acid (ABMDMA)	Sigma-Aldrich, USA	Stock solution (1000µM): Diluted in ultrapure water with addition of 4-5 drops of NaOH. Working solution (150µM): final concentration with nanocomposites	Freshly prepared

2.1.2 Cell Culture

Table 2-3: Information on cell lines investigated

Cell line	Cell type	Cell type	Supplier
MCF7 **(Michigan Cancer Foundation-7)**	Human breast Adenocarcinoma	Epithelial	American Type Culture Collection (ATCC)

Table 2-4: Cell culture complete media

Product	Suppliers
Dulbecco's Modified Eagle Medium (DMEM)	HiMedia, India
Fetal Bovine Serum (FBS) (10%)	Gibco®, UK
L-Glutamine (1%)	Gibco®, UK
Non-essential amino acids (NEEA) (1%)	Gibco®, UK
Penicillin/Streptomycin (0.1 U/ml)	Gibco®, UK

All the products stated above were added to the medium to make a complete media for regular cell culture.

Table 2-5: General cell culture solutions

Solution	Formula
Phosphate Buffer Saline (PBS)	PBS tablet dissolved in ddH_2O and autoclaved to prepare sterile PBS solution (1x)
Trypsin, phenol red (Gibco®, UK)	1x Trypsin diluted in Phosphate Buffered Saline (PBS)
Trypsin-EDTA, no phenol red (Gibco®, UK)	1x Trypsin with EDTA (0.5%) diluted in Dulbecco's Phosphate Buffered Saline (DPBS)
Freezing media	Complete media (as stated above in Table 2-4) supplied with 10% DMSO
Trypan blue, 0.4% (Gibco®, UK)	Trypan blue: media containing cells (1:1)
Minimum Essential Medium (MEM) without Phenol Red (Gibco®, UK)	Used for DCFDA assay

2.1.3 *In-vitro* Assays

Table 2-6: General chemicals for *in-vitro* and biochemical assays

Product	Grade, % purity	Supplier
Chloroform	Molecular Biology Reagent, ≥99%	MP Biomedicals, India
Isopropanol	Molecular biology reagent, 99%	MP Biomedicals, India
Dimethyl sulphoxide (DMSO)	ACS reagent, ≥99.9%	Sigma Aldrich, USA
3-(4,5-dimethylthiazol-2-yl)-2,5-diphenyl tetrazolium bromide (MTT)	98%	Sigma Aldrich, USA
2',7'-dichlorodihydrofluorescein diacetate (DCFDA)	≥97%	Sigma Aldrich, USA
Hydroxy ethyl piperazine ethane sulphonic acid (HEPES)	BioPerformance Certified, ≥99.5%	Sigma Aldrich, USA
5,5'-Dithiobis (2-nitrobenzoic acid) (DTNB)	≥98%, BioReagent	Sigma Aldrich, USA
1-chloro-2,4-dinitrobenzene (CDNB)	≥99%	Sigma Aldrich, USA
Tri carboxylic acid (TCA)		MP Biomedicals, India
β-Nicotinamide adenine dinucleotide (βNADH)	98%	Sisco Research Laboratories (SRL), India
β-Nicotinamide adenine dinucleotide 2′-phosphate reduced tetrasodium salt (βNADPH)	Extra pure, 98%	MP Biomedicals, India
Glutathione reductase (GR)	Extra pure, 99%	MP Biomedicals, India
Oxidised glutathione (GSSG)	For molecular biology, 99.5%	MP Biomedicals, India
Sodium dodecyl sulphate (SDS)	≥95%	MP Biomedicals, India
Nitro blue tetrazolium (NBT)	For molecular biology, 99%	Sisco Research Laboratories (SRL), India
Phenazine methosulphate (PMS)	Extra pure, 99%	Sisco Research Laboratories (SRL), India
Sodium pyrophosphate	Extra pure, 95%	Sisco Research Laboratories (SRL), India
Sulphanilamide	Extra pure, 99%	Sisco Research Laboratories (SRL), India
N-1-nepthylethyldiamine dihydrochloride (NEDD)	ACS grade	MP Biomedicals India
Orthophosphoric acid	ACS grade, 85%	Sisco Research Laboratories (SRL), India

Tris-HCl	For molecular biology, 99%	Sisco Research Laboratories (SRL), India
Sodium pyruvate	Extra pure, 99%	Sisco Research Laboratories (SRL), India
Sodium chloride	Extra pure, 99.9%	Sisco Research Laboratories (SRL), India
Ethylene diamine tetra-acetic acid (EDTA)	Extra pure, 99%	Sisco Research Laboratories (SRL), India
Triton-X		Sisco Research Laboratories (SRL), India
N, N-dimethylformamide (DMF)	Extra pure, 99.9%	Sisco Research Laboratories (SRL), India
Hydrogen peroxide (H_2O_2)		Sisco Research Laboratories (SRL), India
Dibutylphthalate Plasticizer Xylene (DPX)	For histology	Sisco Research Laboratories (SRL), India
Trizol		Sisco Research Laboratories (SRL), India

Table 2-7: *In-vitro* assay kits

List	Supplier
Iron stain kit (Prussian Blue Stain)	Abcam, USA
DCFDA/ H_2DCFDA (Cellular ROS Assay Kit)	Abcam, USA
iScript cDNA synthesis Kit	Bio-Rad, USA

Table 2-8: Solutions for Prussian blue staining

Solution	Formula	Storage
Cell fixation solution	4% paraformaldehyde in PBS buffer	Stored at 4℃
Iron Staining solution	Potassium ferrocyanide solution + 2% HCl solution (1:1)	Freshly prepared kept at room temperature (RT)
Nuclear staining solution	Nuclear Fast Red solution	Stock solution kept at RT

Table 2-9: Solutions for imaging through DCFDA

Solution	Formulation
Dilution Buffer	1x dilution buffer in PBS
1x Supplemented Buffer	MEM in 1x dilution buffer
2',7'-dichlorofluorescin diacetate (DCFDA)	20 µM DCFDA in 1x dilution buffer
Tert-Butyl Hydrogen Peroxide (TBHP)	10 µM or 100 µM (Positive control in MEM)

2.2 Methods

Potential application of iron oxide nanoparticles (IONPs) in nanomedicine has led to number of synthesis procedures with controlled surface properties (hydrophilic or hydrophobic), of which co-precipitation of iron precursors under alkaline condition is one of the convenient and safe synthesis procedure. Utilising the protocol reported by Sen, Sebastianelli and Bruce, (2006) and Sharifabad (2016) with slight modification, the hydrophilic iron oxide nanoparticles were synthesised. Another set of hydrophilic IONPs were synthesised using similar co-precipitation but with modification utilising dialysis tube for slow release of base at room temperature (RT). Similarly, the hydrophobic IONPs were also prepared *via* the same co-precipitation method but by the addition of oleic acid, a hydrophobic stabiliser.

The IONPs were further coated with mesoporous silica as a shell in order to increase the internal surface area and enhanced biocompatibility. Two different methods of silica coating were performed for fabricating core-shell hydrophilic and hydrophobic IONPs. Furthermore, the mesopores formed on the magnetic core silica shell nanocomposites (MS) were filled with Indocyanine Green (ICG) through physical loading in order to produce novel magneto-optical nanocomposites. A schematic of the synthesis of magneto-optical nanocomposites is provided in Figure 2.1. The synthesised magneto-optical nanocomposites were characterised for its potential application *in-vitro* cancer therapy with an ambition of future *in vivo* & *ex-vivo* experiments.

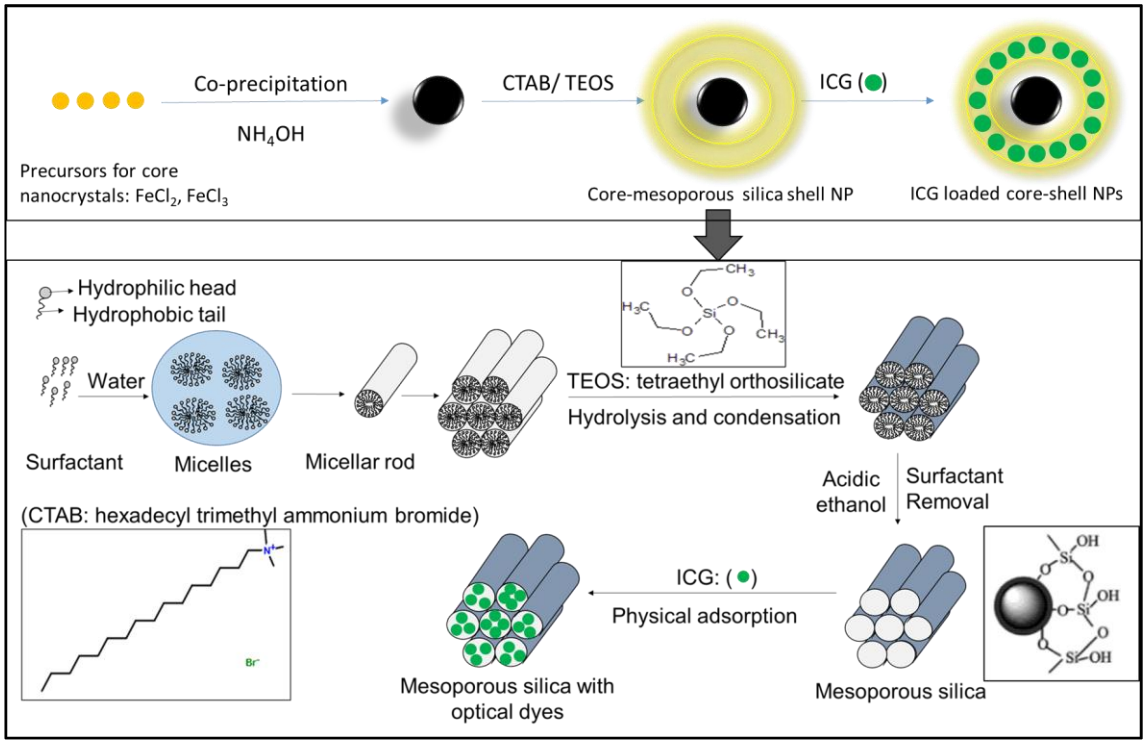

Figure 2-1: Schematic representation of synthesis of magneto-optical nanocomposites.

2.2.1 Synthesis of Hydrophilic Iron Oxide Nanoparticles Using Co-Precipitation Method

Approximately, 22.95 g (0.08 moles, ~0.016 M) of iron (III) chloride hexahydrate ($FeCl_3$. $6H_2O$) and 8.46 g (0.04 moles, ~0.008 M) of iron (II) chloride tetrahydrate ($FeCl_2$. $4H_2O$) were dissolved in pre-heated to 80 ℃ degassed ultrapure deionised water (100 ml) under nitrogen purging in order to remove dissolved oxygen present in the water. Inert conditions were maintained to prevent the oxidation of iron species from Fe^{2+} ($FeCl_2$. $4H_2O$) into Fe^{3+} in aqueous environment (Mascolo, Pei and Ring, 2013). The mixture was poured into degassed ultrapure deionised water (400 ml) in a three-necked round bottom flask. One neck was connected to a water condenser, 2nd neck was connected to an overhead stirrer and the 3rd neck was used for purging nitrogen and inserting a thermocouple to measure 80 ℃ using previously set isomantle. The temperature was maintained at 80 ℃ while stirring under nitrogen. Aqueous ammonium hydroxide [50 ml, 25% (w/v)] was added dropwise over a period of 30 minutes whilst stirring using the overhead stirrer. The resultant reaction mixture was further stirred for an hour. A black suspension formed at the end of the experiment and left overnight for cooling to room temperature (RT) by lifting the reaction flask away from the isomantle heater. The cooled black suspension was transferred into a conical flask and placed on a ferrite magnet slab (152.4 mm x 101.6 mm x 25.4, from E-MAGNETS) for speedy settlement at the bottom. The clear solution was then removed by mechanically fitted water aspirator by creating vacuum as a suction. The pitch-black product at the bottom was washed several times (around 10) with ultrapure deionised water by placing on a magnetic slab in order to remove the surface impurities. The final product was re-dispersed in deionised water and the pH of the resultant washed suspension was measured as 6.1. The stored suspensions were (calculated yield: 99%) synthesised as hydrophilic iron oxide core materials (labelled as NLYPS1), noted as iron oxide nanoparticles number 1 (**IO1)** in this thesis.

The overall reaction can be written as follows:

$$2FeCl_3 + FeCl_2 + 8NH_3 + 4H_2O \rightarrow Fe_3O_4 + 8NH_4Cl$$

2.2.2 Synthesis of Hydrophilic Iron Oxide Nanoparticles Using Modified Co-Precipitation Method

Since the previous method (see Section 2.2.1) synthesised polydispersed nanoparticles, a small batch of nanoparticles were produced by scaling down the synthesis protocol with some optimisation on addition of base. Approximately, 7.65 g (0.02 moles, ~0.17 M) of iron (III) chloride hexahydrate ($FeCl_3$. $6H_2O$) and 2.82 g (0.01 moles, ~0.085 M) of iron (II) chloride tetrahydrate ($FeCl_2$. $4H_2O$) were dissolved in 167

ml of degassed deionised water under nitrogen purging at RT. Then, aqueous ammonium hydroxide [17 ml, 25% (w/v)] was filled in two dialysis bags (9.5 ml each) (3.5 kD MWCO) and transferred into a beaker containing the mixture of iron (II and III) solution for slow release of ammonia in the reaction mixture. The reaction mixture was stirred at RT for an hour. Then, the resultant black-brown iron oxide nanoparticles were washed similar to the procedure described in section 2.2.1. The final pH of the washed suspension was measured as 6.9. The black-brown product (calculated yield: 99%) was re-dispersed in deionised water and labelled as hydrophilic iron oxide core nanomaterial (NLTS11) and noted as iron oxide nanoparticles number 2 (**IO2)** in this thesis.

2.2.3 Synthesis of Hydrophobic Iron Oxide Nanoparticles Using Modified Co-Precipitation Method

Approximately, 24 g (0.09 moles, ~0.018 M) of iron (III) chloride hexahydrate ($FeCl_3$. $6H_2O$) and 9.82 g (0.05 moles, ~0.009 M) of iron (II) chloride tetrahydrate ($FeCl_2$. $4H_2O$) were dissolved in 100 ml of 80 ℃ degassed deionised water under nitrogen gas purging. The mixture was poured into 400 ml of similarly degassed deionised water in a three-necked round bottom flask pre-heated to 80 ℃ using isomantle as described earlier in section 2.2.1. The temperature was maintained at 80 ℃ (temperature recorded using thermocouple) while stirring under nitrogen. Then, 3.76 g (0.01 moles, ~0.02 M) of oleic acid was added and stirred for an hour. Aqueous ammonium hydroxide [50 ml, 25% (w/v)] was then added dropwise over a period of 30 minutes. The reaction mixture was left to stir for overnight (approximately 15 hours). The black precipitate along with supernatant was cooled at RT. On the following day, the cold reaction mixture was transferred into a large conical flask for washing magnetically as described in section 2.2.1. The final pH of the washed suspension was measured as 6.9. Later it was dispersed in 100 ml of hexane and the percentage yield was calculated to be 99% and labelled as hydrophobic iron oxide core material (NLTS2B) and noted as iron oxide nanoparticles number 3 (**IO3)** in this thesis.

2.2.4 Fabrication of Core-Shell Nanocomposites: Mesoporous Silica Coated Hydrophilic Iron Oxide Nanoparticles

The synthesised hydrophilic IONPs were coated with mesoporous silica using the protocol published by Sen, Sebastianelli and Bruce, (2006). Briefly, 0.804 g (0.049 M) of hexadecyl-trimethyl ammonium bromide (CTAB) powder stirred with 45 ml of 0.22 M sodium hydroxide and the final pH measured was approximately 13. Then, 3.78 g (4.05 ml, 0.02 moles) tetraethyl orthosilicate (TEOS) as the silica source was added dropwise to the above mixture under continuous stirring and the pH of the resulted solution was measured as 11.9. Then, 300 ml of previously synthesised hydrophilic iron oxide

suspension (both IO1 & IO2), suspension density of 0.75 mg/ml was added to the above mixture. It was stirred vigorously for about 5 minutes. Then, 2 M HCl was added dropwise until the pH reached to 7. The reaction mixture was stirred for further 30 minutes and afterwards left unstirred about 2 hours for ageing. The material was washed several times with deionised water and then ethanol: water (1:1) using a ferrite magnet slab (152.4 mm x 101.6 mm x 25.4, from E-MAGNETS) *via* magnetic separation in order to remove the surface impurities. Furthermore, to get rid of the CTAB template, the material was washed with acidic ethanol (ratio of 1 ml concentrated nitric acid: 100 ml ethanol) twice followed by one time washing overnight (15 hours). Then, the nanocomposites were washed twice with ethanol: water (1:1). The final product was washed with deionised water (4 times, 500 ml each) and used for further experiments. The resultant nanocomposites were labelled as MS-1A-NLYPS1 (iron oxide from simple co-precipitation method) and MS-3A-NLTS11 (iron oxide from modified co-precipitation method). The resultant core-shell nanocomposites have been named hereafter as magnetic silica nanoparticles number 1 (**MS1)** and 2 (**MS2)**, respectively.

2.2.5 Fabrication of Core-Shell Nanocomposites: Mesoporous Silica Coated Hydrophobic Iron Oxide Nanoparticles

Previously synthesised hydrophobic IONPs (IO3) was used as core in this protocol. The mesoporous silica was coated according to the protocol of Sharifabad (2016) with a slight modification. A suspension of the nanoparticles (1 ml of 35.7 mg/ml) was poured into an aqueous CTAB solution (5 g in 25 ml deionised water, 0.5 M) at RT in a beaker. The resulting solution was stirred vigorously for 30 minutes which led to thick brown solution implying the formation of oil-in-water microemulsion. Then the mixture was heated on a hot plate at 60 ℃ (carefully monitored using a calibrated thermometer) for 20 minutes whilst stirring to get rid of hexane. To this solution, 225 ml of deionised water with 1.5 ml of sodium hydroxide was added. Then, 2.5 ml of TEOS was added dropwise. The resultant reaction mixture was stirred for another 2 hours. The as-prepared mesoporous silica-coated magnetic nanocomposites were washed with deionised water (5×, 300 ml each) using ferrite magnet slab (152.4 mm x 101.6 mm x 25.4, from E-MAGNETS) as described in section 2.2.1. To remove CTAB template from the pores of the nanocomposite, the as-prepared materials were washed twice with 50 ml of acidic ethanol in an end-over-end rotator for 1 hour followed by one time washing overnight (15 hours). Afterwards, the nanocomposites were washed twice with ethanol: water (1:1, 50 ml each). The final product was washed 2-3 times with ultrapure deionised water in order to remove surface impurities and dispersed in 20 ml deionised water. The

samples were labelled as MS-8A-NLTS2 and will be named hereafter as magnetic silica nanoparticles no. 3 (**MS3)**.

2.2.6 Fabrication of Indocyanine Green (ICG) Loaded Magneto-Optical Nanocomposites

For loading ICG, 10 mg (variable volume of suspension depending on pre-determined suspension density) of respective batches (MS1, MS2 or MS3) of core-shell nanocomposites were taken and 2 ml of homogenously mixed ICG solution (approximately, 250 µM, 0.04 g ICG/ g of nanocomposites) was added. The ICG was weighed in Mettler Toledo XP6 micro balance optimised for precise weighing of small samples with instrument repeatability of 0.0008 mg samples. The resultant reaction mixture was stirred for 3 hours at RT to induce encapsulation of ICG inside the silica mesopores of core-shell magnetic nanocomposites (MS). As ICG tends to aggregate when dissolved above a certain concentration, a low concentration of ICG solution (250 µM) was taken and repeated the method successively for higher loading as cumulative intrusion. The amount of ICG loading was determined by measuring the absorbance at wavelength of 778 nm using pre-established standard calibration curve (Figure 2-2). No absorbance at 778 nm was observed before addition of ICG. After each successive loading, the supernatant was removed by magnetic separation using PolyATtract® System 1000 Magnetic Separation Stand (15- 50 ml, Promega) and read absorbance values at 778 nm using UV-vis spectrophotometer. The ICG loaded resultant magneto-optical nanocomposites labelled as **MS1ICG, MS2ICG** and **MS3ICG** depending upon MS1, MS2 or MS3 magnetic nanocomposites.

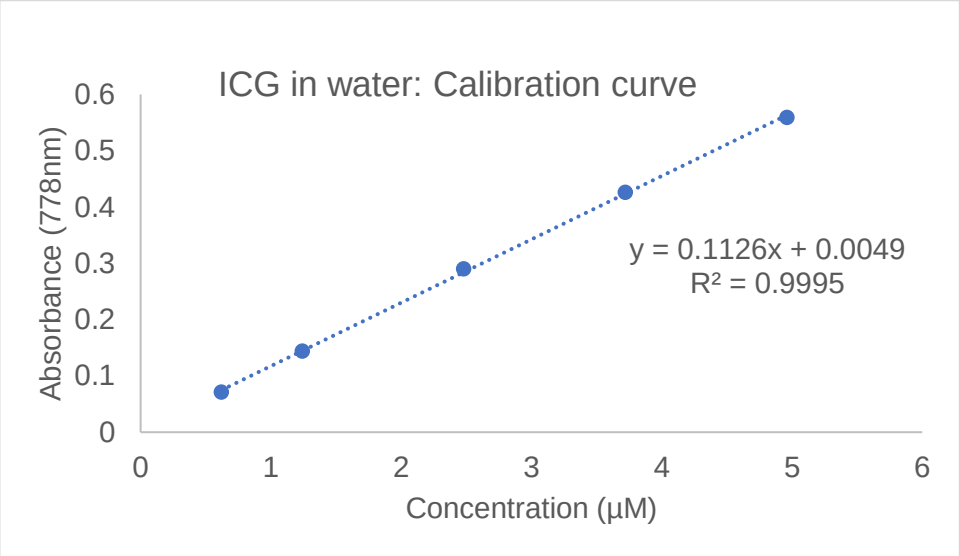

Figure 2-2: Calibration curve of Indocyanine green (ICG) in water using the absorbance values at 778 nm.

Drug loading capacity (DLC) and encapsulation efficiency (EE) was also calculated using the equations (2-1 and 2-2). The weight of ICG in supernatant was calculated based on the calibration curve shown in Figure 2-2. The weight of IONPs used for the fabrication was 10 mg. The suspension density of IONPs (mg/ml) was determined by gravimetric method where a known volume of dispersion was dried at 50 ℃ in an oven, overnight, and the obtained solid residue was weighed.

$$\boldsymbol{DLC}(\%) = \frac{\boldsymbol{Weight\ of\ ICG\ Fed - Weight\ of\ ICG\ in\ supernantant}}{\boldsymbol{Weight\ of\ nanoparticles}} \times \mathbf{100}\% \qquad \text{(Equation 2-1)}$$

$$\boldsymbol{EE}(\%) = \frac{\boldsymbol{Weight\ of\ ICG\ Fed - Weight\ of\ ICG\ in\ supernantant}}{\boldsymbol{Weight\ of\ ICG\ Fed}} \times \mathbf{100}\% \qquad \text{(Equation 2-2)}$$

2.3 Characterisation of Nanoparticles and Nanocomposites

2.3.1 Size and Surface Morphology Using Transmission Electron Microscope (TEM)

Electron micrographs for studying morphology and size of the nanoparticles were obtained by using transmission electron microscope (TEM) [TECNAI 200 Kv TEM (Fei, Electron Optics)]. To achieve higher magnification and resolution, electron beams are used instead of visible light, since the wavelength of high energy electrons is much smaller than visible light. A beam of electrons from the electron gun is focused on the specimen with the condenser lens. The transmitted beam striking on the specimen is focused by the objective lens resulting into a magnified image. The image is viewed through the Gatan digital camera installed and extracted through Gatan Digital Micrograph software.

Specimen preparation: TEM specimens were prepared on commercially available lacey carbon coated copper grids (400 mesh, Agar Scientific). Nanoparticles and nanocomposites suspensions were diluted in either aqueous or organic solvents before sprinkled them on the TEM grid. The TEM grids with sprinkled samples were dried at room temperature under normal atmospheric condition. They were then analysed under TEM. Finally, the size distribution of nanoparticles and nanocomposites were analysed using ImageJ software.

2.3.2 Particle Size Distribution and Zeta Potential Measurement Using Dynamic Light Scattering (DLS)

The particle size and zeta potential of the nanocomposites were obtained from the Zetasizer Nano ZS (Malvern Panalytical) instrument fitted with 633 nm ‘red’ laser. The basic principle for determining the size is by measuring the Brownian motion of the particles in a sample using Dynamic Light Scattering (DLS) and interpreting the size

using established theories. The smaller the size of particles in a sample, higher is the movement, ultimately, higher is the diffraction detected by the photodetectors. Secondly, Zetasizer can also be used to determine the zeta potential of the sample. The importance of zeta potential is to check the surface charges of the nanoparticles and their stability in suspension. Particles with high charges resist flocculation and aggregation due to electrostatic repulsion making them to be stable in suspension.

For measuring the particle size distribution, stock nanoparticles suspensions were diluted in deionised water until a clear suspension was observed and then sonicated for 5 minutes in an ultrasonic bath. Then, the samples were transferred in disposable polystyrene cuvettes up to the optimum level (10 mm) and kept inside the Zetasizer. The temperature was set at 25 ℃ and 3 measurements were carried out (12 scans each) for each sample. The Z-average was taken as the average hydrodynamic diameter of the particles.

A specially designed Zeta cells (DTS1070) were used for Zeta potential measurements. The samples were kept in the Zeta cell making sure no bubbles were formed inside the cell. Then, the Zeta potential was measured from electrophoretic mobility of the charged particles. For each sample, three measurements were run with 20 scans at 25 ℃ and the average values (in mV) was used for analysis.

2.3.3 Determination of Bond Vibrations Using Fourier Transform Infrared Spectroscopy (FTIR)

Fourier Transform Infrared Spectroscopy (FTIR) measures the molecular structure and bonding positions when infrared radiation (IR) is passed through the sample. The absorption observed in an IR spectrum are the result of bond vibrations within a molecule. A simple FTIR instrument consists of interferometer (modulates the wavelength), source, sample compartment and detector (measures the reflected light).

Sample preparation: The samples were dried at 50 ℃ in oven for overnight. The dried samples were directly casted over the ATR-FTIR diamond crystal for analysis using Omnic (8.0 software). The transmittance (%) vs wavenumber (cm^{-1}) spectra were generated over the range of 400 to 4000 cm^{-1}.

2.3.4 Determination of Crystal Structure *Using* X-Ray Diffraction (XRD) Instrument.

X-ray diffraction (XRD) is a common method to study crystal structure and atomic spacing of solid materials. An electromagnetic radiation with short wavelength within the range of 0.5-10 Å is usually used in the diffraction experiments. XRD patterns are generated following the Bragg's diffraction law. When an X-ray beam produced from X-

ray tube hits the sample, it interacts with electrons on the crystal and some of the photons are reflected away from their original path. The path difference between incident reflection on the 1st and 2nd layer is equal to the integer multiple of wavelength of X-ray which is written as:

$$2d\,sin\,\theta = n\,\lambda \qquad \text{(Equation 2-3)}$$

where n is an integer, λ is the wavelength (λ of CuKα = 1.5406 Å) of X-ray radiation, θ is the incidence angle and d is the interplanar spacing of Miller planes in the crystal lattice points

The benchtop powder X-ray diffraction D2 PHASER was used to analyse the X-ray diffraction (XRD) pattern of the nanoparticles and nanocomposites. DIFFRAC.SUITE software was used to control the instrument and analyse the data.

2.3.5 Surface Area and Pore Diameter Analysis Using Brunauer-Emmett-Teller (BET) Method

Brunauer-Emmett-Teller (BET) method based on the BET equation is a technique generally used to determine the surface area and micro/mesopore size distribution of a solid material by the adsorption of an inert gas, such as nitrogen. According to BET theory, gas molecules physically adsorb on a solid surface in layers without any interaction between each adsorbed molecule. The increase in pressure of gas over a solid surface increases the adsorption of gas molecules. The decrease in pressure of gas molecules increases desorption at constant temperature (isotherm). The graph generated according to adsorption and desorption isotherm provides surface area and porosity of the solid materials. The isotherm obtained can be utilised to distinguish the types of porosity. Type IV isotherm (hysteresis loop) occurs in the mesoporous materials (pores in the range of 2-50 nm).

Sample preparation: The experiments were performed in Micromeritics ASAP 2020 instrument. Initially the nanocomposites were dried overnight in a pre-set oven at 100 ℃ in order to remove any adsorbed water and atmospheric gases during storing in the laboratory. In each analysis, approximately, 200 mg of a dried sample transferred in a special sample tube (supplied by Micromeritics, USA) for analysis. The sample tube containing nanocomposites placed for degassing under vacuum at 270 ℃ for the period of 4 hours. Nitrogen gas was used as adsorbent and liquid nitrogen was used to maintain the constant temperature (77 K i.e., -196 ℃). The BET surface area and adsorption isotherm plots were obtained by built-in Micromeritics ASAP 2020 software.

2.3.6 Measurement of Thermal Stability and Organic Contents in Inorganic Nanocomposites Using Thermogravimetric Analysis (TGA)

Thermal stability and the presence of volatile components can be determined using TGA. The resulting thermal curve (% weight loss against temperature rise) depicts the change of mass of a sample in relation to temperature increase. The presence of volatile components, adsorbed water or organic components in nanocomposites was determined by using Mettler Toledo TGA instrument.

Experimental condition: The temperature ramp from 25 ℃ to 600 ℃ (heating rate of 10 ℃/minute) was used for the analysis of TGA curves. Air was used to conduct oxidative studies and identify the percentage of carbon in the materials. Nitrogen can be used as an inert purge gas, if needed. An aluminium pan without any sample was first run as a blank in the system for calibration of the microbalance. Approximately, 2 mg of sample (dried overnight at 100 ℃) was taken for the measurement. The change of mass of the sample vs temperature plots were generated using STARe thermal analysis evaluation software.

2.3.7 Measuring Heating Ability of Nanoparticles upon Alternating Magnetic Field (AMF) Using a Commercial Magnetic Hyperthermia Instrument

The efficiency of nanoparticles in suspension to generate heat from magnetic coupling due to magnetic moment under applied alternating magnetic field (AMF) is measured as Specific Power Absorption (SPA) or Specific Power Loss (SPL). SPA is the power absorbed per unit mass of the magnetic nanoparticles (Mohammad et al., 2010).

$$\boldsymbol{SPA} = \frac{\boldsymbol{C}\,\boldsymbol{V_s}}{\boldsymbol{M}}\frac{\boldsymbol{dT}}{\boldsymbol{dt}} \qquad \text{(Equation 2-4)}$$

where, C= specific heat of the solvents where nanoparticles are suspended (4.185 J/g per °C for water), V_s= Volume of the nanoparticles in suspension (1 ml), M= weight of magnetic nanoparticles (10.8 mg), dT/dt = Gradient of time-dependent magnetic heating curve (J/sec) where T is the temperature, t is the measurement time.

The direct measure of magnetic heating was achieved by using DM100 instrument (nB nanoscale Biomagnetics, Spain) with maximum AMF of 15.8 kA/m at a frequency of 406 kHz. For calculating the SPA, a relatively small volume of nanoparticles was used. A time and field dependent temperature curves were generated using an inbuilt software (Maniac). A measuring condition such as fixed magnetic field of 200 Gauss and hyperthermia temperature (42 ℃) was set. Furthermore, a parameter called Intrinsic Loss Power (ILP) of nanocomposites was introduced to relate the experimental

conditions which are independent of the concentration of magnetic nanoparticles in suspension and type of equipment used.

$$\boldsymbol{ILP} = \frac{\boldsymbol{SPA}}{\boldsymbol{f(H_o)^2}} \quad \text{(Equation 2-5)}$$

where, SPA= SPA or SPL index (W/kg), f = frequency of applied magnetic field (Hz) and H_o = intensity of applied magnetic field (A/m) (where, 1 A/m is equivalent to 0.01256 Gauss).

2.3.8 Measuring Heating Ability of Nanocomposites (Photothermal Effect) Upon Laser Irradiation of Specific Wavelengths

To study the photothermal effect of the nanocomposites, the laser module source (RLDH808–1200-5) from Roithner Lasertechnik Gmbh, Vienna, Austria was used that emitted at a wavelength of 808 nm with output power of 1.2 W/cm^2. The temperature was monitored using a digital temperature probe (Fisher Scientific) at different laser exposure time.

For the experiment, 2 ml of each sample (MS1ICG, MS2ICG, MS3ICG and pure ICG) at a concentration of 20 µM ICG content were taken in the quartz cuvette. The concentration of various nanocomposites used for 2 ml of final suspension were calculated to be 255 µg/ml (MS1ICG), 1.7 mg/ml (MS2ICG) and 1 mg/ml (MS3ICG). The laser was irradiated horizontally inside a box under dark condition (see Figure 2-3 as a photograph of experimental setup). Triplicate experiments were carried out for each sample and temperature changes were measured in every 30 seconds interval. Temperature change versus time curves were drawn in order to show the photothermal effect.

To study the photostability of nanocomposites upon repeated laser irradiation, the temperature change was measured after each laser irradiation cycles performed for 600 seconds (10 minutes). Similar concentration of nanocomposites as stated above were irradiated using the same experimental setup (see Figure 2-3). To make sure the nanocomposites do not settle at the bottom of the cuvette, the nanocomposites were mixed thoroughly after each laser ON/OFF cycles.

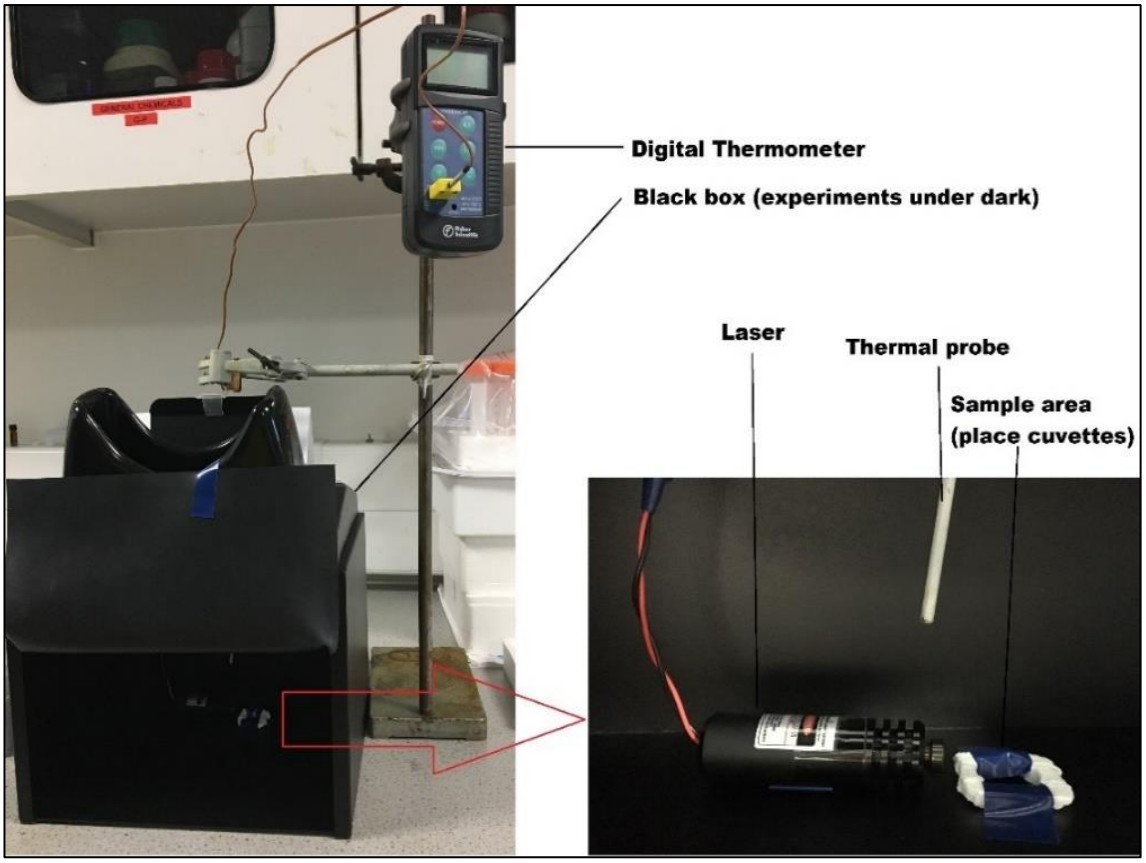

Figure 2-3: Experimental setup for laser irradiation on nanocomposites. Temperature was monitored through digital temperature probe. The laser was irradiated horizontally (as shown on right side) on the cuvettes for PDT (Photodynamic therapy) and PTT (Photothermal therapy) while vertically on well plates for *in-vitro* experiments.

2.3.9 Detection of Generation of Singlet Oxygen Upon Laser Irradiation of Specific Wavelengths

To detect the presence of singlet oxygen in suspension, a chemical probe, 9,10-anthracenediyl-bis (methylene) dimalonic acid (ABMDMA), was used. It is a water-soluble anthracene-based dye which reduces to its corresponding endoperoxide form by photo-bleaching in the presence of singlet oxygen ($^1O_2$) as shown in Figure 2-4. The generation of $^1O_2$ was monitored spectrophotometrically by recording the loss of the absorbance intensity (wavelength, λ = 400 nm) at different time intervals upon laser irradiation. The same setup as Figure 2-3 was used for photodynamic therapy (PDT) study. The decrease in absorbance values *Vs* time curves were generated as an indication of reactive oxygen species (ROS) production indirectly due to the photobleaching of ABMDMA.

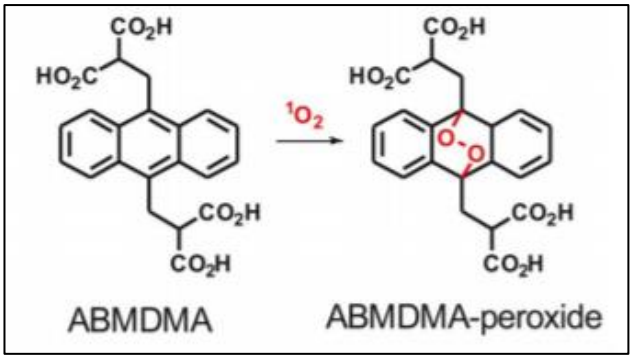

Figure 2-4: Reactivity of 9,10-anthracenediyl-bis (methylene) dimalonic acid (ABMDMA) in presence of $^1O_2$. Adapted from (Galstyan and Dobrindt, 2019)

2.4 *In-vitro* Studies

Commercially available MCF7 cell lines were used for *in-vitro* experiments. All *in-vitro* experiments were performed in Class II cabinets to protect cells from contamination. The cell lines were purchased as frozen aliquots and stored in liquid nitrogen (long-term) or -80 ℃ freezer (short-term). All cells were maintained in the culture media as stated in Table 2-4 and incubated at 37 ℃ in a humidified incubator with 5% CO_2.

A preliminary toxicity studies of nanocomposites were performed on HepG2 liver cancer cell line as well, however, those experiments were not included in this thesis due to inconsistent results. Further experiments were designed specifically for MCF7 cell line which is the most studied and suitable model for breast cancer investigations worldwide.

2.4.1 MTT Assay for Testing Sensitivity of Nanocomposites

MTT assay is a sensitive and reliable colorimetric assay used for assessing cell metabolic activity to predict cellular viability, proliferation, and cytotoxicity. This assay relies on the ability of metabolically active cells to reduce a yellow coloured, water-soluble tetrazolium salt [3-(4,5-dimethylthiazol-2-yl)-2,5-diphenyltetrazolium bromide; MTT] into insoluble purple coloured formazan crystals (Figure 2-5). The viable cells contain NAD(P)H-dependent oxidoreductase enzymes which are responsible for the reduction of MTT. Dissolving the insoluble formazan product in DMSO results into a coloured solution which is quantified by measuring the absorbance (wavelength λ = 550 nm) using a multi-well spectrophotometer. Higher the absorbance, higher the cellular viability. Lower absorbance implies either the cells are dying or already dead.

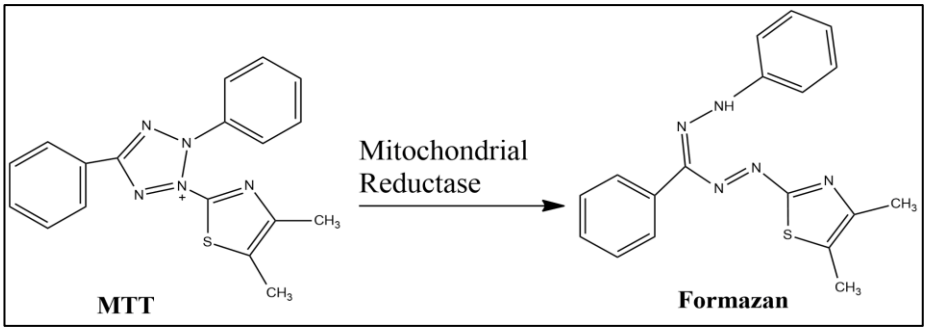

Figure 2-5: Conversion of MTT to Formazan by mitochondrial reductase

The biocompatibility of the nanocomposites was tested on MCF7 cell lines by MTT assay. The cells were seeded in 96-well plate at $5x10^3$ cells/well and incubated in DMEM media supplemented with FBS, 100 IU penicillin and 100 µg streptomycin with different concentrations of MS, MSICG and pure ICG for 24 and 48 hours. After different time points, 20 µl of MTT solution (5 mg/ml in PBS buffer of pH 7.4) was added to each well and incubated at 37 ℃ for 4 hours. Formazan crystals (so formed) were then dissolved in DMSO to get a clear solution. The optical density was recorded at a wavelength of 540 nm in an ELISA-reader (USCN Life Sciences Kit Inc Wuhan).

The percent cytotoxicity was determined by the following equation:

$$\%\ Cytoxicity = \frac{[Absorbance\ of\ Control]-[Absorbance\ of\ Sample]}{[Absorbance\ of\ Control]} \times 100 \qquad \text{(Equation 2-6)}$$

where, “Absorbance of Sample” is the absorbance of the test sample, and “Absorbance of Control” is the absorbance of the control without the addition of test sample (nanocomposites). Considering control cells as 100% viable, the cell viability was determined by subtracting it with the percentage cellular toxicity.

2.4.2 Cellular Toxicity Studies Upon Laser Irradiation

For performing this assay, MCF7 cells were seeded in 96-well plates at $5x10^3$ cells/well. After incubation for 24 hours, the cells were treated with the nanocomposites with/without the presence of loaded ICG and pure ICG dispersed in media at different concentrations. Following 2 hours of treatment, the cells were treated with the laser of wavelength 808 nm at a power density of 1.2 W/cm^2 for 5 minutes. After laser irradiation, the cells were incubated for different time points of study (24 and 48 hours). After different time points, 20 µl of MTT solution (5 mg/ml in PBS buffer, pH 7.4) was added to each well and incubated at 37 ℃ for 4 hours. Formazan crystals (so formed) were then dissolved in DMSO to get a clear solution. The optical density was recorded at a wavelength of 540 nm in an ELISA-reader (USCN Life Sciences Kit Inc Wuhan).

The percentage cell toxicity for cells treated with nanocomposites (treated cells) was calculated with reference to the control cells without nanoparticles / nanocomposite treatment and laser irradiation (untreated cells). Cells without nanoparticles / nanocomposites treatment were also laser irradiated to check the toxicity of laser irradiation alone. The readings were taken with 3 replicates of same concentration.

2.4.3 Trypan Blue Cell Viability Assay upon AMF and Laser irradiation

For performing this assay, MCF7 cells were seeded in a tissue-culture treated Petri dishes (30 mm diameter) at 2,500 cells/well. After incubation for 24 hours, the cells were treated with the nanocomposites (100 µg/ml). Following treatment for another 24 hours, the cells were exposed to AMF (DM100 instrument) for 45 minutes. The cells were incubated again for 24 hours. For experiments with both AMF and laser irradiation, the cells were laser irradiated for 5 minutes after AMF application and incubated for another 24 hours. Then, the cells were treated with trypsin and collected in an Eppendorf tube. Equal volume of trypan blue was added, and the viable and dead cells were counted using haemocytometer. The percentage cell viability of cells was calculated according to the equation below:

$$\%\ Cell\ viability = \frac{Live\ cells}{Live\ cells + Dead\ cells} \times 100 \qquad \text{(Equation 2-7)}$$

2.5 Cellular Uptake of Nanocomposites

2.5.1 Visual Representation of Cellular Uptake Using Scanning Electron Microscope (SEM)

Cellular uptake of ICG loaded nanocomposites (MS2ICG and MS3ICG) was evaluated on MCF7 cells using Scanning Electron Microscope (SEM) [TESCAN Clara with Quoram CPD and Sputter coater]. The cells were seeded on a coverslip in 24-well plates at a concentration of approximately 5x 10^4 cells/well and incubated for 24 hours at 37 ℃ in 5% CO_2. Following incubation, the cells were treated with nanocomposites at a concentration of 100 µg/ml and incubated for 2 hours. Then, the cells were washed with chilled PBS buffer (pH 7.4) to remove the remaining nanocomposites in the buffer media and then fixed with 4% paraformaldehyde for 20 minutes. After fixation, the cells were washed with PBS to remove traces of paraformaldehyde and washed with 0.1 N sodium cacodylate. Afterwards, the cells were incubated in 1% osmium tetra-oxide (OsO_4) for 1 hr in dark. After incubation, the cells were washed with 0.1 N sodium cacodylate to remove OsO_4. Then, the cells were dehydrated in different gradient of ethanol 30%, 50%, 70%, 90%, 95%, 100% for 5 minutes in each. After dehydration, the cells were air dried, and the coverslip was hold on a stub with the help of carbon tape. Then the images were taken using SEM.

2.5.2 Prussian Blue Staining

The cells were seeded in coverslips in 12-well plates in $1.5x10^5$ cells/ml and incubated at 37 ℃ for 24 hours. The cells were treated with 200 µg/ml of both nanocomposites with ICG and incubated again for 24 hours. Then the cells were washed 3 times with 1 ml of warm PBS to get rid of nanocomposites aggregated over the cells. Approximately 300 µl of cell fixation solution (4% paraformaldehyde in PBS) was added to cover the coverslip and incubated at room temperature for 20 minutes. The paraformaldehyde was removed by washing twice with PBS (1 ml). The cells were attached on the coverslip and ready to be stained. The cells were washed with deionised water for 5 minutes and incubated with iron staining solution (see Table 2-8) for 20 minutes at RT. Then, the cells were washed with deionised water and stained with nuclear staining solution for 5 minutes. After the staining experiment, the cells were again washed with deionised water, air dried for few minutes, mounted using a fast-drying mounting media and placed on a slide. The cells were observed under a phase contrast inverted microscope at 20x magnification, and images were taken using Mshot digital imaging system.

2.5.3 Confocal Fluorescence Microscopy

Cellular uptake of ICG loaded nanocomposites was also evaluated on MCF7 cells using confocal florescence microscopy [Leica TCS SP8 Confocal Laser Scanning Microscope with AOBS (Acousto Optical Beam Splitter)]. The cells were seeded in 24-well plates at a concentration of approximately 10^4 cells/well and incubated for 24 hours at 37 ℃ in 5% CO_2. Following incubation, the cells were treated with ICG loaded nanocomposites (MS2ICG and MS3ICG) and incubated for different time points (2 and 4 hours). Then, the cells were washed with PBS buffer (pH 7.4) to remove the remaining nanocomposites on the media and then fixed with 4% paraformaldehyde for 30 minutes. The cells were washed three times with 1 ml PBS (pH 7.4) and incubated with 1 µg/ml DAPI solution for 30 minutes in dark to counterstain the nucleus followed by washing once with PBS buffer. The coverslips were then mounted on the slides and were sealed with Dibutylphthalate Plasticizer Xylene (DPX). The cells were viewed at a magnification of 20x using a Cy5 filter under a Nikon Eclipse 90i Epi-fluorescence upright microscope equipped with a Nikon DXM 1200 digital camera.

2.6 Endocytosis

The MCF7 cell line was exposed to different endocytosis inhibitors diluted with media such as 0.45 M sucrose (clathrin pathway), 0.1% (w/v) sodium azide (micropinocytosis), 10 µg/ml Lovastatin (caveolae pathway) and at 4 ℃ for energy-dependent endocytosis. After 30 minutes, a fresh media containing endocytic inhibitors

and nanocomposites were added to the cells and incubated for further 4 hours. Cells were analysed for qualitative nanoparticles uptake using fluorescence microscope.

Briefly, the cells were seeded on coverslips in 24-well plates at a concentration of $5x10^4$ cells/well and incubated for 24 hours at 37 ℃ in 5% CO_2. Following incubation, the cells were treated and incubated for 30 minutes with different endocytosis inhibitors diluted with DMEM such as 0.45 M sucrose (clathrin pathway), 5 µg/ml sodium azide (micropinocytosis), 10 µg/ml Lovastatin (caveolae pathway) and 4 ℃ for external binding. Then, the cells were washed with media following treatment with the ICG loaded nanocomposites (MS2ICG and MS3ICG) containing same concentration of inhibitors as previously. The cells were incubated for further 4 hours and washed three times with PBS (pH 7.4) to remove the remaining nanocomposites. The cells were fixed with 4% paraformaldehyde for 30 minutes. After fixation, the cells were washed three times with PBS buffer (pH 7.4) and incubated with 1 µg/ml DAPI solution for 30 minutes in dark to counterstain the nucleus followed by washing once with PBS. Then, the coverslips were mounted on the slides and were sealed with Dibutylphthalate Plasticizer Xylene (DPX). The cells were viewed at a magnification of 20x under a Nikon Eclipse 90i Epi-fluorescence upright microscope equipped with a Nikon DXM 1200 digital camera.

2.7 DCFDA Imaging for Testing the Presence of ROS

The generation of ROS in the MCF7 cells upon treatment of nanocomposites after laser irradiation was tested using DCFDA (dichloro-dihydro-fluorescein diacetate) assay. For this, MCF7 cells were seeded in a 24- well black plate with flat and clear bottom (µ-Plate, from ibidi® to lower well-to-well crosstalk in fluorescence microscopy) at a seeding density of $6x10^4$ cells/well. The cells were allowed to attach overnight. Then, cells were treated with 200 µg/ml of MS2ICG, MS3ICG and pure ICG (equivalent amount of encapsulated ICG in nanocomposites) diluted in complete media containing MEM without phenol red. A positive control of 100 µM tert-butyl hydrogen peroxide (THBP) and negative control containing MEM media were included for comparative studies. The cells were treated for 24 hours. Then, upon laser irradiation (1.2 W/cm^2) for 5 minutes, the cells were incubated for additional 2 hours. The buffer solutions and DCFDA mixture were freshly prepared as shown in

Table 2-9. The final concentration of DCFDA was maintained at 20 µM. After staining with DCFDA for 45 minutes at 37 ℃ in dark, the cells were washed once with 1× dilution buffer. The florescence images were captured and analysed on an inverted Zeiss fluorescence microscope and Zen blue software (GmbH, Germany) using an excitation wavelength of 485nm and an emission wavelength of 535nm to detect DCF.

2.8 Quantification of ROS Generation by DCFDA

This experiment quantifies the ROS generated in the MCF7 cells using DCFDA (dichloro-dihydro-fluorescein diacetate) assay. The MCF7 cells were seeded at a density of 1 x 10^6 cells in 6-well plates for 24 hours. Then they were treated with nanocomposites at their specific IC_{50} values and incubated for 2 hours. Following incubation, cells were exposed to laser irradiation (1.2 W/cm^2) for 5 minutes/well and incubated for further 24 hours. Post laser irradiation, the cells were harvested and incubated with 25 µM of DCFDA for 40 minutes at 37 ℃ in dark. The fluorescence intensity values were measured using a spectrofluorometer (Agilent Technologies, U.S.A) with an excitation and emission wavelengths of 485 nm and 529 nm, respectively.

2.9 Biochemical Assays

Different biochemical assays were performed to estimate antioxidant enzymes after treatment with the nanocomposites following the post laser irradiation. MCF7 cells were seeded at density of 1 x 10^6 cells in 6-well plates in DMEM containing 2.5% FBS and incubated for 24 hours. After incubation, they were treated with nanocomposites at their specific predetermined IC_{50} values and incubated for 2 hours. Following incubation, cells were exposed to laser (1.2 W/cm^2, 808 nm wavelength) for 5 minutes/well and incubated for further 24 hours. After the laser treatment, the supernatants were collected for lactate dehydrogenase (LDH) release assay, lipid peroxidation (LPO) assay and Nitric oxide (NO) assay. The cells were washed with PBS once and scraped in the presence of 1 ml media to collect cells in a microcentrifuge tube. The cells were centrifuged and pelleted down by centrifugation at 1100 rpm for 10 minutes at 4 ℃. The supernatant was subsequently discarded, and the cell pellet was resuspended in 200 µl of chilled PBS. Cells were sonicated for 3 minutes maintaining cold condition, followed by syringe pipetting, to break the cells and release the cytoplasmic contents. All the steps were performed on crushed ice to maintain cold temperature. Further, it was centrifuged at 5000 rpm for 10 minutes at 4 ℃. The cell free extract (CFE) was collected to perform other remaining assays.

2.9.1 Lactate Dehydrogenase Release Assay

The supernatant of cells collected post treatment as explained above was centrifuged at 10,000 rpm at 4 ℃ for 15 minutes to remove any cell debris. Each sample was transferred to 3 wells in a 96 well plate (20 µl) and the substrate solution (34 mM sodium pyruvate) along with 0.28 mM β-NADH was added. Then, 20 µl of homogenisation buffer i.e., 100 mM sodium phosphate buffer (SPB) was added on the control wells. The absorbance was measured at 340 nm using a 96-well plate ELISA-

reader (USCN Life Sciences Kit Inc Wuhan). The LDH release of the samples were measured by calculating the decrease in NADH absorbance over time (Bergmeyer and Bernt, 1974). The values were expressed in µM/min/mg protein.

2.9.2 Lipid Peroxidation (LPO) Assay

A stock solution of TCA-TBA-HCl (trichloroacetic acid- thiobarbituric acid-hydrochloric acid) was prepared by adding 15% w/v TCA, 0.375% w/v TBA and 0.25 N HCl. This solution was slightly heated on a hot plate with stirrer to assist the dissolution of TBA. Then, 200 µl of supernatant extracted earlier was vigorously mixed with 800 µl of TCA-TBA-HCl in a microcentrifuge tube. The solution was heated in a water bath at 100 ℃ for 1 hour. After cooling, the flocculent precipitate was removed by centrifugation at 3000 rpm for 10 minutes at room temperature. The absorbance of the sample was read at 535 nm against a blank prepared without supernatant. The calculated percentage increase in optical density (OD) is directly proportional to increase in the level of LPO.

2.9.3 Nitric Oxide (NO) Assay

Briefly, 1% sulphanilamide (Reagent A) and 0.1% N-1-napthylethyldiamine dihydrochloride (NEDD, Reagent B) were prepared in 2.5% orthophosphoric acid, respectively. The reagents were mixed in a ratio of 1:1. To the final assay mixture of 200 µl, 100 µl of supernatant fraction was added to the mixture of Reagents A and B. The absorbance was measured at 540 nm immediately against a blank containing SPB instead of the sample. The values were expressed as µM/mg protein.

2.9.4 Reduced Glutathione (GSH) Activity

The cell free extract (CFE) was taken for GSH activity analysis. Briefly, 100 µL of CFE was taken in a microcentrifuge tube and precipitated using 20 µL of 5% trichloroacetic acid (TCA). The tubes were centrifuged for 10 minutes at 3000 rpm in RT to remove the precipitated proteins. Then, 45 µL of supernatant was added into a well on a 96-well plate with 45 µL of SPB (0.2M, pH 8) and 20 µL (10 mM) of 5,5'- dithiobis 2-nitrobenzoic acid (DTNB) to prepare a final volume of 110 µL. The absorbance was measured immediately at wavelength of 412 nm. A blank was prepared without the extract and subtracted from the OD of samples. The amount of GSH was compared to the total protein amount calculated using BSA assay. The GSH activity was expressed in µM/min/mg protein.

2.9.5 Glutathione Peroxidase (GPx) Assay

The cell free extracts (CFE) were taken for analysis of glutathione peroxidase (GPx) activity as per as the protocol published by Paglia and Valentine (1967). Firstly, 50 mM SPB (pH 7) was prepared with 1 mM sodium azide and 1 mM EDTA. Then, a

reaction mixture was prepared by adding as-prepared SPB with 0.2 mM βNADPH, 1U glutathione reductase (GR), and 1 mM glutathione (GSH). For final assay condition, 50 µl of CFE together with 80 µl of reaction mixture were added in each well in the 96 well plate and further initiated by adding 20 µl of 0.042% (w/w) hydrogen peroxide (H_2O_2) on each well. The OD was recorded immediately using spectrophotometer at wavelength of 340 nm, against a blank containing SPB without sample. The total activity of GPx was expressed as µmol βNADPH oxidized/min/mg protein.

2.9.6 Glutathione Reductase (GR) Assay

Utilising the same principle as explained for GPx assay, the activity of glutathione reductase (GR) was measured. The activity of GR was determined using the CFE. The assay cocktail was prepared by adding 0.02 ml of 12 mM βNADPH, 2 ml of 9 mM of glutathione disulfide (GSSG), 2.6 ml of 6.67 M SPB (pH 7.6). A mixture of 20 µl of CFE and 80 µl of assay cocktail were added in each well of the 96-well plate and the activity of GR was observed immediately by spectrophotometer by measuring the OD at 340 nm. A blank was prepared containing SPB. The activity of GR was expressed in terms of µmol βNADPH oxidized/min/mg protein.

2.9.7 Glutathione-S-Transferase (GST) Assay

GST level was measured by the conjugation reaction of GSH with 1-chloro-2,4-dinitrobenzene (CDNB). The CFE (20 µl) was added to 180 µl of reaction mixture [sodium phosphate buffer, CDNB (100 mM) and reduced GSH (100 mM)]. The activity of GST was measured with an increase in absorbance at 340 nm by spectrophotometry.

2.9.8 Superoxide Dismutase (SOD) Assay

The activity of SOD was measured utilising the protocol of Kakkar, Das and Viswanathan (1984). The reaction mixture was prepared using 0.025 M sodium pyrophosphate (pH 8), 180 µM phenazine methosulfate (PMS) and 300 µM nitroblue tetrazolium (NBT). For the final assay mixture of 100 µl, 20 µl of CFE was taken on each well of 96-well plate and 60 µl of reaction mixture was added along with 20 µl of 780 µM NADH. The absorbance was measured at 560 nm immediately against a blank containing SPB without sample. The OD calculated was interpolated on a standard curve for crude extract of SOD enzyme and further expressed as ng/mg of protein.

2.10 Iron Assay

The presence of total iron and iron ions (Fe^{2+}, Fe^{3+}) in MCF7 cell lines upon treatment with nanocomposites and laser irradiation were determined using iron assay kit from Sigma Aldrich, UK.

2.10.1 Sample Preparation

MCF7 cells were seeded at density of 1 x 10^6 cells in 6-well plates in DMEM containing 2.5% FBS and incubated for 24 hours. After incubation, they were treated with nanocomposites (MS2ICG and MS3ICG) at their specific predetermined IC_{50} values and incubated for 2 hours. Following incubation, cells were exposed to laser irradiation (1.2 W/cm^2, 808 nm wavelength) for 5 minutes/well and incubated for further 24 hours. Cells without laser irradiation were directly incubated for 24 hours after treatment with nanocomposites. Then, the cells were washed with PBS thrice and scraped in the presence of 1 ml of cold PBS to collect cells in a microcentrifuge tube. The cells were centrifuged at 3000 rpm for 10 minutes at 4 ℃. The supernatant was discarded, and the cell pellet was resuspended in 100 µl of Iron Assay Buffer. Cells were sonicated for 3 minutes whilst maintaining the cold condition, followed by syringe pipetting to break the cells and release the cytoplasmic contents. All steps were performed on crushed ice to maintain cold temperature. Further, it was centrifuged at 5000 rpm for 10 minutes at 4 ℃. The supernatant was collected to perform the iron assay.

2.10.2 Assay Reaction

For measuring Fe^{2+} iron, 20 µl of supernatant of each sample was taken in a sample well of a 96-well plate and 32.5 µl of assay buffer was added to make the final volume of 52.5 µl. For measuring total iron, 20 µl of supernatant of each sample was taken in sample wells in a 96-well plate. Then, 30 µl of iron assay buffer and 2.5 µl of iron reducer was added to reduce Fe^{3+} to Fe^{2+} iron. The plate was kept on a horizontal shaker and incubated for 30 minutes at RT, under dark using metal foil for the protection from light. After incubation, 50 µl of Iron Probe was added to each well and mixed thoroughly using a horizontal shaker. It was further incubated for an hour at RT under dark condition by protecting from light. The absorbance was measured using the spectrophotometer at 593 nm. The total iron, Fe^{2+} and Fe^{3+} iron concentrations were measured through this experiment.

2.10.3 Preparation of Iron Standard Curve:

5 µl of 100 mM Iron Standard was diluted with 495 µl of water to generate 1 mM standard solution. Then, different concentrations of iron standard were prepared in duplicate by adding 1 mM standard solution at a concentration of 0, 2, 4, 6, 8, 10 µl into 96-well plate with iron assay buffer to bring final volume to 100 µl. Then, 5 µl of iron reducer was added to each well. The plate was kept in horizontal shaker and incubated at RT for 30 minutes in dark. Then, 100 µl of iron probe was added to each well and mixed in horizontal shaker. It was further incubated at RT for 60 minutes. The absorbance was read at 593 nm.

2.11 Gene Expression Studies by Real Time Polymerase Chain Reaction (RT-PCR)

RT-PCR was performed to analyse the genes responsible for different pathways of cellular death after treatment with nanocomposites following laser irradiation. Total RNA was extracted from treated and untreated MCF7 cells incubated with selected concentration of the MS2, MS2ICG, MS3, MS3ICG, pure ICG and untreated as control for 24 hours in the presence or absence of laser irradiation (1.2 W/cm^2, 808 nm, 5 minutes).

2.11.1 RNA and cDNA Synthesis:

1 x 10^6 MCF7 cells were plated in 6-well plate and allowed to adhere overnight in DMEM containing 10% FBS. The following day after 24 hours, cells were treated with different treatment groups i.e., MS2, MS2ICG, MS3, MS3ICG, ICG and untreated (as a control experiment) in the presence and absence of laser irradiation for 5 minutes (808 nm, 1.2 W/cm^2). After 24 hours of incubation, the cells were washed with PBS and 300 µl of Trizol solution was added and thoroughly mixed using a vortex followed by addition of 200 µl chloroform and vortex for further 15 minutes. Then the sample was incubated at RT for 5 minutes and centrifuged at 14000 rpm for 15 minutes, the supernatant was collected in a fresh tube and an equal amount of isopropanol was added and incubated on ice for 10 minutes. After incubation, it was centrifuged for 15 minutes at 14000 rpm and the pellet was washed with 75% ethanol and air dried. The pellet was dissolved in 30 µl DEPC treated water. cDNA synthesis was carried out using the reagents (Table 2-10) according to the protocol (Table 2-11) provided on the kit (Bio Rad, iScript™ cDNA Synthesis Kit).

Table 2-10: Components of cDNA synthesis setup

Reagents (Stored at –20 ℃)	**Volume**
5X iScript Reaction Mix	4 µl
iScript Reverse Transcription	1 µl
Nuclease free water	13 µl
RNA template	2 µl

Table 2-11: Reaction protocol for synthesis of cDNA

Thermal cycler reaction	**Time/ Temperature**
Priming	5 minutes/ 25 ℃
Reverse transcription	20 minutes/ 46 ℃
RT inactivation	1 minutes/ 95 ℃
Optional step (if hold needed)	Hold at 4 ℃

2.11.2 Quantitative Real Time PCR

After cDNA synthesis as described above, the real time PCR experiment was performed in a final volume of 20 µl with 10 µl Taq premix, 2 µl cDNA, 2 µl primers (forward and reverse) and nuclease free water (Fouz et al. 2014). The sequences of primer used for Bax, Bcl-2, p53, Cas 9, GAPDH were designed as described in Table 2-12. Real time PCR was done on the Quant Studio 5 Applied Biosystem PCR by specifying the annealing temperature for specific genes. To check the expressions of apoptotic and anti-apoptotic pathway genes, Quantitative Real Time PCR (SYBR® Green) was carried out with the help of separate primer for each gene, however, GAPDH was taken as an internal control for every set of experiments.

Table 2-12: Details of primer sequences and their size

Serial number	Genes	Sequences	Length
1	Bax	For 5'-GAGCTGCAGAGGATGATTGC-3' Rev 5'-CCGGGAGCGGCTGTTGGGCT-3'	20 20
2	Bcl-2	For 5'-CTGCACCTGACGCCCTTCACC-3' Rev 5'CACATGACCCCACCGAACTCAAAGA-3'	21 25
3	p53	For 5'- CAGCACATGACGGAGGTTGT-3' Rev 5'- TCATCCAAATACTCCACACGC-3'	20 21
4	Cas 9	For 5'-CTTCATCCAGGCCTCCGGTGGTGA -3' Rev 5'-TCACCACCGGAGGCCTGGATGAAG-3'	24 24
5	GAPDH	For 5'-GAAGGTGAAGGTCGGAGTC -3' Rev 5'-GAAGATGGTGATGGGATTTC -3'	19 20

2.12 *Ex-vivo* Haemolysis Assay

For assessing the haemolytic activity of nanocomposites MS2ICG and MS3ICG, *ex-vivo* haemolysis was performed using mice blood (ethical approval protocol number-DU/KR/IAEC/2019/10). 2 ml of mice blood was collected in EDTA containing falcon tube (Kumar et al 2017). The whole mouse blood was added with an equal volume of PBS buffer (pH= 7.4), centrifuged at 1500 rpm for 5 minutes and plasma was discarded. The collected blood cells after centrifugation were again washed with PBS buffer (pH= 7.4) and the supernatant was discarded. The washed red blood cells were added to an equal volume of PBS buffer (pH= 7.4). Then, 100 µl of the cells were taken in each micro-centrifuge tube and predetermined IC_{50} of each nanocomposite (MS2ICG and MS3ICG) were added to it. Microcentrifuge tubes were kept at room temperature, under continuous stirring on a shaker for different time dependent studies (2 and 4 hours). At the end of

each incubation period, the tubes were centrifuged at 11,000 rpm for 5 minutes and the supernatant was shifted to 96-well plate to read absorbance at the wavelength of 540 nm. Triton-X (0.1% in water) was taken as a positive control and PBS buffer (pH= 7.4) was taken as a negative control. Percent haemolysis was calculated by the formula:

$$\%\ Haemolysis = \frac{[\text{Absorbance}]\text{sample} - [\text{Absorbance}]\text{PBS}}{[\text{Absorbance}]\text{Triton X} - [\text{Absorbance}]\text{PBS}} \times 100 \qquad \text{(Equation 2-8)}$$

Where, [Absorbance] sample, [Absorbance] PBS and [Absorbance] Triton-X are absorbance measured after haemolysis assay using sample, PBS buffer (negative control), and Triton-X (positive control), respectively.

2.13 Statistical Analysis

For the characterisation of nanoparticles, the graphs were prepared using Origin Pro software. Three sets of experiments were repeated, and results were expressed as mean ± SD. For *in-vitro* and biochemical assays, comparison among groups were evaluated by ANOVA on GraphPad Prism (9.0) software (Prism software Inc. CA). The significant differences between different treatments were calculated using Tukey's multiple comparisons test and comparison with control was performed by Dunnett test. The significant difference between cytotoxicity with and without laser irradiation was calculated with unpaired t-test. Levels of significance were accepted at $p \leq 0.05$ level. All the results were expressed as replicates of three sets of experiments, unless otherwise stated.

CHAPTER 3

SYNTHESIS AND CHARACTERISATION OF BARE IRON OXIDE NANOPARTICLES AND IRON OXIDE-INDOCYANINE GREEN MAGNETO-OPTICAL NANOCOMPOSITES

3.1 Introduction

As discussed earlier in Chapter 2, iron oxide nanoparticles were synthesised by three different methods and their surface functionalisation was carried out using silica as precursors. The physical characterisation of the synthesised iron oxide (IO) nanoparticles, magnetic silica (MS) nanoparticles involved iron oxide coated with mesoporous silica and Indocyanine Green (ICG) loaded on MS, labelled as MSICG nanocomposites have been systematically presented in this chapter.

Different characterisation techniques were utilised in order to evaluate the true nature of the synthesised nanomaterials / nanocomposites. Even though iron oxide nanoparticles, silica nanoparticles and ICG are all deemed safe for clinical applications due to their biocompatibility, knowing their characteristic properties is prerequisite to identify their potential in biomedical applications. For example, in order to maximise magnetic hyperthermia efficiency, the iron oxides should be within a narrow size distribution (<15 nm) with superparamagnetic properties due to enhanced relaxations (Néel or Brownian), known to be responsible for heating the fluid under an external AMF (Rosensweig, 2002). Similarly, the silica coating can dramatically change the size, surface topography, surface charge and saturation magnetisation of IONPs (Wu, He and Jiang, 2008), therefore, hyperthermia efficiency.

3.2 Result and Discussion

3.2.1 Iron Oxide Nanoparticles

The iron oxide nanoparticles (IONPs) were synthesised using three different coprecipitation methods, modified from literature reports. First one, a simple coprecipitation method making hydrophilic IONPs (IO1) was synthesised by simultaneous precipitation of 1:2 molar ratio of ferrous and ferric ions initiated by the addition of ammonium hydroxide (NH_4OH) whilst heating the reaction mixture at 80 ℃. A new coprecipitation synthesis method presented (IO2) the importance of controlled slow mixing of chemicals *via* osmotic pathway using dialysis tubing for reproducible co-precipitation syntheses. IO1 and IO2 were dispersed in water while hydrophobic IONPs (IO3) synthesised with coprecipitation was stabilised with oleic acid and dispersed in hexane. IO1 observed to be black precipitate, while IO2 was a deep brown precipitate. They were highly magnetic as observed by quick separation under a permanent magnet (Figure 3-1). IO3 were black in suspension which was stable without separating under an external magnetic field (strength) even after a day (Figure 3-1).

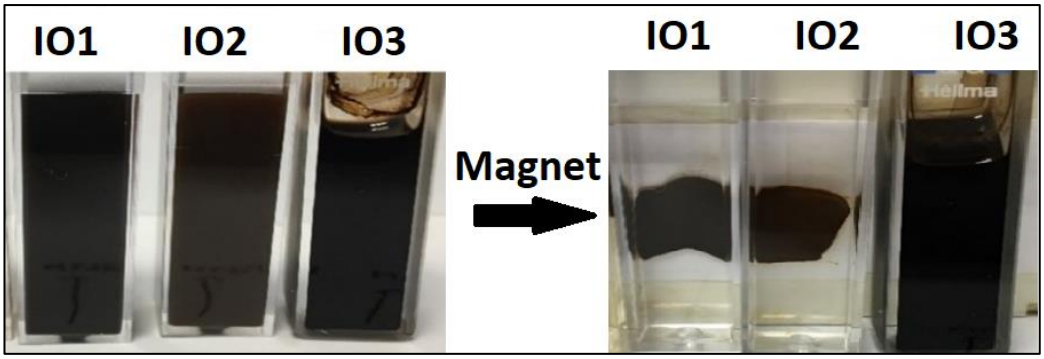

Figure 3-1: Visual representation of magnetic response on a magnetic stand: Hydrophilic IONPs (IO1 and IO2) and hydrophobic IONPs (IO3)

3.2.1.a Transmission Electron Microscope (TEM)

Figure 3-2 represents the TEM image of IO1 (see Figure 3-2, left panel) displaying spherical morphology with a relatively broad size distribution (Figure 3-2, right panel) showing an average size of around 42 nm. This method resulted in polydisperse IONPs and agglomerates due to simultaneous nucleation and continuous growth of particles (Besenhard *et al.*, 2020).

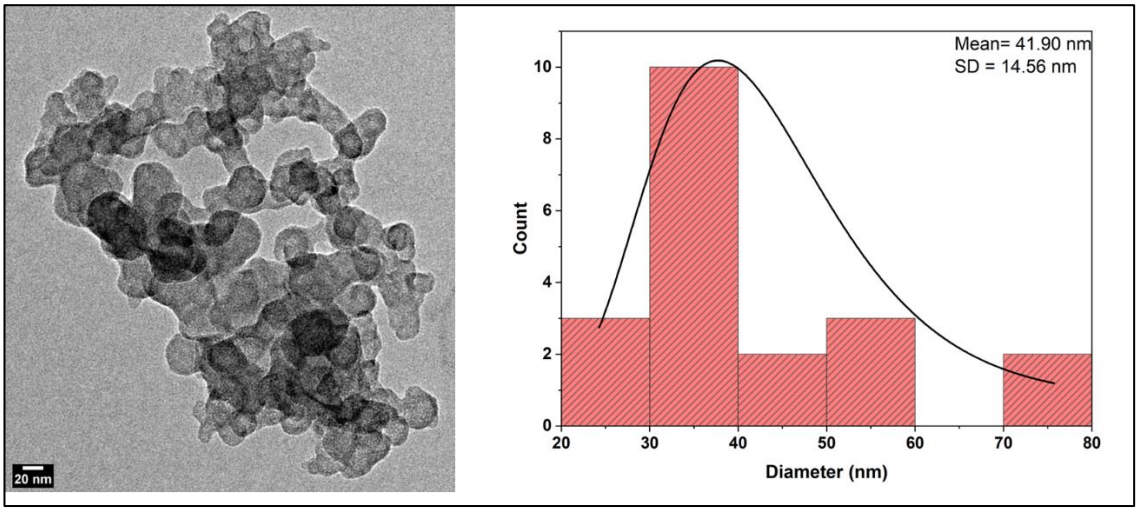

Figure 3-2: Transmission Electron Microscope (TEM) micrograph (left panel) and histogram (right panel) showing particle size distribution for IO1 (Hydrophilic iron oxide nanoparticles). Total count= 20, Mean= 41.90 nm, Standard deviation (SD)= 14.56 nm. The black curve represents a Gaussian fit to the size distribution.

TEM image of IO2 is presented in Figure 3-3. The nanoparticles were observed to be nearly monodispersed in sizes and spherical in shape (Figure 3-3, left panel). The size distribution analysis (Figure 3-3, right panel) showed an average size of around 14 nm with relatively smaller diameter compared to IO1. The narrow size distribution of IO2 could be due to short burst of nucleation as observed visually by sudden dark brown precipitate formation upon addition of dialysis bag containing ammonium hydroxide

(NH_4OH) followed by subsequent slow controlled growth with its slow release of NH_4OH from the dialysis bag to the reaction solution (Lu, Salabas and Schüth, 2007).

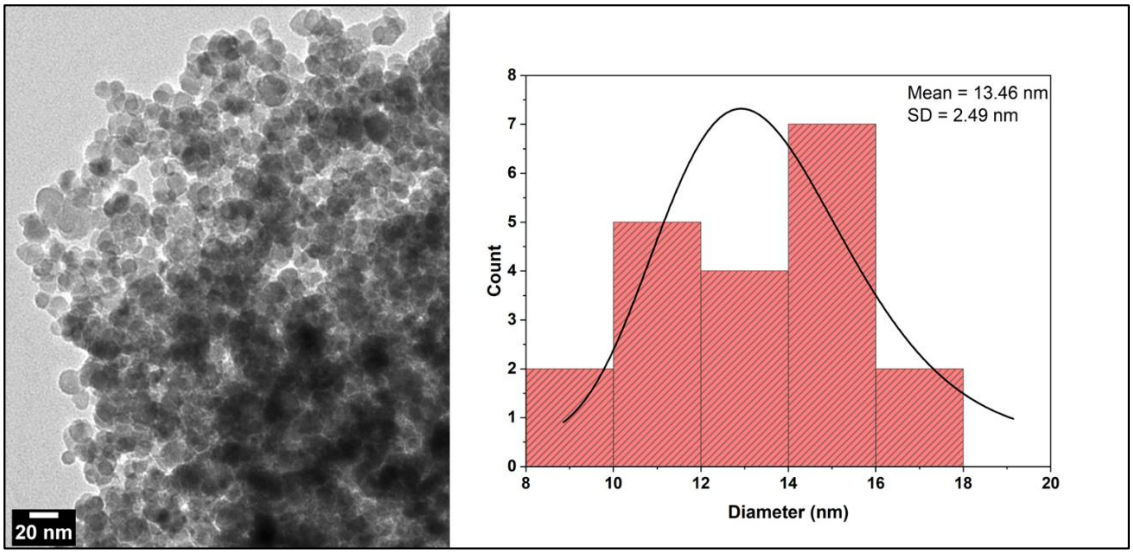

Figure 3-3: TEM micrograph (left panel) and histogram (right panel) of IO2. Total count= 20, Mean= 13.46 nm, Standard deviation (SD)= 2.49 nm. The black curve represents a Gaussian fit to the size distribution.

TEM image of IO3 is shown in Figure 3-4 and exhibited near spherical morphology (Figure 3-4, left panel). The size distribution curve (Figure 3-3, right panel) showed a narrow size distribution of IO3 nanoparticles with an average diameter around 9 nm. IO3 observed to be smallest in diameter compared to IO1 or IO2 nanoparticles.

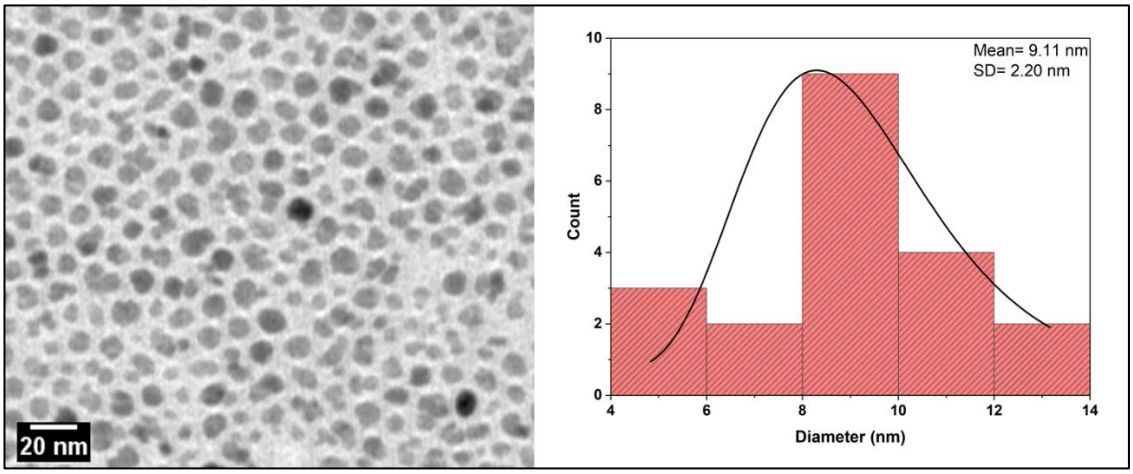

Figure 3-4: TEM micrograph (left panel) and histogram (right panel) showing particle size distribution for IO3. Total count= 20, Mean= 9.11 nm, Standard deviation (SD)= 2.20 nm. The black curve represents a Gaussian fit to the size distribution.

3.2.1.b Particle Size Distribution and Zeta Potential Measurement Using Dynamic Light Scattering (DLS)

The hydrodynamic diameters of IO1 and IO2 in water suspension were measured using DLS. DLS is a technique that primarily measures the Brownian motion of macromolecules/nanoparticles in liquid phase (suspension), which relates to the

hydrodynamic size of the particles in their dispersed medium. TEM images shown earlier represents the size and shape of the nanoparticles as their dried form. However, it is important to understand the hydrodynamic behaviour of particles dispersed in fluids and their surface charges as those parameters provide information interlinked with their true sizes and aggregation behaviour (Stetefeld, McKenna and Patel, 2016).

Table 3-1 shows the particle size and zeta potential of IO1 and IO2 dispersed in water. To determine the size, Z-average value was taken as it takes an average from the intensity weighted distribution curves observed in DLS measurements. The average size of IO1 and IO2 were measured to be around 163 nm and 158 nm, respectively. The average sizes of IO1 and IO2 were measured to be larger in values than that shown from TEM results because DLS takes in account the hydrodynamic diameter (nanoparticles covered with a thin layer of water in suspension) of the nanoparticles. The figures corresponding to hydrodynamic size distribution curves are provided in Appendix 1 (see Figure S1-2), showing monomodal distribution with a narrow size distribution due to minimal aggregation in suspension.

Furthermore, the surface charges of both IO1 and IO2 nanoparticles were found to be positively charged. The zetapotential of IO1 and IO2 were +19.1 ± 5.6 mV and +26.4 ± 5.5 mV, respectively. The higher zeta potential of IO2 represents higher electrostatic repulsion between the particles with an enhanced stability in suspension as compared to IO1. The figures representing each zeta potential experiments are provided in Appendix 1 (see Figure S1-3).

Table 3-1: Particle size evaluation and zeta potential of synthesised iron oxide nanoparticles as analysed by Dynamic light scattering (DLS)

Nanoparticles	**Particle Size (DLS)**		**Zeta Potential**	
	Diameter (nm)	**Polydispersity Index (PDI)**	**Zeta Potential (mV)**	**Std. Deviation (mV)**
IO1	163.2	0.191	+19.1	5.6
IO2	158.1	0.445	+26.4	5.5

3.2.1.c Determination Of Crystal Structure Using X-Ray Diffraction (XRD)

The crystallinity and purity of synthesised IONPs have been verified by X-ray diffraction (XRD) technique and the detailed method including sample preparation are described in Chapter 2, section 2.3.4.

Powder XRD patterns of IO1, IO2 and IO3 are shown in Figure 3-5 and exhibited multiple peaks in the 2θ values ranging from 5 to 80 (see Figure 3-5). Each diffraction pattern corresponds to the multiple peaks (indexed as three letters h,k,l) due to the presence of various crystalline planes with certain interplanar spacing (d-spacing). These h,k,l values are called Miller indices corresponding to different Miller planes. The position of the peaks (different h,k,l values) and their intensity distribution correspond to the specific crystalline phase. The XRD pattern of the materials were compared with fingerprint patterns of various iron oxide phases from the dataset available in the built-in software. All the IONPs produced a characteristic pattern of pure magnetite Fe_3O_4 fingerprint similar to JCPDS No. 19-0629 with Miller indices of 220, 311, 400, 422, 511 and 440. No other impurity peaks were found, indicating synthesis of magnetite. However, some of the diffraction patterns of magnetite (Fe_3O_4) and maghemite (γ-Fe_2O_3) are rather similar which require further characterisation such as Mossbauer or FTIR spectroscopy to confirm the true nature of the oxides.

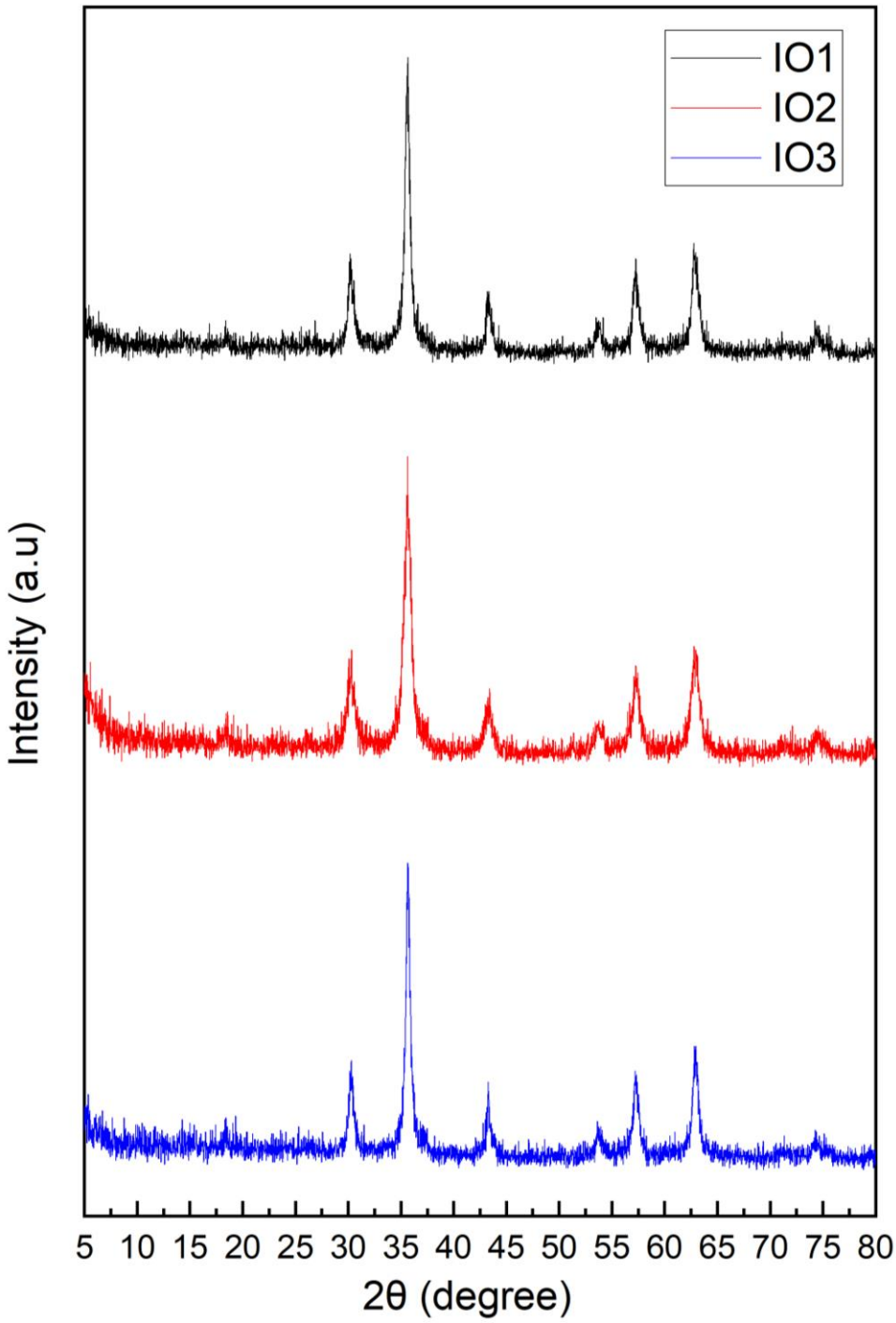

Figure 3-5: XRD patterns of IO1, IO2 and IO3 nanoparticles.

3.2.1.d Fourier Transform Infrared (FTIR) Spectroscopy

FTIR spectroscopy provided information related to chemical bonding and functional groups *via* bond vibrations (both stretching or bending modes) of heteroatomic bonds of synthesised IONPs. The samples were prepared as explained in section 2.3.3.

In case of hydrophilic SPIONs (IO1 and IO2), characteristic peak observed at around 550 cm^{-1} (Figure 3-6) corresponds to the Fe-O bond of IONPs relating to the Fe (II) and Fe (III) ions and oxygen bonding (Casillas, Gonzalez and Pérez, 2012). IO3 showed two strong peaks at around 2925 and 2852 cm^{-1} which have been assigned as symmetrical and asymmetrical -CH_2 stretching vibrations (Casillas, Gonzalez and Pérez, 2012). Those two peaks correspond to the characteristic organic hydrocarbon chains present in oleic acid (OA) (Gupta *et al.*, 2019). Low intensity spectra observed at around 1709 cm^{-1} is due to the carbonyl (C=O) vibrations from carboxyl groups confirming the presence of chemisorbed OA that acts as surfactant improving the dispersion of IONPs (Gupta *et al.*, 2019). The low intensity spectra could be because of low concentration of OA in the nanocomposite. The bond vibration at 1434 cm^{-1} is due to symmetrical vibration of COO which is not present in the hydrophilic SPIONs (Figure 3-6). The characteristic Fe-O stretching at 550 cm^{-1} confirms the inclusion of Fe_3O_4 (Casillas, Gonzalez and Pérez, 2012) while the absence of characteristic high frequency shoulder at 633 cm^{-1} suggest the absence of maghemite γ-Fe_2O_3 (Fu *et al.,* 2008).

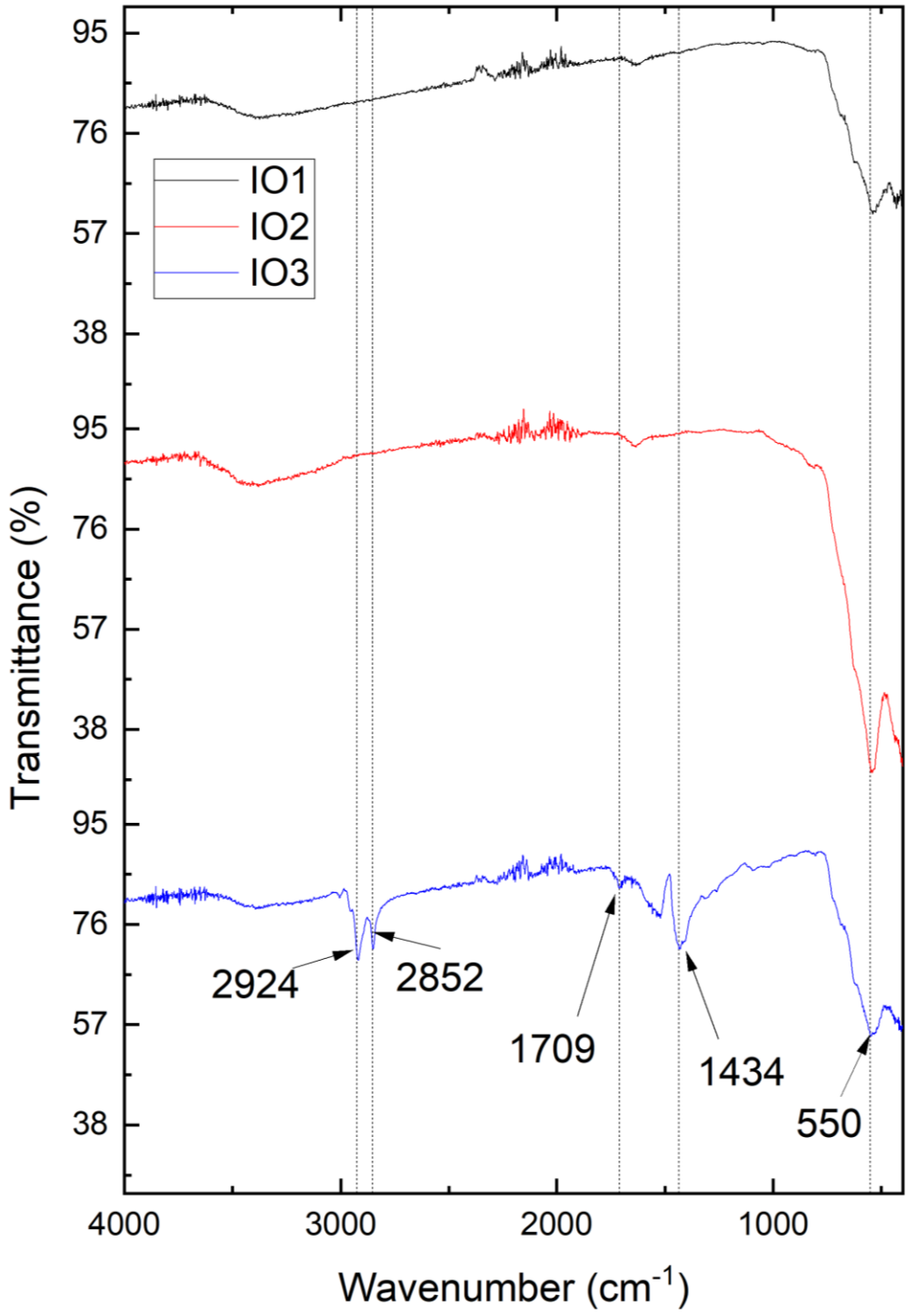

Figure 3-6: FTIR spectra of hydrophilic (IO1 and IO2) and hydrophobic (IO3) iron oxide nanoparticles.

3.2.1.e Vibrating Sample Magnetometer (VSM)

Vibrating sample magnetometer (VSM) was used to determine the magnetic parameters of IONPs at room temperature (RT). The magnetisation vs field (M-H) graphs were generated from VSM data to identify whether IONPs exhibited superparamagnetic properties. The magnetisation curve for IO1, IO2 and IO3 are shown in Figure 3-7 and exhibited S-like shape with near-zero hysteresis. Furthermore, both the remanence and

coercivity were nearly zero, indicating superparamagnetic properties. The saturation magnetisation values of IO1, IO2 and IO3 were measured to be 63.6 emu/g, 59.4 emu/g and 49.3 emu/g, respectively. The saturation magnetisation values of IONPs measured to be lower than the values of bulk ferrimagnetic materials (92 emu/g) similar to published reports of IONPs of diameter below 100 nm (Sato *et al.*, 1987; Patil-Sen *et al.*, 2020). The saturation magnetisation of IO3 is the lowest of all bare IONPs. It could be due to the sharp decrease in size of IO3 nanoparticles around 10 nm as indicated by TEM (Figure 3-4) and supported by Sato *et al.* (1987). The decrease in particle size to single domain and decrease in exchange interaction between them results in reduced saturation magnetisation (Sato *et al.*, 1987; Santra *et al.*, 2001).

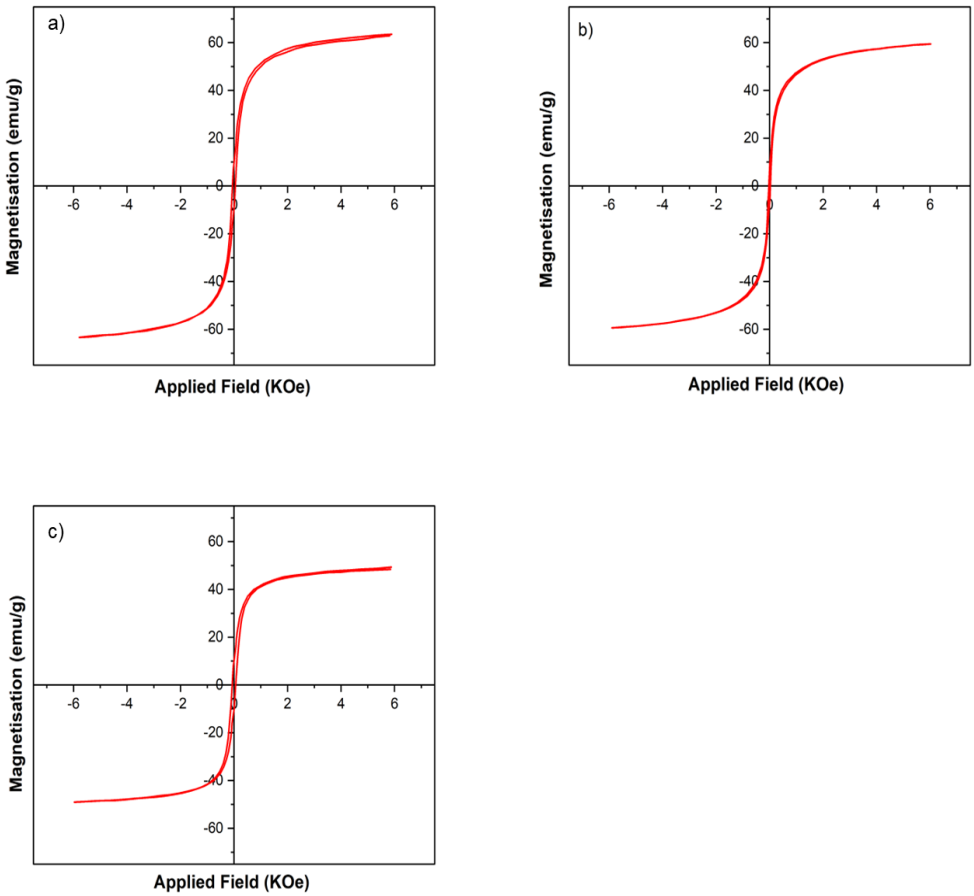

Figure 3-7: Magnetisation vs field (M-H) graphs of a) IO1, b) IO2 and c) IO3 nanoparticles using vibrating sample magnetometer (VSM).

3.2.2 Magnetic Silica Nanocomposites

The as-synthesised iron oxide cores were surface functionalised with mesoporous silica to produce magnetic silica (MS) nanocomposites (MS1, MS2 and MS3). Figure 3-8 shows high dispersibility of MS nanoparticles in suspension and their magnetic response under the influence of an external magnetic field. The fabricated MS nanocomposites were further characterised to understand the core-shell properties.

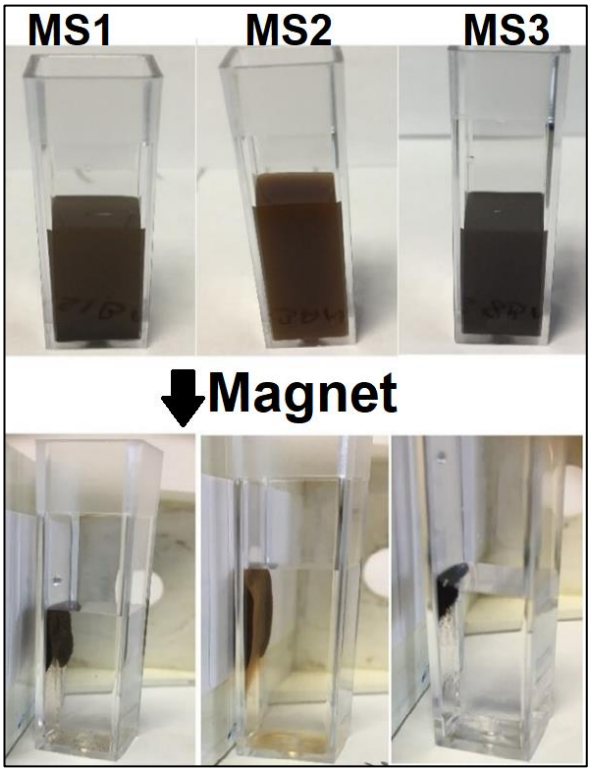

Figure 3-8: Visual representation of core-shell magnetic silica nanoparticles (MS) under an external magnetic field. MS1, MS2 and MS3 nanocomposites are prepared by coating silica on three different magnetic iron oxide cores (IO1, IO2 and IO3), respectively.

3.2.2.a Transmission Electron Microscope (TEM)

Figure 3-9 represents the TEM images of magnetic silica nanoparticles (MS1) with hydrophilic iron oxide core, IO1. The silica coating was performed according to the method described in section 2.2.4. The TEM images display near spherical morphology with core-shell structure due to a contrast difference between the magnetic core (dark) and thin silica shell (greyish) (Figure 3-9). The average diameter of MS1 nanoparticles was ~129 nm with a broad size distribution (see Figure 3-9, right panel).

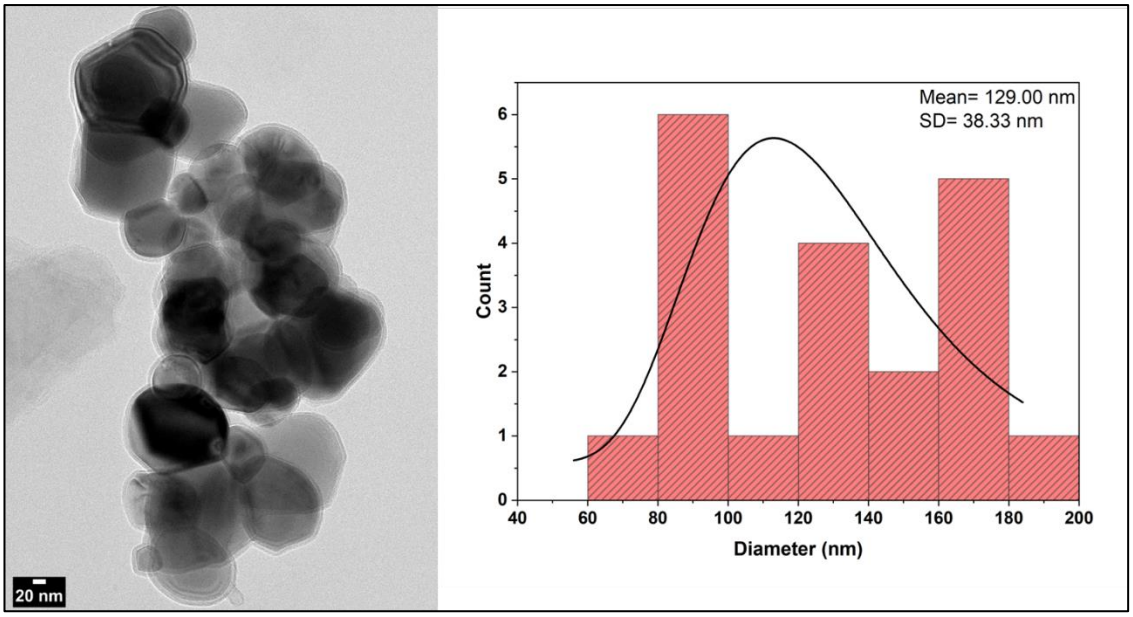

Figure 3-9: TEM (Transmission Electron Microscope) micrograph (left) and histogram (right) data of MS1 (Magnetic silica nanoparticles with iron oxide core IO1). Total count= 20, Mean= 129.00 nm, Standard deviation (SD)= 38.33 nm. The black curve represents a Gaussian fit to the size distribution.

TEM image of magnetic silica nanoparticles (MS2) prepared using core iron oxide nanoparticles (IO2) is shown in Figure 3-10. The nanoparticles are nearly spherical in morphology with a broad size distribution due to uncontrolled polymerisation of mesoporous silica. The average particle size was around 83 nm as shown in the histogram (Figure 3-10, right panel). The iron oxide core is not distinctly visualised as compared to MS1. A contrast difference once again indicated two different compositions due to iron oxide core (dark) and mesoporous silica (lighter region).

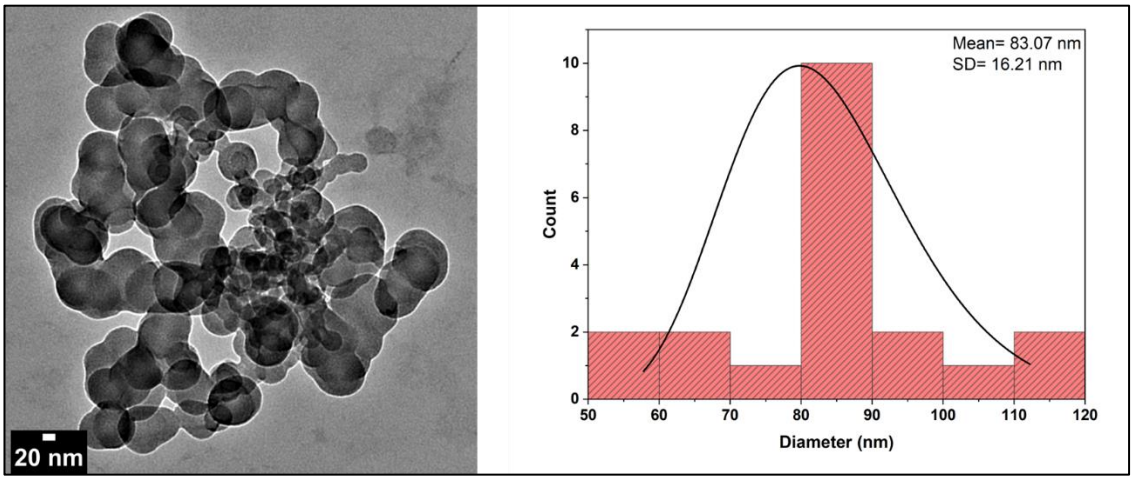

Figure 3-10: TEM (Transmission Electron Microscope) micrograph and histogram of MS2 (Magnetic silica nanoparticles with iron oxide core IO2). Total count= 20, Mean= 83.07 nm, Standard deviation (SD)= 16.21 nm. The black curve represents a Gaussian fit to the size distribution.

The TEM image of magnetic silica nanoparticles (MS3) prepared using hydrophobic iron oxide (IO3) is shown in Figure 3-11. The nanoparticles are observed to be near spherical in morphology with poorly dispersed form. The average particle size was measured to be around 38 nm from histogram (see Figure 3.11, right panel) with a relatively narrow size distribution range. A contrast difference once again indicates two different compositions due to iron oxide core (dark) and mesoporous silica (lighter region). Mesopores were difficult to visualise from TEM micrographs, therefore, an alternate technique (nitrogen gas adsorption) utilised to confirm the mesoporosity of the MS nanoparticles and presented later in section 3.2.2.f.

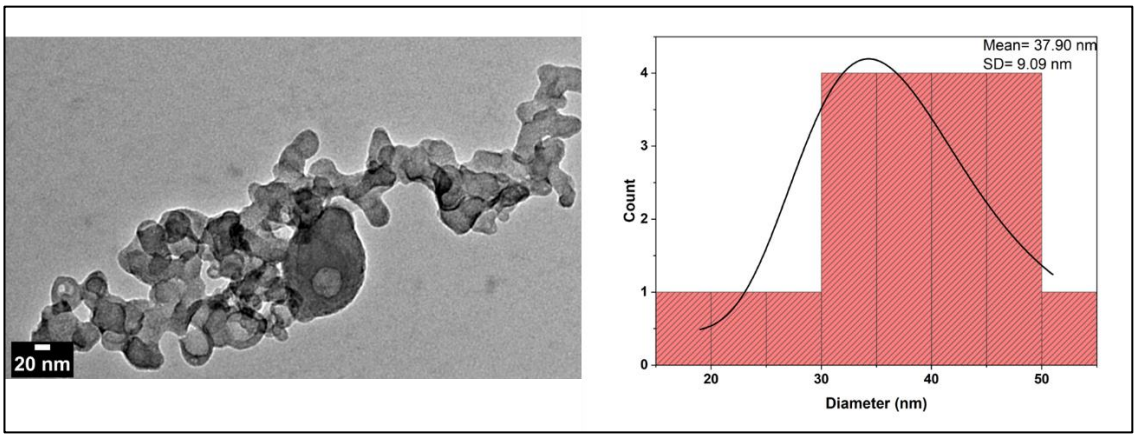

Figure 3-11: TEM (Transmission Electron Microscope) micrograph and histogram of MS3 (Magnetic silica nanoparticles with iron oxide core IO3). Total count= 20, Mean= 37.90 nm, Standard deviation (SD)= 9.09 nm. The black curve represents a Gaussian fit to the size distribution.

3.2.2.b Size Distribution and Zeta potential

The hydrodynamic diameter of the MS nanocomposites (MS1, MS2 and MS3) dispersed in water were measured using DLS. The average size of MS1, MS2 and MS3 were around 210 nm, 241 nm, and 244 nm, respectively. The hydrodynamic diameter of the nanoparticles has increased after silica coating as shown in Table 3-2. The average hydrodynamic sizes are larger as compared to TEM images, which could be due to the hydrated state or aggregation (Yiyu Wang *et al.*, 2020). The figures corresponding to each hydrodynamic size distribution are provided in Appendix 1 (see Figure S1-2) showing monomodal size distribution.

Table 3-2: Size evaluation *via* TEM and DLS, and Zeta potential analysis of the synthesized nanoparticles

Samples	Particle Size (TEM)		Particle Size (DLS)		Zeta Potential	
	Diameter (nm)	Std. Deviation (nm)	Diameter (nm)	Polydispersity Index (PDI)	Zeta Potential (mV)	Std. Deviation (mV)
IO1	41.9	14.6	163.2	0.191	19.1	5.6
IO2	13.5	2.5	158.1	0.445	26.4	5.5
IO3	9.1	2.2	-	-	-	-
MS1	129.0	38.3	210.0	0.428	-23.2	4.8
MS2	83.0	16.2	240.7	0.274	-25.0	4.0
MS3	37.9	9.1	244.2	0.387	-24.0	3.9

Furthermore, the surface charges of MS nanocomposites were found to be negatively charged and provided in Appendix 1 (see Figure S1-3). The zeta potential of MS1, MS2 and MS3 were -23.2 ± 4.8 mV, -25 ± 4.0 mV, and -24 ± 3.9 mV, respectively. The change in zeta potential from positive to negative values indicate the difference in surface charge due to silica coating confirming the fabrication of silica on iron oxides (Figure 3-12). This is due to the difference in their isoelectric point (IONPs: ~5, SiO_2: ~7) due to surface silanol groups in the latter. Additionally, the higher negatively charged particles represents higher electrostatic repulsion with higher stability and dispersibility in suspension as compared to their iron oxide cores (Zou, Peng and Tang, 2014).

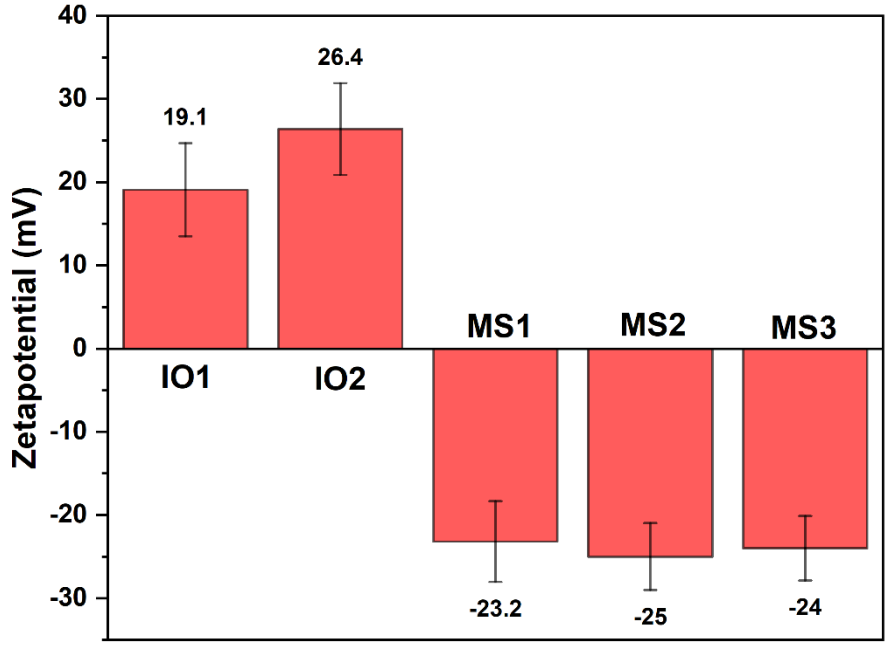

Figure 3-12: Changes in Zetapotential of IONPs (IO1, IO2) after silica coating as evident in MS nanocomposites (MS1, MS2 and MS3)

3.2.2.c Identification of Crystalline Structure Using XRD

The wide-angle XRD pattern of MS nanoparticles confirmed the presence of amorphous silica structure due to the presence of a broad peak at around 15-30 degree as shown in Figure 3-13 (Q. Yin *et al.*, 2017). The crystalline structure of magnetite was unchanged as position and intensity ratio due to pure magnetite remained same as bare IONPs (Figure 3-13).

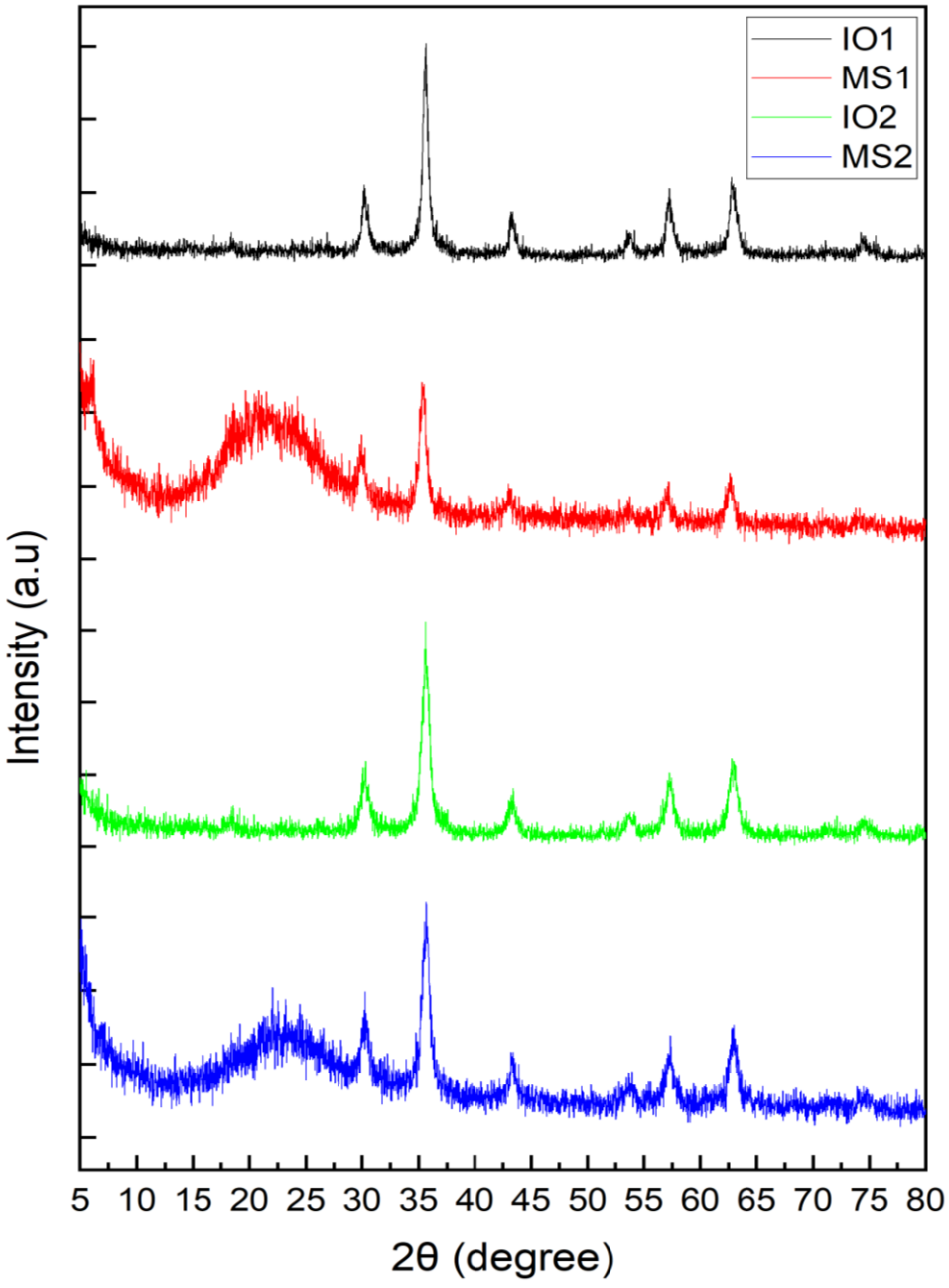

Figure 3-13: XRD patterns of MS1 and MS2 nanocomposites compared with respective bare IONPs, IO1 and IO2.

Small-angle XRD pattern of MS1 showed distinct peaks in the 2θ values ranging from 1 to 5 degrees (Figure 3-14). A strong peak at 2θ values of 2.27° in MS1 along with

additional two weak peaks within 10 degrees are the indication of an ordered mesoporous structure, similar to earlier report (Sen, Sebastianelli and Bruce, 2006; Wang *et al.*, 2008).

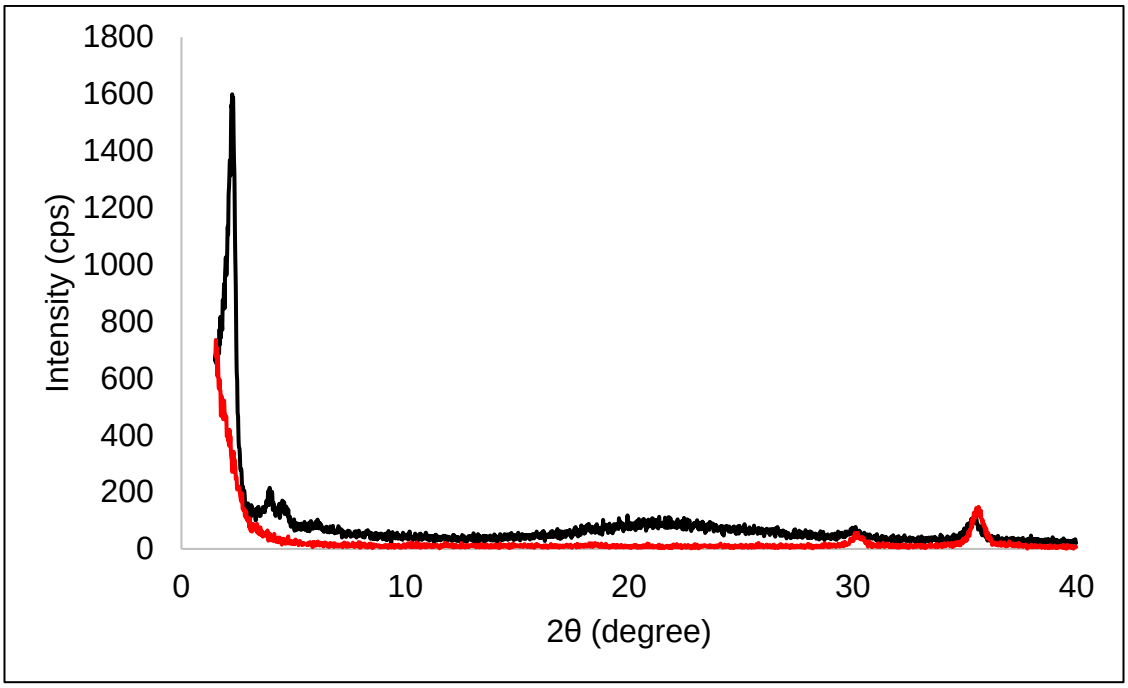

Figure 3-14: Small-angle XRD pattern of MS1 (Black) with distinct peaks in the low angle region compared to IO1 (Red) having no such peaks.

3.2.2.d Confirmation of Surface Modification Due to Silica Coating in IONPs by FTIR

The FTIR spectra of MS nanoparticles (MS1 and MS2) synthesised using hydrophilic IONPs IO1 and IO2 are presented in Figure 3-15. The presence of silica is indicated by specific bond vibrations at 1080 cm^{-1} suggesting Si-O-Si asymmetric stretching (Wang *et al.*, 2008). Similarly Si-O-Si symmetric stretching and O-Si-O vibrations were also observed at 795 and 440 cm^{-1}, respectively (Wang *et al.*, 2008). A characteristic peak due to Fe-O bond vibration at 550 cm^{-1} observed in bare IONPs is also visible in the FTIR spectrum of silica coated IONPs, proving no changes in the core magnetic particles during the fabrication of core-shell MS nanocomposites.

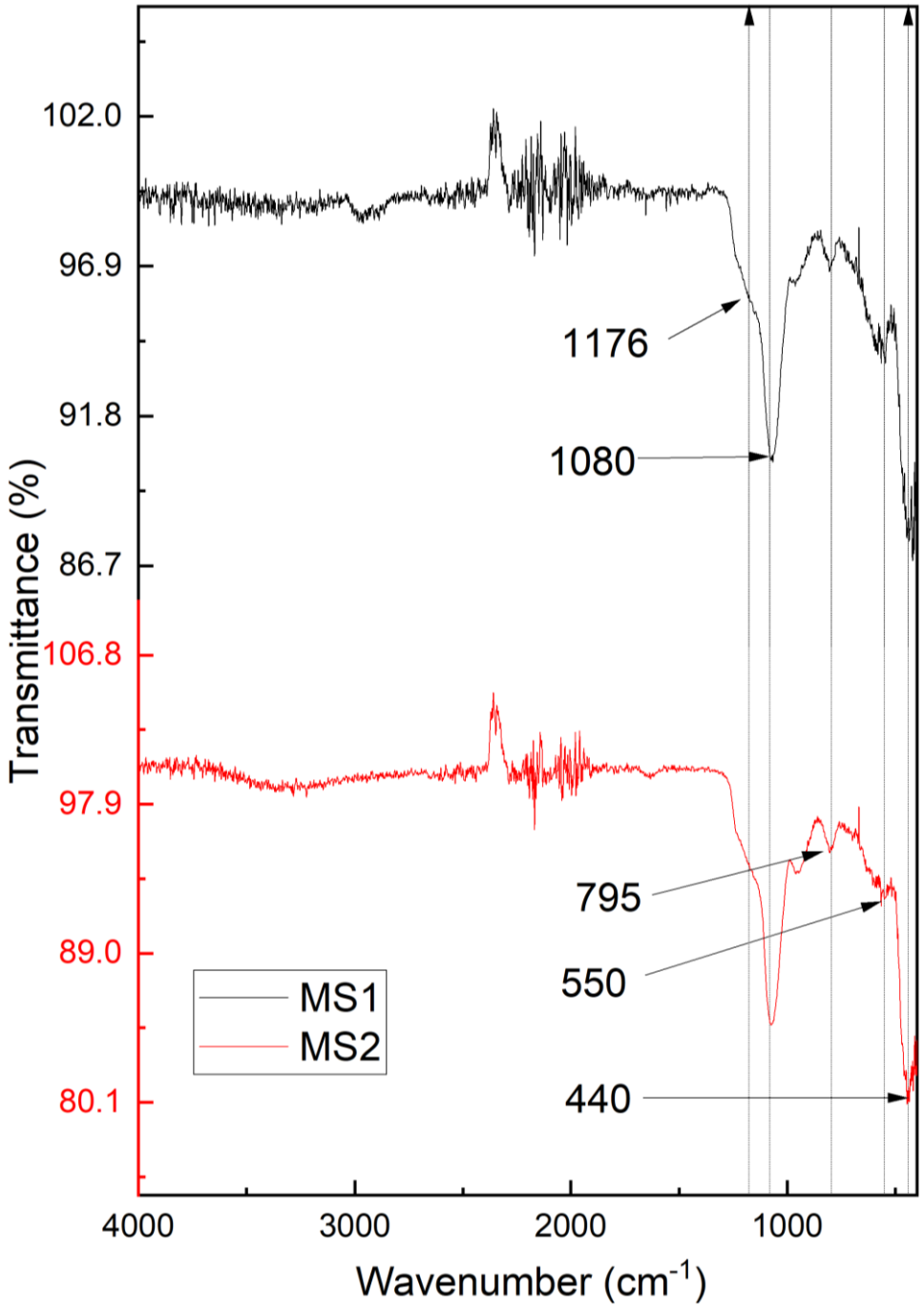

Figure 3-15: FTIR spectra of MS1 and MS2 nanocomposites synthesised using hydrophilic IONPs IO1 and IO2, respectively.

The FTIR spectrum of MS3 nanocomposites synthesised using hydrophobic IO3 nanoparticles is presented in Figure 3-16. The FTIR peak due to Si-O-Si asymmetric bond vibration has slightly shifted to 1050 cm^{-1} with relatively weak intensity compared to MS hydrophilic nanocomposites at 1080 cm^{-1} suggesting the low silica content in the MS3 nanocomposites. The band at 550 cm^{-1} exhibits Fe-O bond, characteristic of pure magnetite. The intensity of Si-O-Si symmetric stretching represented by vibration at 795 cm^{-1} had significantly reduced as compared to MS1 and MS2 nanocomposites.

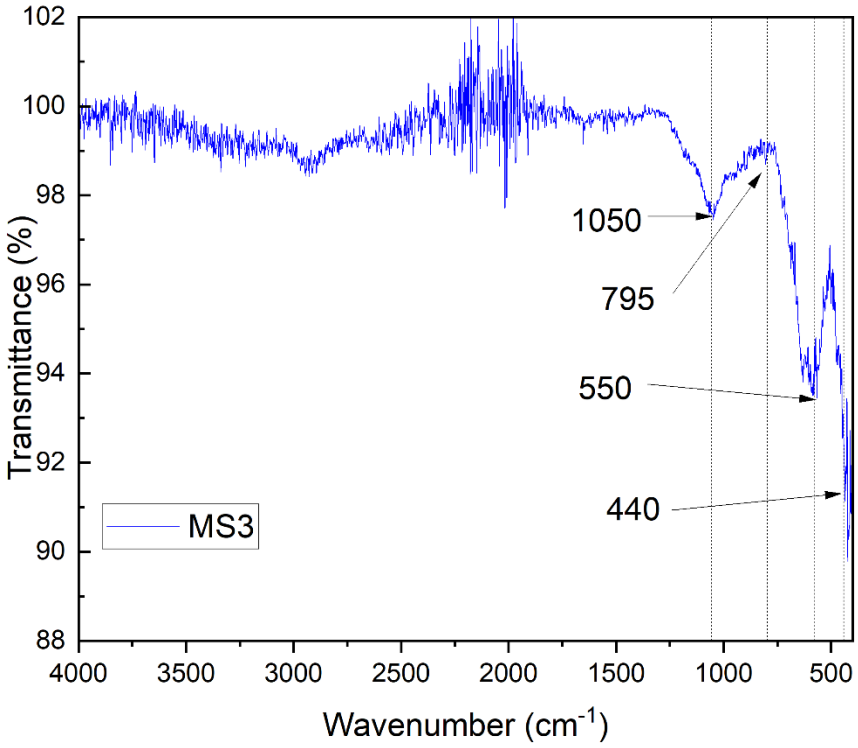

Figure 3-16: FTIR spectra of MS3 nanocomposites synthesised using hydrophobic IONPs IO3.

3.2.2.e Confirmation of Template Removal by FTIR and TGA

To confirm the removal of CTAB as a structure directing agent (template) by acidic ethanol washing steps, FTIR spectra before and after washing are presented in Figure 3-17. A characteristic peak at 2900 cm^{-1} due to C-H stretching of surfactant is reported to be due to the presence of CTAB which is nearly absent after acidic ethanol wash, confirming that the mesopores are empty for drug or ICG loading experiments.

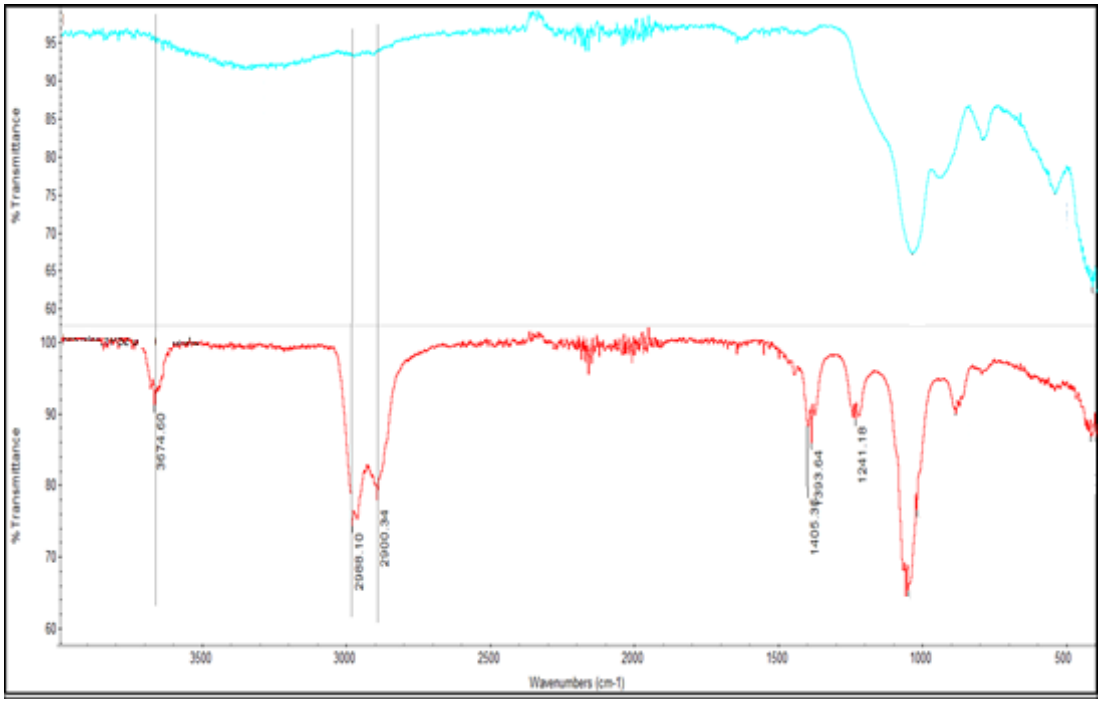

Figure 3-17: FTIR spectra of MS1 nanocomposites after (top, blue line) and before (bottom, red line) acidic ethanol wash.

The quantitative information on the removal of CTAB after acidic ethanol wash on MS1 is confirmed by using thermogravimetric analysis (TGA) and presented in Figure 3-18. The total weight loss profile by heating the samples from RT to 600 ℃ in the presence of air is clearly visible in two stages. In the first stage, between 30 and 200 ℃, the weight loss due to evaporation of physically absorbed water (high boiling point solvents) either outside or inside the mesopores. Mesopores filled with CTAB before the acidic ethanol washing exhibited only 4.5% weigh loss compared to 22.42% in the washed sample, perhaps due to empty pores filled with moisture. In the second stage, between 200 and 600 ℃, the weight loss is related to the decomposition of organics, such as CTAB. Unwashed sample exhibited a significant weight loss (21.4%) compared to washed sample (only 3.4%) confirming that acidic ethanolic washing was efficient for the removal of template CTAB.

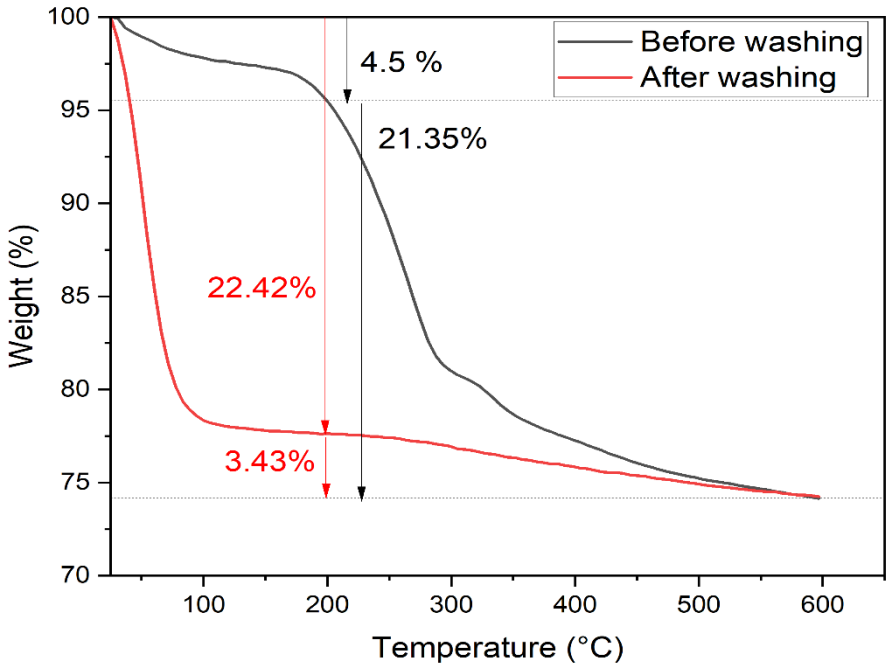

Figure 3-18: TGA curves for MS1 nanocomposites before and after acidic ethanol washing.

3.2.2.f Measurement of Surface Area and Pore Diameter of Magnetic Silica Nanocomposites using Brunauer-Emmett-Teller (BET) Surface Area Analysis

The nitrogen gas adsorption-desorption isotherms of MS1 and MS2 nanocomposites showed hysteresis with type IV isotherm (see Figures 3-19 and 3-20), a characteristic feature of mesoporous structure. More specifically, both the MS1 and MS2 exhibited H1-type hysteresis loops indicating the presence of well-defined cylindrical pore channels (Mitran *et al.*, 2017). Identical results were expected since both nanocomposites were synthesised using the same silica coating method. MS3 nanocomposites synthesised using hydrophobic IONPs showed H2-type hysteresis loop (Figure 3-21) suggesting the presence of disorder 'ink-bottle' mesopores as reported earlier (Mitran *et al.*, 2017). BJH pore size distribution graphs for MS1 to MS3 nanocomposites are also presented in the inset of Figures 3-19 to 3-21. The average pore diameter, pore volume and surface area values are presented in Table 3-3.

BET surface area values of the hydrophilic core mesoporous silica nanocomposites (MS1 and MS2) were higher than the hydrophobic core mesoporous silica nanocomposites (MS3). The highest value was measured to be 965 m^2g^{-1} for MS1 indicating a large internal surface area due to ordered mesopores with a large silica component in consistent with TEM and XRD data presented in Figure 3-9 and Figure 3-13, respectively. In addition, the percentage of silica to iron oxide content was higher with SiO_2: Fe_3O_4 = 68: 32 in MS1 nanocomposites. MS2 exhibited BET surface area of 655 m^2g^{-1} which is lower than MS1 and consistent with TEM data (Figure 3-10).

Furthermore, the low surface area of MS3 (142 m^2g^{-1}) may be due to thin mesoporous silica shell contributing relatively low silica content which is consistent with TEM data shown earlier (Figure 3-11) and the percentage of silica to iron oxide in the nanocomposites (SiO_2: Fe_3O_4= 4.4: 95.6). The average pore diameter of all materials is in the order of 3 nm (range: 2.5 to 3.4 nm) in consistent with the hexagonal micellar structure of CTAB in water (Zhang *et al.*, 2011). XRD analysis of small angle region provided a repeating distance of 3 nm from 100 Miller plane indicating pore diameter of around 3 nm, consistent with TEM and BJH pore diameter data.

Table 3-3: BET surface area, average pore diameter and pore volume values for the synthesised MS nanocomposites

Sample name	BET surface area (m^2g^{-1})	Average pore diameter (nm)	Average pore volume (cm^3g^{-1})
MS1	965 ± 48.2	2.9	0.3
MS2	655 ± 8.48	2.6	0.2
MS3	142 ± 0.41	3.4	0.1

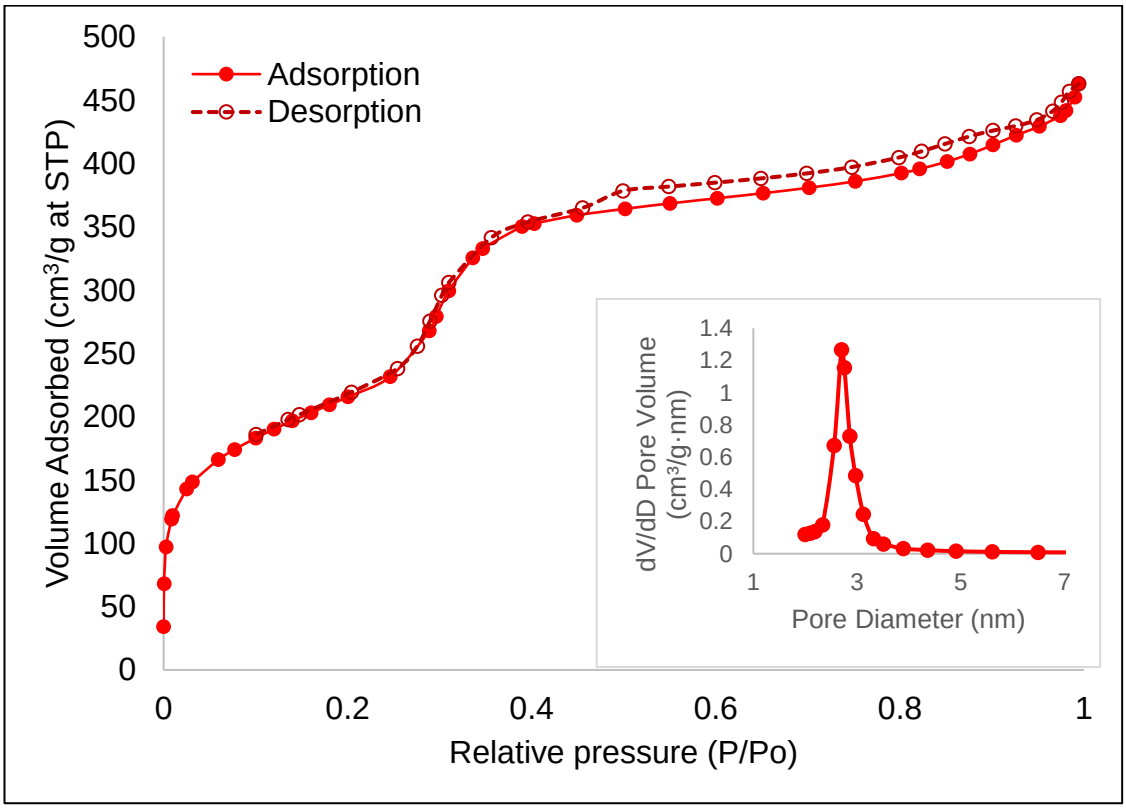

Figure 3-19: N_2 adsorption-desorption isotherm of MS1. Inset: BJH pore size distribution curve with peak centred at 2.9 nm

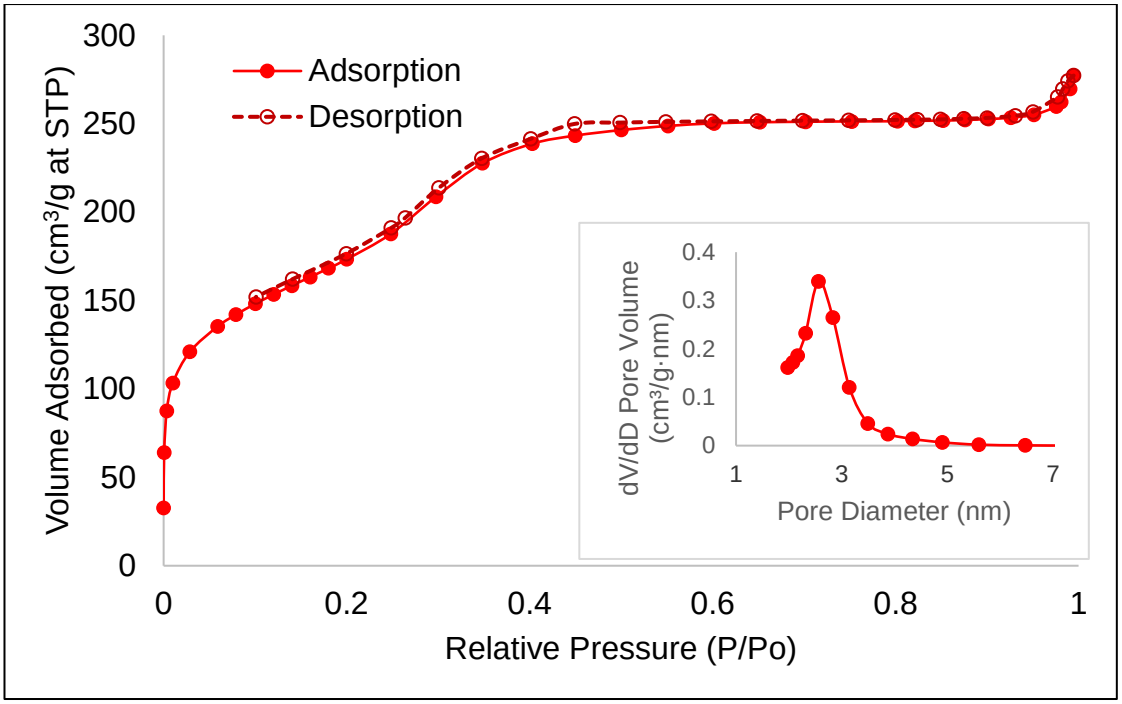

Figure 3-20: N_2 adsorption-desorption isotherm of MS2. Inset: BJH pore size distribution curve with peak centred at 2.6 nm

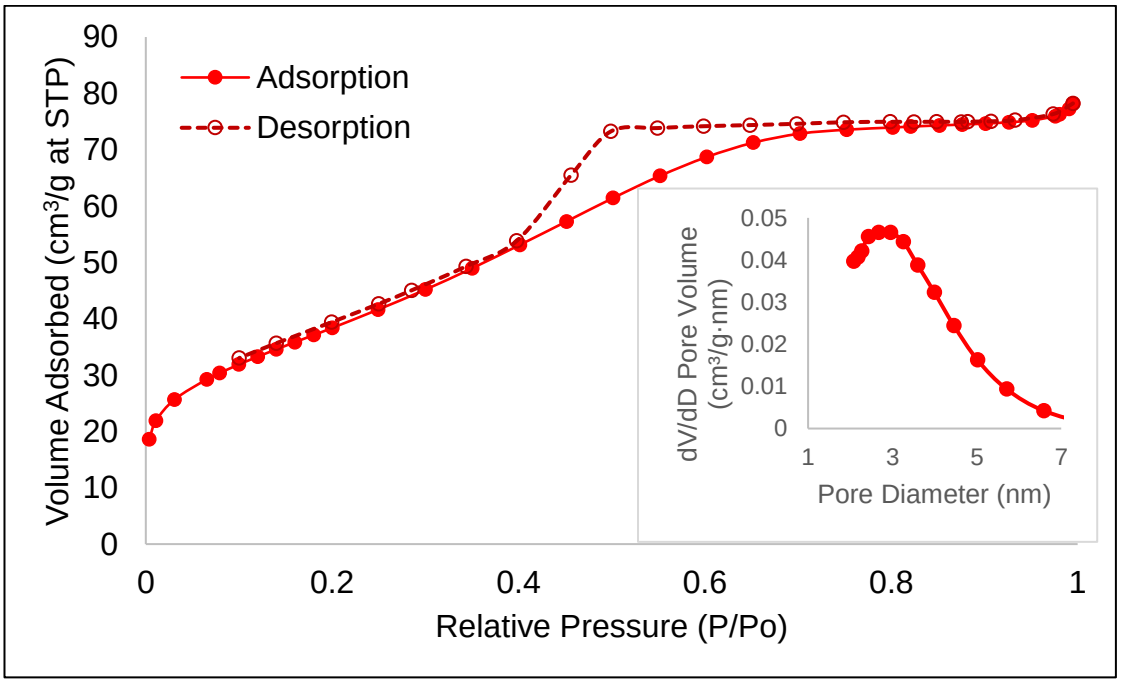

Figure 3-21: N_2 adsorption-desorption isotherm of MS3 Inset: BJH pore size distribution curve with peak centred at 3.4 nm

3.2.2.g Determining Magnetic Properties of MS Nanocomposites Using VSM

The VSM was used to analyse the magnetic properties of magnetic silica nanocomposites (MS1, MS2 and MS3). The magnetisation curve showed the near-zero hysteresis with negligible remanence and coercivity indicating superparamagnetic

properties (Figure 3-22). The saturation magnetisation (M_s) of MS nanocomposites was lower than their core IONPs, as expected. M_s of MS1, MS2 and MS3 were 5.88, 12.5 and 44.51 emu/g, respectively. It is known that the saturation magnetisation of uncoated magnetite is always higher than the silica coated IONPs mainly because the diamagnetic silica coating dilutes the overall magnetic content in the overall nanocomposites, contributing to lower saturation magnetisation (Santra *et al.*, 2001; Sen, Sebastianelli and Bruce, 2006). In case of MS3 nanocomposites, the higher magnetic saturation could be due to thin silica coating as demonstrated by TEM and BET analyses. The higher percentage of iron oxide content in the MS3 nanocomposites as shown by gravimetric analysis (Appendix 1, Table S 1-2) proves to be effective for higher saturation magnetisation as compared to other nanocomposites (i.e., the percentage of SiO_2: Fe_3O_4: Fe was calculated as MS1- 68%: 32%: 23%, MS2- 64%: 36%: 26% and MS3- 4.4%: 95.6%: 69.2%).

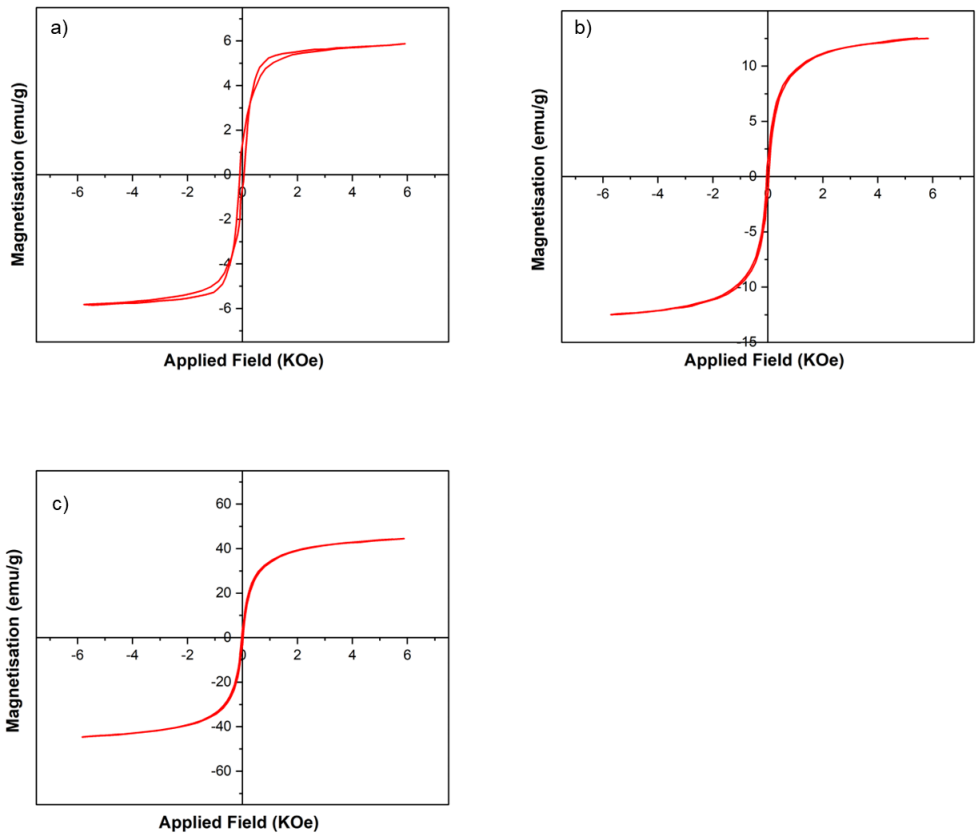

Figure 3-22: Magnetisation vs field (M-H) graphs of a) MS1, b) MS2 and c) MS3 nanoparticles using vibrating sample magnetometer (VSM).

3.2.3 Indocyanine Green (ICG) Loaded Magneto-Optical Nanocomposites

The quantification of ICG loading on MS nanocomposites was performed by monitoring the free ICG concentrations in the supernatant after the loading experiments as explained in section 2.2.6. A pre-established standard calibration curve of known ICG concentrations in water (Figure 2-2) was used to calculate the unknown ICG concentrations in supernatants after each loading experiment.

The drug loading capacity (DLC%) and encapsulation efficiency (EE%) values of MS nanocomposites in order to form magneto-optical nanocomposites (MS1ICG, MS2ICG and MS3ICG) were calculated by monitoring the absorbance value of ICG in solution before and after the loading experiments and the results are summarised in Table 3-4. The ICG loading capacity was measured to be higher in MS1 nanocomposites than MS2 and MS3 nanocomposites. It has been reported that MS nanocomposites with surface positive charges can adsorb more ICG by strong electrostatic attraction between sulfonic groups of ICG (Yiyu Wang et al., 2020). Low percentage of drug loading could be attributed to this fact as well, since the MS nanocomposites were negatively charged. Silica coated hydrophilic IONPs (MS1) showed better encapsulation efficiency than other two methods which could be due to the ordered pore size and high surface area as shown earlier using TEM, XRD experiments and nitrogen gas adsorption (Figure 3-9, Figure 3-14 and Figure 3-19).

Table 3-4: Encapsulation of ICG in magnetic silica nanocomposites with calculated drug loading capacity (DLC%) and encapsulation efficiency (EE%)

Sample	**ICG Fed (nmol/mg)**	**ICG loaded (nmol/mg)**	**DLC (%)**	**EE (%)**
MS1ICG	69.6	47.8	3.7	68.6
MS2ICG	46.1	10.8	0.8	23.4
MS3ICG	46.1	14.8	1.1	32.2

3.2.3.a Particle Size Distribution and Zetapotential Data of MSICG Nanocomposites

The particle size distribution and zetapotential of MSICG nanocomposites were performed using DLS and represented in Table 3-5. The z-average size of MS1ICG, MS2ICG and MS3ICG nanocomposites were measured to be around 217 nm, 247 nm, and 279 nm, respectively. The size distribution of the nanocomposites increased slightly as compared to nanocomposites before loading of ICG.

Table 3-5: Particle size distribution and zeta potential values of various ICG loaded MS nanocomposites

Nanoparticles	Particle Size (DLS)		Zeta Potential	
	Diameter (nm)	Polydispersity Index (PDI)	Zeta Potential (mV)	Std. Deviation (mV)
MS1ICG	216.8	0.365	-28.0	7.5
MS2ICG	246.7	0.533	-27.9	3.7
MS3ICG	279.0	0.294	-24.3	4.4

Furthermore, the change in surface charge of the functionalised nanoparticles could be observed by their differences in zetapotential. As shown in Figure 3-23, zetapotential of the MSICG nanocomposites are negative in values indicting the surface of silica remained unchanged after ICG loading. A slight increase in zetapotential values (see Figure 3-23) also implied better stability and dispersibility of the MSICG nanocomposites compared to MS nanocomposites.

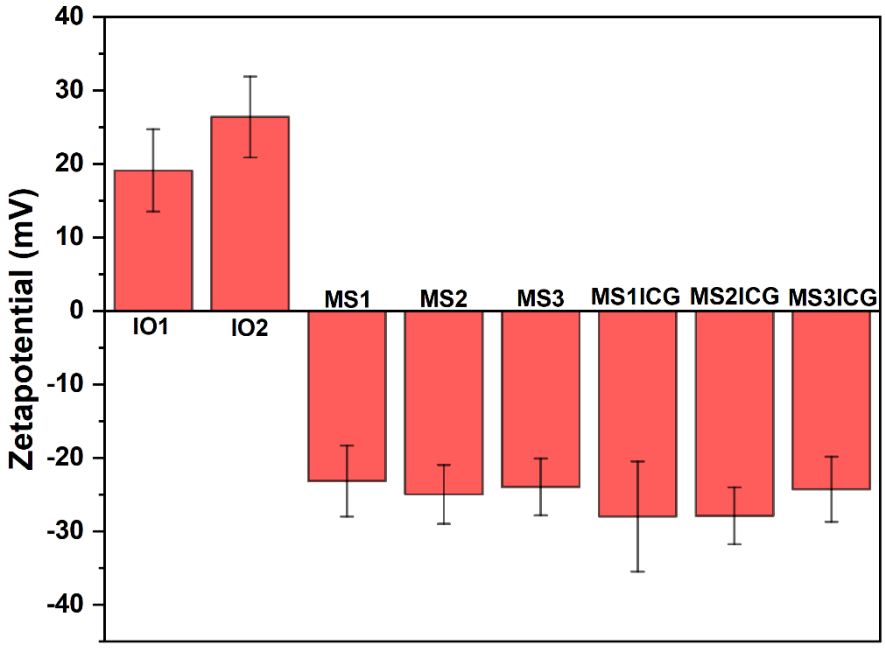

Figure 3-23: Zetapotential of IONPs (IO1, IO2), MS nanocomposites (MS1, MS2, MS3) and ICG loaded MS nanocomposites (MS1ICG, MS2ICG, MS3ICG).

3.2.3.b Confirmation of ICG Encapsulation in MSICG Nanocomposites by FTIR and TGA

The presence of ICG in encapsulated nanocomposites was further studied using FTIR spectroscopy and TGA. The FTIR spectra of pure ICG, MS1 nanocomposite before and after ICG loading are presented in Figure 3-24. Pure ICG and MS1ICG samples exhibited a specific bond vibration at around 1409 cm^{-1} due to N-H bending which was absence in MS nanocomposites. The multiple peaks at distinct positions of ICG were

not very prominent in MS1ICG nanocomposites due to low ICG content in the nanocomposites.

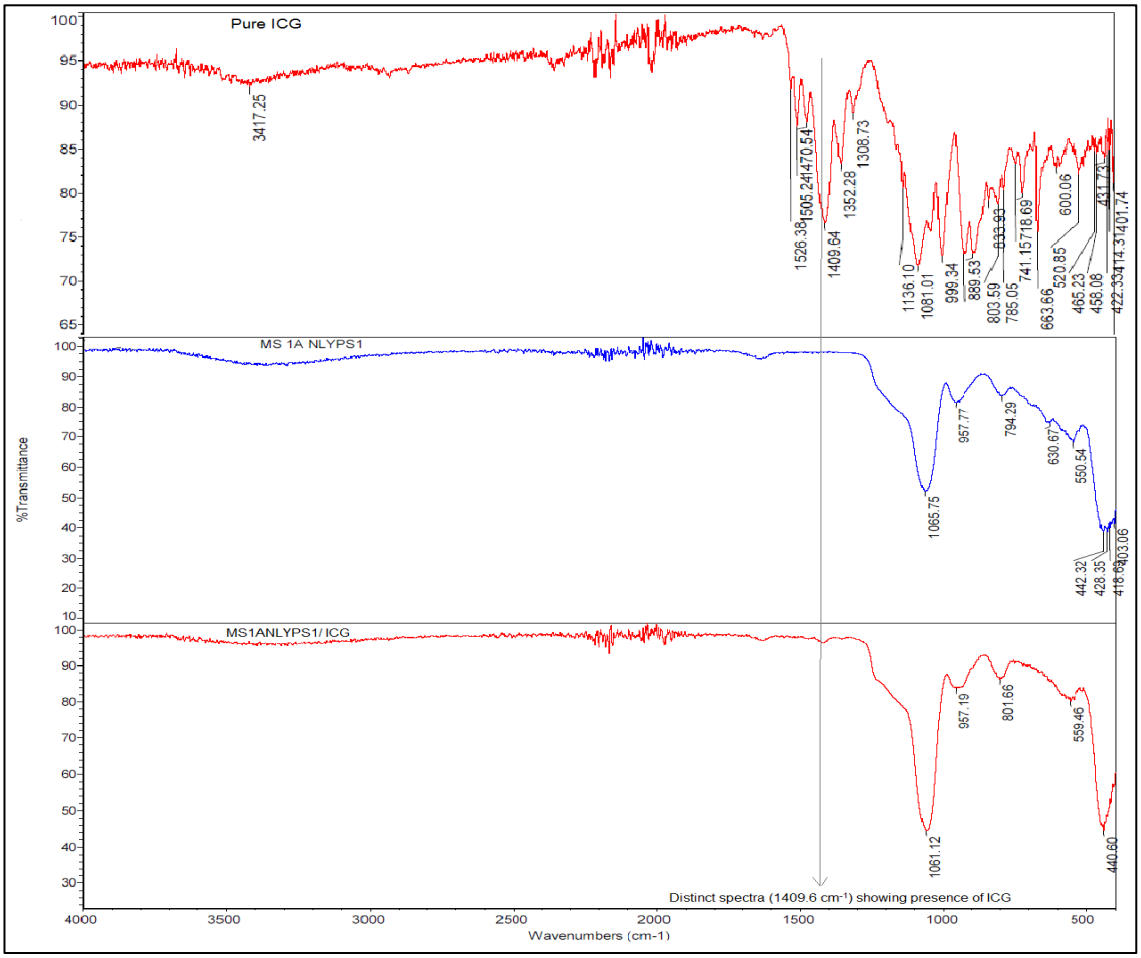

Figure 3-24: FTIR spectra showing the presence of ICG in ICG-encapsulated nanoparticles

The thermogravimetric analysis (TGA) of MS3 nanocomposites is presented here confirming the presence of ICG in MS nanocomposites (Figure 3-25). The small weight loss from 25 to 200 ℃ is due to the presence of physically adsorbed water. The weight loss from 200- 650 ℃ is due to decomposition of organic molecules such as oleic acid and ICG for MS3ICG nanocomposites. Considering the weight loss percentage after decomposition of oleic acid in MS3 nanocomposites, the additional weight loss for MS3ICG was around 1.55%, due to the presence of a small amount of loaded ICG.

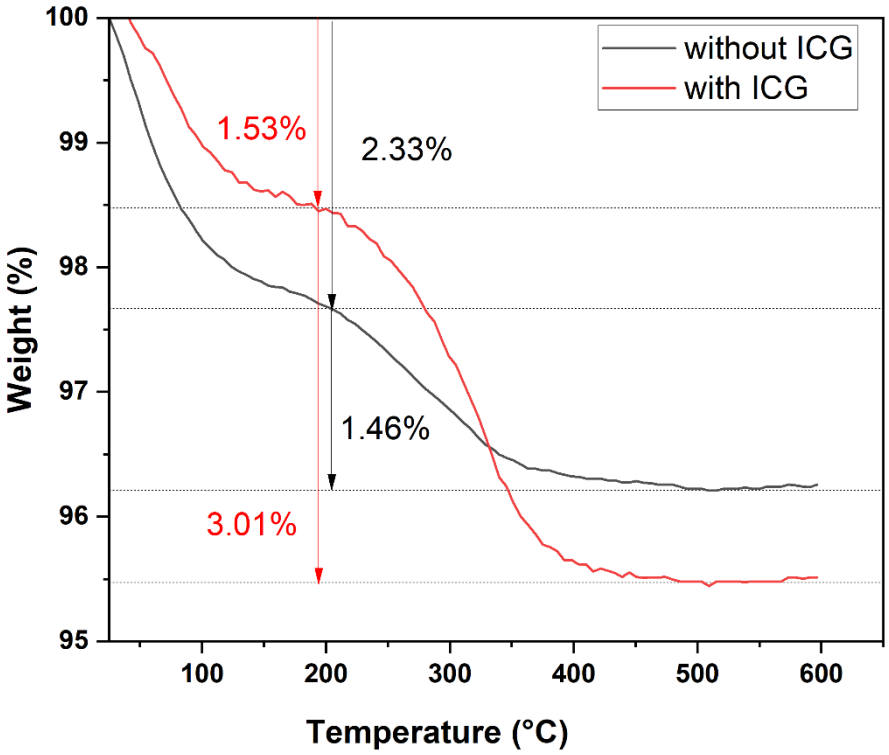

Figure 3-25: TGA curves of MS3 nanocomposites with and without ICG to show the percentage of ICG encapsulated in the nanocomposites.

3.3 Conclusion

This chapter of the thesis was focused on the synthesis and characterisation of various IONPs, fabrication of IONPs with mesoporous silica and loading ICG to develop magneto-optical nanocomposites. The hydrophilic (IO1, IO2) and hydrophobic (IO3) IONPs were synthesised using simple co-precipitation method. The TEM images showed IO1 and IO2 nanoparticles were nearly spherical. IO2 was monodispersed with a narrow particle size distribution of mean particle size calculated from TEM: 14 ± 2.5 nm and DLS: 158 nm, respectively compared to IO1 with average diameter of TEM: 42 ± 15 nm and DLS: 163 nm, respectively. The DLS showed the average hydrodynamic diameter for IO1 to be 163 nm and IO2 158 nm. The increase in diameter as calculated by DLS was because of the hydrodynamic layer of water in suspension. It could also be because of the aggregated IONPs. The positive zetapotential values of +19.1 ± 5.6 mV and +26.4 ± 5.5 mV were observed for IO1 and IO2 respectively, suggesting higher electrostatic repulsion between the particles of IO2 with an enhanced stability in suspension as compared to IO1. IO3 as analysed by TEM showed nearly spherical morphology with average diameter of 9 nm. IO3 was not analysed by DLS since it was dispersed in hexane.

FTIR showed a distinct peak at around 550 cm^{-1} corresponding to the bond vibrations between Fe-O in IO1 and IO2. An additional peak corresponding to the

presence of oleic acid was found in IO3 at 1709 cm^{-1} due to the carbonyl (C=O) vibrations, confirming the oleic acid acted as a stabiliser on IONPs. The magnetisation vs field (M-H) graphs showed that IONPs (IO1, IO2, IO3) exhibited superparamagnetic properties. The saturation magnetisation of IO1 and IO2 were calculated to be 63.6 emu/g and 59.4 emu/g, while IO3 showed lower magnetisation of 49.3 emu/g.

Fabrication of IONPs with mesoporous silica shell was performed using CTAB as a surfactant / structure directing template where TEOS was used as a silica source. The TEM images showed nearly spherical magnetic silica nanocomposites formation. MS1 nanocomposites were aggregating and larger in size with an average diameter around 129 nm whilst MS2 and MS3 were 83 nm and 38 nm, respectively. DLS data showed increase in size upon fabrication, MS1: 210 nm, MS2: 241 nm and MS3: 244 nm. The average zetapotential of MS nanocomposites showed change in surface charge from positive to negative due to the silanol groups present on the surface of upon silica coating on the IONPs. The zetapotential were higher in all MS nanocomposites at around -24 mV suggesting higher stability and dispersibility in suspension.

XRD at long angle (5- 80 degrees) range showed broad peak at around 15- 30 degrees confirming the presence of silica on the iron oxides. Similarly, FTIR data confirmed the presence of silica due to the presence of specific bond vibrations at 1080 cm^{-1} for Si-O-Si asymmetric stretching, 795 cm^{-1} for Si-O-Si symmetric stretching and 440 cm^{-1} for O-Si-O vibration. MS3 showed highest magnetisation values of 44.5 emu/g compared to MS1 and MS2 with 5.9 and 12.5 emu/g, respectively. Superiority in magnetisation of MS3 could be due to thin silica layer formation. Furthermore, the MS1 nanocomposites showed higher BET surface area of 965 ± 48.2 m^2g^{-1} indicating a large internal surface area due to ordered mesopores. The surface area decreased for MS2 and MS3 i.e., 655 ± 8.48 m^2g^{-1} and 142 ± 0.41 m^2g^{-1}, respectively. The magnetisation saturation decreased significantly for MS1 and MS2 while MS3 still possessed high magnetisation of 44.51 emu/g which could be due to the difference in silica and iron content and thin silica layer on the surface. The percentage of SiO_2: Fe_3O_4 for MS3 was 4.4: 95.6 (equivalent to 69.2% Fe) showing high iron content compared to other nanocomposites (MS1- 68: 32 (23% Fe), MS2- 64: 36 (26% Fe). Furthermore, the removal of CTAB from the nanocomposites was performed by acidic ethanol wash which was confirmed by FTIR and TGA analyses.

ICG tends to aggregate in water solution at higher concentration losing its properties. Therefore, low concentration of ICG was prepared and loaded onto the mesopores of MS nanocomposites through physical loading. To increase the amount of ICG in the nano-system, cumulative loading was performed. The loading of ICG on MS

nanocomposites was found to be dependent on the surface area with highest encapsulation on MS1 (68.6%) compared to MS2 and MS3 with 23.4% and 32.2%, respectively. The average size of nanocomposites were calculated by DLS: MS1ICG was 217 nm compared to MS2ICG (247nm) and MS3ICG (279 nm). The zetapotential values after the ICG loading were slightly higher (MS1ICG: -28 mV, MS2ICG: -28 mV, MS3ICG: -24.3 mV) as compared to their respective MS nanocomposites, which may be due to the presence of ICG in nanocomposites. Furthermore, the presence of ICG was confirmed by FTIR and TGA analysis.

CHAPTER 4

TESTING MATERIALS PERFORMANCE; LOCALISED HEATING AND FORMATION OF REACTIVE OXYGEN SPECIES (ROS) UNDER EXTERNAL STIMULI

4.1 Introduction

The efficiency of IONPs, MS and MSICG nanocomposites for biomedical applications depends on ability to heat under an alternating magnetic field (AMF) or laser light or in combination along with the ability to form reactive oxygen species (ROS) for cell death. The well-characterised nanoparticles and nanocomposites as explained in Chapter 3 were used for magnetic heating application and has been discussed in this chapter. A relatively small amount of IONPs and MS nanocomposites were studied under specific magnetic field that would be able to convert magnetic energy into localised heat under an AMF. A slight increase of physiological temperature (i.e., 37 ℃) to over 42 ℃ would be sufficient to kill cancer cells by localising the nanoparticles by an external magnetic field before applying the AMF of certain filed and frequency.

Similarly, ICG loaded MS nanocomposites (MSICG) were studied for testing their performance in photodynamic therapy (PDT), generation of ROS and photothermal therapy (PTT), localised heating upon laser irradiation. The generation of singlet oxygen ($^1O_2$) after laser irradiation (λ= 808 nm, power density= 1.2 W/cm^2) by suspensions containing MSICG nanocomposites was tested and quantified by analysing the light-sensitive form of ABMDMA which degrades to another form by reacting with singlet oxygen. Similarly, the heating efficiency of MSICG upon laser irradiation was also tested for PTT effect. The photostability of nanocomposites upon laser irradiation was also tested by repeating the laser ON/OFF cycles by monitoring the heating / cooling curves.

4.2 Magnetic Hyperthermia (MHT) under an AMF

4.2.1 MHT of IONPs

In order to develop a direct measure of magnetic heat generation by IONPs under an AMF, time and field dependent temperature curves were generated (see figures 4-1 and 4-2). In the actual experiment, suspension of IONPs placed at the centre of the magnetic coil, generating a maximum AMF of 15.8 kA/m at a frequency of 406 kHz. The experiments were conducted in DM100 instrument (nB nanoscale Biomagnetics, Spain) as explained in Chapter 2 section 2.3.7.

Figure 4-1 represents the time and field dependent temperature curves of hydrophilic IONPs (IO1 and IO2) at the maximum set temperature of 42 ℃. The maximum field was set at 200 Gauss with a constant frequency of 406 kHz. Both the bare IONPs (IO1 and IO2) were efficient in generating heat under AMF and reached a maximum set temperature of 42 ℃ within 196 and 88 seconds, respectively (Figure 4-1 and Figure 4-2). IO3 was not used for hyperthermia experiments as it is suspended in hexane which can damage the temperature probe of the instrument.

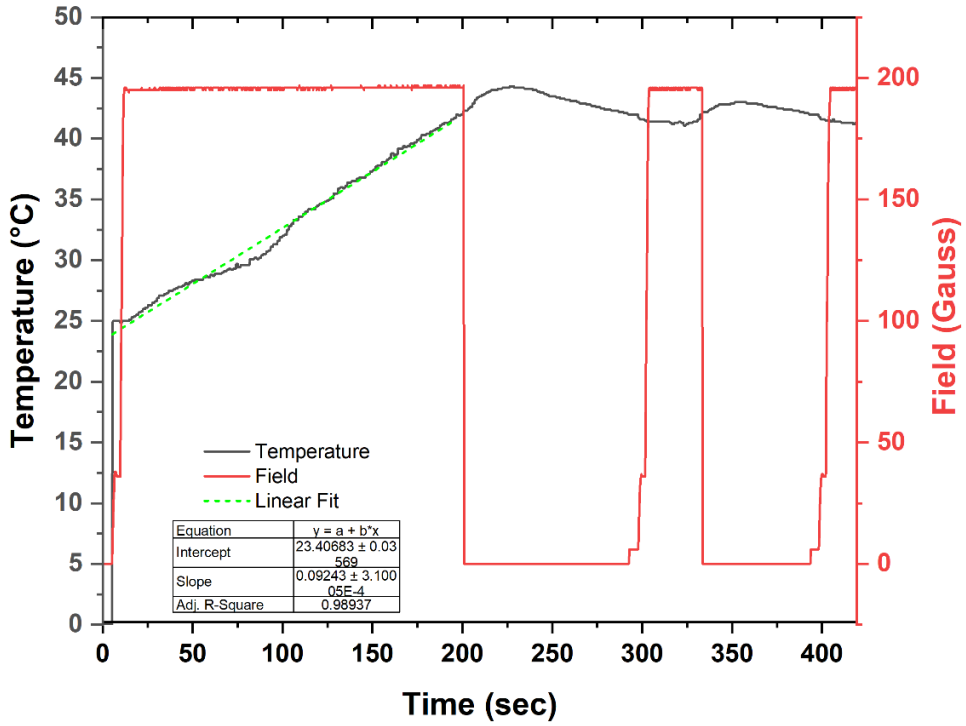

Figure 4-1: Time and field dependent temperature curve of IO1 under alternating magnetic field (AMF)

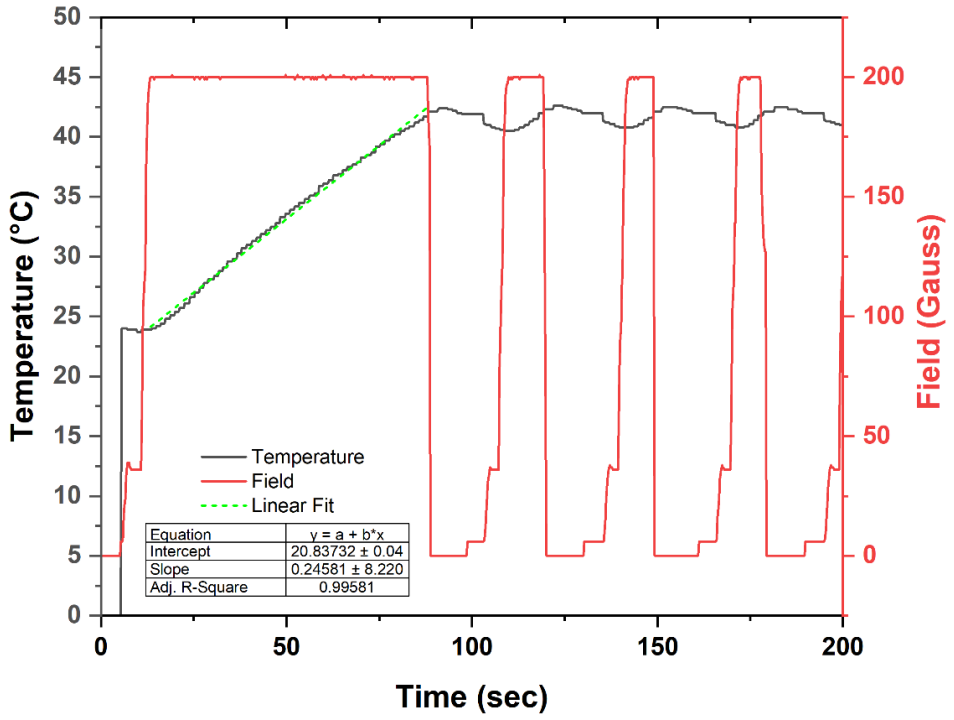

Figure 4-2: Time and field dependent temperature curve of IO2 under alternating magnetic field (AMF)

4.2.3 MHT of MS Nanocomposites

The localised heating efficiency of MS nanocomposites under an AMF was much lower (Figure 4-3) compared to IO1 nanoparticles. The time dependent temperature curve (black trace, Figure 4-3) showed that the time taken to reach the maximum set temperature of 42 ℃ was about 827 seconds compared to 196 sec for bare IO1.

Figure 4-4 represents the MHT profile of MS2 which showed similar effect as MS1 nanocomposites i.e., slower rate of heating (129 seconds to reach the maximum set temperature of 42 ℃) compared to bare IO2 nanoparticles (88 seconds to reach the maximum set temperature of 42 ℃). The results of this study also indicated that MS2 performed better than MS1.

Figure 4-5 represents MS3 nanocomposites where it took 296 seconds to reach the maximum set temperature of 42 ℃. Mesoporous silica coating on IO3 helped to dispersed MS3 in aqueous suspension, therefore, MHT study was performed unlike IO3 dispersed in hexane. The slow heating rate of MS1 and MS2 compared to their bare counterparts (IO1 and IO2) could be due to the shielding effect of diamagnetic silica layer with higher silica content on bare IONPs.

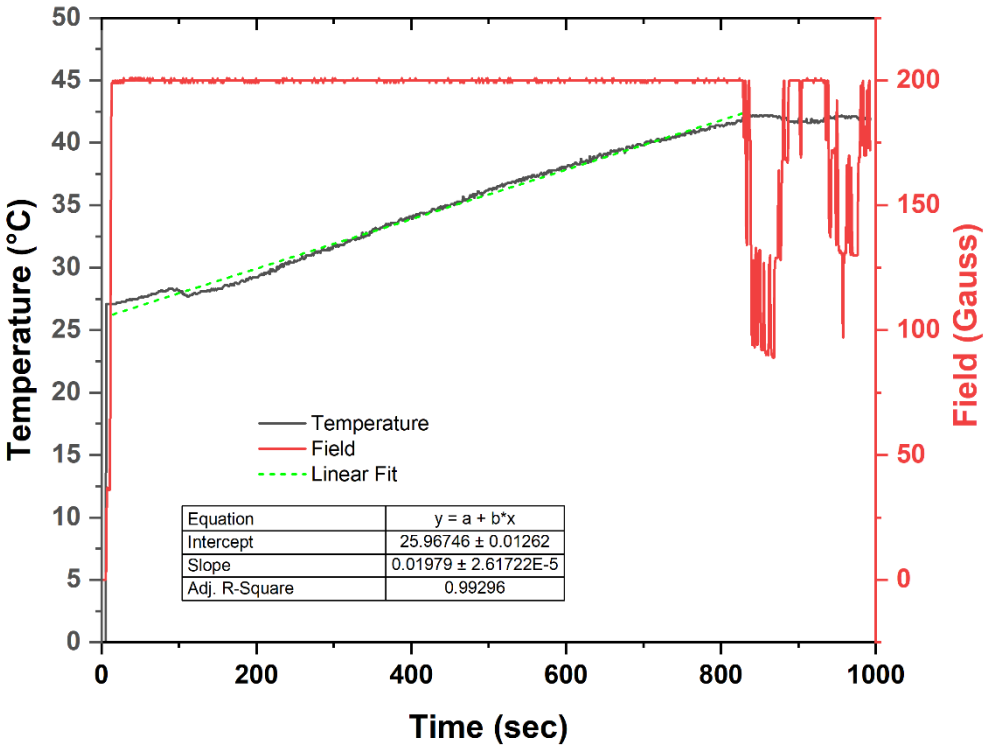

Figure 4-3: Time and field dependent temperature curve of magnetic silica nanocomposite (MS1) upon application of an alternating magnetic field (AMF)

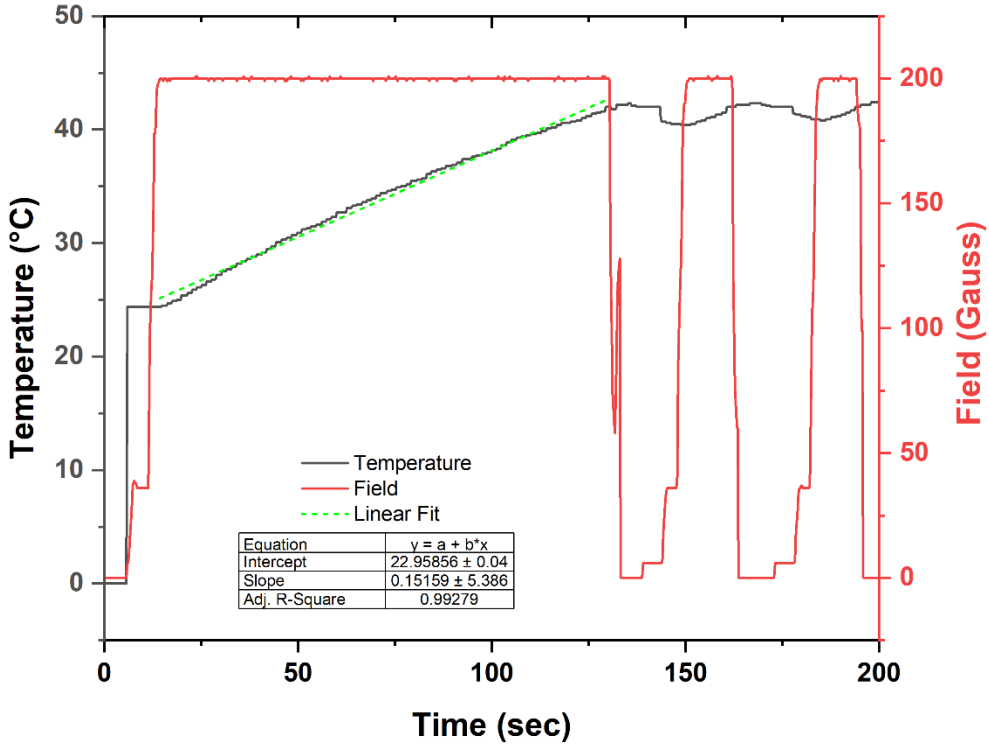

Figure 4-4: Time and field dependent temperature curve of magnetic silica nanocomposite (MS2) upon application of an alternating magnetic field (AMF)

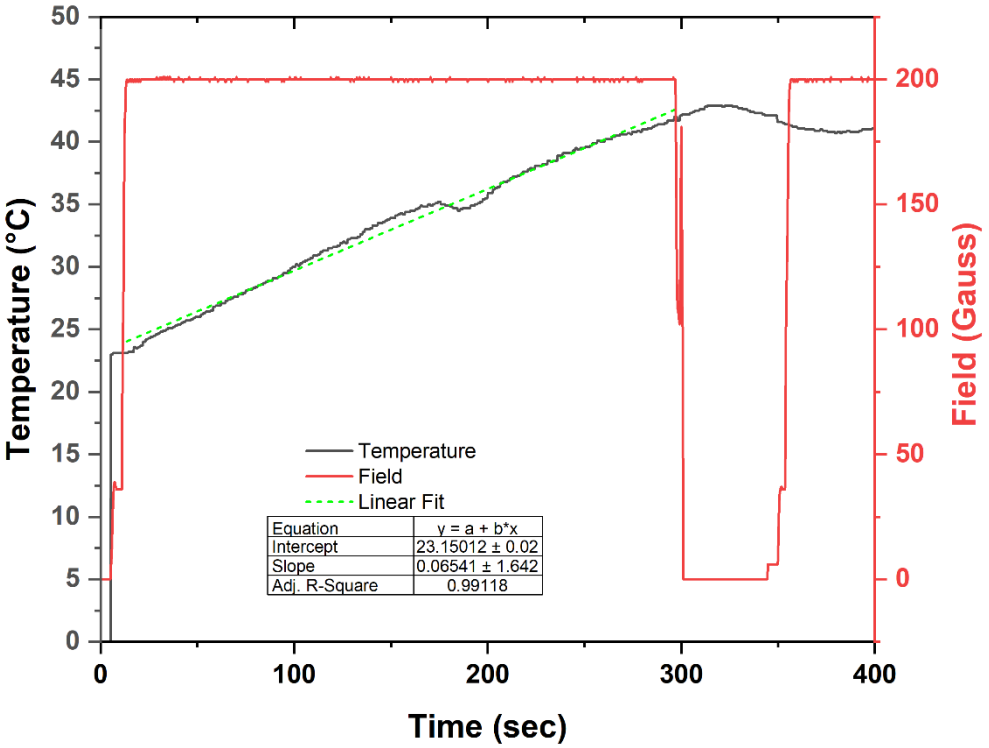

Figure 4-5: Time and field dependent temperature curve of magnetic silica nanocomposite (MS3) upon application of an alternating magnetic field (AMF)

4.2.4 Specific Power Absorption (SPA) and Intrinsic Loss Power (ILP) of Bare IONPs and MS Nanocomposites

The efficiency of nanoparticles in suspension to generate heat under an applied alternating magnetic field (AMF) is measured by calculating the power absorbed per unit mass of magnetic nanoparticles as explained earlier in Chapter 2, section 2.3.7. This power loss is termed as specific power absorption (SPA) or specific absorption rate (SAR) or specific power loss (SPL) and calculated using equation 2.4. Different instruments have got different setups for generating heat under AMF with respect to the frequencies and field intensities. Therefore, it is important to normalise by calculating intrinsic loss power (ILP) which has been presented in Table 4-1. ILP evaluates this difference and calculates the power loss which is validated for frequencies of up to several MHz (Behdadfar *et al.*, 2012).

The SPA values for IO1 and IO2 were 35.8 W/g and 94.1 W/g, respectively, where W/g represents Watt per gram. The ILP of IO1 and IO2 were 0.35 nHm^2/kg and 0.93 nHm^2/kg, respectively. The SPA and ILP values for both IONPs were different and similar to the values reported earlier (Behdadfar *et al.*, 2012). Similarly, the SPA values for MS nanocomposites MS1, MS2 and MS3 were calculated to be 6.8 W/g, 58.1 W/g and 25.2 W/g, respectively. The ILP values of each of these nanocomposites were 0.7 nHm^2/kg, 0.57 nHm^2/kg, and 0.25 nHm^2/kg, respectively.

Table 4-1: SPA and ILP of bare IONPs and MS nanocomposites calculated to evaluate their magnetic heating properties.

Samples	Magnetic field (H) (kA/m)	Frequency (f) (kHz)	Specific power Absorption (SPA) (W/g)	Intrinsic Loss Power (ILP) (nHm^2/kg)
IO1	15.8	406	35.8	0.35
IO2	15.8	406	94.1	0.93
MS1	15.8	406	6.8	0.07
MS2	15.8	406	58.1	0.57
MS3	15.8	406	25.2	0.25

The SPA values are ruled by various physical and magnetic properties of the IONPs such as particle size, size distribution and several extrinsic parameters like frequency (f), applied magnetic field (H), viscosity of the medium (η) and the particle concentration (Gonzalez-Fernandez *et al.*, 2009; Harabech *et al.*, 2017; Jamir *et al.*, 2021). The difference in SPA values of IO1 and IO2 could be attributed to their particle size and size distribution. Hergt *et al.*, (2006) reported that the SPA value of 1 kW/g at the frequency of 410 kHz and field sweep rate of 10 kA/m proven to be effective in

generating high heating power using mean size of 18 nm IONPs with a narrow size distribution.

Moreover, the SPA and ILP values of corresponding bare IONPs were higher compared to MS nanocomposites. One of the main reasons for this difference could be attributed to the insulating nature of silica coating, shielding the heat generated by the magnetic core in core-shell nanoparticles (Gonzalez-Fernandez *et al.*, 2009) as well as decrease in iron content in MS nanocomposites. The largest reduction is observed in MS1 nanocomposites due to relatively thick mesoporous silica shell and higher silica content compared to other MS nanocomposites. Therefore, one has to take in account on the optimum thickness of silica coating as well as the percentage of silica content for stabilising IONPs or generating mesoporosity without compromising the heating efficiency.

4.3 Study of Heating Efficiency of Nanocomposites Upon Laser Irradiation for Testing Potential Photothermal Therapy (PTT)

The heating ability of nanoparticles by laser irradiation (808 nm wavelength of power density 1.2 W/cm^2) for a period of 6 minutes was recorded for pure ICG, MSICG nanocomposites and solvent water (Figure 4-6). Water and pure ICG were taken as controls. The concentration of 20 µM (equivalent to 0.04 moles) of pure ICG and a calculated amount of MSICG nanocomposites equivalent to 0.04 moles ICG were taken to run the experiments. Pure ICG solution in water exhibited the largest temperature rise (22.7 ℃) as compared to all MSICG nanocomposites. MS3ICG exhibited the highest photothermal effect with change in temperature up to 22 ℃. MS1ICG and MS2ICG showed less temperature change of 19 ℃ and 13 ℃, respectively. The lower temperature rise in MS1ICG and MS2ICG nanocomposites could be due to the thick silica layer affecting the penetration of laser irradiation as suggested by Huang *et al.* (2019). It also implies that the change in temperature upon laser irradiation is distinct to the synthesised nanocomposites and does not depend on the weight of nanocomposites used (MS1ICG: 255 µg/ml, MS2ICG: 1.7 mg/ml and MS3ICG: 1 mg/ml). Laser irradiation using water as a control showed no significant changes. Therefore, photothermal efficiency can be due to the optical probe ICG either in its' free form or encapsulated form in nanocomposites.

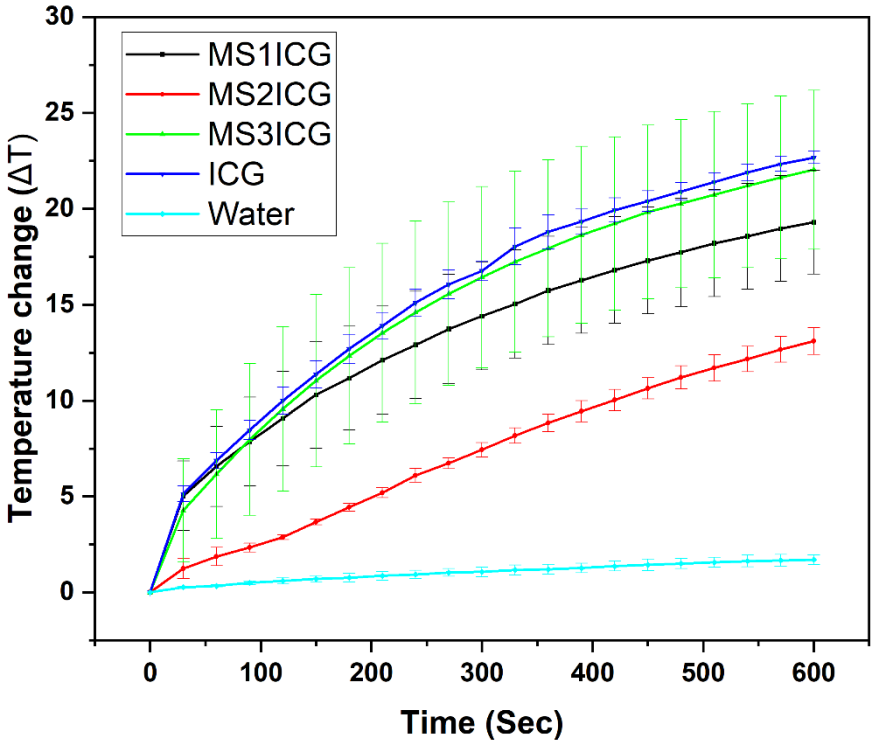

Figure 4-6: PTT effect: Temperature rise upon continuous laser irradiation (808 nm, 1.2 W/cm^2) in solution of MS1ICG, MS2ICG, MS3ICG, free ICG and water.

4.4 Photostability Study

To test the photostability of ICG when loaded inside the nanocomposites as MSICG, a number of laser ON/OFF cycles were performed using laser irradiation (λ = 808 nm of 1.2 W/cm^2 power density). The temperature change was measured using thermal probe. The samples were mixed after each cycle to retain sample in suspension. Pure ICG solution was also taken for comparison to MSICG nanocomposites. The MSICG nanocomposites showed increase in temperature with time (Figure 4-7) for each three cycles with a small reduction of maximum temperature. However, heating efficiency of pure ICG after 1st cycle reduced during 2nd and 3rd cycles and this is mainly due to the degradation in its free form. Reduced heating efficiency with complete photodegradation is observed upon continuous laser irradiation up to 5 cycles (Niu *et al.*, 2017; Ma *et al.*, 2018; Zhang *et al.*, 2021; Huang *et al.*, 2022) (data not provided). This is also visible with colour change from dark green to faint yellow as shown in Figure 4-7, inset. The photobleaching of ICG is mainly caused by the generation of ROS triggered upon photoexcitation (Lee *et al.*, 2009). To protect ICG from photobleaching researchers confined ICG inside the silica pores where the water diffusion is markedly slowed, thus increasing ICG stability (Ferrauto *et al.*, 2017; Lv *et al.*, 2017). Photodegradation of ICG in MSICG nanocomposites is observed to be minimal due to the encapsulated form. This is utmost important for *in-vivo* experiments for the delivery of ICG in the encapsulated

form to cancer cells without losing the photothermal efficiency of ICG upon repetitive laser irradiation.

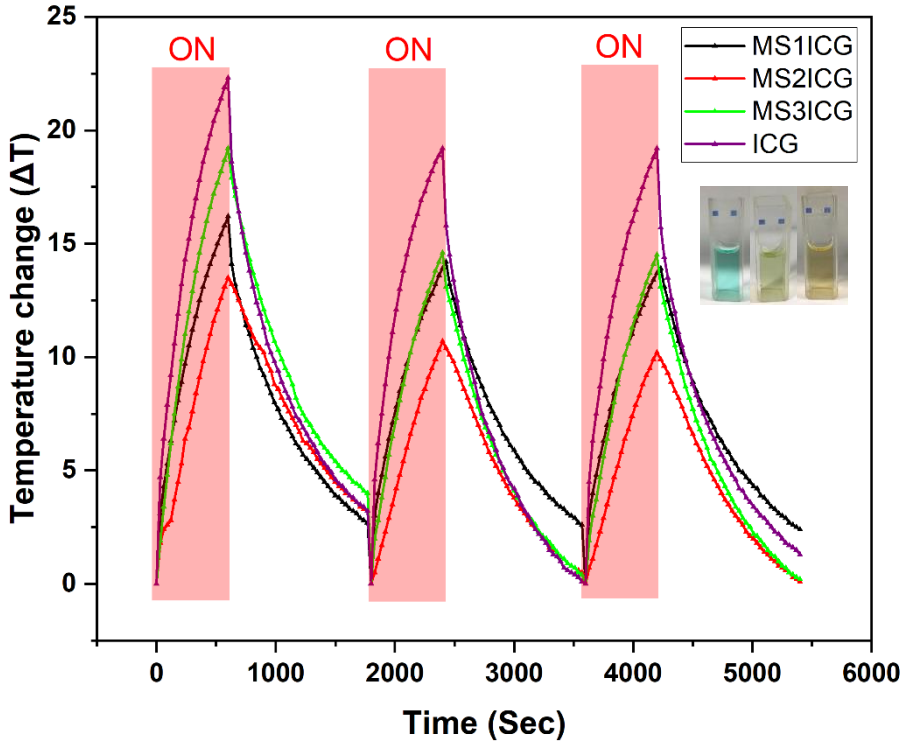

Figure 4-7: Photostability study upon laser irradiation. Temperature changes of MS1ICG, MS2ICG, MS3ICG and free ICG over three NIR laser (808 nm, 1.2 W/cm^2) ON/OFF cycles. Inset: Photodegradation of pure ICG over laser irradiation ON/OFF cycles with visible colour change from green to yellow.

4.5 Photodynamic Therapy: Generation of Singlet Oxygen

The reactive oxygen species (ROS) generation is a crucial indicator for evaluating the PDT efficiency. Out of the two pathways of ROS generation i.e., generation of radicals or singlet oxygen ($^1O_2$) (Kumar, Anuradha and Roy, 2014). The efficiency of $^1O_2$ generation after laser irradiation on MSICG has been presented in this section since ICG is capable of generating $^1O_2$ upon laser irradiation. $^1O_2$ generation in biological system is a short-lived process where $^1O_2$ reacts rapidly with the surrounding molecules capable of killing cancer cells.

To assess the quenching ability of nanocomposites, suspensions containing MSICG nanocomposites mixed with 9,10-anthracenediyl-bis (methylene) dimalonic acid (ABMDMA) were used for laser irradiation (λ =808 nm,1.2 W/cm^2 power density). The reaction of ABMDMA with $^1O_2$ leads to the formation of non-emissive endoperoxide form (Figure 2-3). The relative loss of absorbance intensity at 400 nm was used as an indirect measurement of the amount of $^1O_2$ formation.

Figure 4-10 indicates the change in absorbance at 400 nm, a characteristic absorption of aromatic anthracene moiety of ABMDMA due to the change in

endoperoxide form of ABMDMA at different time intervals upon laser exposure. A clear reduction of absorbance of ABMDMA in the presence of pure ICG solution, MS1ICG and MS2ICG suspension after 30 seconds of laser irradiation indicates the formation of singlet oxygen ($^1O_2$). The thin silica coating allows laser to pass to the ICG molecules generating ROS (Huang *et al.*, 2019). The reduction in absorbance of MS1ICG and MS2ICG solution was similar to that of ICG. The slight increase in absorbance after 60 seconds of laser irradiation could be due to short lived $^1O_2$. Dysart and Patterson (2005) observed that the lifetime of $^1O_2$ is very short i.e., ~10–320 nanoseconds which can negatively affect the results. MS3ICG showed an increase in absorbance after laser irradiation. An increase in absorbance could be due to the release of iron oxide nanoparticles after laser irradiation since iron oxides gives absorbance around 400 nm (Kwon *et al.*, 2007; Mahdavi *et al.*, 2013). Additionally, the release of iron ions could be due to the degradation of silica layer as the experiment was performed in alkaline condition to dissolve ABMDMA (Staniford *et al.*, 2015). Thus, loss of thin silica layer could have increased the release of iron oxides in case of MS3ICG. The iron oxides released from MS3ICG could not be magnetically separated and stayed in the mixture hence contributed artifact in the absorbance study (picture not included).

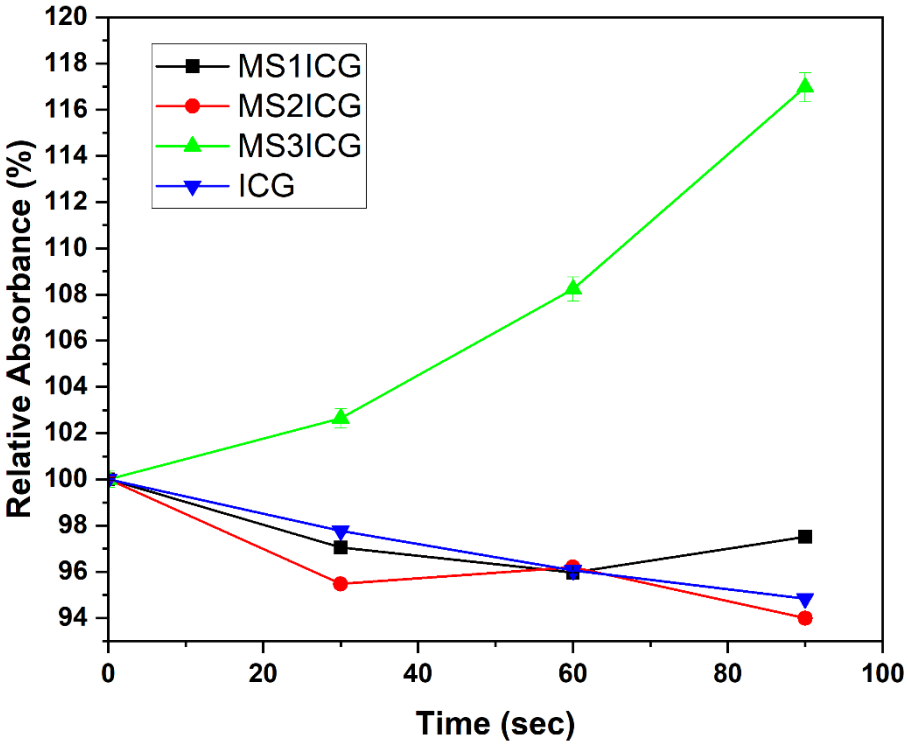

Figure 4-8: PDT effect. Relative absorbance of ABMDMA at 400 nm in different solutions (MS1ICG, MS2ICG, MS3ICG with ICG concentration of 20 µM and free ICG) at different time points under 808 nm laser irradiation (1.2 W/cm^2).

4.6 Conclusion

In this chapter, the aim was to test the efficiency of MS and MSICG nanocomposites in suspension for MHT/PDT/PTT in the presence of external stimuli such as AMF and laser irradiation. The study using hydrophilic IONPs and AMF with magnetic field intensity of 15.8 kA/m and frequency 406 kHz showed that IO2 was efficient in generating heat and reaching a maximum set temperature of 42 ℃ within 88 seconds. IO1 reached the set temperature at 196 seconds. These findings suggested that IO2 is more efficient than IO1 in generating heat upon applied AMF. Similarly, MS1, MS2 and MS3 nanocomposites could also generate heat upon applied AMF, however, the time taken to reach the set temperature was significantly higher compared to core IONPs without silica coating. In general, MS2 nanocomposites showed better heating efficiency (SPA- 58.1 W/g) than MS1 (SPA- 6.8 W/g) and MS3 nanocomposites (SPA- 25.2 W/g). The significant decrease in heating efficiency of MS1 could be due to the presence of higher silica content compared to other MS nanocomposites.

Similarly, the synthesised MSICG nanocomposites were tested for their efficiency in PTT and PDT using laser irradiation (λ= 808 nm, power density= 1.2 W/cm^2). MS3ICG exhibited the highest photothermal effect with change in temperature up to 22 ℃. MS1ICG and MS2ICG showed relatively low temperature rise such as 19 ℃ and 13 ℃, respectively. The lower temperature rise in MS1ICG and MS2ICG nanocomposites could be due to the thick silica layer compared to MS3ICG which can affect the penetration of laser irradiation to induce PTT effect as suggested by Huang *et al.* (2019). The change in temperature upon laser irradiation did not depend on the weight of nanocomposites, however, depend on the ICG and silica content in the nanocomposites. The PDT effect as indicated by change in absorbance of ABMDMA was higher in MS2ICG as compared to other nanocomposites. These experiments confirmed that MS2ICG showed better MHT/PDT effect, however, showed lower PTT effect compared to other nanocomposites.

CHAPTER 5

DETERMINING POTENTIAL THERAPEUTIC EFFICACY OF MAGNETO-OPTICAL NANOCOMPOSITES *IN-VITRO*

5.1 Introduction

The aim of the work presented in Chapter 5 is to investigate the therapeutic efficacy of nanoparticles in cancer treatment, *in-vitro* using cancer cell lines. Two sets of magneto-optical nanocomposites (MS2ICG and MS3ICG) were used for testing their therapeutic efficacy on a commercial breast cancer cell line, MCF7.

The cellular toxicity of MS2ICG and MS3ICG nanocomposites was evaluated using a standard MTT assay as explained in Chapter 2, section 2.4.2 in the absence or presence of an external stimuli such as laser irradiation (λ= 808 nm, power density = 1.2 W/cm^2). Trypan blue assay was performed to evaluate the cellular toxicity in (i) presence or absence of magnetic field strength of 15.8 kA/m and frequency of 406 kHz, and (ii) a combination of AMF + laser. The cellular toxicity of magneto-optical nanocomposites was compared with a control experiment without nanocomposites. The cellular uptake of nanocomposites was studied using Prussian blue staining, SEM and Confocal fluorescence microscopy. Furthermore, the uptake mechanism of nanocomposites was established using different endocytic inhibitors. Biocompatibility of nanocomposites was also tested in an *ex-vivo* system using red blood cells.

5.2 Result and Discussion

5.2.1 Biocompatibility Evaluation: MTT Assay

Biocompatibility of nanoparticles on cancer cell lines is an initial test for assessing their efficacy as potential drug delivery system. It has been suggested that nanoparticles maintaining cell viability of more than 80% are considered to be biocompatible (Mahmoudi *et al.*, 2009). To evaluate the cellular biocompatibility of magnetic silica nanocomposites without encapsulated ICG (MS2, MS3) or magneto-optical nanocomposites with encapsulated ICG (MS2ICG, MS3ICG); a series of experiments were carried out at varying concentrations (50, 100, 200, 400 µg/ml) at two different time points (24 and 48 hours) *via* MTT assay using MCF7 cell lines as explained earlier in Chapter 2 section 2.4.1. The precise quantification of changes in rate of cell viability is acquired by linear relationship between metabolically active cells and the produced formazan colour.

The percentage cell viabilities of MS2, MS3, MS2ICG and MS3ICG nanocomposites and pure ICG on MCF7 cell lines at 24 and 48 hours (three measurements for each sample) are shown in Figure 5-1 (A-E). The cell viability was found to be dependent on both dose and time of incubation. Both MS and MSICG nanocomposites showed biocompatibility (80% or above cell viability) up to 100 µg/ml concentration at 24 hours of incubation. It has been reported that MS nanocomposites

can induce toxicity in cells above 100-200 µg/ml (Tao *et al.*, 2009; Rosenholm, Sahlgren and Lindén, 2010). Above 100 µg/ml of nanocomposites, they showed cytotoxic effect and highest toxicity was observed at a concentration of 400 µg/ml. The toxicity at higher concentration of nanocomposites (having more iron oxide content) could be due to the catalytic effect of Fe^{3+}/Fe^{2+} in increasing the cytotoxicity by damaging DNA as reported by Sun *et al.* (2018). The cell viability significantly decreased at 48 hours compared to 24 hours incubation period. No significant differences in cell survival rates were observed for ICG treated cells at different concentration and time points, similar results reported by (Lin *et al.*, 2021), suggesting ineffective cytotoxicity of ICG in MSICG nanocomposites (Figure 5-1 E). As shown in Figure 5-1 F, the cell viability decreased in MS3ICG treated cells when compared to MS2ICG at 24 hours incubation suggesting cytotoxic effect of MS nanocomposites with hydrophobic iron oxide core. The cell viability decreased significantly with MS3 and MS3ICG at 48 hours of incubation when compared to MS2 and MS2ICG suggesting advantage of MS2 and MS2ICG nanocomposites (Figure 5-1 G). Table 5-1 and 5-2 summarises the results of all the cell viability assays discussed for MS2, MS3, MS2ICG and MS3ICG nanocomposites, and pure ICG.

Table 5-1: Cell viability (% of control) of MCF7 cells treated with various nanocomposites (MS2, MS3, MS2ICG, MS3ICG) at varying concentration (50, 100, 200, 400 µg/ml) post 24 and 48 hours of incubation.

Concentration (µg/ml)	MS2		MS3		MS2ICG		MS3ICG	
	24 hours	48 hours	24 hours	48 hours	24 hours	48 hours	24 hours	48 hours
Control	100 ± 2.62	100 ± 5.45	100 ± 2.62	100 ± 5.45	100 ± 2.62	100 ± 5.45	100 ± 2.62	100 ± 5.45
50	85.63 ± 0.12	81.65 ± 0.78	84.65 ± 0.3	79.39 ± 0.52	85.16 ± 0.27	81.19 ± 0.64	84.04 ± 1.14	78.19 ± 0.63
100	79.72 ± 0.34	74.41 ± 0.87	79.01 ± 0.23	72.76 ± 0.43	78.92 ± 0.65	73.91 ± 0.09	78.14 ± 0.29	71.7 ± 0.43
200	65.73 ± 0.73	59.69 ± 0.14	64.27 ± 0.7	58.12 ± 0.43	64.98 ± 0.63	58.85 ± 0.25	63.11 ± 1.18	57.25 ± 0.93
400	59.67 ± 0.18	53.03 ± 0.38	53.47 ± 1.31	47.78 ± 0.6	58.97 ± 0.24	52.3 ± 1.31	52.72 ± 0.72	46.34 ± 0.79

Table 5-2: Cell viability (% of control) of MCF7 cells treated with pure ICG at varying concentration (2.5, 5, 10, 20, 40, 80 µg/ml) post 24 and 48 hours of incubation.

Concentration (µg/ml)	ICG	
	24 hours	48 hours
Control	100 ± 2.62	100 ± 5.45
2.5	98.27 ± 0.57	96.83 ± 1.37
5	97.94 ± 0.49	96 ± 0.61
10	97.14 ± 1.19	94.62 ± 0.91
20	96.49 ± 0.74	93.75 ± 0.63
40	95.51 ± 1.11	93.02 ± 0.61
80	94.66 ± 0.88	91.38 ± 0.35

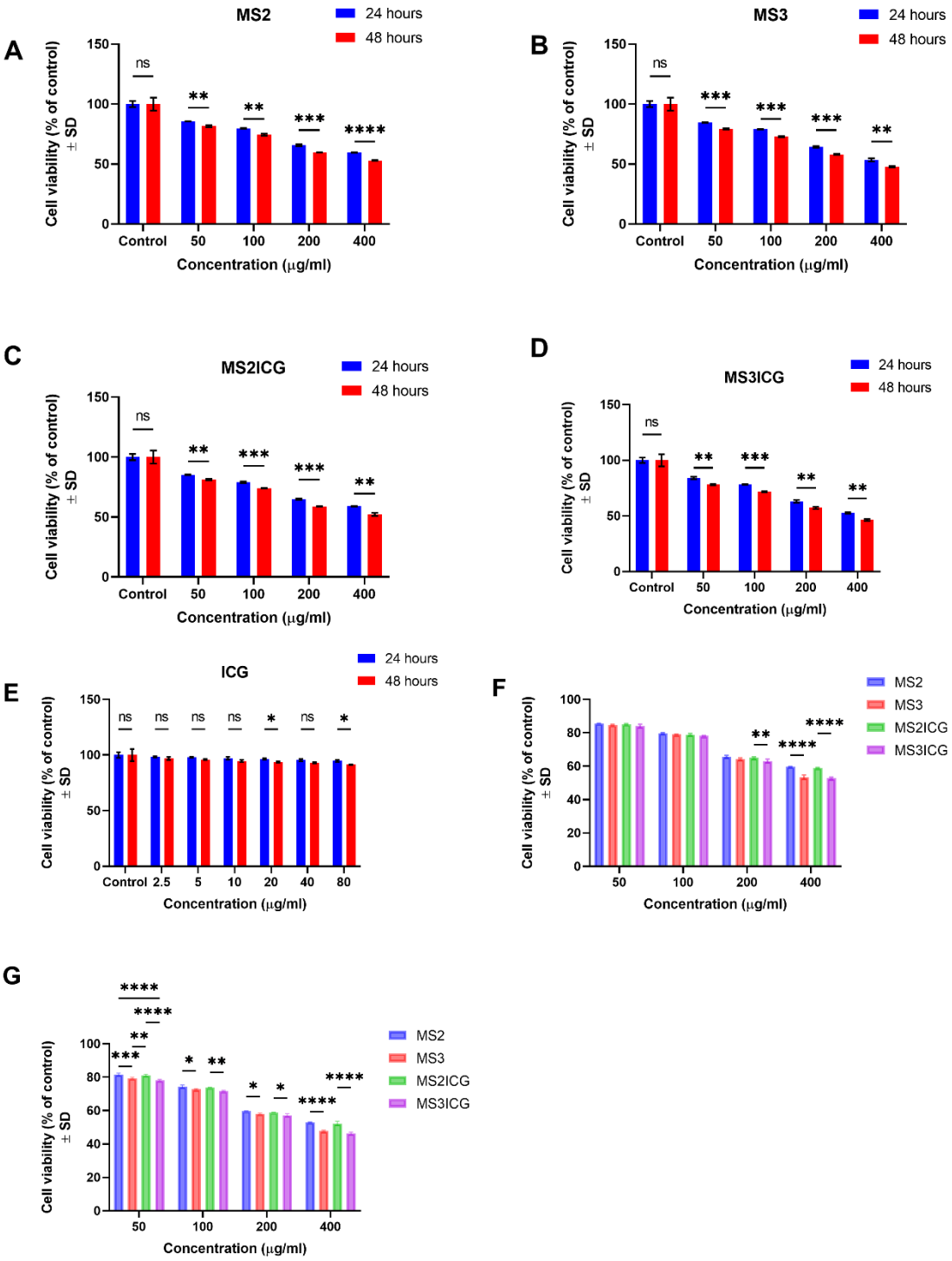

Figure 5-1: MCF7 cell viability upon incubation with different nanocomposites for 24 and 48 hours. A: MS2, B: MS3, C: MS2ICG, D: MS3ICG at various concentrations 50, 100, 200, 400 µg/ml, E: pure ICG at concentration of 2.5, 5, 10, 20, 40, 80 µg/ml. F, G: Comparison between different nanoparticles at 24 and 48 hours, respectively. All data were analysed by GraphPad Prism, shown as mean ± SD (Standard Deviation) of 3 replicates in each group. The significant differences are indicated with asterisks (*P < 0.05, **P < 0.01, ***P < 0.001, ****P < 0.0001, ns- not significant)

5.2.2 Cellular Toxicity: Optical Microscopy Images of Cells with/without Laser Irradiation

Optical microscopy was used for direct visualisation of MCF7 cells in the presence/ absence of MS2ICG and MS3ICG nanocomposites in the presence/ absence of laser irradiation as shown in Figures 5-2 and 5-3, respectively. Cells were treated with various concentrations (50, 100 and 200 µg/ml) of MS2ICG, MS3ICG nanocomposites and incubated for 24 hours. After incubation, the cells were laser irradiated (λ= 808 nm, power density= 1.2 W/cm^2) for 5 minutes and further incubated for 24 hours. Cells without nanocomposites was taken as a negative control and cells treated with Tert-Butyl Hydrogen Peroxide (THBP) (100 µM) was taken as a positive control. Pure ICG was also used for comparison against nanocomposites. The cells were visualised before and after laser irradiation under inverted optical microscope and images were analysed using MShot software.

The cells showed no significant changes in morphology upon treatment with nanocomposites before or after laser irradiation, when compared with the negative control. Higher accumulation of MSICG nanocomposites around the cells was evident (black spots) from the images (Figure 5-2 and 5-3), indicated as green arrows and dependent on the concentration and type of nanocomposites used. For example, increasing the concentration of MS2ICG showed higher killing efficiency both before and after laser irradiation (Figure 5-2, d-f). The efficiency of killing cells upon laser irradiation was evident when treated with pure ICG and MS2ICG nanocomposites of higher concentration (200 µg/ml) (see (Figure 5-2 b, f). THBP treatment showed maximum killing efficiency as a positive control experiment (Figure 5-2 c).

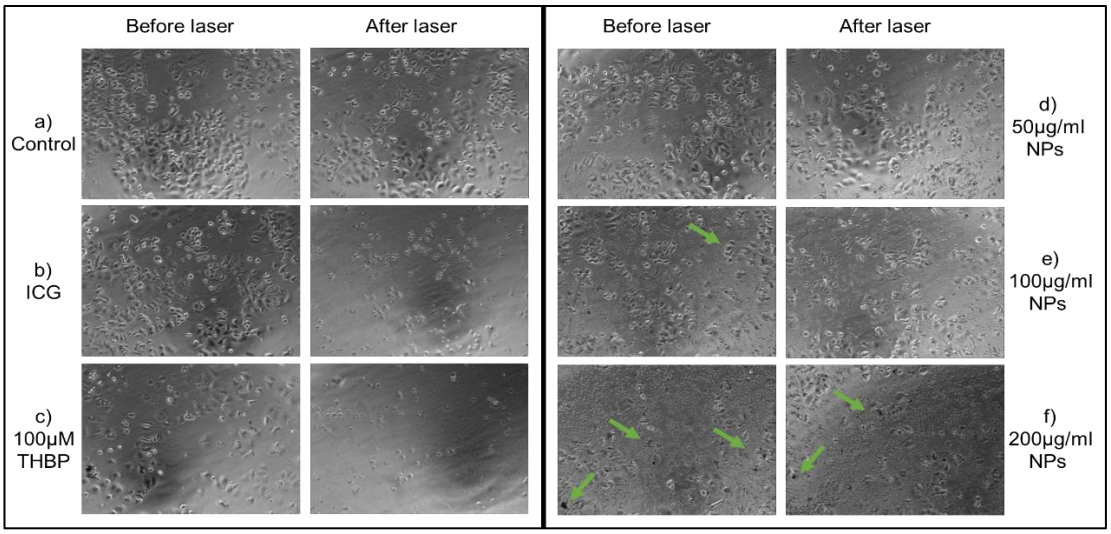

Figure 5-2: Optical microscopy images of MCF7 cells comparing pre and post 24 hours incubation upon laser irradiation (808 nm, 1.2 W/cm^2, 5 minutes) treated with MS2ICG (10X). a) to f) are cells treated with Control (no nanoparticles), ICG (20 µM), THBP (100 µM) and three different concentrations of MS2ICG (50, 100, 200µg/ml), respectively.

Similarly, MCF7 cells treated with various concentrations of MS3ICG nanocomposites showed concentration dependent cells killing efficiency upon laser irradiation (Figure 5-3, d-f). A higher accumulation is clearly visible at higher concentration of nanocomposites (indicated by green arrows).

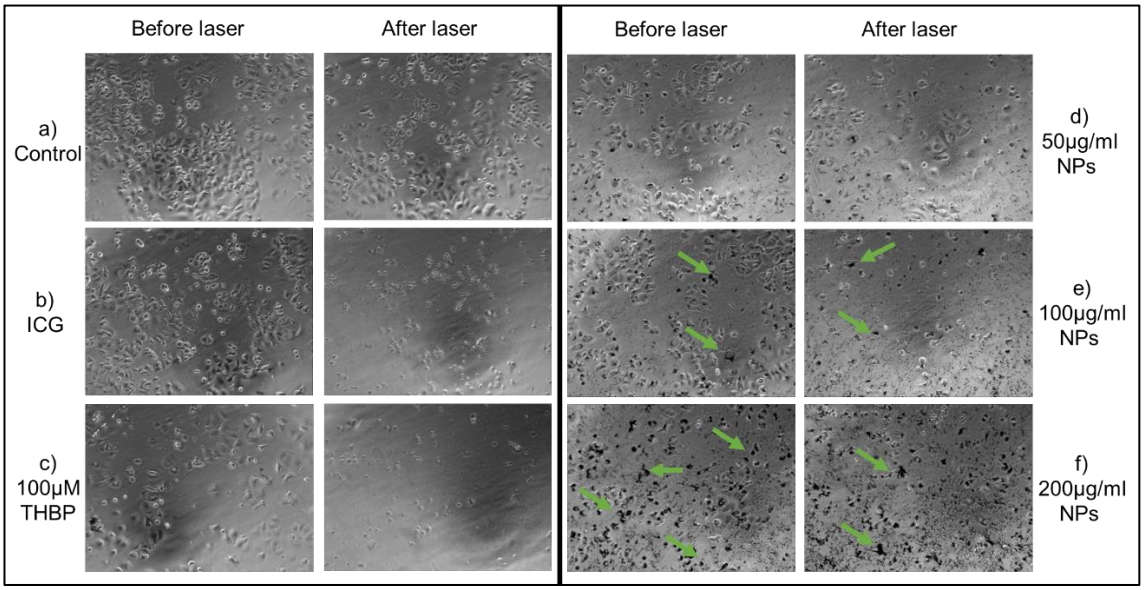

Figure 5-3: Optical microscopy images of MCF7 cells comparing pre and post 24 hours incubation upon laser irradiation (808 nm, 1.2 W/cm^2, 5 minutes) treated with MS3ICG (10X). a) to f) are cells treated with Control (no nanoparticles), ICG (20 µM), THBP (100 µM) and three different concentrations of MS3ICG (50, 100, 200µg/ml), respectively.

5.2.3 Effect of Nanocomposites on Cancer Cells Upon Laser Irradaition as an External Stimuli: MTT Assay

The cellular toxicity of nanocomposites before and after laser irradiation was analysed using MTT assay in MCF7 cells as explained earlier in Chapter 2, section 2.4.2. MCF7 cells were treated with various concentrations (50, 100, 200 and 400 µg/ml) of MS2ICG and MS3ICG nanocomposites for 2 hours and laser was irradiated (λ = 808 nm, power density = 1.2 W/cm^2) for 5 minutes. Afterwards the cells were incubated for 24 and 48 hours, and cell toxicity was analysed using MTT assay.

As shown in Figure 5-4, there was a significant difference in cytotoxicity towards MCF7 cells when treated with MSICG nanocomposites (both MS2ICG and MS3ICG) upon laser irradiation compared to dark (without laser irradiation) at two different time points, 24 and 48 hours. The significant difference (***p< 0.001, ****p< 0.0001) in cell toxicity with/ without laser irradiation supports the evidence of improved PDT and PTT effect in cells upon NIR laser irradiation, thus suggesting localised cancer cells killing efficiency. The cellular toxicity was observed to be dependent on both the concentration and time of incubation. Increasing the concentration of MS2ICG from 50 to 400 µg/ml increased the toxicity both under dark (from 15% to 41%, over 2 folds) or upon laser

irradiation (21% to 70%, ~3 folds) after 24 hours incubation. However, minimal difference was observed while increasing the incubation time from 24 to 48 hours (for example, at 400 µg/ml: 41% to 48% at dark and 71% to 78% upon laser irradiation). Control cells were not affected by laser irradiation suggesting no toxic effect of laser irradiation alone. MS3ICG also showed comparable results to MS2ICG, with increased cancer cells killing efficiency upon laser irradiation. The cellular toxicity of various concentrations of pure ICG upon laser irradiation is provided in Figure 5-4 (E, F) at 24 and 48 hours showing substantial cancer cells killing properties even at low concentration of 2.5 µg/ml from 1.7% to 17.7% and 3.2% to 31.3%, respectively. Table 5-3 provides the cytotoxicity (%) values for all experiments.

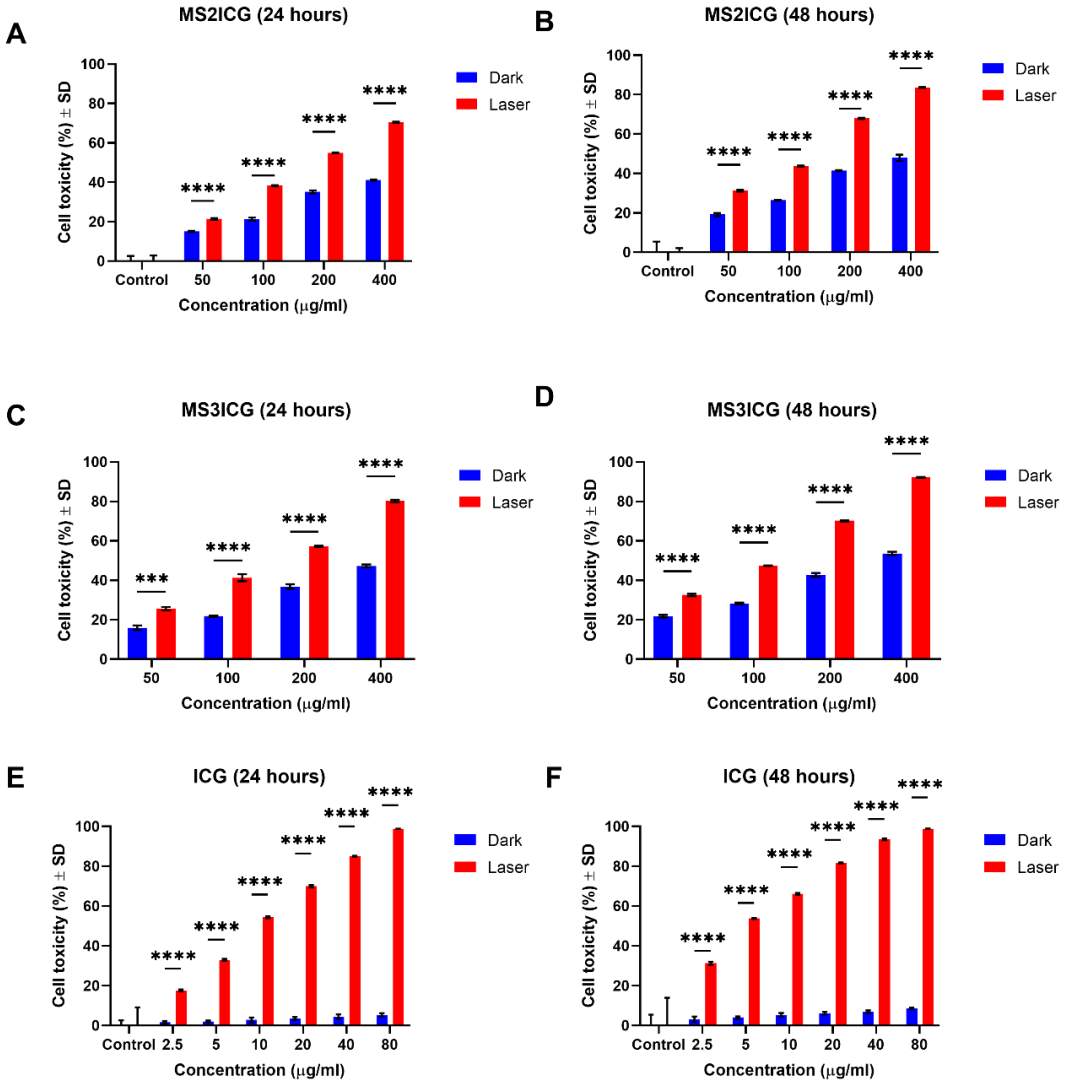

Figure 5-4: Cytotoxicity studies of MSICG nanocomposites (A, B- MS2ICG; 8 µg of ICG/ mg of nanocomposites and C, D- MS3ICG; 10 µg of ICG/ mg of nanocomposites) and E, F- pure ICG on MCF7 cells with and without laser irradiation after 24 and 48 hours. The significant differences between cytotoxicity with and without laser irradiation was calculated with unpaired t-test and indicated with asterisks (***p < 0.001, ****p < 0.0001). All data were analysed by GraphPad Prism, shown as mean ± SD with 3 replicates in each group.

Table 5-3: Cellular toxicity values as measured using MTT assay on MCF7 cells treated with MS2ICG and MS3ICG nanocomposites and pure ICG at various concentration with/without laser irradiation at 24 and 48 hours of incubation. The data shows cell toxicity (%) ± SD with 3 replicates in each group.

Samples	Concentration (µg/ml)	24 hours		48 hours	
		Dark	Laser	Dark	Laser
MS2ICG	Control	0 ± 2.6	0 ± 2.9	0 ± 5.5	0 ± 2.2
	50	15.1 ± 0.3	21.4 ± 0.4	19.2 ± 0.8	31.3 ± 0.5
	100	21.3 ± 0.8	38.3 ± 0.3	26.4 ± 0.1	43.7 ± 0.3
	200	35.2 ± 0.8	55 ± 0.2	41.4 ± 0.3	67.9 ± 0.3
	400	41.2 ± 0.3	70.5 ± 0.4	47.9 ± 1.6	83.7 ± 0.2
MS3ICG	50	16 ± 1.1	25.6 ± 0.9	21.8 ± 0.6	32.6 ± 0.6
	100	21.9 ± 0.3	41.3 ± 1.8	28.3 ± 0.4	47.4 ± 0.1
	200	36.9 ± 1.2	57.2 ± 0.4	42.8 ± 0.9	70.2 ± 0.3
	400	47.3 ± 0.7	80.2 ± 0.6	53.7 ± 0.8	92.2 ± 0.2
ICG	Control	0 ± 2.6	0 ± 9.1	0 ± 5.5	0 ± 13.9
	2.5	1.7 ± 0.6	17.7 ± 0.4	3.2 ± 1.4	31.3 ± 0.7
	5	2.1 ± 0.5	33 ± 0.4	4 ± 0.6	53.8 ± 0.2
	10	2.9 ± 1.2	54.4 ± 0.4	5.4 ± 0.9	66.1 ± 0.5
	20	3.5 ± 0.7	70 ± 0.6	6.3 ± 0.6	81.6 ± 0.3
	40	4.5 ± 1.1	85.1 ± 0.2	7 ± 0.6	93.6 ± 0.4
	80	5.3 ± 0.9	98.8 ± 0.1	8.6 ± 0.3	98.8 ± 0.1

Based on the cytotoxicity of nanocomposites, IC_{50} value was determined which represents the concentration of drugs/ nanoparticles inhibiting 50% growth of cells. The IC_{50} values for MS2 and MS3 nanocomposites were calculated to be 498 µg/ml, 417 µg/ml after 24 hours and 403 µg/ml, 350 µg/ml after 48 hours of incubation respectively (Table 5-4). The IC_{50} values of MSICG nanocomposites and pure ICG were also calculated with and without laser irradiation at 24 and 48 hours of treatment (Table 5-5). The IC_{50} values for both MS2ICG and MS3ICG nanocomposites without laser irradiation (dark) was higher as compared to laser irradiation. The IC_{50} values were used as guided dose for further experiments on cellular uptake and endocytosis. Data were plotted as mean values ± SD of experiments performed in triplicate wells.

Table 5-4: IC_{50} values (µg/ml) of MS2 and MS3 after incubation for 24 hours and 48 hours without laser irradiation.

Samples	IC_{50} values (µg/ml)	
	24 hours	48 hours
MS2	498	403
MS3	417	350

Table 5-5: IC_{50} values (µg/ml) of MS2ICG and MS3ICG after incubation for 24 hours and 48 hours without laser irradiation.

Samples	IC_{50} values (µg/ml)			
	24 hours		48 hours	
	without laser	laser (808nm)	without laser	laser (808nm)
MS2ICG	488	207	393	142
MS3ICG	408	172	339	124
ICG	1080	16	744	9

5.2.4 Effect of AMF Only as an External Stimulus; a Combination of AMF and Laser Irradiation as Dual External Stimuli on Cell Viability: Trypan Blue Assay

The application of an AMF known as magnetic hyperthermia treatment allows localised heat generation due to superparamagnetism of IONPs to kill cancer cells. To perform magnetic hyperthermia treatment in MCF7 using MSICG nanocomposites, MCF7 cells grown on Petri dishes were treated with both MS2ICG and MS3ICG nanocomposites and placed in an AMF (15.8 kA/m, frequency- 406 kHz) for 45 minutes.

The trypan blue assay results for MS2ICG showed that the magnetic hyperthermia treatment (MS2ICG + AMF) significantly decreased the cell viability (* $p < 0.05$) (82 ± 2.6%) as compared to control (93.7 ± 3.1%) (Figure 5-5). The magnetic hyperthermia treatment along with laser irradiation (MS2ICG + AMF + laser) significantly decreased the cell viability (*** $p < 0.001$) (71.7 ± 4.7%) as compared to a control showing the efficiency of the combination of both hyperthermia treatment and laser irradiation. Furthermore, cell viability of cells treated with MS3ICG, MS3ICG + AMF and MS3ICG + AMF + laser showed significant differences (**** $p < 0.0001$) compared to control (Figure

5-5 B). There was significant difference (* $p < 0.05$) on the cell viability of MS3ICG along with AMF and laser (74 ± 1.7%) compared to MS3ICG + AMF (78 ± 1.7%) showing the significance of using dual therapy. Table 5-6 represents the cell viability (%) values for all experiments.

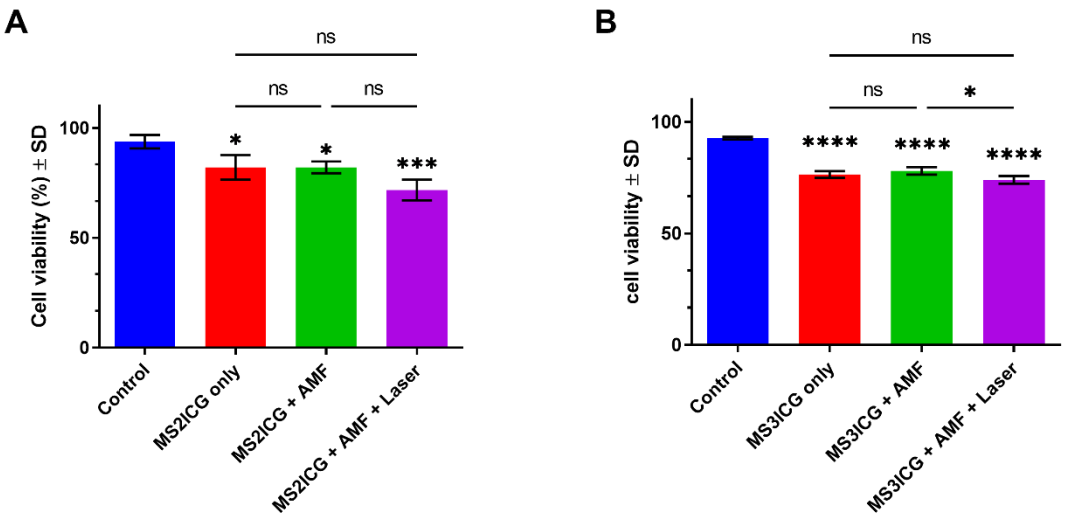

Figure 5-5: Cytotoxicity studies on MCF7 cell line treated with MS2ICG (A) and MS3ICG (B) at a concentration of 100 µg/ml, 24 hours post hyperthermia (single stimuli) or a combination of hyperthermia and laser irradiation (dual stimuli). The significant differences between treatments were calculated with one-way ANOVA (Tukey's multiple comparisons test). Data presented as mean ± SD with statistical significance represented as *$p < 0.05$, ***$p < 0.001$, ****$p < 0.0001$, ns: not significant.

Table 5-6: Effect of treatment of MSICG nanocomposites upon AMF only as an external stimulus; a combination of AMF and laser irradiation as dual external stimuli on cell viability (%) ± SD as shown by Trypan Blue assay

Samples condition	Cell viability (%) ± SD	Samples condition	Cell viability (%) ± SD
Control	93.7 ± 3.1	**Control**	92.7 ± 0.6
MS2ICG only	82 ± 5.6	**MS3ICG only**	76.3 ± 1.5
MS2ICG + AMF	82 ± 2.6	**MS3ICG + AMF**	78 ± 1.7
MS2ICG + AMF + Laser	71.7 ± 4.7	**MS3ICG + AMF + Laser**	74 ± 1.7

5.2.5 Photodynamic Therapy (PDT): Detection of ROS Generation by DCFDA Assay

The efficiency of PDT due to the generation of ROS upon laser irradiation (λ = 808 nm, power density = 1.2 W/cm^2) at various concentrations of both MSICG nanocomposites were tested after the incubation period of 24 hours on MCF7 cells. Cells without nanocomposites (negative control) and tert-butyl hydrogen peroxide (TBHP) solution (positive control) were used for comparison. Then, DCFDA (2′,7′-dichlorodihydrofluorescein diacetate) staining was performed to check the generation of

ROS. DCFDA is a fluorogenic dye that measures different ROS activity within the cell. After diffusion into the cells, DCFDA is deacetylated by cellular esterase into a non-fluorescent compound which gets oxidised (by the ROS generated inside the cells) into a highly fluorescent DCF (2', 7'- dichlorofluorescin). DCF can then be detected by fluorescence microscope (Excitation = 485 nm, Emission = 535 nm).

As shown in Figure 5-6, dose-dependent ROS generation was found on exposure of MS2ICG and MS3ICG nanocomposites. The ROS intensity increased with increase in concentration of nanocomposites; however, there was significant reduction in the fluorescent intensity in case of MS3ICG as compared to MS2ICG. Discrepancy in ROS production may be due to the types of nanocomposites and their influential interaction with oxidative stress regulatory proteins such as SOD (Verma *et al.*, 2021), which has been discussed later in Chapter 6. A negative control showed no fluorescence whereas incubation with THBP (100 µM) as positive control showed DCF fluorescence. Nanocomposites with ICG as well as pure ICG showed higher fluorescence intensity compared to positive control (THBP) suggesting that ICG is superior in generating ROS upon laser irradiation in MCF7 cells. The quantitative information of ROS generation using DCFDA in microplate reader has also been discussed later in Chapter 6.

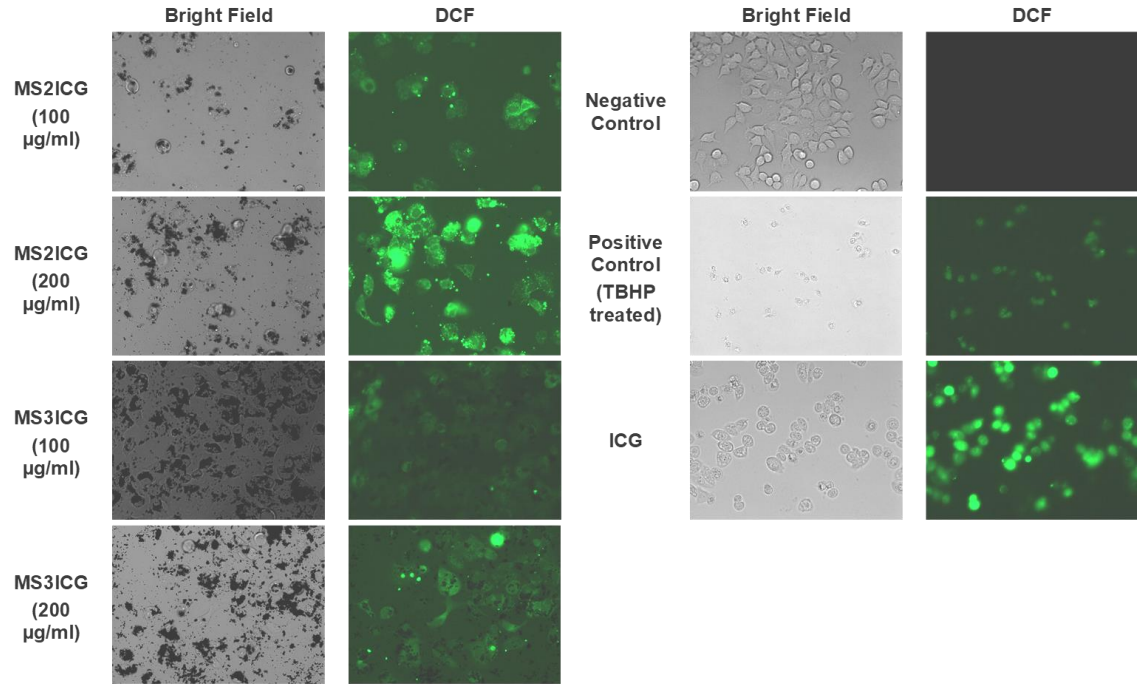

Figure 5-6: Intracellular reactive oxygen species (ROS) detection with DCFDA staining by fluorescence microscopy upon laser irradiation (808 nm, 1.2 W/cm^2). MCF7 cells were treated with MS2ICG (100 µg/ml, 200 µg/ml) or MS3ICG (100 µg/ml, 200 µg/ml). Negative control: no treatment, positive control: TBHP treated (100uM) and pure ICG (0.04 moles) were used for comparative study. (DCF: 2′,7′-dichlorofluorescein; TBHP: tert-butyl Hydrogen Peroxide)

5.2.6 Cellular Uptake Studies

Cellular uptake and accumulation of nanoparticles in target cells are the crucial parameters to achieve high therapeutic efficacy. The uptake of nanoparticles can be elevated by physicochemical characteristics of nanoparticles such as size, shape, surface charge, surface topography and surface functionalisation with bio-inspired molecules such as silica (Akinc and Battaglia, 2013; Almeida *et al.*, 2021). Different methods of cellular uptake were performed in this thesis to observe the accumulation and uptake of MSICG nanocomposites in MCF7 cells.

5.2.6.a Visual Representation of Cellular Uptake Using Scanning Electron Microscope (SEM)

SEM was used to visualise the cellular uptake of MS2ICG and MS3ICG nanocomposites using the procedure explained in Chapter 2, section 2.5.1. The internalisation of nanocomposites to the cells was clearly visible as shown with red arrows under different magnification in Figure 5-7. Cells without treatment were taken as negative control. The uptake of nanocomposites can be clearly differentiated compared to control.

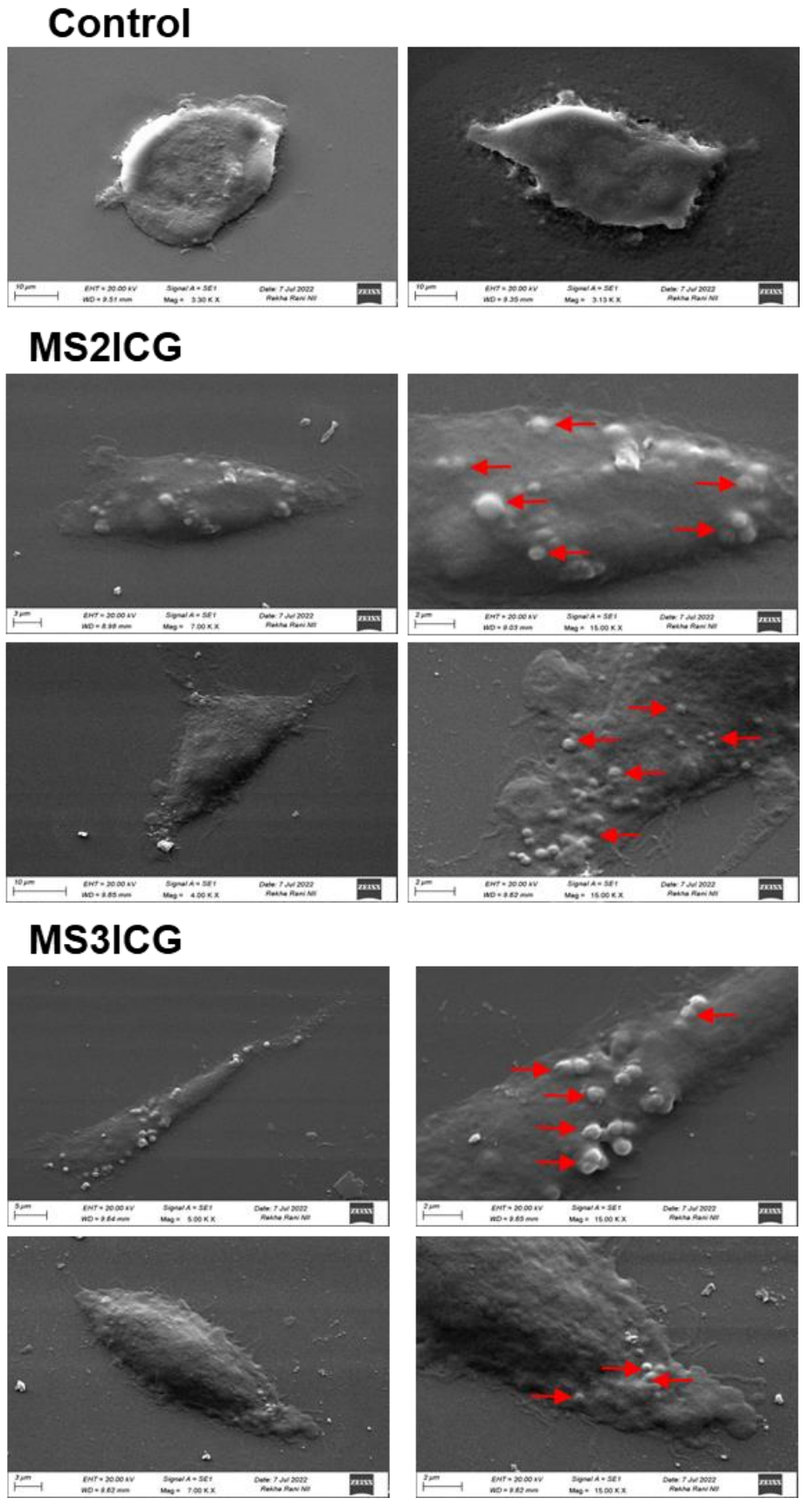

Figure 5-7: SEM micrographs of MCF7 cells after treatment with MS2ICG and MS3ICG nanocomposites at different magnification scales. Cells without treatment were taken as negative control. The red arrow indicates the internalised nanoparticles.

5.2.6.b Prussian Blue Staining

Cellular uptake study was carried out using Prussian blue staining on both MS2ICG and MS3ICG nanocomposites and the details methodology has been presented in Chapter 2, section 2.5.2. Both nanocomposites observed to be internalised or agglomerated around MCF7 cells, clearly visualised by the presence of blue granules in optical microscopy images (see Figure 5.8). The presence of blue granule is indicative of iron content in the cells upon reaction with potassium ferrocyanide (the iron staining solution). The control cells without nanocomposites showed no blue precipitate but only darker red colour showing nuclear stain as a comparison. Regardless of the internalisation of MSICG nanocomposites into MCF7 cells, they remained on their typical morphology without severe deformation compared to control cells, indicating the biocompatibility of MSICG nanocomposites at lower concentration of 100 µg/ml.

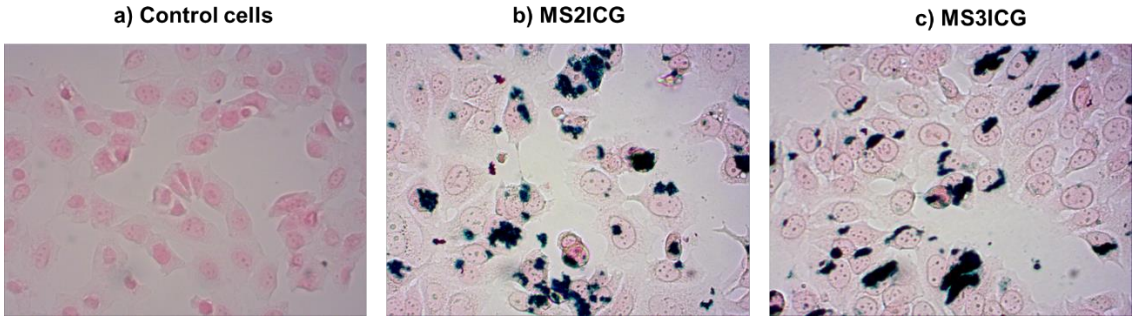

Figure 5-8: Phase contrast inverted microscope images of MCF7 cells stained with Prussian blue after treatment with MS2ICG (b) and MS3ICG (c) at the concentration of 200 µg/ml for 24 hours. Cells without treatment were taken as negative control (a).

5.2.6.c Qualitative and Quantitative Time Dependent Cellular Uptake Study

The time dependent cellular uptake study of MSICG nanocomposites was carried out using a confocal fluorescence microscope as described in the methodology section in Chapter 2, section 2.5.3. DAPI was used for staining the nucleus under excitation of 359 nm. The internalisation of MSICG nanocomposites into MCF cells was investigated by looking at the ICG signals on the near-infrared fluorescence channel (red; excitation at 633 nm; emission at 650–800 nm) as suggested by Lee *et al.* (2014). The methodology for time dependent cellular uptake study of MSICG on MCF7 cells using confocal microscopy is provided in Chapter 2, section 2.5.3.

Figures 5-9 A and B shows internalisation of MSICG nanocomposites after incubation for 2 and 4 hours, respectively. Visualisation of cells using confocal microscopy demonstrated the fluorescence of ICG (red colour), illustrating high internalisation of nanocomposites inside the cells. The colour intensity after 4 hours of treatment is observed to be stronger compared to 2 hours treatment. The uptake of

MS2ICG and MS3ICG nanocomposites in MCF7 cells was significantly less as observed by relative fluorescence intensity (**** $p < 0.0001$) when incubated for 2 hours. Therefore, 4 hours treatment is better than 2 hours treatment for cellular internalisation indicating the time dependent effect.

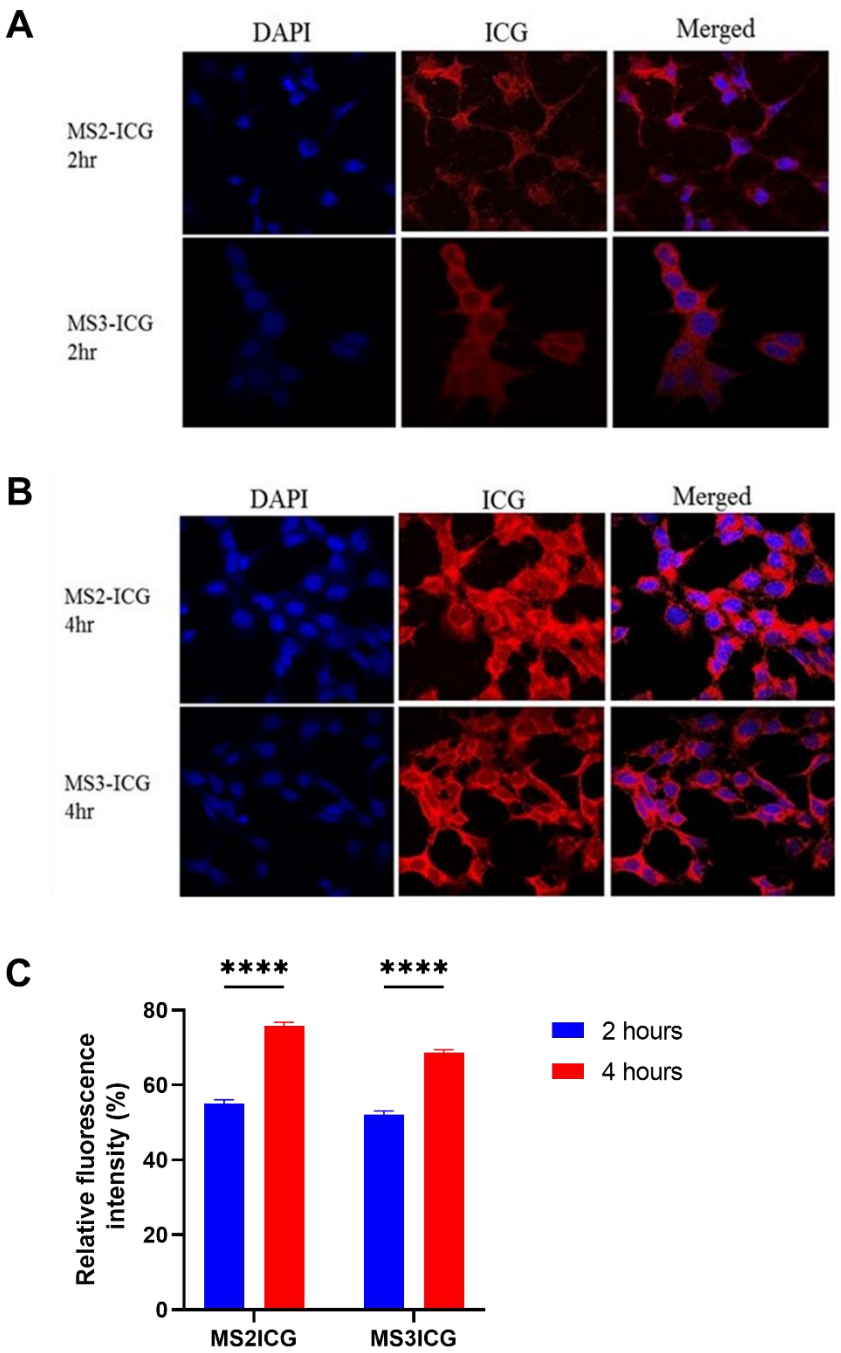

Figure 5-9: Intracellular localisation of MS2ICG and MS3ICG in MCF7 cells after incubation for 2 hours (A) and 4 hours (B). The florescence intensities of DAPI (blue) and ICG (red) were measured at a magnification scale of 60× through confocal microscope under excitation at 359 nm and 633 nm, respectively. C: A bar chart showing a comparison of two different nanocomposites at 2 separate times of treatment with significant difference of **** $p < 0.0001$. Data is presented as mean ± SD (n = 3).

5.2.7 Cellular Uptake Pathway Studies Using Endocytic Inhibitors

In order to characterise the endocytosis mechanism for the internalisation of MSICG nanocomposites inside the cells, endocytosis inhibitors were used to perturb their entry. In general, the inhibitors that affect specific endocytic pathways were used to elucidate particular pathways, potentially involved during the internalisation of nanoparticles. The experimental procedure to perform endocytosis is explained in Chapter 2, section 2.6. The inhibitory effects produced by the inhibitors on nanoparticles during cellular uptake were imaged and compared without inhibitors (control). Table 5-7 provides information about the concentration of various inhibitors used along with their functions.

Table 5-7: Inhibitors with their concentration and functions

Inhibitor	**Concentration**	**Function**
Low temperature	4 ℃	Represent the amount of external binding
Sucrose	0.45 M	Non-selective clathrin endocytosis inhibition
Sodium azide	0.1% w/v	Macropinocytosis, active transport inhibitor
Lovastatin	10 µg/ml	Blocks the caveolar and lipid rafts mediated endocytosis *via* cholesterol depletion

5.2.7.a Low Temperature

Low temperature primarily decreases the cell metabolism. The low temperature can inhibit the internalisation of nanoparticles without influencing the external binding at the surface of the cell. Therefore, the cellular uptake at 4 ℃ may depict the amount of external binding. The uptake of MS2ICG and MS3ICG in MCF7 cells lowered by around 44% as observed by low florescence intensity within cells (Figure 5-10 A, Figure 5-10 B; lower panel) and a bar graph showing low relative florescence intensity (**** $p < 0.0001$) (Figure 5-10 C) when incubated at 4 ℃ compared to control at 37 ℃. The lower florescence at 4 ℃ indirectly proves that nanocomposites were not just agglomerated around the cells but was internalised inside the cells at standard incubation experiments.

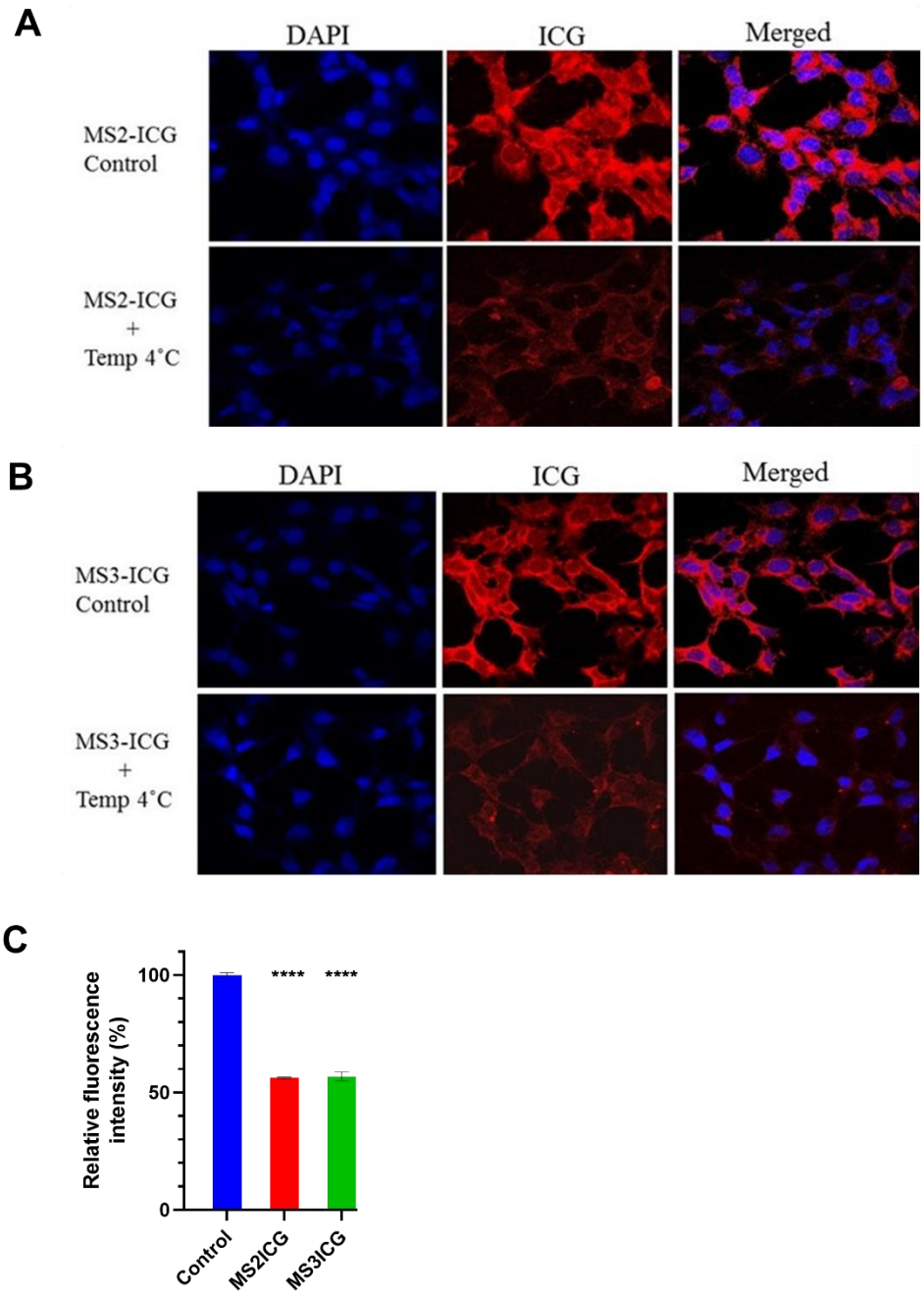

Figure 5-10: Low temperature (at 4 ℃) vs control experiment (at 37 ℃) on the internalisation of MS2ICG (A) and MS3ICG (B) as measured by confocal microscopy (60x). C: A bar graph is based on the calculation of relative florescence intensity of control (at 37 ℃) as 100% with significant difference of ****$p < 0.0001$. Data is presented as mean ± SD (n = 3).

5.2.7.b Sodium Azide

Sodium azide is used as a micropinocytosis and active transport inhibitor. Sodium azide inhibits oxidative phosphorylation by inhibiting cytochrome oxidase, enzyme in the mitochondrial electron transport chain, resulting in a rapid depletion of intracellular ATP (Kim *et al.*, 2006). The reduction in uptake of nanoparticles upon treatment with sodium azide is indicator of energy-dependent cellular uptake pathway. The qualitative and

quantitative uptake of MS2ICG and MS3ICG in MCF7 cells was significantly low as observed by low florescence intensity within cells (Figure 5-11 A, Figure 5-11 B) when incubated with sodium azide compared to a control experiment without the addition of sodium azide. The relative florescence intensity was significantly low (*** $p < 0.001$, **** $p < 0.0001$) in both nanocomposites as compared to control as shown in Figure 5-11 C. The low cellular uptake of MSICG nanocomposites in the presence of sodium azide indicates that the uptake was most likely an energy-dependent process.

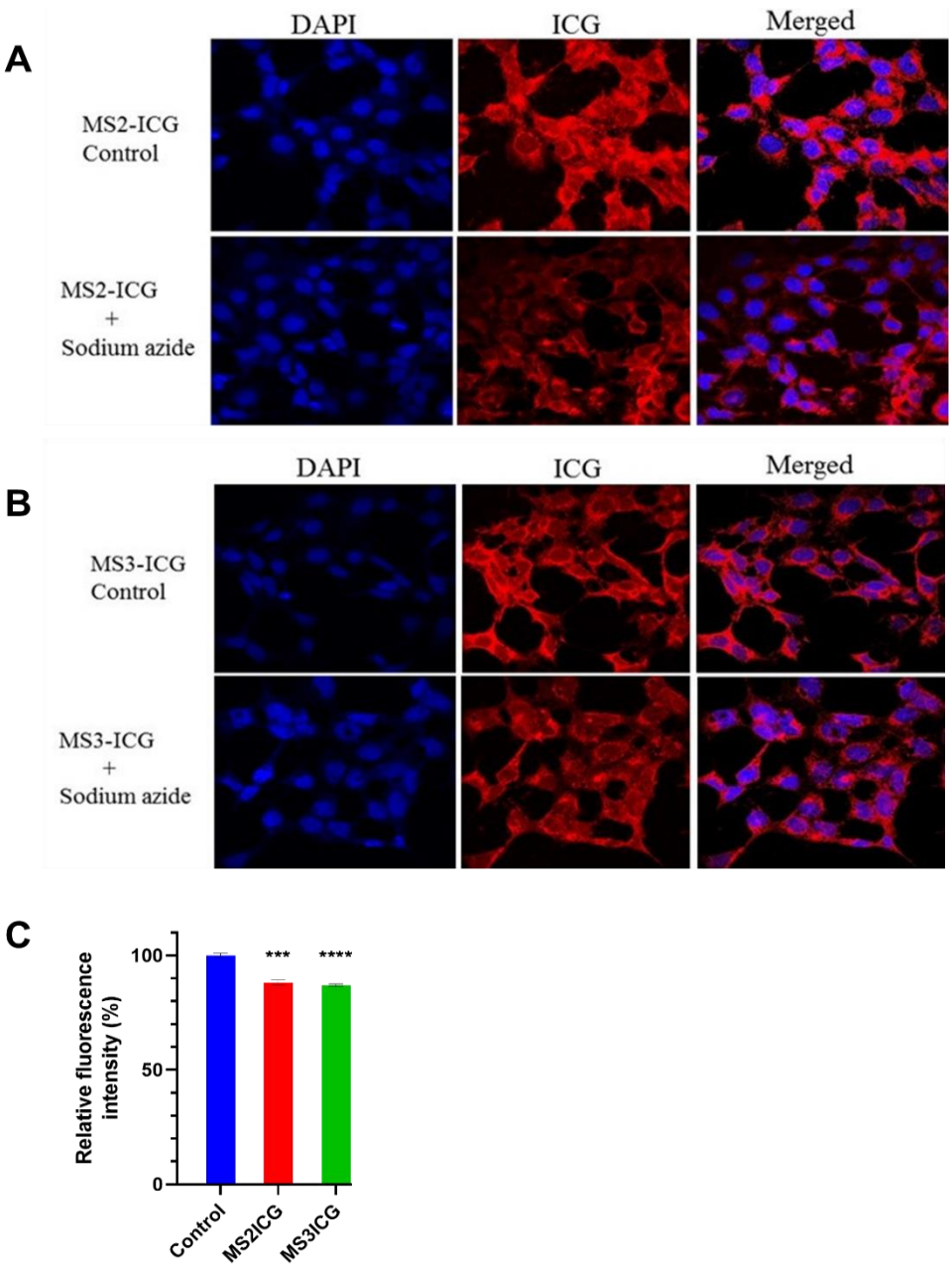

Figure 5-11: Effect of sodium azide (0.1% w/v) on the internalisation of MS2ICG (A) and MS3ICG (B) by confocal microscopy (60x). C: A bar chart presented as a comparison based on the calculation of relative florescence intensity of control (no inhibitor) as 100% with significant difference of ***$p < 0.001$, ****$p < 0.0001$. Data is presented as mean ± SD (n = 3).

5.2.7.c Lovastatin

Lovastatin blocks the caveolar and lipid raft mediated endocytosis *via* cholesterol depletion. It suggests that in the presence of lovastatin, the caveolar or lipid raft mediated uptake is reduced. On pre-treatment with lovastatin at a concentration of 10 µg/ml, the uptake of MS2ICG and MS3ICG in MCF7 cells was significantly reduced as observed by low florescence intensity within cells (85 ± 1.3% and 86.8 ± 0.2%, respectively) when compared to a control experiment without lovastatin (Figure 5-12 A, Figure 5-12 B). The relative florescence intensity was significantly low (**** $p < 0.0001$) for both MS2ICG and MS3ICG nanocomposites when incubated with Lovastatin as compared to the control, as shown in Figure 5-12 C. Thus, low uptake of nanocomposites indicated that the mechanism of cellular uptake of MSICG nanocomposites could likely be due to the caveolar mediated endocytosis.

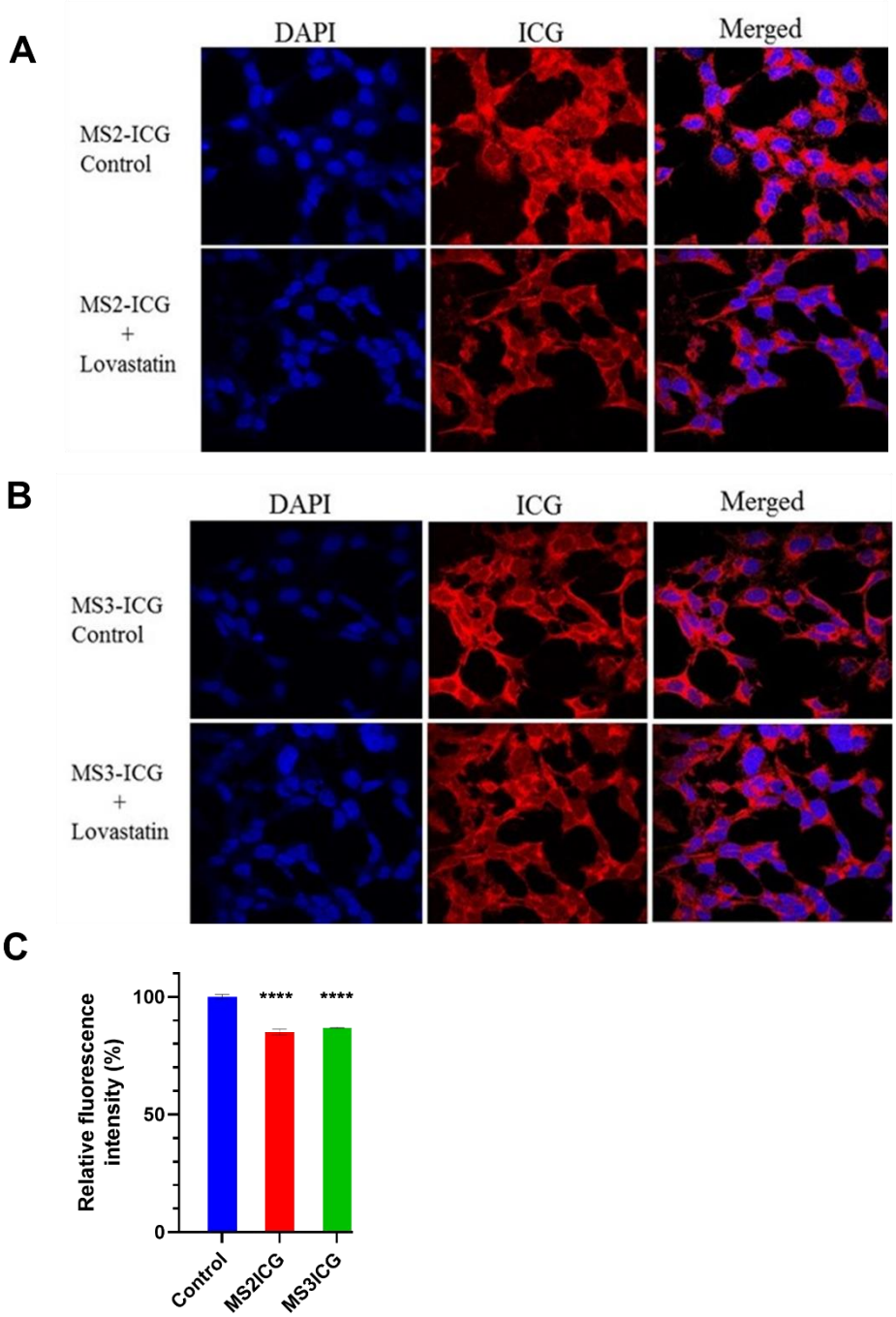

Figure 5-12: Effect of lovastatin (10µg/ml) on the internalisation of MS2ICG (A) and MS3ICG (B) by confocal microscopy (60x). C: A bar chart presented as a comparison based on the calculation of relative florescence intensity of control (no inhibitor) as 100% with significant difference of ****$p < 0.0001$. Data is presented as mean ± SD (n = 3).

5.2.7.d Sucrose

Sucrose is a non-selective clathrin endocytosis inhibitor. Exposing the cells to a hypotonic media with sucrose has been reported to be responsible for non-selectively blocking the fluid-phase endocytosis. Fluid-phase endocytosis also termed pinocytosis is a process by which cells uptake fluid along with any dissolved small molecules from

their surroundings. After the cells were treated with sucrose, a significant reduction in cellular uptake was observed based on the intensity of the colour as compared to the controls (Figure 5-13 A, Figure 5-13 B). The uptake of MS2ICG and MS3ICG nanocomposites significantly reduced (84.2 ± 0.6% and 81.2 ± 0.8%, respectively) when compared to control (Figure 5-13 C). Thus, the low uptake of both MSICG nanocomposites by MCF7 cells is indicative of dependence on the fluid-phase endocytosis/ clathrin endocytosis.

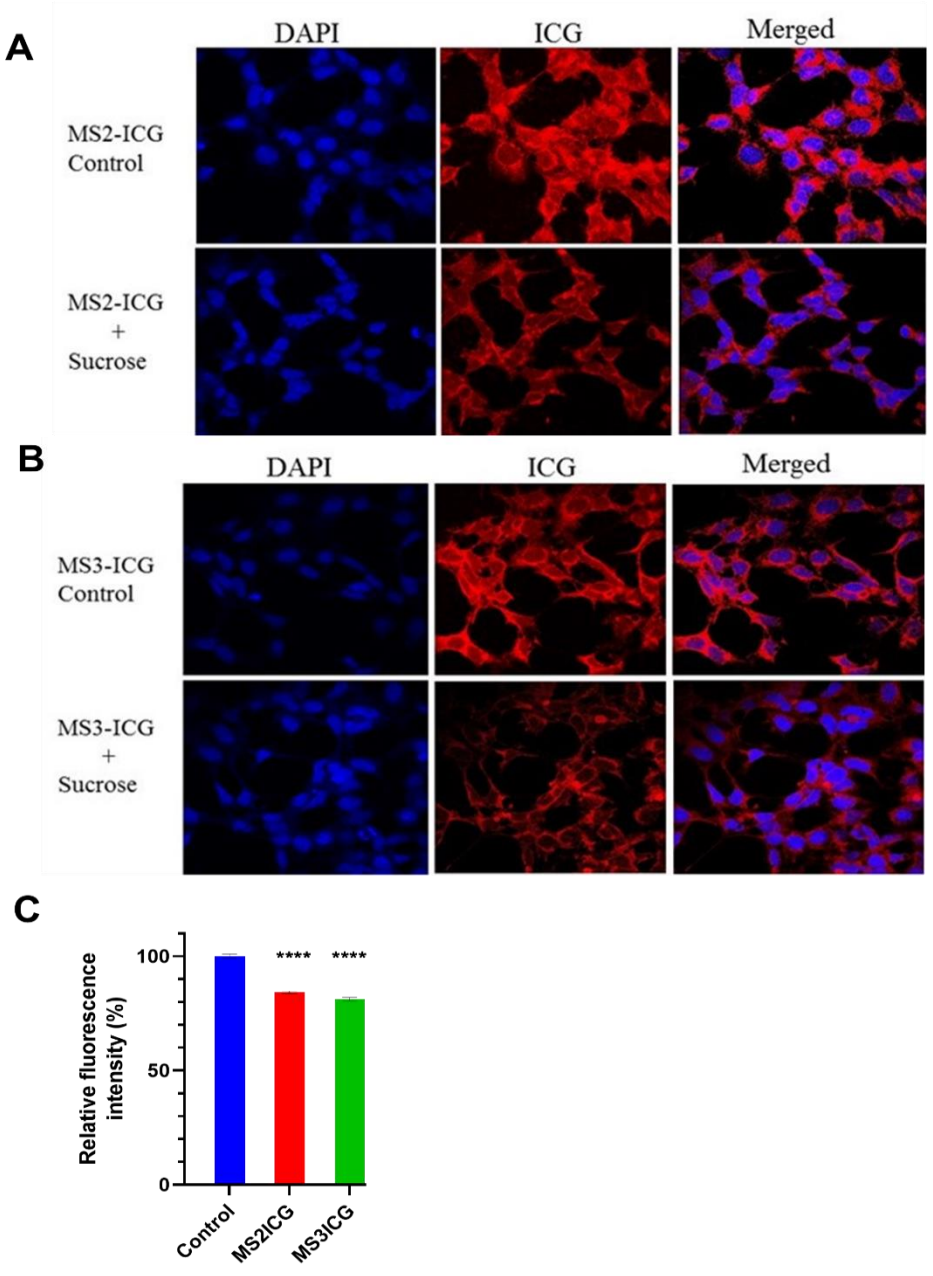

Figure 5-13: Effect of sucrose (0.45M) on the internalisation of MS2ICG (A) and MS3ICG (B) by confocal microscopy (60x). C: A bar chart presented as a comparison based on the calculation of relative florescence intensity of control (no inhibitor) as 100% with significant difference of ****$p < 0.0001$. Data is presented as mean ± SD (n = 3).

Collectively, cellular internalisation of MSICG nanocomposites was observed to follow multiple internalisation pathways. The results illustrate that the cellular uptake of both MS2ICG and MS3ICG is an active energy-dependent endocytosis process as demonstrated from decreased uptake of nanocomposites in low temperature showing higher effect (Table 5-8). In addition, clathrin-mediated endocytosis (sucrose inhibition) is found to be the general internalisation pathway for the MSICGs in MCF7 cells. However, caveolae/lipid rafts (Lovastatin inhibition) and micropinocytosis (sodium azide) also contributed to nanocomposites uptake in cells. In conclusion, all three pathways such as clathrin mediated, caveolae mediated and micropinocytosis were equally involved in the internalisation of both MSICG nanocomposites with significant difference of **** $p < 0.0001$ as shown in Figure 5-14.

Table 5-8: Inhibitor treatment outcome after incubation with MS2ICG and MS3ICG in MCF7 cells compared to untreated control cells (100%).

Inhibitor	**MS2ICG**	**MS3ICG**	**Effect**
Temperature	56.1 ± 0.38	56.9 ± 1.90	+++
Sucrose	84.2 ± 0.58	81.2 ± 0.79	++
Lovastatin	85 ± 1.26	86.8 ± 0.24	+
Sodium Azide	88.2 ± 1.14	86.9 ± 0.56	+

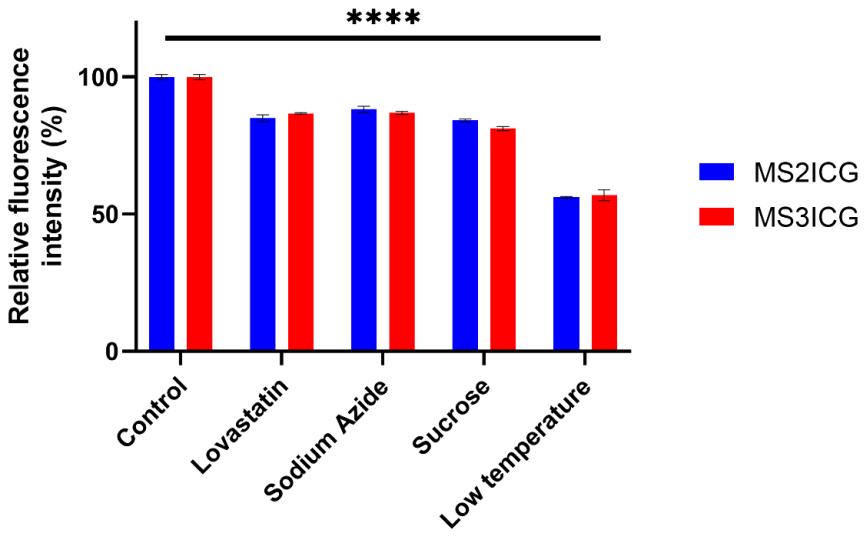

Figure 5-14: Determination of endocytosis pathways following treatment of MCF7 cells with various inhibitors. A bar chart displaying significant difference in relative fluorescence intensity upon treatment with inhibitors (**** $p < 0.0001$). Data is presented as mean ± SD (n = 3).

5.2.8 Haemolysis Assay

The *ex-vivo* biocompatibility study of MS nanocomposites with/without ICG were performed on whole mouse blood cells at two different time points (2 and 4 hours) as explained earlier in Chapter 2, section 2.12. For assessing the haemolytic activity of nanocomposites MS2, MS2ICG, MS3 and MS3ICG, and pure ICG, the optimum concentrations used based on predetermined IC_{50} values. Triton X was used as a positive and PBS as a negative control. As shown in Figure 5-15, around 5% haemolysis was detected in all experimental groups post 2 hours showing the biocompatibility with red blood cells. The percentage haemolysis is low compared to the positive control at both 2- and 4-hours interval however, it is significantly higher than the negative control (PBS alone). The toxicity (above 5% haemolysis) of nanocomposites was observed for experiments involved with 4 hours of incubation for all MS and MSICG nanocomposites.

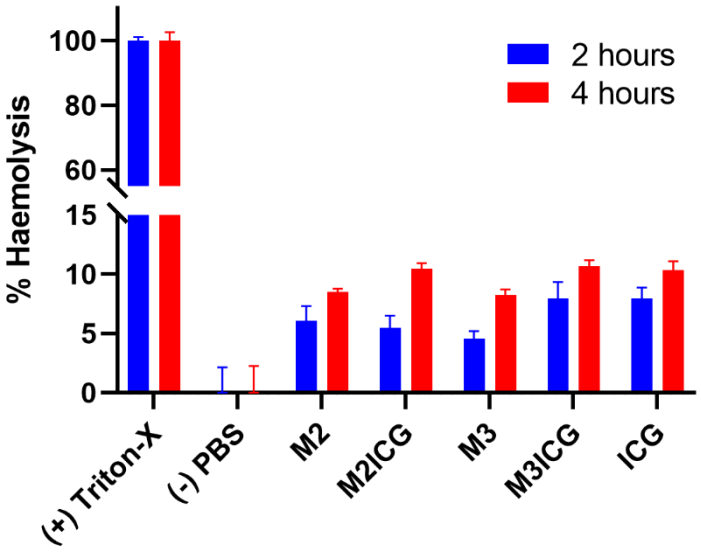

Figure 5-15: Ex-vivo haemolysis activity of MS2, MS3, M2ICG, M3ICG and ICG in 2 h and 4 h. Triton X was used as a positive control, PBS only was taken as a negative control.

5.3 Conclusion

The study on safety of nanomaterials is essential for clinical application and *in-vitro* viability or toxicity studies are performed as preliminary safety assessments. Two magneto-optical nanocomposites (hydrophilic core: MS2ICG and hydrophobic core: MS3ICG) were tested for their biocompatibility and cancer therapeutic efficiency *in-vitro* using commercial MCF7 cells The physiochemical properties of nanoparticles play critical role in determining the fate of nanoparticles inside the cells. However, both nanocomposites exhibited similar biocompatibility in spite of differences in their physiochemical properties. The cell viability (%) upon treatment with nanocomposites

showed both dose and time dependent toxicity. Similarly, the MCF7 cells showed toxicity above the concentration of 100 µg/ml. The cellular toxicity could be attributed to the presence of both IONPs and silica shell which can induce ROS in the cells. Additionally, the trace amount of CTAB present in the nanocomposites can induce toxicity in cells. The *ex-vivo* haemolysis assay was performed to test the biocompatibility of nanocomposites. Less than 5% cytotoxicity is considered safe for clinical application. The results showed their biocompatibility within 24 hours of incubation and a slight toxicity at 48 hours when compared with a control experiment.

The cellular toxicity under laser irradiation for 5 minutes showed cytotoxicity of both nanocomposites being dose (50, 100, 200 and 400 µg/ml) and time (24 and 48 hours) dependent. The cellular toxicity increased 3 folds after laser irradiation demonstrating their efficient therapeutic effect. Furthermore, MHT therapy was performed on MCF7 cells followed by the laser irradiation as dual therapies and monitored by trypan blue assay. The cellular viability (%) of MCF7 cells upon treatment with MS2ICG under an AMF significantly decreased (82 ± 2.6%) compared to a control (93.7 ± 3.1%) experiment. Additional laser irradiation treatment decreased the cell viability to 71.7 ± 4.7%. Likewise, the MS3ICG nanocomposites showed equivalent results, decreasing the cell viability to 74 ± 1.7%, thus proving to be effective as dual therapeutic agents. However, the cell viability upon AMF alone did not show any significant difference when compared to control, suggesting AMF alone was not effective for cancer cells killing efficiency.

To test whether the MSICG nanocomposites could be internalised inside cells through passive targeting, the uptake of MSICG nanocomposites by MCF7 cells was tested using different imaging techniques. SEM images of cells upon treatment with nanocomposites clearly showed their uptake as compared to control without the presence of nanoparticles. Prussian blue assay also confirmed the increase in iron content inside the cells with accumulation of nanocomposites around the cells. Finally, the confocal microscopy, depending upon the fluorescence activity of ICG at excitation of 633 nm, showed internalisation of nanocomposites as time dependent process. The internalisation pathways of nanocomposites were tested using endocytic inhibitors. An active energy-dependent endocytosis process was highly effective for internalisation of nanocomposites followed by clathrin-mediated endocytosis. The results showed that the internalisation of both MS2ICG and MS3ICG occurred through multiple internalisation pathways.

CHAPTER 6

MAGNETO-OPTICAL NANOCOMPOSITES INDUCED OXIDATIVE STRESS AND ASSESSMENT OF REGULATED CELL DEATH PATHWAYS UPON LASER IRRADIATION *IN-VITRO*

6.1 Introduction

The main objective of my PhD thesis is to apply dual therapy using novel magneto-optical nanocomposites by introducing optical probe (i.e., ICG in this case) in magnetic silica nanocomposites (MS) which can significantly increase therapeutic efficiency in cancer cells upon laser irradiation (λ= 808 nm, power density = 1.2 W/cm^2) as shown earlier in Chapter 5. ROS generation influencing the PDT and localised heating on PTT have been discussed earlier in Chapters 4 and 5. To further investigate the cytotoxic effect due to oxidative stress and cell death pathways due to the treatment with magneto-optical nanocomposites by laser irradiation, different biochemical assays and gene expression studies were performed which have been systematically presented in this chapter.

It has been reported that ROS levels in cancer cells are already elevated as compared to normal cells, reflecting a disruption of redox homeostasis, either due to elevated ROS production or decline of ROS-scavenging capacity (Trachootham, Alexandre and Huang, 2009; Ciccarese *et al.*, 2020). The increase of ROS up to certain threshold level exerts cytotoxic effect, leading to the death of malignant cells. The study of change in the biochemical properties exerted by nanoparticles can provide an insight in their therapeutic efficacy. A range of *in-vitro* cellular integrity markers, ROS generation markers along with antioxidant enzyme activity assays have been performed for the determination of therapeutic performance of MSICG nanocomposites, as shown in Figure 6-1 with the brief discussion of each.

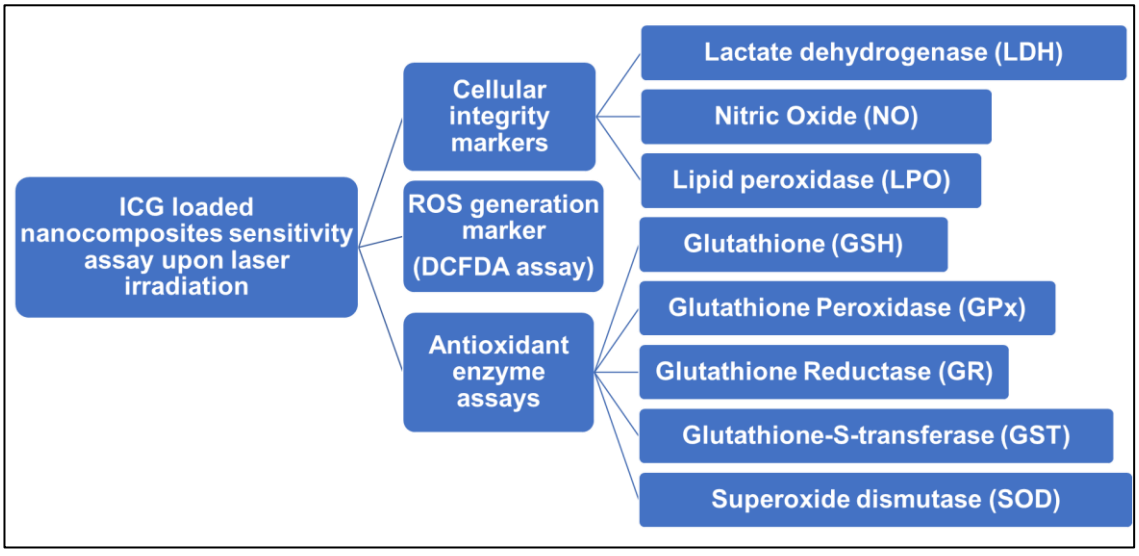

Figure 6-1: Biochemical assays to test ROS generation and inter-related pathways *in-vitro.*

6.1.1 *In-Vitro* Cellular Integrity Markers

Cellular membrane integrity is adversely affected due to modification of lipids and proteins in response to the oxidative stress (Noeman, Hamooda and Baalash, 2011). The release of enzymes or lipids *in-vitro* following cellular damage can be studied by different biochemical assays such as lactate dehydrogenase (LDH), nitric oxide (NO) and lipid peroxidation (LPO) which have been discussed in brief.

6.1.1.a Lactase Dehydrogenase Release Assay (LDH Assay)

LDH is a cytoplasmic enzyme that is found in all cells and is involved in interconversion of (i) pyruvate to L-lactate and (ii) NADH to NAD^+ during glycolysis (Decker and Lohmann-Matthes, 1988). In response to cellular damage, it is released from the cytoplasm into the extracellular environment. LDH release is a marker for cell membrane damage, one of the key features of cells undergoing apoptosis, ferroptosis, necrosis or other forms of cellular damage (Kumar, Nagarajan and Uchil, 2018). The release of LDH is biochemically analysed by observing the decrease of NADH level which gets converted to NAD^+ upon reaction with sodium pyruvate as shown in the following reaction scheme. The change in absorbance is measured at 340 nm.

$$\text{Pyruvate} + \text{NADH} + H^+ \xrightarrow{\text{D-LDH}} \text{D-Lactate} + NAD^+$$

6.1.1.b Nitric Oxide Assay (NO Assay)

NO-induced toxicity has been linked to cell death involving inhibition of DNA synthesis, damage to mitochondria and loss of cell membrane integrity leading to regulated cell death (RCD) such as apoptosis (Burney *et al.*, 1997). NO has been found to react with superoxide anion ($O_2^{-\cdot}$) to yield peroxynitrite ($ONOO^-$) which can cause cell death. NO assay is performed based on the principle of a diazotization reaction known as Griess reaction. The chemical reaction between Griess reagent 1 (sulphanilamide) and Griess reagent 2 (N-1-napthylethylenediamine dihydrochloride, NEDD) under acidic conditions (orthophosphoric acid – 88% purity) with nitric oxides results in the formation of an azo chromophores (Abs- 540 nm) as shown in Figure 6-2.

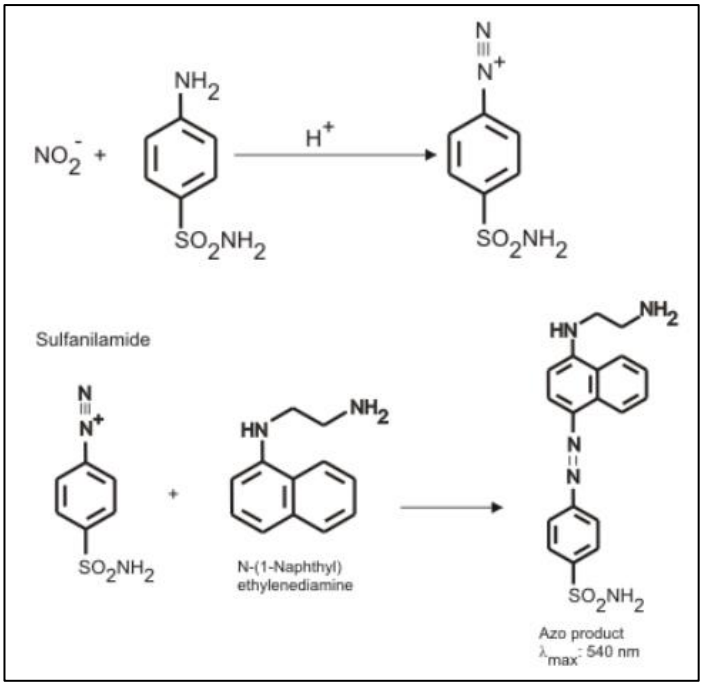

Figure 6-2: Griess reaction for determination of nitrate. Reproduced from Held,(2010)

6.1.1.c Lipid Peroxidation Assay (LPO Assay)

LPO is another indicator for free radical formation and degradation of cell membrane. The LPO assay also used for understanding ROS-mediated cellular toxicity, hypothesised to affect ferroptosis pathway (Latunde-Dada, 2017). Upon generation of ROS, the peroxidation of polyunsaturated fatty acids (PUFAs) of cell membrane, an unstable form, results in the formation of malondialdehyde (MDA) which when reacted with thiobarbituric acid (TBA) under acidic condition at 90-100 ℃ forms an MDA-TBA adduct (Figure 6-3). This pink/red coloured product can be analysed using spectrophotometry at an absorbance of 535nm.

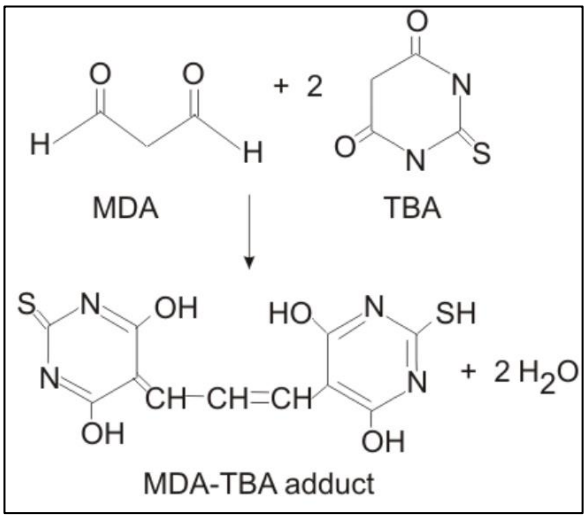

Figure 6-3: Reaction between MDA and TBA forming MDA-TBA adduct. Reproduced from Held, (2010)

6.1.2 Quantification of ROS Species (DCFDA Assay)

A range of ROS such as hydrogen peroxide (H_2O_2), hydroxyl radicals (OH^-), and peroxyl radicals (ROO^-) can be measured directly by staining with 2′,7′-dichlorodihydrofluorescein diacetate (DCFDA). DCFDA gets hydrolysed by intracellular esterase to DCFH in cells which reacts with ROS species (such as H_2O_2) generating the fluorescent 2′,7′-dichlorofluorescein (DCF) (Held, 2010). The amount of ROS species produced by cells is thus quantitatively measured by the fluorescence intensity of DCF ($\lambda_{excitation}$= 488 nm and $\lambda_{emission}$= 530 nm) as analysed on a microplate reader. The higher the fluorescence intensity, is the greater the amount of ROS in the cells.

6.1.3 Antioxidant Enzyme Assays

6.1.3.a Reduced Glutathione

Free glutathione (GSH) exists in cells as reduced GSH (r-GSH) or oxidized GSH (GSSG) forms. The r-GSH form is primarily maintained in cells by glutathione reductase (GR) in the presence of NADPH (Held, 2010). Glutathione (GSH) plays a critical role in metabolic protective functions and is responsible for scavenging free radicals, ROS and RNS directly or indirectly through enzymatic reactions, however, is compromised in case of cancer cells upon oxidative stress. Because of low levels of GSH, the ROS level inside the cells increases leading to cellular damage. GSH reacts with 5,5'-dithiobis (2-nitrobenzoic acid) (DTNB) to form a coloured compound called 2-nitro-5-thiobenzoic acid (TNB) which can be measured by spectrophotometry (Absorbance = 412 nm).

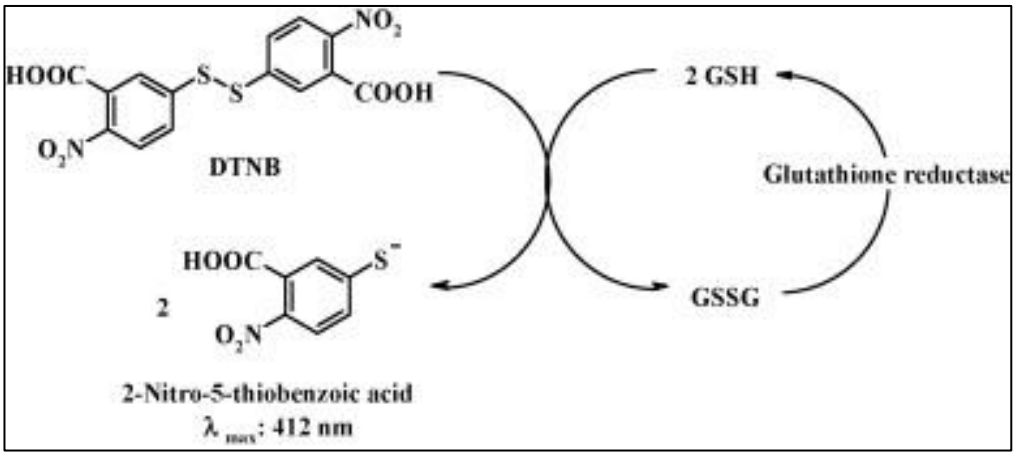

Figure 6-4: Total glutathione quantification. Reproduced from Araujo, Saraiva and Lima, (2008)

6.1.3.b Glutathione Peroxidase (Gpx Assay)

Glutathione Peroxidase (GPx) is a glycoprotein that protects cells from oxidative damage by catalysing the reduction of H_2O_2 to water and lipid hydroperoxides (ROOH) to alcohol and water (Figure 6-5) (Held, 2010). In the presence of ROS, reduced GSH (r-GSH) is converted to oxidised form of GSH (GSSG) by GPx while GSSG is converted

to r-GSH by GR in the presence of NADPH (Figure 6-5) (Brittanie *et al.*, 2018). The reduction in GPx is a marker for oxidative stress in cells as well as marker for ferroptosis-cell death pathway (Latunde-Dada, 2017). This assay indirectly evaluates the activity of GPx by measuring the oxidation of NADPH to $NADP^+$ by monitoring the change in absorbance at 340 nm. The rate of decrease in absorbance is directly proportional to the decreased GPx activity in the sample.

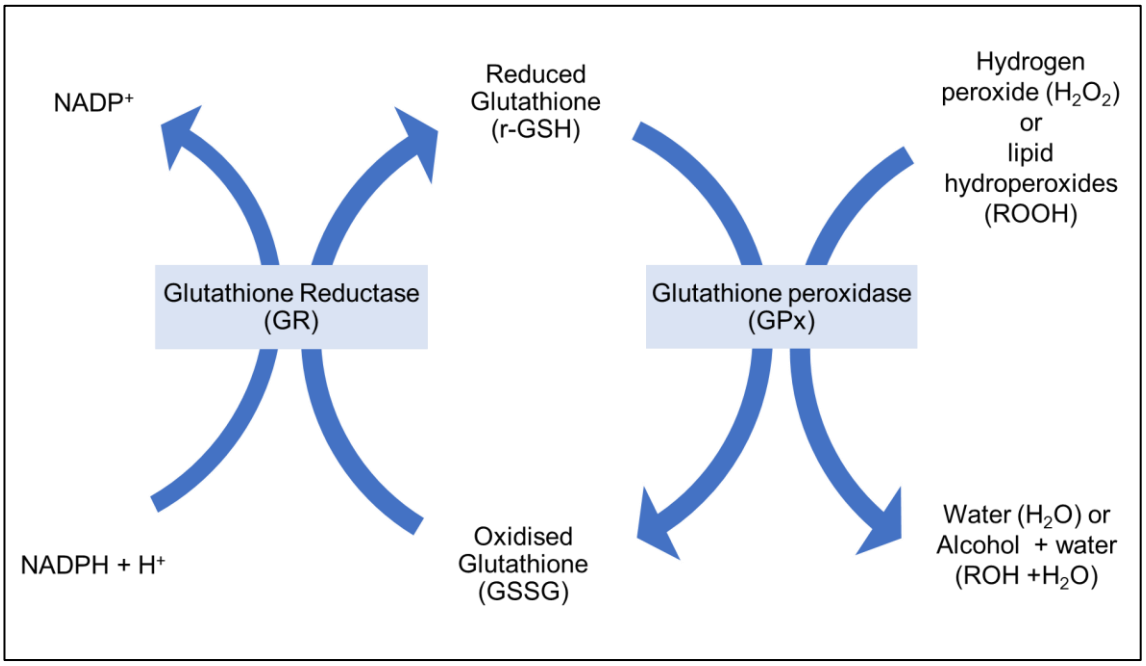

Figure 6-5: Glutathione redox reaction. Lamichhane *et al.* (under preparation).

6.1.3.c Glutathione Reductase (GR Assay)

Glutathione reductase (GR) is a NADPH-dependent oxidoreductase enzyme that catalyses the reduction of oxidized GSH (GSSG) to reduced GSH (GSH) as shown earlier in Figure 6-5. GR maintains adequate levels of reduced cellular GSH *via* maintaining high ratio of GSH/GSSG (Doroshow, 1995). In oxidative stress, the level of GR is reduced which could be measured by decreased NADPH absorbance at 340 nm.

6.1.3.d Glutathione-S-Transferase (GST Assay)

Glutathione-S-transferase (GST) is involved in detoxification of peroxides. The extent of reaction can be measured by quantifying the conjugation of 1-chloro-2,4-dinitrobenzene (CDNB) with reduced glutathione (GSH) (Tsuchida and Yamada, 2014). The rate of increase of absorbance at 340 nm is directly proportional to the GST activity in cells.

6.1.3.e Superoxide Dismutase (SOD Assay)

Superoxide dismutase (SOD) is responsible for clearing highly reactive superoxide ($\bullet O_2^-$) from cells by dismutation into oxygen or peroxides. SOD acts as a first line of defence against free radicals and indicate oxidative stress in cells (Held, 2010). The reaction of $\bullet O_2^-$ with nitroblue tetrazolium (NBT) and a mixture of NADH and phenozonium methosulphate (PMS) results in reduction of NBT to blue formazan at pH 8 (Folgueira *et al.*, 2019) and can be measured spectrophotometrically at 560 nm. The reduction in blue colour indicates the enzymatic activation.

6.1.4 Iron Assay

The iron oxide nanoparticles after entering into cells through different endocytic pathways are transported into endosomes *via* endosomal-lysosomal pathways (Mazuel *et al.*, 2016). The iron-based nanoparticles get degraded into subsequent iron ions (Fe^{3+} is reduced to Fe^{2+}) in the endosomes and released into a labile iron pool (LIP) in the cytoplasm. Extra iron (Fe^{3+}) is stored in ferritin, an iron storage protein complex, which upon higher iron uptake, releases excess iron ions, generating highly reactive hydroxyl radicals *via* the Fenton reaction (explained earlier in Chapter 1.4.2). In this context, the precise role of iron in RCD such as ferroptosis remains unclear, however, it has been reported that Fenton reaction is important for iron-based ferroptosis to happen (Shen *et al.*, 2018).

6.2 Result and Discussion

6.2.1 *In-Vitro* Cellular Integrity Markers

The effectiveness of MSICG nanocomposites in degrading cellular membranes by altering antioxidant enzyme activity by the application of an external stimuli (laser irradiation) was studied extensively through different biochemical assays.

6.2.1.a Lactase Dehydrogenase Release Assay (LDH Release Assay)

LDH release assay was performed on MCF7 cells upon treatment of MS (MS2, MS3) or MSICG (MS2ICG, MS3ICG) nanocomposites with or without laser irradiation. There was a significant increase in LDH level in cells when treated with nanocomposites upon laser irradiation as shown in Figure 6-6 A. No significant difference was observed in control cells with/without laser irradiation suggesting the laser irradiation did not damage normal cells without the treatment with nanocomposites. A significant increase in LDH was observed in both MS2ICG and MS3ICG nanocomposites upon laser irradiation (61.03 ± 0.85 nM/ml/mg, 58.77 ± 1.10 nM/ml/mg) when compared to release without laser irradiation (27.16 ± 1.22 nM/ml/mg, 28.44 nM/ml/mg), respectively. Higher LDH level in cells treated with pure ICG with laser irradiation demonstrates the

importance of using ICG for PTT and PDT effect. Similarly, cells treated with MS nanocomposites without the presence of ICG show relatively lower LDH release and a small enhancement upon laser irradiation. Figure 6-6 B represents a comparative plot of nanocomposites induced LDH release upon laser irradiation with negative control. MSICG nanocomposites released the highest LDH compared to pure ICG or MS nanocomposites. Similarly, treatment with nanocomposites containing ICG (MSICG) or pure ICG exhibited higher LDH release upon laser irradiation compared to control experiment indicating an additional stress, thus increasing cytotoxicity in cancer cells.

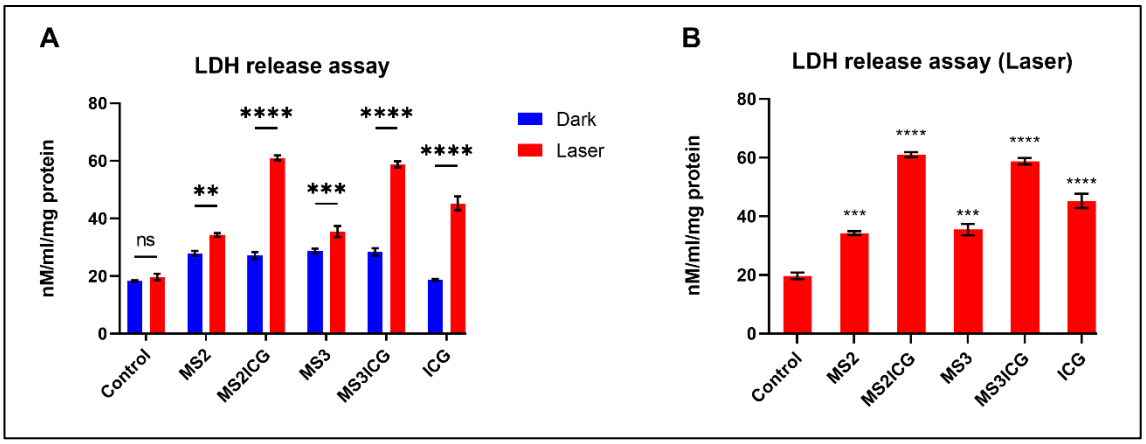

Figure 6-6: Lactase dehydrogenase (LDH) release activity in supernatant of MCF7 cells treated with MS (MS2, MS3), MSICG nanocomposites (MS2ICG, MS3ICG) and pure ICG with/without laser irradiation. A: Bar plot comparing LDH release with/without laser irradiation, B: Bar plot comparing LDH release upon laser irradiation with control to show the efficiency of PDT / PTT effect. All data were analysed by GraphPad Prism, shown as mean ± SD (Standard Deviation) of 3 replicates in each group. The significant differences are indicated with asterisks (** P < 0.01; *** P < 0.001, **** P < 0.0001, ns- not significant)

6.2.1.b Nitric Oxide Assay (NO Assay)

The NO activity in MCF7 cells was detected and quantified to evaluate the generation of nitrogen radicals upon treatment with nanocomposites. MCF7 cells treated with both MS2ICG and MS3ICG nanocomposites upon laser irradiation showed significant increase in NO activity compared to cells without laser irradiation (Figure 6-7 A). No significant difference was observed in control cells and cells treated with MS nanocomposites with/without laser irradiation suggesting no laser toxicity in absence of ICG nanocomposites. The role of pure ICG and ICG loaded in nanocomposites (MSICG) for creating PTT/PDT effects upon laser irradiation can be easily compared with control and MS nanocomposites. All four nanocomposites (MS1, MS2, MS1ICG and MS2ICG) showed similar NO release values in the absence of laser irradiation, however, a significant increase is observed for MSICG nanocomposites compared to MS nanocomposites upon laser irradiation (see red bars in figure 6-7). Similarly, pure ICG upon laser irradiation showed significant increase (****p < 0.0001) in NO activity suggesting the role of ICG in generating NO radicals in cells. The cells treated with

nanocomposites and pure ICG when compared to control cells showed significant increase in NO activity upon laser irradiation (Figure 6-7 B).

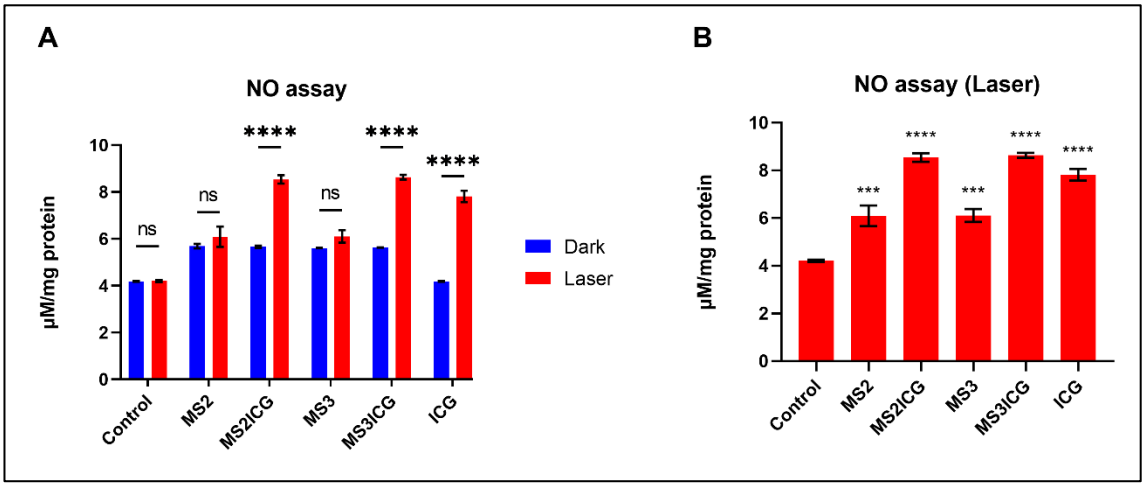

Figure 6-7: Estimation of Nitric oxide (NO) levels in supernatant of MCF7 cells treated with MS (MS2, MS3), and MSICG nanocomposites (MS2ICG, MS3ICG) and pure ICG with/without laser irradiation. A: Bar plot comparing NO levels with/without laser irradiation, B: Bar plot comparing NO levels upon laser irradiation with control to show the efficiency of PDT / PTT effect. All data were analysed by GraphPad Prism, shown as mean ± SD (Standard Deviation) of 3 replicates in each group. The significant differences are indicated with asterisks (*** $P < 0.001$, **** $P < 0.0001$, ns- not significant)

6.2.1.c Lipid Peroxidation Assay (LPO Assay)

LPO assay was performed to evaluate the treatment efficacy in generating ROS-mediated cellular toxicity, hypothesised to affect ferroptosis pathway. A significant increase in LPO activity ($p < 0.0001$) was observed in cells treated with MS2ICG and MS3ICG upon laser irradiation (52.86 ± 2.54 µM/min/mg, 51.68 ± 1.05 µM/min/mg) when compared to treatment without laser irradiation (23.16 ± 1.24 µM/min/mg, 23.10 ± 0.06 µM/min/mg), respectively (Figure 6-8 A). No significant difference was observed in control cells with/without laser irradiation suggesting laser irradiation was safe in absence of ICG nanocomposites. The significant increase in LPO level in ICG as a pure and loaded nanocomposites (MSICG) implies their role in creating PTT/PDT effects upon laser irradiation when compared with control and MS nanocomposites. All four nanocomposites (MS1, MS2, MS1ICG and MS2ICG) showed similar LPO level in the absence of laser irradiation, however, a significant increase is observed for MSICG nanocomposites compared to MS nanocomposites upon laser irradiation (see red bars in Figure 6-8). Similarly, pure ICG upon laser irradiation showed significant increase (****$p < 0.0001$) in LPO level suggesting the role of ICG degrading lipids to induce lipid peroxidation upon laser irradiation. The cells treated with MS nanocomposites when compared to control cells showed significant increase in LPO activity demonstrating their cytotoxic effect upon laser irradiation (Figure 6-8 B).

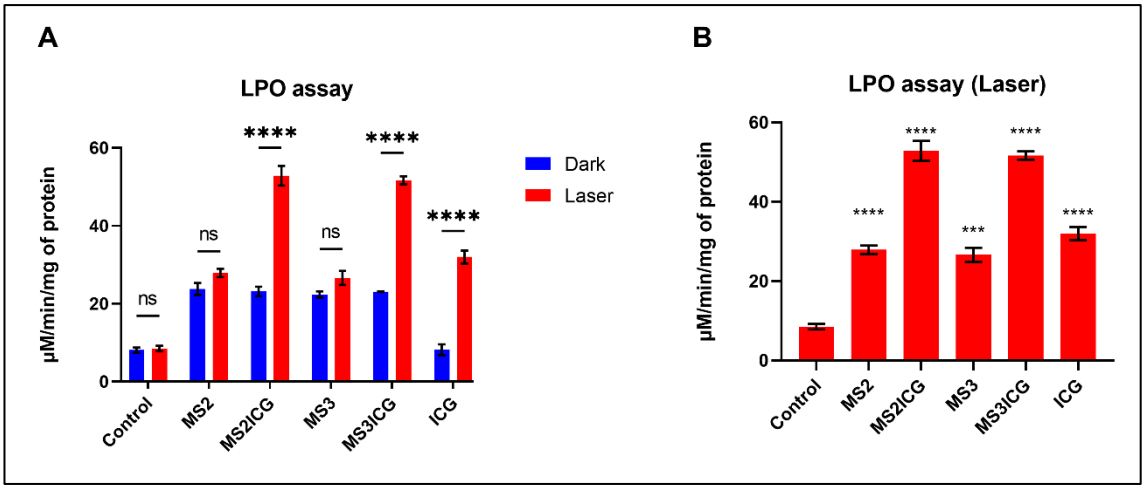

Figure 6-8: Lipid peroxidation (LPO) activity in MCF7 cells treated with MS (MS2, MS3), MSICG nanocomposites (MS2ICG, MS3ICG) and pure ICG with/without laser irradiation. A: Bar plot comparing LPO activity with/without laser irradiation, B: Bar plot comparing LPO activity upon laser irradiation with control to show the efficiency of PDT / PTT effect. All data were analysed by GraphPad Prism, shown as mean ± SD (Standard Deviation) of 3 replicates in each group. The significant differences are indicated with asterisks (*** $P < 0.001$, **** $P < 0.0001$, ns- not significant)

6.2.2 Quantification of ROS Species (DCFDA Assay)

Earlier in Chapter 5 section 5.2.3, the presence of ROS was qualitatively observed through fluorescence microscope using DCFDA assay in MCF7 cells treated with nanocomposites with laser irradiation. Herein, the DCFDA assay was performed and measured using spectrofluorometer to quantitatively identify and evaluate the generation of ROS in MCF7 cells with/without laser irradiation as explained in Chapter 2, section 2.8 and Chapter 6, section 6.1.2. Control experiment with/without laser irradiation shows no significant difference (dark: 249.33 ± 3.4, laser: 279.33 ± 2.05) in ROS production suggesting no cytotoxicity of laser irradiation alone. The graph shows significant increase in fluorescence intensity in cells treated with MS and MSICG nanocomposites upon laser irradiation (MS2: 528.67 ± 10.78 a.u., MS3: 521.67 ± 5.56 a.u., MS2ICG: 718.67 ± 14.61 a.u., MS3ICG: 693.67 ± 13.12 a.u.) compared to treated cells without laser irradiation (MS2: 445.67 ± 12.5 a.u., MS3: 449.33 ± 9.03 a.u., MS2ICG: 450.33 ± 13.27 a.u., MS3ICG: 450.67 ± 4.64 a.u.) indicating ROS generation upon laser irradiation with higher PDT/ PTT effect (Figure 6-9 A). It was also found that in dark (without laser irradiation) MS and MSICG nanocomposites produce ROS as compared to control. This indicates the inherent cytotoxic effect of magnetic and silica component in the nanocomposites. Significant increase of ROS generation due to the treatment with MSICG nanocomposites upon laser irradiation when compared to control ($p < 0.0001$) (Figure 6-9 B) is similar to earlier observation qualitatively presented in Chapter 5, Figure 5.6.

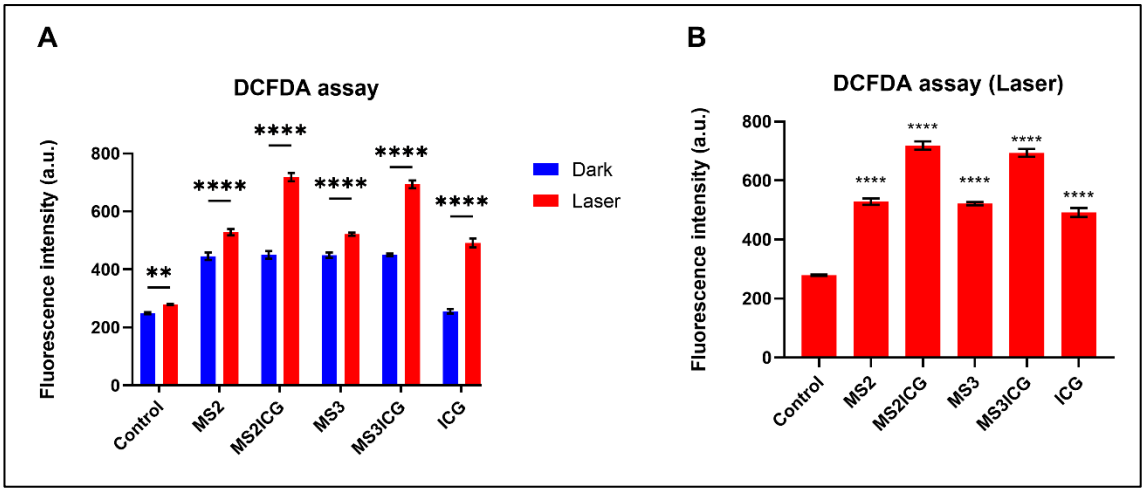

Figure 6-9: Quantitative estimation of ROS generation on MCF7 cells when treated with MS (MS2, MS3) and MSICG nanocomposites (MS2ICG, MS3ICG) and pure ICG with/without laser irradiation *via* fluorescent spectrofluorometer. A: Bar plot comparing DCF fluorescence with/without laser irradiation, B: Bar plot comparing DCF fluorescence upon laser irradiation with control to show the efficiency of PDT / PTT effect. All data were analysed by GraphPad Prism, shown as mean ± SD (Standard Deviation) of 3 replicates in each group. The significant differences are indicated with asterisks (** P < 0.01, **** P < 0.0001)

6.2.3 Antioxidant Enzyme Assays

6.2.3.a Reduced Glutathione

MCF7 cells treated with MS2ICG and MS3ICG nanocomposites upon laser irradiation showed significant decrease in GSH activity (2.15 ± 0.06 nM/ml/mg, 2.16 ± 0.18 nM/ml/mg, respectively) compared to cells without laser irradiation (4.13 ± 0.01 nM/ml/mg, 4.1 ± 0.12 nM/ml/mg, respectively) (Figure 6-10 A). Similarly, a reduction in GSH activity was observed when pure ICG was used under laser irradiation (3.13 ± 0.08 nM/ml/mg) compared to cells without laser irradiation (4.6 ± 0.03 nM/ml/mg). When compared to control cells upon laser irradiation, GSH level was significantly reduced in all treated cells (Figure 6-10 B). However, higher significant difference ($p < 0.0001$) was observed in both MSICG nanocomposites confirming that the loaded ICG in nanocomposites upon laser irradiation efficiently reduce GSH level. This suggests the presence of oxidative stress in MSICG treated cells due to laser irradiation.

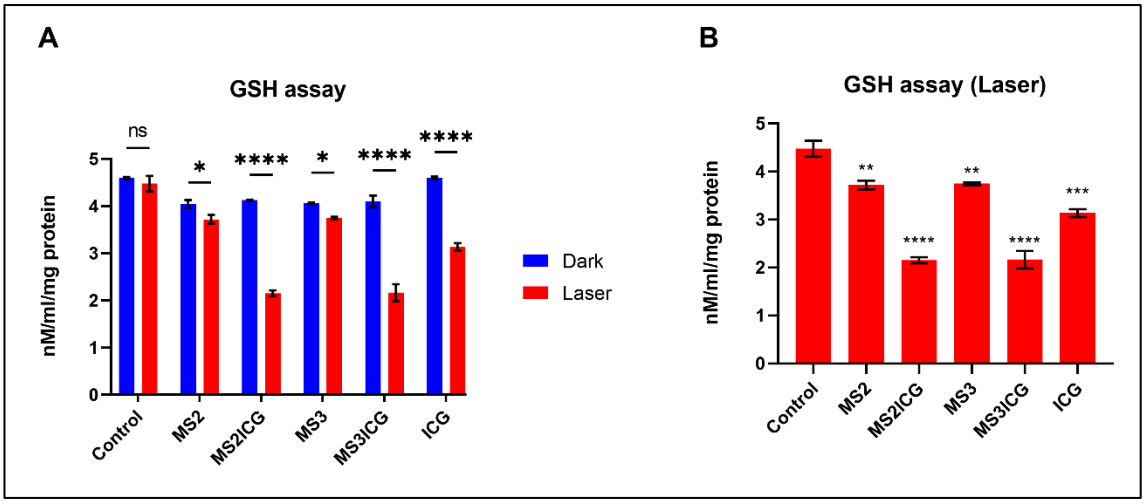

Figure 6-10: Antioxidant reduced glutathione (GSH) level in cytosolic traction of MCF7 cells treated with MS (MS2, MS3), MSICG nanocomposites (MS2ICG, MS3ICG) and pure ICG with/without laser irradiation *via* fluorescent spectrofluorometer. A: Bar plot comparing GSH level with/without laser irradiation, B: Bar plot comparing GSH level upon laser irradiation with control to show the efficiency of PDT / PTT effect. All data were analysed by GraphPad Prism, shown as mean ± SD (Standard Deviation) of 3 replicates in each group. The significant differences are indicated with asterisks (* P < 0.05, ** P < 0.01, ***P < 0.001, **** P < 0.0001)

6.2.3.b Glutathione Peroxidase (Gpx Assay)

Glutathione peroxidase (GPx) metabolises H_2O_2, phospholipid hydroperoxides and fatty acid hydroperoxide in mammalian cells and reduce the cytotoxic effect (Doroshow, 1995). The reduction of GPx indicates the presence of oxidative stress in the cells. The generation of ROS reduces the GSH level which in turn reduces the GPx thus leading to lipid peroxidation (An *et al.*, 2019). MCF7 cells treated with MS2ICG and MS3ICG nanocomposites upon laser irradiation showed significant decrease in GPx activity (60.66 ± 0.91 nM/min/mg, 60.07 ± 1.72 nM/min/mg, respectively) ($p < 0.0001$) compared to cells without laser irradiation (77.39 ± 0.35 nM/min/mg, 76.03 ± 0.35 nM/min/mg) (Figure 6-11 A). The decrease in GPx was observed in cells treated with ICG and laser irradiation (72.76 ± 1.51 nM/min/mg) compared to dark (93.47 ± 0.34 nM/min/mg). However, there was no significant difference in GPx on cells treated with both MS2 and MS3 nanocomposites upon laser irradiation (MS2: 75.92 ± 0.5 nM/min/mg, MS3: 75.81 ± 0.56 nM/min/mg) compared to dark (MS2: 76.2 ± 1.15 nM/min/mg, MS3: 75.98 ± 1.31 nM/min/mg). It could be confirmed that the presence of ICG and laser irradiation reduced the GPx activity, increasing the oxidative stress in the cells. When compared to control cells upon laser irradiation, GSH level was significantly reduced in cells treated with nanocomposites (see Figure 6-10 B). This suggests the presence of oxidative stress in cells due to the treatment with nanocomposites loaded with ICG and pure ICG due to the laser irradiation.

The ferroptosis pathway of cell death is accompanied by the inactivation of the function of GPx, specifically GPx4 leading to depletion of PUFAs in lipid bilayers and

accumulation of lipid ROS (Yang *et al.*, 2014; Hao *et al.*, 2018). The GPx assay has been utilised to study the ferroptosis pathway of cell death (Yang *et al.*, 2014). A reduction in GPx level in MCF7 cells when treated with MSICG and laser irradiation supports the presence of ferroptosis cell death pathway.

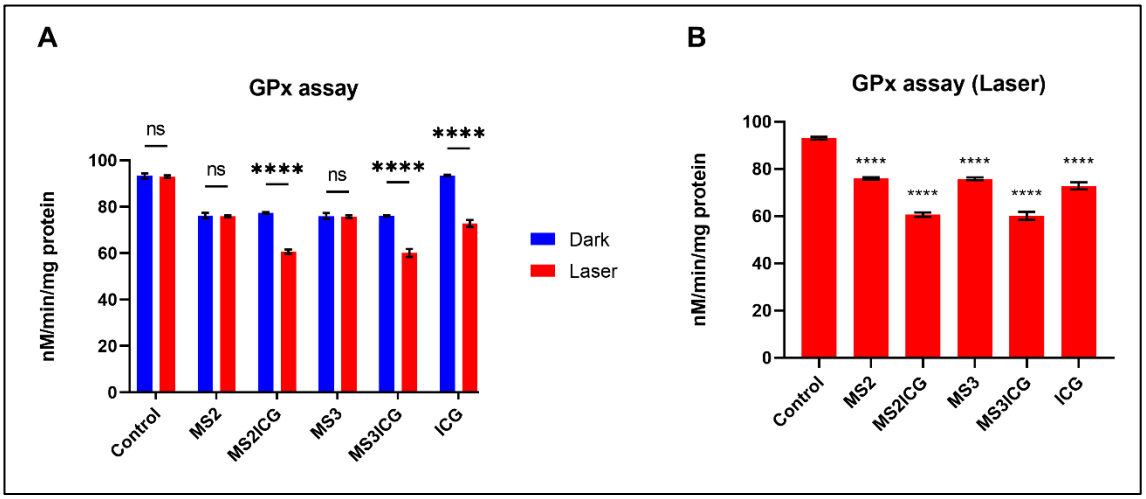

Figure 6-11: Glutathione peroxidase (GPx) activity in cytosolic fractions of MCF7 cells treated with MS (MS2, MS3), MSICG nanocomposites (MS2ICG, MS3ICG) and pure ICG with/without laser irradiation *via* fluorescent spectrofluorometer. A: Bar plot comparing GPx level with/without laser irradiation, B: Bar plot comparing GPx level upon laser irradiation with control to show the efficiency of PDT / PTT effect. All data were analysed by GraphPad Prism, shown as mean ± SD (Standard Deviation) of 3 replicates in each group. The significant differences are indicated with asterisks (**** P < 0.0001, ns- not significant)

6.2.3.c Glutathione Reductase (GR Assay)

Glutathione Reductase (GR) is involved in maintaining the levels of GSH and GSSG thus having antioxidant effect. Reduction of GR in cells is indicative of the oxidative stress in the cells. MSICG nanocomposites and pure ICG upon laser irradiation showed highly significant difference ($p < 0.0001$) in GR (MS2ICG: 53.39 ± 1.56 nM/min/mg, MS3ICG: 52.73 ± 1.1 nM/min/mg, ICG: 60.85 ± 1.04 nM/min/mg) compared to the ones without laser irradiation (MS2ICG: 65.08 ± 0.23 nM/min/mg, MS3ICG: 64.68 ± 0.39 nM/min/mg, ICG: 73.35 ± 0.23 nM/min/mg) (Figure 6-12 A). Figure 6-12 B shows the reduction in GR levels upon treatment with nanocomposites and laser. Both MSICG nanocomposites are superior in decreasing GR thus generating ROS compared to MS nanocomposites (MS2: 66.96 ± 0.76 nM/min/mg, MS3: 67.17 ± 0.73 nM/min/mg), pure ICG (60.85 ± 1.04 nM/min/mg) and control (76.6 ± 0.06 nM/min/mg) upon laser irradiation.

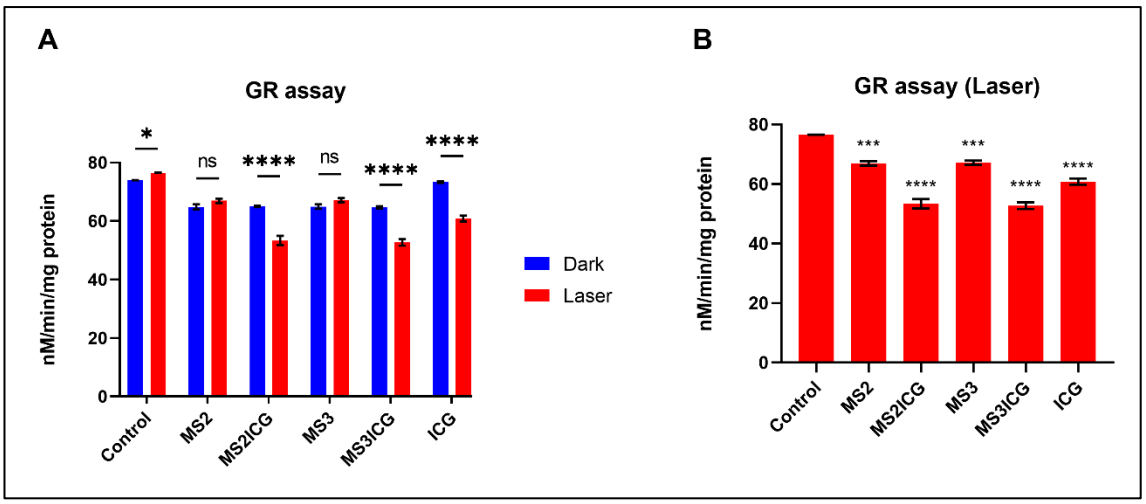

Figure 6-12: Glutathione Reductase (GR) activity in cytosolic fraction of cells treated with MS (MS2, MS3) and MSICG nanocomposites (MS2ICG, MS3ICG) and pure ICG with/without laser irradiation *via* fluorescent spectrofluorometer. A: Bar plot comparing GR activity with/without laser irradiation, B: Bar plot comparing GR activity upon laser irradiation with control to show the efficiency of PDT / PTT effect. All data were analysed by GraphPad Prism, shown as mean ± SD (Standard Deviation) of 3 replicates in each group. The significant differences are indicated with asterisks (* P < 0.05, ***P < 0.001, **** P < 0.0001, ns- not significant)

6.2.3.d Glutathione-S-Transferase (GST Assay)

Glutathione-S-transferase (GST) level was studied upon treatment of nanocomposites and laser. No significant differences were observed in the cells upon treatment with nanocomposites or pure ICG (see Figure 6-13). However, the mean GST values indicate decrease in GST levels in cells treated with both MS2ICG and MS3ICG nanocomposites (5 ± 1.88 and 5.2 ± 2.92 nM cDNB conjugated/min/mg) upon laser irradiation when compared to control (11.39 ± 1.01 nM cDNB conjugated/min/mg).

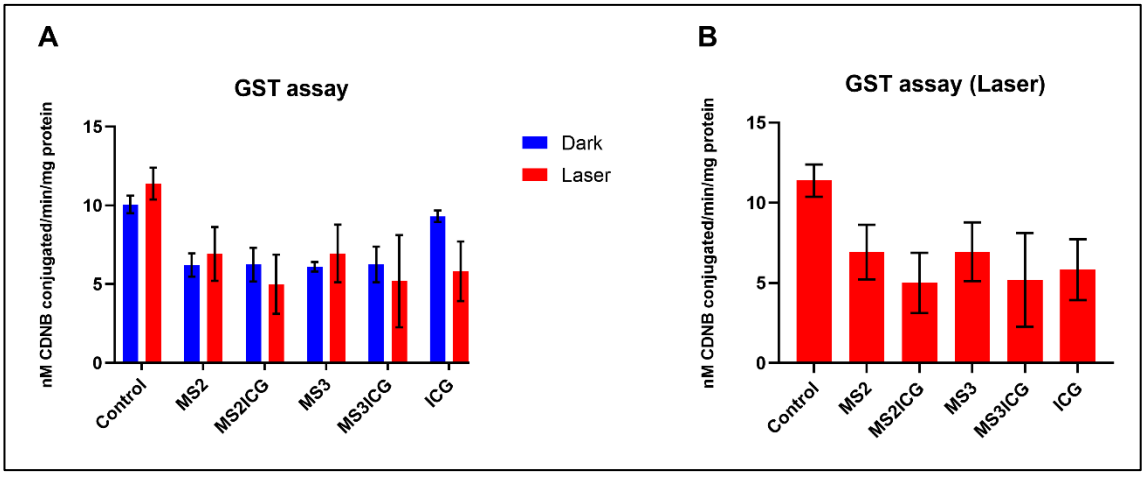

Figure 6-13: Glutathione-S-transference (GST) activity in cytosolic fractions of MCF7 cells treated with MS (MS2, MS3), MSICG nanocomposites (MS2ICG, MS3ICG) and pure ICG with/without laser irradiation *via* fluorescent spectrofluorometer. A: Bar plot comparing GST activity with/without laser irradiation, B: Bar plot comparing GST activity upon laser irradiation with control to show the efficiency of PDT / PTT effect. All data were analysed by GraphPad Prism, shown as mean ± SD (Standard Deviation) of 3 replicates in each group. No significant difference was observed.

6.2.3.e Superoxide Dismutase (SOD Assay)

Superoxide dismutase (SOD) activity was studied with/without laser irradiation upon treatment of different nanocomposites. A significant increase in SOD level was observed in cells upon treatment of MS2ICG and MS3ICG compared to cells without laser irradiation. However, no significant difference was observed in cells when compared to control and MS nanocomposites (Figure 6-14). A reasonable increase in mean SOD values could be seen in cells when treated with MS2ICG (0.55 ± 0.07 ng/mg protein) and MS3ICG (0.56 ± 0.08 ng/mg protein) nanocomposites compared to control (0.42 ± 0.05 ng/mg protein) upon laser irradiation.

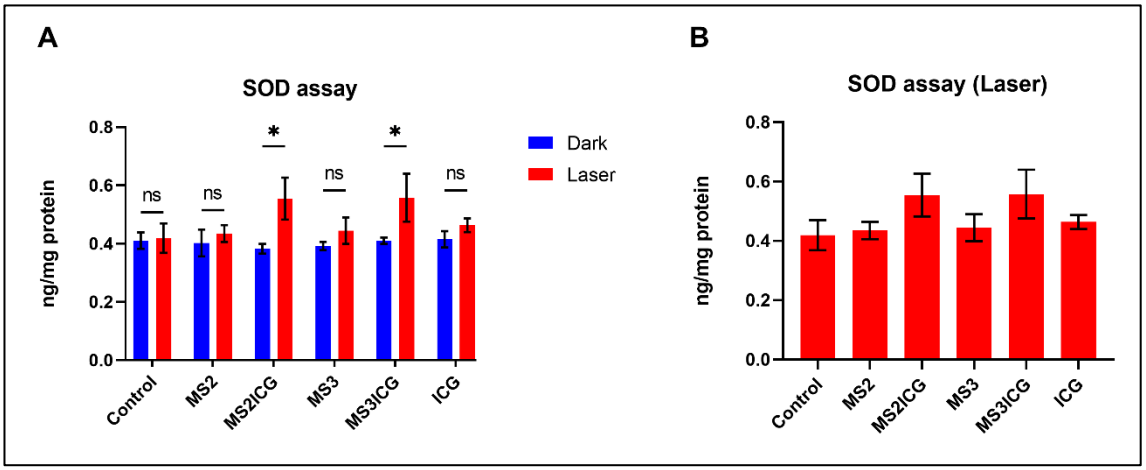

Figure 6-14: Superoxide dismutase (SOD) activity in cytosolic fraction of cells treated with MS (MS2, MS3), MSICG nanocomposites (MS2ICG, MS3ICG) and pure ICG with/without laser irradiation *via* fluorescent spectrofluorometer. A: Bar plot comparing SOD activity with/without laser irradiation, B: Bar plot comparing SOD activity upon laser irradiation with control to show the efficiency of PDT / PTT effect. All data were analysed by GraphPad Prism, shown as mean ± SD (Standard Deviation) of 3 replicates in each group. The significant differences are indicated with asterisks (* $P < 0.05$, ns- not significant). No significant difference in cells observed when compared to control cells upon laser irradiation.

Table 6-1 summarises the results of all the biochemical assays. Both MS2ICG and MS3ICG nanocomposites showed comparable results for cellular damage and antioxidant levels upon laser irradiation. Reduced levels of antioxidants are directly proportional to the enhanced ROS production in cells resulting to the damage of cell membrane, proteins, lipids, and DNA leading to cellular death.

Table 6-1: Evaluation of biochemical assays in MCF7 cells.

Biochemical assays	Laser condition	Samples					
		Control	MS2	MS2ICG	MS3	MS3ICG	ICG
LDH	Dark	18.32 ± 0.22	27.89 ± 0.85	27.16 ± 1.22	28.71 ± 0.87	28.44 ± 1.28	18.72 ± 0.29
	Laser	19.73 ± 1.09	34.3 ± 0.69	61.03 ± 0.85	35.52 ± 1.93	58.77 ± 1.1	45.27 ± 2.46
NO	Dark	4.18 ± 0.01	5.69 ± 0.1	5.66 ± 0.05	5.62 ± 0.01	5.63 ± 0	4.19 ± 0.02
	Laser	4.21 ± 0.04	6.1 ± 0.43	8.54 ± 0.18	6.11 ± 0.27	8.63 ± 0.11	7.82 ± 0.24
LPO	Dark	8.1 ± 0.66	23.79 ± 1.53	23.16 ± 1.24	22.37 ± 0.79	23.1 ± 0.06	8.2 ± 1.39
	Laser	8.53 ± 0.69	27.92 ± 1.07	52.86 ± 2.54	26.62 ± 1.8	51.68 ± 1.05	32.02 ± 1.68
DCFDA	Dark	249.33 ± 3.4	445.67 ± 12.5	450.33 ± 13.27	449.33 ± 9.03	450.67 ± 4.64	255.67 ± 7.93
	Laser	279.33 ± 2.05	528.67 ± 10.78	718.67 ± 14.61	521.67 ± 5.56	693.67 ± 13.12	491.67 ± 15.17
GSH	Dark	4.59 ± 0.03	4.05 ± 0.08	4.13 ± 0.01	4.06 ± 0.02	4.1 ± 0.12	4.6 ± 0.03
	Laser	4.48 ± 0.16	3.72 ± 0.09	2.15 ± 0.06	3.75 ± 0.03	2.16 ± 0.18	3.13 ± 0.08
GPx	Dark	93.26 ± 1.15	76.2 ± 1.15	77.39 ± 0.35	75.98 ± 1.31	76.03 ± 0.35	93.47 ± 0.34
	Laser	92.98 ± 0.56	75.92 ± 0.5	60.66 ± 0.91	75.81 ± 0.56	60.07 ± 1.72	72.76 ± 1.51
GR	Dark	74.03 ± 0.03	64.85 ± 0.9	65.08 ± 0.23	64.98 ± 0.77	64.68 ± 0.39	73.35 ± 0.23
	Laser	76.6 ± 0.06	66.96 ± 0.76	53.39 ± 1.56	67.17 ± 0.73	52.73 ± 1.1	60.85 ± 1.04
GST	Dark	10.06 ± 0.56	6.22 ± 0.74	6.24 ± 1.08	6.11 ± 0.31	6.25 ± 1.13	9.31 ± 0.37
	Laser	11.39 ± 1.01	6.93 ± 1.71	5 ± 1.88	6.95 ± 1.83	5.2 ± 2.92	5.83 ± 1.89
SOD	Dark	0.41 ± 0.03	0.4 ± 0.05	0.38 ± 0.02	0.39 ± 0.01	0.41 ± 0.01	0.42 ± 0.03
	Laser	0.42 ± 0.05	0.43 ± 0.03	0.55 ± 0.07	0.44 ± 0.05	0.56 ± 0.08	0.46 ± 0.02

6.2.4 Iron Assay

Ferroptosis is an iron dependent cell death and the increase in iron ions inside cells is observed upon treatment with iron-based nanoparticles (Fang *et al.*, 2018; Shen *et al.*, 2018). To investigate the change in concentration of total iron content in the cells, iron assay was performed. The total iron concentration increased significantly ($p < 0.0001$) when cells were treated with nanocomposites compared to cells treated with pure ICG and control (no treatment) (Figure 6-15 A). There was no significant difference in iron concentration in different MS and MSICG nanocomposites both with/without laser irradiation. However, there was significant decrease in Fe^{2+} ions in cells treated with MSICG nanocomposites upon laser irradiation (Figure 6-15 B). The decrease in Fe^{2+} ions in cells treated with MSICG nanocomposites with laser irradiation might suggest that the cells are following Fenton reaction due to presence of ROS as evident from earlier biochemical assays (LPO and GPx) as well.

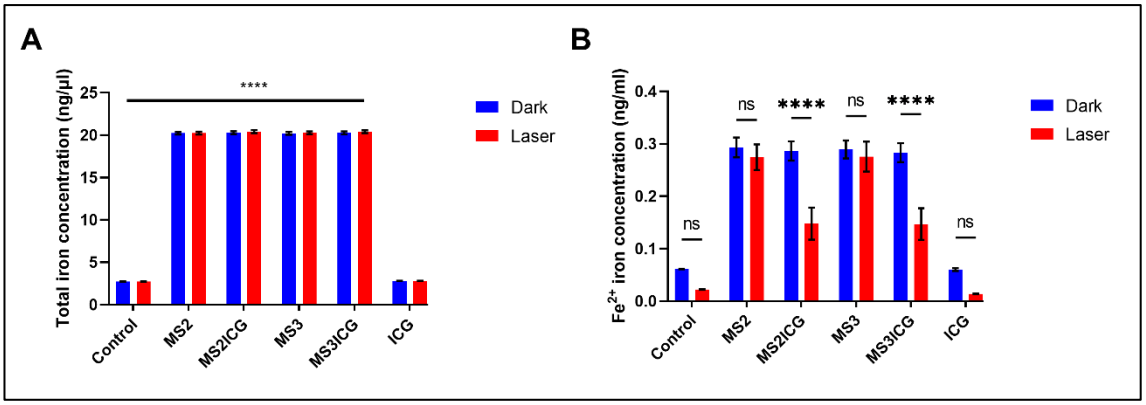

Figure 6-15: Concentration of iron in MCF7 cells due to the treatment with MS (MS2, MS3), MSICG nanocomposites (MS2ICG, MS3ICG) and pure ICG with/without laser irradiation. A: A bar chart showing total iron (Fe^{2+}+Fe^{3+}) concentration B: A bar chart showing only Fe^{2+} ions concentration. All data were analysed by GraphPad Prism, shown as mean ± SD (Standard Deviation) of 2 replicates in each group. The significant differences are indicated with asterisks (**** $P < 0.0001$, ns- not significant)

6.2.5 Evaluation of Apoptotic Gene Expression

The effects of MS2, MS2ICG, MS3, MS3ICG and ICG on the regulated cell death (RCD) pathway were examined with MCF7 cell line by monitoring mRNA expression of apoptosis-related genes p53, Bcl-2, Bax and Cas 9 with expression of GAPDH as an internal control. The gene expression was compared with and without laser irradiation. The graph presented in Figure 6-16 suggest higher impact of laser irradiation on increasing the expression of pro-apoptotic genes. It was found that expression of p53 and Cas9 are significantly higher in MS2ICG treated groups whereas MS3ICG show slight increase in gene expression upon laser irradiation. In case of gene expression of Bax, higher expression in MS2ICG was observed followed by MS3ICG when compared to control group. MS2ICG and MS3ICG decrease the expression of Bcl-2 significantly in comparison to other treatment and control groups. Therefore, our findings confirm that MS2ICG treated MCF7 cells followed by MS3ICG in the presence of laser irradiation showed much higher expressions of apoptotic genes (p53, Bax and Cas9) and lower expression of anti-apoptotic gene (Bcl-2) which suggested that majority of cells undergo apoptotic cell death pathway. However, the elevated expression of pro-apoptotic genes such as p53 and Bax is also related to the induction of apoptosis-ferroptosis pathways (Jiang *et al.*, 2015). It has been reported that the nanoparticles can induce cell death by hybrid apoptosis and ferroptosis pathways through the photoinduced production of singlet oxygen and superoxide anion radicals (Ke *et al.*, 2022). More detailed analysis with higher sample size is required to determine the level of significance of the gene expression studies to prove the cell death mechanism. However, it is clearly evident that the pro-apoptotic genes are higher in MSICG nanocomposites treated cells upon laser irradiation. Table 6-2 enumerates the gene expression values of all the experiments.

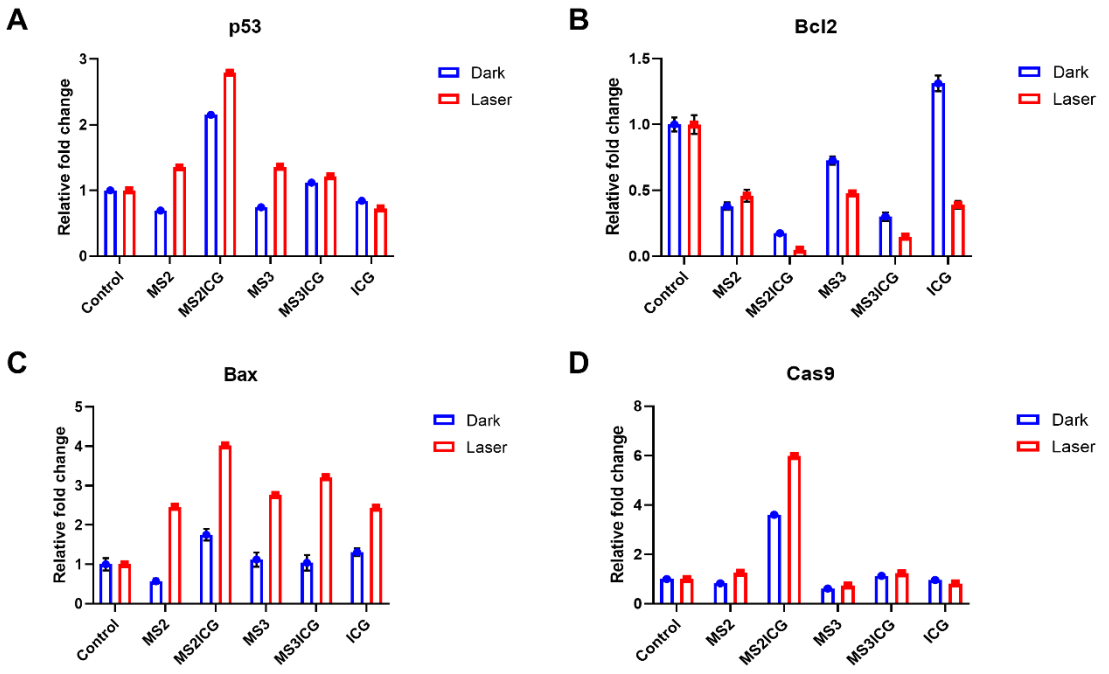

Figure 6-16: Gene expression of p53, Bcl-2, Bax and Cas9 (with and without laser irradiation) on MCF7 cell lines with Control, MS2, MS2ICG, MS3, MS3ICG and ICG treated groups. Expression of GAPDH was taken as internal control.

Table 6-2: Gene expression values of p53, Bcl-2, Bax and Cas9 (with and without laser irradiation) for MS2, MS2ICG, MS3, MS3ICG treated MCF7 cells. Control (without treatment) and ICG treated groups were also taken for comparative studies.

	p53		Bcl-2		Bax		Cas9	
	Dark	Laser	Dark	Laser	Dark	Laser	Dark	Laser
Control	1.000±0.0007	1.000±0.00002	1.0000±0.0536	0.9996±0.071	1.000±0.1546	1.000±0.0001	1.000±0.0046	1.000±0.0008
MS2	0.694±0.0008	1.351±0.00003	0.3790±0.0285	0.4589±0.046	0.573±0.0709	2.459±0.0007	0.833±0.0063	1.258±0.0005
MS2ICG	2.151±0.0011	2.791±0.00003	0.1742±0.0100	0.0493±0.004	1.753±0.1467	4.023±0.0010	3.602±0.0276	5.982±0.0101
MS3	0.744±0.0006	1.358±0.00004	0.7265±0.0304	0.4767±0.016	1.121±0.1826	2.759±0.0005	0.618±0.0052	0.741±0.0001
MS3ICG	1.118±0.0009	1.217±0.00000	0.3003±0.0321	0.1476±0.014	1.038±0.1981	3.214±0.0005	1.128±0.0136	1.235±0.0014
ICG	0.842±0.0005	0.725±0.00002	1.3121±0.0592	0.3899±0.030	1.310±0.1024	2.441±0.0002	0.962±0.0054	0.822±0.0000

6.3 Conclusion

Extensive data represented with *in-vitro* cellular integrity markers and antioxidant enzyme activities has shown that the magneto-optical nanocomposites and pure ICG upon laser irradiation increased the production of ROS and RNS in the cells leading to cellular damage. MSICG nanocomposites in the presence of molecular oxygen and laser irradiation generated free radicals that react rapidly with oxygen to produce ROS. The ROS such as superoxide ($O_2^{\bullet -}$) either reacts with nitric oxide ($NO^{\bullet}$) to produce peroxy-nitrite ($ONOO^-$) or undergoes dismutation catalysed by SOD to generate H_2O_2.There was a significant increase in LDH level demonstrating the cell membrane damage. The increase in NO suggested the presence of RNS species. Similarly, the LPO level was also found to be increased which is a sign of cellular damage of cell membranes. The increase in number of H_2O_2 in cells either gets detoxified by antioxidants such as

GSH/GPx or generate $OH^{\bullet}$ by the Fenton reaction. The free radicals damage cellular proteins, lipids, and nucleic acids, leading to regulated cell death pathways. The findings of possible oxidative stress induced by nanocomposites upon laser irradiation is schematically shown in Figure 6-17.

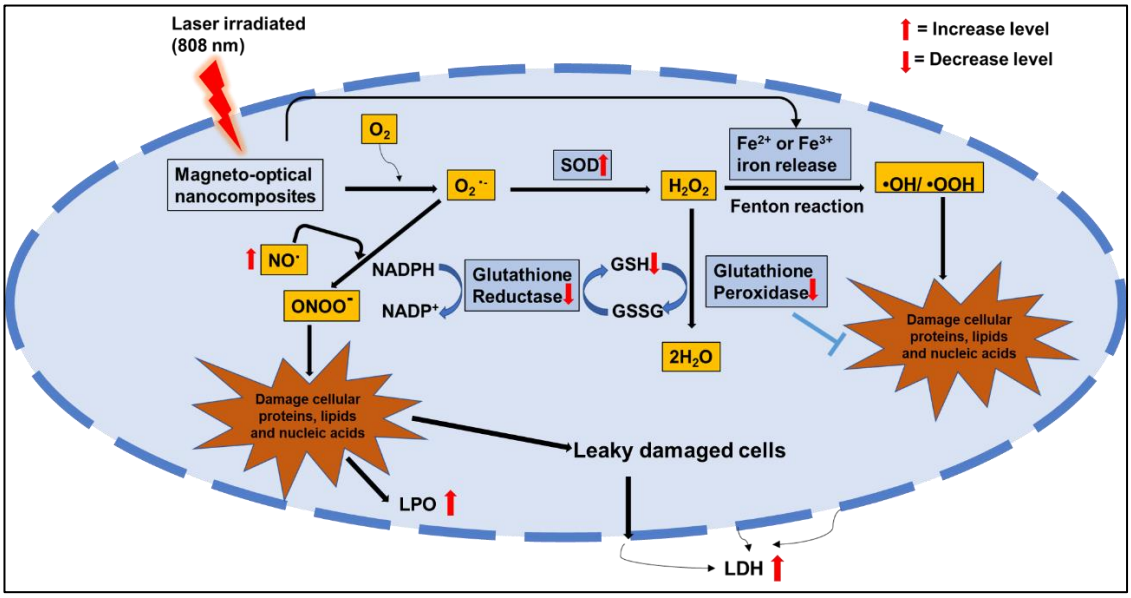

Figure 6-17: Schematic representation of MSICG nanocomposites induced oxidative stress in MCF7 cells upon laser irradiation when investigated with various *in-vitro* cellular integrity markers and antioxidant enzyme activities.

Regarding the gene expression study, because of difficulty in performing statistical analysis due to low sample size (n=2) to prove the distinct cell death pathways gene expression, conclusions are difficult to draw in this case. Despite this limitation, the findings of this study are important because it provides an initial results of possible cell death mechanisms. This study so far has four important findings which are schematically represented in Figure 6-18.

Upon intracellular uptake of magneto-optical nanocomposites through different endocytic pathways, the nanocomposites under laser irradiation produce ROS species. Similarly, upon uptake of magneto-optical nanocomposites, the accumulation of iron in cells was increased which may possibly be stored as labile iron pool or reacted with generated ROS to undergo Fenton reaction. Fenton reaction generates H_2O_2 or hydroxyl ions (OH^-) that increases the oxidative stress inside the cells and oxidises PUFAs leading to elevated lipid peroxidation inside the cells. In addition, the increased ROS induces mitochondrial dysfunction and DNA damage. The elevated expression of pro-apoptotic genes such as p53 and Bax is related to the induction of apoptosis. Conversely, the level of anti-apoptotic Bcl-2 gene is decreased. It is because the stimulation that triggers apoptosis leads to downregulation of anti-apoptotic proteins and upregulation of pro-

apoptotic proteins. Both mitochondrial ROS and cellular ROS resulted in enhanced expression of Caspase 9 (cas9) (specifically in MS2ICG) thus resulting in apoptosis. Finally, we conclude that the treatment with magneto-optical nanocomposites causes a mixed or hybrid form of concurrent apoptosis and ferroptosis pathways thereby showing enhanced anticancer effects.

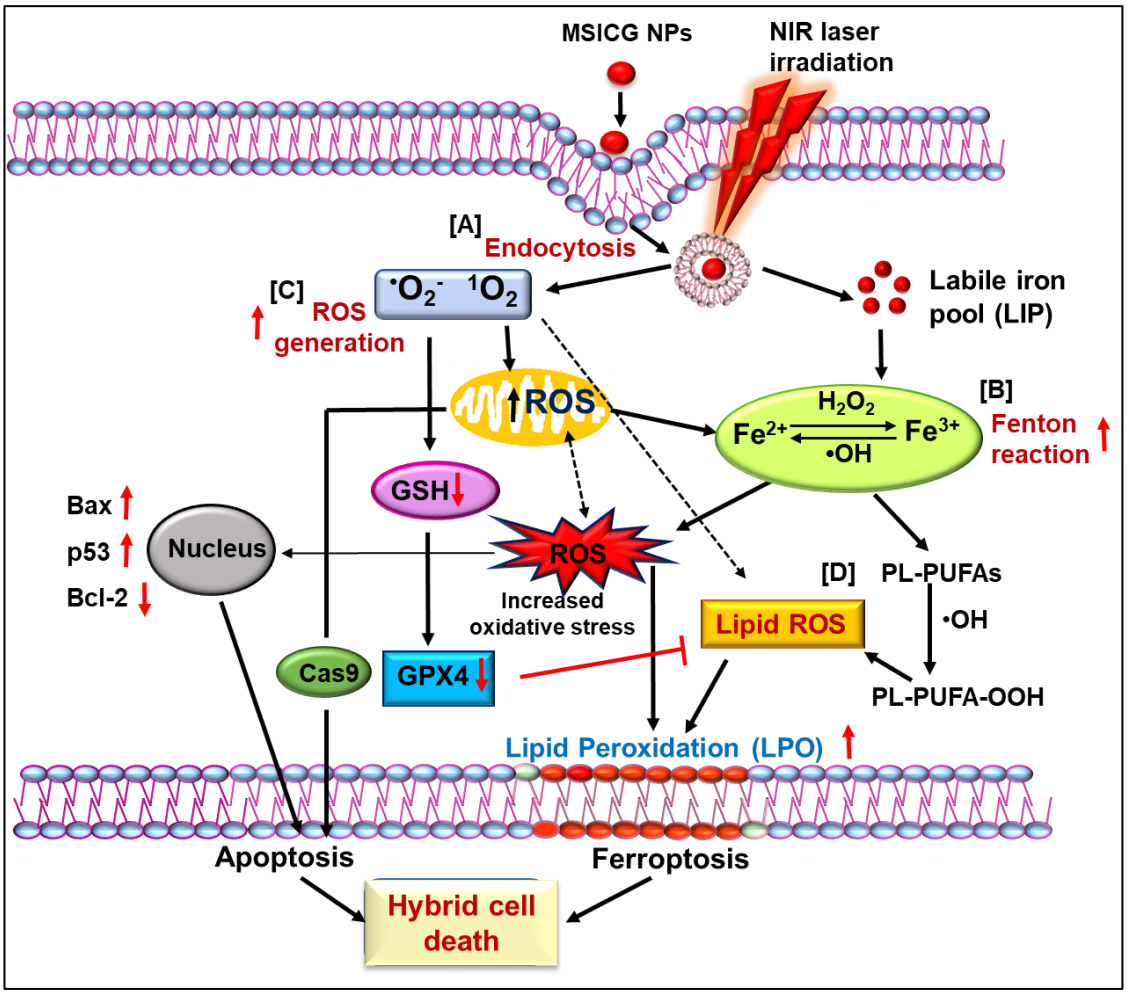

Figure 6-18: Schematic of proposed magneto-optical nanocomposites mediated cell death upon laser irradiation in MCF7 cells. [A] Endocytosis of MSICG [B] Fenton reaction induced by MSICG [C] ROS generation upon laser irradiation causes mitochondrial dysfunction, both mitochondrial ROS and cellular ROS results in enhanced expression of Caspase 9 (cas9), p53 and Bax (pro-apoptotic), whereas decreased expression of anti-apoptotic Bcl2, thus initiating apoptosis [D] Fenton reaction regulated LPO accumulation *via* peroxidation of polyunsaturated fatty acids (PUFAs) of cell membrane or organelle membrane. The depletion of both GSH and GPx4 (lipid peroxide repair enzyme) leads to lipid peroxidation and caused ferroptosis.

CHAPTER 7

CONCLUSION AND FUTURE WORK

7.1 Conclusion

The work presented in this thesis involved nanomedicine *via* a combination of nanotechnology, materials chemistry, cell biology and biochemical studies to provide recent advances towards the development of magneto-optical nanocomposites for cancer therapeutics. This thesis has explored the synthesis methods of both hydrophilic and hydrophobic iron oxide nanoparticles (IONPs), coating IONPs with mesoporous silica shell, loading a NIR active photosensitiser; Indocyanine Green (ICG), and testing their performance in cancer therapeutics using multifunctionality such as a combination of magnetic and optical *via*; magnetic hyperthermia therapy (MHT), photodynamic therapy (PDT) and photothermal therapy (PTT).

Understanding the physico-chemical properties of nanoparticles/ nanocomposites is of utmost importance for designing cancer therapeutics since their properties determine their fate in systemic availability, and the possibility of clinical application. In general, physico-chemical properties of nanoparticles can induce oxidative stress and cytotoxicity in cells through direct generation of ROS (Sen, Sebastianelli and Bruce, 2006; Shi *et al.*, 2017; Mohammadinejad *et al.*, 2019). For instance, the size and shape of nanoparticles affect its blood circulation which in turn relates to the tumour accumulation, tumour retention, and drug release (Shi *et al.*, 2017). Therefore, a number of characterisation techniques such as TEM, DLS, XRD, FTIR, VSM, BET, TGA were used to evaluate their physico-chemical properties.

The first part of the thesis focused on the synthesis of various IONPs. The hydrophilic IONPs (IO1) were synthesised using simple co-precipitation method where simultaneous precipitation of 1:2 molar ratio of ferrous and ferric ions was initiated by the addition of a base (NH_4OH) whilst heating the reaction mixture at 80 ℃ using an isomantle heater. The coprecipitation method is more simple than other thermal decomposition methods, however, this method results in polydisperse IONPs and agglomerates due to simultaneous nucleation and continuous growth of particles (Besenhard *et al.*, 2020). To overcome this effect, a new method of coprecipitation is presented (IO2) to demonstrate the importance of controlled slow mixing of chemicals *via* osmotic pathway using dialysis tubing for reproducible co-precipitation syntheses. The base was added in the solution of iron precursors using dialysis bag for initial burst of iron oxide formation with subsequent slow release for controlled growth of nanoparticles with no or negligible agglomerates with a narrow particle size distribution. The TEM and DLS data analyses showed that the IO2 nanoparticles were monodispersed with a narrow particle size distribution of mean particle size 14 ± 2.5 nm and 158 nm, respectively compared to IO1 with average diameter of 42 ± 15 nm and 163

nm, respectively. The zetapotential values of +19.1 ± 5.6 mV and +26.4 ± 5.5 mV were observed for IO1 and IO2 respectively, suggesting higher electrostatic repulsion between the particles of IO2 with an enhanced stability in suspension as compared to IO1.

The hydrophobic IONPs (IO3) were also synthesised using co-precipitation method but with the addition of oleic acid to stabilise the nanoparticles in hexane. The previous studies have used oleic acid after the formation of IONPs to stabilise them in suspension, however, in this thesis, the oleic acid was added in the mixture of iron salts solution, stirred for an hour to stabilise the system before adding the required number of base solutions for coprecipitation. The TEM data showed a narrow size distribution of synthesised IONPs with a mean size of around 9 nm. Baumgartner *et al.* (2013) showed that the nucleation followed by rapid growth of magnetite nanoparticles causes agglomeration on nanometric primary particles without any intermediates. Likewise, a combination of XRD and FTIR analyses showed synthesised IONPs were pure iron oxides of magnetite (Fe_3O_4) due to the appearance of a distinct peak at around 550 cm^{-1} corresponding to the bond vibrations between Fe-O in IO1 and IO2. However, an additional peak corresponding to the presence of oleic acid was found in IO3 at 1709 cm^{-1} due to the carbonyl (C=O) vibrations, confirming the oleic acid acted as a stabiliser on IONPs. The magnetisation vs field (M-H) graphs showed that IONPs (IO1, IO2, IO3) exhibited superparamagnetic properties with nearly zero coercivity and zero remanence values. The saturation magnetisation of IO1, IO2 and IO3 were calculated to be 63.6 emu/g, 59.4 emu/g and 49.3 emu/g respectively which is lower than the values of bulk magnetite (92 emu/g).

The second phase involved coating IONPs with mesoporous silica shell *via* chemical method in suspension using CTAB as a surfactant / structure directing template and TEOS as a silica source. The resultant core-shell nanocomposites were nearly spherical in morphology. TEM showed MS1 nanocomposites were larger in size with an average diameter around 129 nm whilst MS2 and MS3 were 83 nm and 38 nm, respectively. The smaller size of MS2 compared to MS1 could be attributed to the well dispersed IO2 nanoparticles in suspension compared to IO1. IO3 nanoparticles with a thin layer of silica (MS3) showed the highest dispersibility and stability in suspension. DLS data showed that MS1 nanocomposites had smaller hydrodynamic diameter of 210 nm compared to MS2 (241 nm) and MS3 (244 nm). The zetapotential of MS nanocomposites showed a complete shift in surface charge from positive to negative due to the silica coating on the IONPs. The zetapotential were higher in all MS nanocomposites at around -24 mV suggesting higher stability and dispersibility in suspension.

The XRD and FTIR analyses also confirmed the silica coating on IONPs. A small angle peak at 2θ value of around 2 nm corresponding to long range ordering due to mesopores with overall amorphous silica walls (presence of broad peak at 2θ values at around 15-30 degrees) confirmed the fabrication of silica on IONPs. Similarly, FTIR data confirmed the presence of silica due to the presence of specific bond vibrations. Vibrations at 1080 cm^{-1} suggest Si-O-Si asymmetric stretching, at 795 cm^{-1} due to Si-O-Si symmetric stretching and at 440 cm^{-1} due to O-Si-O vibration. VSM showed magnetic silica nanocomposites with hydrophobic core (MS3) had the highest magnetisation values of 44.5 emu/g compared to MS1 and MS2 with 5.9 and 12.5 emu/g respectively. Thus, suggesting MS3 nanocomposites containing hydrophobic IONPs, and a thin silica shell is superior on superparamagnetic property. Furthermore, the MS1 nanocomposites showed higher BET surface area of 965 ± 48.2 m^2g^{-1} indicating a large internal surface area due to ordered mesopores. MS2 nanocomposites also showed higher surface area of 655 ± 8.48 m^2g^{-1} compared to MS3 with 142 ± 0.41 m^2g^{-1} confirming the presence of mesoporosity in the silica shell.

The CTAB used as the structure directing agent (template) for mesoporosity can have adverse effect in the cellular level, posing cytotoxicity in cells. Similarly, presence of CTAB can also block the mesopores hence optimum ICG loading. Therefore, removal CTAB from the MS nanocomposites was carried out using multiple acidic ethanol washings. A complete removal of CTAB from MS1 nanocomposites was confirmed through FTIR and TGA. The absence of characteristic peak of CTAB at 2900 cm^{-1} due to C-H stretching of CTAB molecules after acidic wash confirmed the removal of CTAB. TGA analysis also showed the removal of CTAB with weight loss of 21.4% after heating the unwashed nanocomposites compared to only 3.4% weight loss due to ad-layer of water in washed nanocomposites.

The multi-modality of IONPs was achieved by combining the magnetic silica (MS) nanocomposites with a photosensitiser; ICG. This has been successfully carried out by physically adsorbing ICG on the mesopores of MS nanocomposites. The physical loading was achieved by mixing an aqueous solution of ICG with MS nanocomposites for the period of 2 hours with cumulative loading until no more ICG can be loaded in the mesopores of MS nanocomposites. The ICG was added cumulatively on the MS nanocomposites because of the inherent property of ICG to aggregate at higher concentration leading to addition of low concentration ICG at each cumulative loading steps. The loading of ICG was higher in MS1 nanocomposites with encapsulation efficiency of 68.6% compared to MS2 and MS3 with 23.4% and 32.2%, respectively. The low encapsulation efficiency of both MS2 and MS3 could be due to relatively low surface

areas. The z-average size as calculated by DLS showed slight increase in size of MSICG nanocomposites compared to MS nanocomposites. The average size of MS1ICG was 217 nm compared to MS2ICG (247nm) and MS3ICG (279 nm). The zetapotential values after the ICG loading were slightly higher (MS1ICG: -28 mV, MS2ICG: -28 mV, MS3ICG: -24.3 mV) as compared to their respective MS nanocomposites, which may be due to the presence of ICG in nanocomposites.

Another phase of this thesis was to investigate the therapeutic efficacy of the synthesised magneto-optical nanocomposites *via* MTT, PTT and PDT under the influence of an external stimuli such as AMF or a laser irradiation or in combination. An increase in temperature up to 42 ℃ under an AMF (200 Gauss and frequency of 406 kHz) for almost all materials. However, IO2 nanocomposites showed better heating efficiency by reaching the maximum set temperature of 42 ℃ within 88 seconds compared to IO1 at 196 seconds and proven further by calculating the SPA values; IO1: 35.8 W/g and IO2: 94.1 W/g. Similarly, the MS2 nanocomposites showed better heating efficiency by reaching 42 ℃ within 129 seconds with SPA values of 58.1 W/g compared to MS1 (6.8 W/g) and MS3 (25.2 W/g).

The heating efficiency of MSICG nanocomposites upon laser irradiation (λ = 808 nm, power density= 1.2 W/cm^2) for 6 minutes was also measured using a thermal probe. MS3ICG nanocomposites could generate heat at the same rate as pure ICG i.e., temperature change of 22 ℃ in 6 minutes, while MS1ICG and MS2ICG showed slightly slower heating efficiency. The difference in heating efficiency under laser irradiation could be due to the nature of the silica layer around IONPs. For example, a thick silica layer can affect the penetration of laser as compared to its pure form. An increase in temperature up to 19 ℃ was observed for MS1ICG and 13 ℃ for MS2ICG. Such a temperature change is enough for generating heat to kill cancer cells thus proving to be an effective PTT agent.

Furthermore, the PDT efficacy of three different MSICG nanocomposites tested using ABMDMA as an indicator for the identification of generated singlet oxygen ($^1O_2$) species. There was a slight change in generation of $^1O_2$ in MS1ICG and MS2ICG within 30 seconds of laser light exposure. However, the data for MS3ICG was inconclusive and may be due to the release of iron ions upon laser irradiation which cannot be separated magnetically. To test the photothermal stability of all three MSICG nanocomposites after 3 cycles of laser ON/OFF modes, a slight change observed in their heating profile. The photodegradation of pure ICG without encapsulated in nanocomposites visually observed by its change in colour upon each cycle of laser irradiation. Thus, the loading

of ICG inside the mesopores increased the stability of ICG with enhanced PDT and PTT effects.

The third phase of the thesis was to test their performance in multifunctional application *in-vitro*. Two types of magneto-optical nanocomposites (hydrophilic core: MS2ICG and hydrophobic core: MS3ICG) were chosen to test their toxicity and cancer therapeutic efficiency *in-vitro* using commercial MCF7 cells. Both nanocomposites exhibited similar profile of cellular toxicity in spite of having differences in their physiochemical properties. The cell viability (%) upon treatment with nanocomposites was tested using the well-established MTT assay and showed both dose and time dependent toxicity. The nanocomposites were nontoxic up to the concentration of 100 µg/ml and above that, they showed cytotoxic effect. This result is similar to those reported by Rosenholm, Sahlgren and Lindén (2010). The highest toxicity was observed at a concentration of 400 µg/ml within the experimental concentration range of 50 to 400 µg/ml. The cellular toxicity could be attributed to the presence of both IONPs and silica shell. A slight increase in cellular toxicity of MS3ICG compared to MS2ICG may be due to the nature of IONPs core which tends to leach due to a thin silica shell. Additionally, the trace amount of CTAB remaining in the nanocomposites could be responsible for additional cytotoxicity. The cellular toxicity also evaluated using haemolysis assay and the results showed their biocompatibility within 24 hours of incubation and a slight toxicity at 48 hours when compared with a control experiment.

To test PTT and PDT effects of nanocomposites under laser irradiation, the cells incubated with MSICG nanocomposites showed significant increase in cytotoxicity upon 5 minutes of laser light irradiation compared to nanocomposites without laser irradiation *via* MTT assay. The cytotoxicity of both nanocomposites showed dose (50, 100, 200 and 400 µg/ml) and time (24 and 48 hours) dependent profiles. The cellular toxicity increased 3 folds after laser irradiation demonstrating their efficient PTT effect on potential cancer therapeutics. Furthermore, the application of AMF for MHT therapy due to superparamagnetic properties of core IONPs on MCF7 cells followed by the laser irradiation as dual therapies was monitored by the cell viability assay using trypan blue. The treatment with laser irradiation for 5 minutes following the initial AMF, decreased the cell viability to 71.7 ± 4.7%. Likewise, the MS3ICG nanocomposites showed equivalent results, decreasing the cell viability to 74 ± 1.7% upon AMF (MHT) and laser irradiation (PTT & PDT). However, the treatment of nanocomposites with AMF alone showed low cancer cells killing efficiency. This is a direct proof of their efficiency on dual therapies stimulated or triggered by external sources (AMF and laser) targeted to specific tumour regions as shown on MCF7 cells.

The ongoing progress of cancer research show unique properties of cancer cells differentiating them from normal cells (Hanahan, 2022). One of the properties of cancer cells that has been exploited by cancer nanomedicine is the EPR effect which allows release of cancer therapeutic agents in tumour cells. The specific internalisation of nanomedicines by cancer cells is a barrier that needs to be addressed for increasing therapeutic effects. The uptake of MSICG nanocomposites by MCF7 cells was directly visualised by different imaging techniques. SEM images of cells upon treatment with nanocomposites clearly showed their internalisation inside the cells as compared to control without the presence of nanoparticles. The accumulation and internalisation of nanocomposites was also visualised by optical microscopy using Prussian blue assay. The accumulation and internalisation of nanocomposites in MCF7 cells were clearly visible due to the colouration of blue pigments in the presence of iron oxides. Finally, confocal microscopy helped to prove the cellular internalisation by monitoring the fluorescence characteristic of ICG. When excited with 633 nm laser, the fluorescence of MSICG nanocomposites was clearly visible and showed a time dependent profile i.e., higher at 4 hours compared to 2 hours.

The cellular endocytosis of nanocomposites is critical for cancer therapeutics. Therefore, Chapter 5 has been dedicated to the study of the plausible mechanism of internalisation using a variety of endocytic inhibitors. The results showed that the internalisation of both MS2ICG and MS3ICG occurred through multiple internalisation pathways. Evidence of active energy-dependent endocytosis process was confirmed due to a decrease in cellular uptake of nanocomposites at low temperature (4 ℃). Clathrin-mediated endocytosis (sucrose inhibition) has also been proven to be a general internalisation pathway for both MSICGs (MS2ICG and MS3ICG) in MCF7 cells. In addition, caveolae/lipid rafts (Lovastatin inhibition) and micropinocytosis (sodium azide) also contributed to cellular endocytosis pathways.

When tested *in-vitro* for ROS generation using DCFDA assay, treatment with MSICG nanocomposites showed an increased level of ROS *via* the measurement of DCF, both qualitatively and quantitatively. A small amount of ROS generation without laser irradiation also suggests the intrinsic cytotoxic properties of MSICG nanocomposites due to the presence of core IONPs and silica coating. However, upon laser irradiation, an increase level of both ROS and RNS was observed due to the presence of ICG as a photosensitiser in MSICG nanocomposites. The increased level of LDH, NO, SOD and LPO suggested the cellular damage induced by nanocomposites and laser. Additionally, the increased LPO level is associated with cells undergoing stress though higher lipid ROS formation thus reinforcing the general belief of cells

undergoing ferroptosis pathway. The decreased level of antioxidant enzymes such as GSH, GPx, GR and GST indicated an enhanced ROS production in cells, resulting into cellular death. The decrease in GPx level is also a marker for cells undergoing ferroptosis. The iron assay also indicated a significant increase in total iron ions (Fe^3 and Fe^{2+}) inside the cells. However, the level of Fe^{2+} in total iron ions decreased by half upon laser irradiation as compared to cells treated with MSICG without laser irradiation suggesting the Fe^{2+} ions are undergoing Fenton reaction.

Finally, the cell death mechanism upon treatment with MSICG nanocomposites was also investigated on specific pro- and anti-apoptotic genes. This initial data suggested the increase in Cas9 and pro-apoptotic genes such as p53 and Bax whereas a decrease in Bcl-2 genes suggesting that most of the cellular death undergoes apoptosis pathway. However, the increased level of LPO, reduced GPx and cells undergoing Fenton reaction suggested the cellular death *via* ferroptosis. In conclusion, the cells treated with MSICG nanocomposites under laser irradiation could have gone through a hybrid cell death i.e., both apoptosis and ferroptosis induced pathways.

7.2 Scope for future studies

A detailed investigation of the fabrication protocol by tuning the size and morphology of IONPs, tunning the shell structure with variable pore sizes, thickness and surface functionality can enhance the material's performance. The higher the surface area due to the internal porosity of mesoporous silica shell in MS and MSICG nanocomposites, the greater the drug loading capacity and encapsulation efficiency. Thus, the formation of stable uniform biocompatible porous shell structure with magnetic core has the potential to lead to the development of several multimodal therapeutic and diagnostic agents.

The chemical synthesis of magneto-optical nanocomposites can be altered with a variety of other suitable photosensitisers or optical probes in the NIR region (e.g., Ce6, IR820, up conversion nanoparticles, etc) possibly to create a range of new magneto-optical therapeutic agents. Similarly, addition of specific targeting moieties such as antibodies for active targeting is another area of research of high interest for clinical studies. Initial results on cytotoxicity data of MSICG nanocomposites under laser irradiation and AMF justify further development for potential laser-induced cancer therapeutics.

The laser-induced cell death mechanism after treatment with nanocomposites could not be statistically proved due to small sample size. Hence, an in-depth experiment on gene expression and transcription protein activity after laser irradiation is necessary

to elucidate and offer clear explanations. This work forms a basis for further experiments involving ferroptosis gene expression and other cell damage studies such as DNA fragmentation, intracellular Ca^{2+} level etc.

By combining multimodal treatment such as PDT, PTT and MHT for cancer therapeutics, this thesis has clearly identified the potential of MSICG nanocomposites. It would also be of great interest to investigate the potential use in diagnostics using imaging techniques such as magnetic resonance imaging (MRI), magnetic particle imaging (MPI) and florescence imaging.

As the synthesised magneto-optical nanocomposites showed slight toxicity at higher concentration, the fabrication of nanocomposites with polymers such as polyethylene glycol or liposomes can significantly improve the delivery and retention of IONPs with reduced toxicity in breast tumours with higher tumour accumulation as reported by Kato *et al.* (2015).

IONPs induce a pro-inflammatory immune response. According to Zanganeh *et al.* (2016), iron oxide nanoparticles significantly suppressed tumour growth by inducing pro-inflammatory M1 macrophages that later induce Fenton reaction to cause cancer cell apoptosis. Therefore, a trans-well system with co-incubation of breast cancer cell lines and macrophages can be prepared to study the migration of nanocomposites to study its efficacy in tumour immunotherapy. Furthermore, this research will provide an insight on nano-bio interaction for potential application in cancer therapy.

This research was mainly focused on *in-vitro* biocompatibility and cytotoxicity to find out the possible mechanisms of internalisation and cellular death. This research can be further expanded by using 3D *in-vitro* cells or spheroids followed by *in-vivo* experiments to investigate killing efficiency of tumour cells. The work presented in this thesis paved the foundation in an important topic of multifunctional nanocomposites for cancer therapeutics, has raised new questions and directed the need for an extensive study on magneto-optical nanocomposites for real life solution from early-stage detection of cancer to its remedy.

REFERENCES

Abrahamse, H., & Hamblin, M. R. (2016). New photosensitizers for photodynamic therapy. *The Biochemical Journal*, *473*(4), 347–364. https://doi.org/10.1042/BJ20150942

Akinc, A., & Battaglia, G. (2013). Exploiting Endocytosis for Nanomedicines. *Cold Spring Harbor Perspectives in Biology*, *5*(11), a016980. https://doi.org/10.1101/cshperspect.a016980

Algorri, J. F., Ochoa, M., Roldán-Varona, P., Rodríguez-Cobo, L., & López-Higuera, J. M. (2021). Photodynamic Therapy: A Compendium of Latest Reviews. *Cancers*, *13*(17), 4447. https://doi.org/10.3390/cancers13174447

Ali, A., Zafar, H., Zia, M., ul Haq, I., Phull, A. R., Ali, J. S., & Hussain, A. (2016). Synthesis, characterization, applications, and challenges of iron oxide nanoparticles. *Nanotechnology, Science and Applications*, *9*, 49–67. https://doi.org/10.2147/NSA.S99986

Almeida, M. S. de, Susnik, E., Drasler, B., Taladriz-Blanco, P., Petri-Fink, A., & Rothen-Rutishauser, B. (2021). Understanding nanoparticle endocytosis to improve targeting strategies in nanomedicine. *Chemical Society Reviews*, *50*(9), 5397–5434. https://doi.org/10.1039/D0CS01127D

Amirshaghaghi, A., Yan, L., Miller, J., Daniel, Y., Stein, J. M., Busch, T. M., Cheng, Z., & Tsourkas, A. (2019). Chlorin e6-Coated Superparamagnetic Iron Oxide Nanoparticle (SPION) Nanoclusters as a Theranostic Agent for Dual-Mode Imaging and Photodynamic Therapy. *Scientific Reports*, *9*(1), 2613. https://doi.org/10.1038/s41598-019-39036-1

An, Y., Zhu, J., Liu, F., Deng, J., Meng, X., Liu, G., Wu, H., Fan, A., Wang, Z., & Zhao, Y. (2019). Boosting the Ferroptotic Antitumor Efficacy *via* Site-Specific Amplification of Tailored Lipid Peroxidation. *ACS Applied Materials & Interfaces*, *11*(33), 29655–29666. https://doi.org/10.1021/acsami.9b10954

Araujo, A. R. T. S., Saraiva, M. L. M. F. S., & Lima, J. L. F. C. (2008). Determination of total and oxidized glutathione in human whole blood with a sequential injection analysis system. *Talanta*, *74*(5), 1511–1519. https://doi.org/10.1016/j.talanta.2007.09.028

Arruebo, M., Vilaboa, N., Sáez-Gutierrez, B., Lambea, J., Tres, A., Valladares, M., & González-Fernández, Á. (2011). Assessment of the Evolution of Cancer Treatment Therapies. *Cancers*, *3*(3), 3279–3330. https://doi.org/10.3390/cancers3033279

Ashkarran, A. A., & Mahmoudi, M. (2021). Magnetic Levitation Systems for Disease Diagnostics. *Trends in Biotechnology*, *39*(3), 311–321. https://doi.org/10.1016/j.tibtech.2020.07.010

Atkinson, W. J., Brezovich, I. A., & Chakraborty, D. P. (1984). Usable frequencies in hyperthermia with thermal seeds. *IEEE Transactions on Biomedical Engineering*, BME-31(1), 70–75. https://doi.org/10.1109/TBME.1984.325372

Auría-Soro, C., Nesma, T., Juanes-Velasco, P., Landeira-Viñuela, A., Fidalgo-Gomez, H., Acebes-Fernandez, V., Gongora, R., Almendral Parra, M. J., Manzano-Roman, R., & Fuentes, M. (2019). Interactions of Nanoparticles and Biosystems: Microenvironment of Nanoparticles and Biomolecules in Nanomedicine. *Nanomaterials*, *9*(10), 1365. https://doi.org/10.3390/nano9101365

Bakhtiary, Z., Saei, A. A., Hajipour, M. J., Raoufi, M., Vermesh, O., & Mahmoudi, M. (2016). Targeted superparamagnetic iron oxide nanoparticles for early detection of cancer: Possibilities and challenges. *Nanomedicine: Nanotechnology, Biology, and Medicine*, *12*(2), 287–307. https://doi.org/10.1016/j.nano.2015.10.019

Bandhu, A., Mukherjee, S., Acharya, S., Modak, S., Brahma, S. K., Das, D., & Chakrabarti, P. K. (2009). Dynamic magnetic behaviour and Mössbauer effect measurements of magnetite nanoparticles prepared by a new technique in the co-precipitation method. *Solid State Communications*, *149*(41), 1790–1794. https://doi.org/10.1016/j.ssc.2009.07.018

Baumgartner, J., Dey, A., Bomans, P. H. H., Le Coadou, C., Fratzl, P., Sommerdijk, N. A. J. M., & Faivre, D. (2013). Nucleation and growth of magnetite from solution. *Nature Materials*, *12*(4), 310–314. https://doi.org/10.1038/nmat3558

Bedard, K., & Krause, K.-H. (2007). The NOX Family of ROS-Generating NADPH Oxidases: Physiology and Pathophysiology. *Physiological Reviews*, *87*(1), 245–313. https://doi.org/10.1152/physrev.00044.2005

Behdadfar, B., Kermanpur, A., Sadeghi-Aliabadi, H., Morales, M. del P., & Mozaffari, M. (2012). Synthesis of high intrinsic loss power aqueous ferrofluids of iron oxide nanoparticles by citric acid-assisted hydrothermal-reduction route. *Journal of Solid State Chemistry*, *187*, 20–26. https://doi.org/10.1016/j.jssc.2011.12.011

Benton Swanson, W., Durdan, M., Eberle, M., Woodbury, S., Mauser, A., Gregory, J., Zhang, B., Niemann, D., Herremans, J., X. Ma, P., Lahann, J., Weivoda, M., Mishina, Y., & F. Greineder, C. (2022). A library of Rhodamine6G-based pH-sensitive

fluorescent probes with versatile in vivo and in vitro applications. *RSC Chemical Biology*. https://doi.org/10.1039/D2CB00030J

Bergmeyer, H. U., & Bernt, E. (1974). UV-Assay with Pyruvate and NADH. In H. U. Bergmeyer (Ed.), *Methods of Enzymatic Analysis (Second Edition)* (pp. 574–579). Academic Press. https://doi.org/10.1016/B978-0-12-091302-2.50010-4

Besenhard, M. O., LaGrow, A. P., Hodzic, A., Kriechbaum, M., Panariello, L., Bais, G., Loizou, K., Damilos, S., Margarida Cruz, M., Thanh, N. T. K., & Gavriilidis, A. (2020). Co-precipitation synthesis of stable iron oxide nanoparticles with NaOH: New insights and continuous production *via* flow chemistry. *Chemical Engineering Journal*, *399*, 125740. https://doi.org/10.1016/j.cej.2020.125740

Bhavsar, D., Patel, V., & Sawant, K. (2019). Systematic investigation of in vitro and in vivo safety, toxicity and degradation of mesoporous silica nanoparticles synthesized using commercial sodium silicate. *Microporous and Mesoporous Materials*, *284*, 343–352. https://doi.org/10.1016/j.micromeso.2019.04.050

Bourgeois, P., Veys, I., Noterman, D., De Neubourg, F., Chintinne, M., Vankerckhove, S., & Nogaret, J. M. (2021). Near-Infrared Fluorescence Imaging of Breast Cancer and Axillary Lymph Nodes After Intravenous Injection of Free Indocyanine Green. *Frontiers in Oncology*, *11*. https://www.frontiersin.org/article/10.3389/fonc.2021.602906

Brittanie, R., Munjal, S., D'Agostino, J., & Venketaraman, V. (2018). Liposomal-Glutathione as a Potential Therapeutic Agent to Control HIV-1 Infection and Tuberculosis. *European Medical Journal, 3*(4), 62–69.

Burney, S., Tamir, S., Gal, A., & Tannenbaum, S. R. (1997). A Mechanistic Analysis of Nitric Oxide-Induced Cellular Toxicity. *Nitric Oxide*, *1*(2), 130–144. https://doi.org/10.1006/niox.1996.0114

Cai, H., An, X., Cui, J., Li, J., Wen, S., Li, K., Shen, M., Zheng, L., Zhang, G., & Shi, X. (2013). Facile Hydrothermal Synthesis and Surface Functionalization of Polyethyleneimine-Coated Iron Oxide Nanoparticles for Biomedical Applications. *ACS Applied Materials & Interfaces*, *5*(5), 1722–1731. https://doi.org/10.1021/am302883m

Casillas, P. E. G., Gonzalez, C. A. R., & Pérez, C. A. M. (2012). Infrared Spectroscopy of Functionalized Magnetic Nanoparticles. In *Infrared Spectroscopy—Materials Science, Engineering and Technology*. IntechOpen. https://doi.org/10.5772/35481

Chen, Y.-C., Huang, X.-C., Luo, Y.-L., Chang, Y.-C., Hsieh, Y.-Z., & Hsu, H.-Y. (2013). Non-metallic nanomaterials in cancer theranostics: A review of silica- and carbon-based drug delivery systems. *Science and Technology of Advanced Materials*, *14*(4), 044407. https://doi.org/10.1088/1468-6996/14/4/044407

Chen, Z., Yin, J.-J., Zhou, Y.-T., Zhang, Y., Song, L., Song, M., Hu, S., & Gu, N. (2012). Dual Enzyme-like Activities of Iron Oxide Nanoparticles and Their Implication for Diminishing Cytotoxicity. *ACS Nano*, *6*(5), 4001–4012. https://doi.org/10.1021/nn300291r

Ciccarese, F., Raimondi, V., Sharova, E., Silic-Benussi, M., & Ciminale, V. (2020). Nanoparticles as Tools to Target Redox Homeostasis in Cancer Cells. *Antioxidants*, *9*(3), 211. https://doi.org/10.3390/antiox9030211

Cole, A. J., Yang, V. C., & David, A. E. (2011). Cancer Theranostics: The Rise of Targeted Magnetic Nanoparticles. *Trends in Biotechnology*, *29*(7), 323–332. https://doi.org/10.1016/j.tibtech.2011.03.001

Curry, T., Kopelman, R., Shilo, M., & Popovtzer, R. (2014). Multifunctional theranostic gold nanoparticles for targeted CT imaging and photothermal therapy. *Contrast Media & Molecular Imaging*, *9*(1), 53–61. https://doi.org/10.1002/cmmi.1563

Dadfar, S. M., Camozzi, D., Darguzyte, M., Roemhild, K., Varvarà, P., Metselaar, J., Banala, S., Straub, M., Güvener, N., Engelmann, U., Slabu, I., Buhl, M., van Leusen, J., Kögerler, P., Hermanns-Sachweh, B., Schulz, V., Kiessling, F., & Lammers, T. (2020). Size-isolation of superparamagnetic iron oxide nanoparticles improves MRI, MPI and hyperthermia performance. *Journal of Nanobiotechnology*, *18*(1), 22. https://doi.org/10.1186/s12951-020-0580-1

Dai, H., Shen, Q., Shao, J., Wang, W., Gao, F., & Dong, X. (2021). Small Molecular NIR-II Fluorophores for Cancer Phototheranostics. *The Innovation*, *2*(1), 100082. https://doi.org/10.1016/j.xinn.2021.100082

Decker, T., & Lohmann-Matthes, M.-L. (1988). A quick and simple method for the quantitation of lactate dehydrogenase release in measurements of cellular cytotoxicity and tumor necrosis factor (TNF) activity. *Journal of Immunological Methods*, *115*(1), 61–69. https://doi.org/10.1016/0022-1759(88)90310-9

Deng, Y.-H., Wang, C.-C., Hu, J.-H., Yang, W.-L., & Fu, S.-K. (2005). Investigation of formation of silica-coated magnetite nanoparticles *via* sol–gel approach. *Colloids and Surfaces A: Physicochemical and Engineering Aspects*, *262*(1), 87–93. https://doi.org/10.1016/j.colsurfa.2005.04.009

Di Corato, R., Béalle, G., Kolosnjaj-Tabi, J., Espinosa, A., Clément, O., Silva, A. K. A., Ménager, C., & Wilhelm, C. (2015). Combining magnetic hyperthermia and photodynamic therapy for tumor ablation with photoresponsive magnetic liposomes. *ACS Nano*, *9*(3), 2904–2916. https://doi.org/10.1021/nn506949t

Dolmans, D. E. J. G. J., Fukumura, D., & Jain, R. K. (2003). Photodynamic therapy for cancer. *Nature Reviews Cancer*, *3*(5), 380–387. https://doi.org/10.1038/nrc1071

Doroshow, J. H. (1995). Glutathione peroxidase and oxidative stress. *Toxicology Letters*, *82–83*, 395–398. https://doi.org/10.1016/0378-4274(95)03570-2

Dutta Chowdhury, A., Ganganboina, A. B., Tsai, Y.-C., Chiu, H.-C., & Doong, R.-A. (2018). Multifunctional GQDs-Concanavalin A@Fe_3O_4 nanocomposites for cancer cells detection and targeted drug delivery. *Analytica Chimica Acta*, *1027*, 109–120. https://doi.org/10.1016/j.aca.2018.04.029

Dysart, J. S., & Patterson, M. S. (2005). Characterization of Photofrin photobleaching for singlet oxygen dose estimation during photodynamic therapy of MLL cells$\less$i$\greater$in vitro$\less$/i$\greater$. *Physics in Medicine and Biology*, *50*(11), 2597–2616. https://doi.org/10.1088/0031-9155/50/11/011

Estelrich, J., & Busquets, M. A. (2018). Iron Oxide Nanoparticles in Photothermal Therapy. *Molecules*, *23*(7), 1567. https://doi.org/10.3390/molecules23071567

Fan, Y., & Zhang, Q. (2013). Development of liposomal formulations: From concept to clinical investigations. *Asian Journal of Pharmaceutical Sciences*, *8*(2), 81–87. https://doi.org/10.1016/j.ajps.2013.07.010

Fang, J., Islam, W., & Maeda, H. (2020). Exploiting the dynamics of the EPR effect and strategies to improve the therapeutic effects of nanomedicines by using EPR effect enhancers. *Advanced Drug Delivery Reviews*, *157*, 142–160. https://doi.org/10.1016/j.addr.2020.06.005

Fang, S., Lin, J., Li, C., Huang, P., Hou, W., Zhang, C., Liu, J., Huang, S., Luo, Y., Fan, W., Cui, D., Xu, Y., & Li, Z. (2017). Dual-Stimuli Responsive Nanotheranostics for Multimodal Imaging Guided Trimodal Synergistic Therapy. *Small*, *13*(6), 1602580. https://doi.org/10.1002/smll.201602580

Fang, S., Yu, X., Ding, H., Han, J., & Feng, J. (2018). Effects of intracellular iron overload on cell death and identification of potent cell death inhibitors. *Biochemical and Biophysical Research Communications*, *503*(1), 297–303. https://doi.org/10.1016/j.bbrc.2018.06.019

Feng, G., Zhang, G.-Q., & Ding, D. (2020). Design of superior phototheranostic agents guided by Jablonski diagrams. *Chemical Society Reviews*, *49*(22), 8179–8234. https://doi.org/10.1039/D0CS00671H

Ferlay, J., Colombet, M., Soerjomataram, I., Parkin, D. M., Piñeros, M., Znaor, A., & Bray, F. (2021). Cancer statistics for the year 2020: An overview. *International Journal of Cancer*, *149*(4), 778–789. https://doi.org/10.1002/ijc.33588

Fernández-Barahona, I., Muñoz-Hernando, M., & Herranz, F. (2019). Microwave-Driven Synthesis of Iron-Oxide Nanoparticles for Molecular Imaging. *Molecules*, *24*(7), 1224. https://doi.org/10.3390/molecules24071224

Ferrauto, G., Carniato, F., Gregorio, E. D., Tei, L., Botta, M., & Aime, S. (2017). Large photoacoustic effect enhancement for ICG confined inside MCM-41 mesoporous silica nanoparticles. *Nanoscale*, *9*(1), 99–103. https://doi.org/10.1039/C6NR08282C

Folgueira, I., Lamas, J., de Felipe, A. P., Sueiro, R. A., & Leiro, J. M. (2019). Identification and Molecular Characterization of Superoxide Dismutases Isolated from A Scuticociliate Parasite: Physiological Role in Oxidative Stress. *Scientific Reports*, *9*(1), 13329. https://doi.org/10.1038/s41598-019-49750-5

Fox, L., Beyer, K., Rammant, E., Morcom, E., Van Hemelrijck, M., Sullivan, R., Vanderpuye, V., Lombe, D., Tsunoda, A. T., Kutluk, T., Bhoo-Pathy, N., Pramesh, S. C., Yusuf, A., Booth, C. M., Shamieh, O., Siesling, S., & Mukherji, D. (2021). Impact of the COVID-19 Pandemic on Cancer Researchers in 2020: A Qualitative Study of Events to Inform Mitigation Strategies. *Frontiers in Public Health*, *9*. https://www.frontiersin.org/article/10.3389/fpubh.2021.741223

Friedrichs, S., & Bowman, D. M. (2021). COVID-19 may become nanomedicine's finest hour yet. *Nature Nanotechnology*, *16*(4), 362–364. https://doi.org/10.1038/s41565-021-00901-8

Fu, R., Wang, W., Han, R., & Chen, K. (2008). Preparation and characterization of γ-Fe_2O_3/ZnO composite particles. *Materials Letters,* *62*(25), 4066–4068. https://doi.org/10.1016/j.matlet.2008.05.006

Fuentes-García, J. A., Carvalho Alavarse, A., Moreno Maldonado, A. C., Toro-Córdova, A., Ibarra, M. R., & Goya, G. F. (2020). Simple Sonochemical Method to Optimize the Heating Efficiency of Magnetic Nanoparticles for Magnetic Fluid Hyperthermia. *ACS Omega*, *5*(41), 26357–26364. https://doi.org/10.1021/acsomega.0c02212

Galluzzi, L., Vitale, I., Aaronson, S. A., Abrams, J. M., Adam, D., Agostinis, P., Alnemri, E. S., Altucci, L., Amelio, I., Andrews, D. W., Annicchiarico-Petruzzelli, M., Antonov, A. V., Arama, E., Baehrecke, E. H., Barlev, N. A., Bazan, N. G., Bernassola, F.,

Bertrand, M. J. M., Bianchi, K., … Kroemer, G. (2018). Molecular mechanisms of cell death: Recommendations of the Nomenclature Committee on Cell Death 2018. *Cell Death & Differentiation*, *25*(3), 486–541. https://doi.org/10.1038/s41418-017-0012-4

Galstyan, A., & Dobrindt, U. (2019). Determining and unravelling origins of reduced photoinactivation efficacy of bacteria in milk. *Journal of Photochemistry and Photobiology B: Biology*, *197*, 111554. https://doi.org/10.1016/j.jphotobiol.2019.111554

Gilchrist, R. K., Medal, R., Shorey, W. D., Hanselman, R. C., Parrott, J. C., & Taylor, C. B. (1957). Selective Inductive Heating of Lymph Nodes. *Annals of Surgery*, *146*(4), 596–606.

Golombek, S. K., May, J.-N., Theek, B., Appold, L., Drude, N., Kiessling, F., & Lammers, T. (2018). Tumor targeting *via* EPR: Strategies to enhance patient responses. *Advanced Drug Delivery Reviews*, *130*, 17–38. https://doi.org/10.1016/j.addr.2018.07.007

Gonzalez-Fernandez, M. A., Torres, T. E., Andrés-Vergés, M., Costo, R., de la Presa, P., Serna, C. J., Morales, M. P., Marquina, C., Ibarra, M. R., & Goya, G. F. (2009). Magnetic nanoparticles for power absorption: Optimizing size, shape and magnetic properties. *Journal of Solid State Chemistry*, *182*(10), 2779–2784. https://doi.org/10.1016/j.jssc.2009.07.047

Gupta, R., Pancholi, K., De Sa, R., Murray, D., Huo, D., Droubi, G., White, M., & Njuguna, J. (2019). Effect of Oleic Acid Coating of Iron Oxide Nanoparticles on Properties of Magnetic Polyamide-6 Nanocomposite. *JOM*, *71*(9), 3119–3128. https://doi.org/10.1007/s11837-019-03622-5

Hadian, K., & Stockwell, B. R. (2020). SnapShot: Ferroptosis. *Cell*, *181*(5), 1188-1188.e1. https://doi.org/10.1016/j.cell.2020.04.039

Hameed, S., Chen, H., Irfan, M., Bajwa, S. Z., Khan, W. S., Baig, S. M., & Dai, Z. (2019). Fluorescence Guided Sentinel Lymph Node Mapping: From Current Molecular Probes to Future Multimodal Nanoprobes. *Bioconjugate Chemistry*, *30*(1), 13–28. https://doi.org/10.1021/acs.bioconjchem.8b00812

Han, C., Liu, Y., Dai, R., Ismail, N., Su, W., & Li, B. (2020). Ferroptosis and Its Potential Role in Human Diseases. *Frontiers in Pharmacology*, *11*. https://www.frontiersin.org/articles/10.3389/fphar.2020.00239

Hanahan, D. (2022). Hallmarks of Cancer: New Dimensions. *Cancer Discovery*, *12*(1), 31–46. https://doi.org/10.1158/2159-8290.CD-21-1059

Hanahan, D., & Weinberg, R. A. (2000). The Hallmarks of Cancer. *Cell*, *100*(1), 57–70. https://doi.org/10.1016/S0092-8674(00)81683-9

Hao, S., Liang, B., Huang, Q., Dong, S., Wu, Z., He, W., & Shi, M. (2018). Metabolic networks in ferroptosis. *Oncology Letters*, *15*(4), 5405–5411. https://doi.org/10.3892/ol.2018.8066

Harabech, M., Leliaert, J., Coene, A., Crevecoeur, G., Van Roost, D., & Dupré, L. (2017). The effect of the magnetic nanoparticle's size dependence of the relaxation time constant on the specific loss power of magnetic nanoparticle hyperthermia. *Journal of Magnetism and Magnetic Materials*, *426*, 206–210. https://doi.org/10.1016/j.jmmm.2016.11.079

Held, P. (2010). *An Introduction to Reactive Oxygen Species Measurement of ROS in Cells*. https://www.semanticscholar.org/paper/An-Introduction-to-Reactive-Oxygen-Species-of-ROS-Held/ed3385e1ac7f8d604e2d3e4fa91c668d925f51fe

Hergt, R., Dutz, S., Müller, R., & Zeisberger, M. (2006). Magnetic particle hyperthermia: Nanoparticle magnetism and materials development for cancer therapy. *Journal of Physics: Condensed Matter*, *18*(38), S2919–S2934. https://doi.org/10.1088/0953-8984/18/38/S26

Herrero de la Parte, B., Rodrigo, I., Gutiérrez-Basoa, J., Iturrizaga Correcher, S., Mar Medina, C., Echevarría-Uraga, J. J., Garcia, J. A., Plazaola, F., & García-Alonso, I. (2022). Proposal of New Safety Limits for In Vivo Experiments of Magnetic Hyperthermia Antitumor Therapy. *Cancers, 14*(13), 3084. https://doi.org/10.3390/cancers14133084

Holohan, C., Van Schaeybroeck, S., Longley, D. B., & Johnston, P. G. (2013). Cancer drug resistance: An evolving paradigm. *Nature Reviews Cancer*, *13*(10), 714–726. https://doi.org/10.1038/nrc3599

Hong, G., Antaris, A. L., & Dai, H. (2017). Near-infrared fluorophores for biomedical imaging. *Nature Biomedical Engineering*, *1*(1), 1–22. https://doi.org/10.1038/s41551-016-0010

Hong, S. ho, & Choi, Y. (2018). Mesoporous silica-based nanoplatforms for the delivery of photodynamic therapy agents. *Journal of Pharmaceutical Investigation*, *48*(1), 3–17. https://doi.org/10.1007/s40005-017-0356-2

Huang, C., Zhang, Z., Guo, Q., Zhang, L., Fan, F., Qin, Y., Wang, H., Zhou, S., Ou-Yang, W., Sun, H., Leng, X., Pan, X., Kong, D., Zhang, L., & Zhu, D. (2019). A Dual-Model Imaging Theragnostic System Based on Mesoporous Silica Nanoparticles for

Enhanced Cancer Phototherapy. *Advanced Healthcare Materials*, *8*(19), 1900840. https://doi.org/10.1002/adhm.201900840

Huang, M., Xu, C., Yang, S., Zhang, Z., Wei, Z., Wu, M., & Xue, F. (2022). Vehicle-Free Nanotheranostic Self-Assembled from Clinically Approved Dyes for Cancer Fluorescence Imaging and Photothermal/Photodynamic Combinational Therapy. *Pharmaceutics*, *14*(5), 1074. https://doi.org/10.3390/pharmaceutics14051074

ISO/TR 10993-22:2017. (2017). *Biological evaluation of medical devices—Part 22: Guidance on nanomaterials*. https://www.iso.org/obp/ui/#iso:std:iso:tr:10993:-22:ed-1:v1:en (Accessed: 30 April 2022)

Iyer, A. K., Khaled, G., Fang, J., & Maeda, H. (2006). Exploiting the enhanced permeability and retention effect for tumor targeting. *Drug Discovery Today*, *11*(17), 812–818. https://doi.org/10.1016/j.drudis.2006.07.005

Jamir, M., Islam, R., Pandey, L. M., & Borah, J. P. (2021). Effect of surface functionalization on the heating efficiency of magnetite nanoclusters for hyperthermia application. *Journal of Alloys and Compounds*, *854*, 157248. https://doi.org/10.1016/j.jallcom.2020.157248

Jayakiran, M. (2015). Apoptosis-Biochemistry: A Mini Review. *Journal of Clinical & Experimental Pathology*, *05*(01). https://doi.org/10.4172/2161-0681.1000205

Jiang, L., Kon, N., Li, T., Wang, S.-J., Su, T., Hibshoosh, H., Baer, R., & Gu, W. (2015). Ferroptosis as a p53-mediated activity during tumour suppression. *Nature*, *520*(7545), 57–62. https://doi.org/10.1038/nature14344

Jiang, Y., & Pu, K. (2018). Multimodal Biophotonics of Semiconducting Polymer Nanoparticles. *Accounts of Chemical Research*, *51*(8), 1840–1849. https://doi.org/10.1021/acs.accounts.8b00242

Jung, B., Vullev, V. I., & Anvari, B. (2014). Revisiting Indocyanine Green: Effects of Serum and Physiological Temperature on Absorption and Fluorescence Characteristics. *IEEE Journal of Selected Topics in Quantum Electronics*, *20*(2), 149–157. https://doi.org/10.1109/JSTQE.2013.2278674

Kaja, S., Payne, A. J., Naumchuk, Y., & Koulen, P. (2017). Quantification of lactate dehydrogenase for cell viability testing using cell lines and primary cultured astrocytes. *Current Protocols in Toxicology*, *72*, 2.26.1-2.26.10. https://doi.org/10.1002/cptx.21

Kakkar, P., Das, B., & Viswanathan, P. N. (1984). A modified spectrophotometric assay of superoxide dismutase. *Indian Journal of Biochemistry & Biophysics*, *21*(2), 130–132.

Kato, Y., Zhu, W., Backer, M. V., Neoh, C. C., Hapuarachchige, S., Sarkar, S. K., Backer, J. M., & Artemov, D. (2015). Noninvasive Imaging of Liposomal Delivery of Superparamagnetic Iron Oxide Nanoparticles to Orthotopic Human Breast Tumor in Mice. *Pharmaceutical Research*, *32*(11), 3746–3755. https://doi.org/10.1007/s11095-015-1736-9

Ke, L., Wei, F., Xie, L., Karges, J., Chen, Y., Ji, L., & Chao, H. (2022). A Biodegradable Iridium(III) Coordination Polymer for Enhanced Two-Photon Photodynamic Therapy Using an Apoptosis–Ferroptosis Hybrid Pathway. *Angewandte Chemie International Edition*, *61*(28), e202205429. https://doi.org/10.1002/anie.202205429

Kemp, J. A., & Kwon, Y. J. (2021). Cancer nanotechnology: Current status and perspectives. *Nano Convergence*, *8*(1), 34. https://doi.org/10.1186/s40580-021-00282-7

Kenchegowda, M., Rahamathulla, M., Hani, U., Begum, M. Y., Guruswamy, S., Osmani, R. A. M., Gowrav, M. P., Alshehri, S., Ghoneim, M. M., Alshlowi, A., & Gowda, D. V. (2021). Smart Nanocarriers as an Emerging Platform for Cancer Therapy: A Review. *Molecules*, *27*(1), 146. https://doi.org/10.3390/molecules27010146

Kettiger, H., Sen Karaman, D., Schiesser, L., Rosenholm, J. M., & Huwyler, J. (2015). Comparative safety evaluation of silica-based particles. *Toxicology in Vitro*, *30*(1, Part B), 355–363. https://doi.org/10.1016/j.tiv.2015.09.030

Kim, D., Lee, N., Park, M., Kim, B. H., An, K., & Hyeon, T. (2009). Synthesis of Uniform Ferrimagnetic Magnetite Nanocubes. *Journal of the American Chemical Society*, *131*(2), 454–455. https://doi.org/10.1021/ja8086906

Kim, J.-S., Yoon, T.-J., Yu, K.-N., Noh, M. S., Woo, M., Kim, B.-G., Lee, K.-H., Sohn, B.-H., Park, S.-B., Lee, J.-K., & Cho, M.-H. (2006). Cellular uptake of magnetic nanoparticle is mediated through energy-dependent endocytosis in A549 cells. *Journal of Veterinary Science*, *7*(4), 321–326. https://doi.org/10.4142/jvs.2006.7.4.321

Kim, K. S., Kim, J., Lee, J. Y., Matsuda, S., Hideshima, S., Mori, Y., Osaka, T., & Na, K. (2016). Stimuli-responsive magnetic nanoparticles for tumor-targeted bimodal imaging and photodynamic/hyperthermia combination therapy. *Nanoscale*, *8*(22), 11625–11634. https://doi.org/10.1039/C6NR02273A

Klem, M. T., Young, M., & Douglas, T. (2005). Biomimetic magnetic nanoparticles. *Materials Today*, *8*(9), 28–37. https://doi.org/10.1016/S1369-7021(05)71078-6

Kohl, C., Weil, T., Qu, J., & Müllen, K. (2004). Towards Highly Fluorescent and Water-Soluble Perylene Dyes. *Chemistry – A European Journal*, *10*(21), 5297–5310. https://doi.org/10.1002/chem.200400291

Kokudo, N., & Ishizawa, T. (2012). Clinical Application of Fluorescence Imaging of Liver Cancer Using Indocyanine Green. *Liver Cancer*, *1*(1), 15–21. https://doi.org/10.1159/000339017

Kraft, J. C., & Ho, R. J. Y. (2014). Interactions of Indocyanine Green and Lipid in Enhancing Near-Infrared Fluorescence Properties: The Basis for Near-Infrared Imaging in Vivo. *Biochemistry*, *53*(8), 1275–1283. https://doi.org/10.1021/bi500021j

Kudr, J., Haddad, Y., Richtera, L., Heger, Z., Cernak, M., Adam, V., & Zitka, O. (2017). Magnetic Nanoparticles: From Design and Synthesis to Real World Applications. *Nanomaterials*, *7*(9), 243. https://doi.org/10.3390/nano7090243

Kumar, P., Anuradha, & Roy, I. (2014). Optically and magnetically doped ormosil nanoparticles for bioimaging: Synthesis, characterization, and in vitro studies. *RSC Advances*, *4*(31), 16181–16187. https://doi.org/10.1039/C4RA00331D

Kumar, P., Nagarajan, A., & Uchil, P. D. (2018). Analysis of Cell Viability by the Lactate Dehydrogenase Assay. *Cold Spring Harbor Protocols*, *2018*(6). https://doi.org/10.1101/pdb.prot095497

Kwon, S. G., Piao, Y., Park, J., Angappane, S., Jo, Y., Hwang, N.-M., Park, J.-G., & Hyeon, T. (2007). Kinetics of Monodisperse Iron Oxide Nanocrystal Formation by "Heating-Up" Process. *Journal of the American Chemical Society*, *129*(41), 12571–12584. https://doi.org/10.1021/ja074633q

Lakshminarayanan, S., Shereen, M. F., Niraimathi, K. L., Brindha, P., & Arumugam, A. (2021). One-pot green synthesis of iron oxide nanoparticles from Bauhinia tomentosa: Characterization and application towards synthesis of 1, 3 diolein. *Scientific Reports*, *11*(1), 8643. https://doi.org/10.1038/s41598-021-87960-y

Lamichhane, N., Sharifabad, M. E., Hodgson, B., Mercer, T., & Sen, T. (2022). Chapter 13-Superparamagnetic iron oxide nanoparticles (SPIONs) as therapeutic and diagnostic agents. In P. Kesharwani & K. K. Singh (Eds.), *Nanoparticle Therapeutics* (pp. 455–497). Academic Press. https://doi.org/10.1016/B978-0-12-820757-4.00003-X

Lamichhane, N., Sharma, S., Parul, Verma, A. K., Roy, I., & Sen, T. (2021). Iron Oxide-Based Magneto-Optical Nanocomposites for In Vivo Biomedical Applications. *Biomedicines*, *9*(3), 288. https://doi.org/10.3390/biomedicines9030288

Lassenberger, A., Grünewald, T. A., van Oostrum, P. D. J., Rennhofer, H., Amenitsch, H., Zirbs, R., Lichtenegger, H. C., & Reimhult, E. (2017). Monodisperse Iron Oxide Nanoparticles by Thermal Decomposition: Elucidating Particle Formation by Second-Resolved in Situ Small-Angle X-ray Scattering. *Chemistry of Materials*, *29*(10), 4511–4522. https://doi.org/10.1021/acs.chemmater.7b01207

Latunde-Dada, G. O. (2017). Ferroptosis: Role of lipid peroxidation, iron and ferritinophagy. *Biochimica Et Biophysica Acta. General Subjects*, *1861*(8), 1893–1900. https://doi.org/10.1016/j.bbagen.2017.05.019

Laurent, S., Dutz, S., Häfeli, U. O., & Mahmoudi, M. (2011). Magnetic fluid hyperthermia: Focus on superparamagnetic iron oxide nanoparticles. *Advances in Colloid and Interface Science*, *166*(1–2), 8–23. https://doi.org/10.1016/j.cis.2011.04.003

Lee, C.-H., Cheng, S.-H., Wang, Y.-J., Chen, Y.-C., Chen, N.-T., Souris, J., Chen, C.-T., Mou, C.-Y., Yang, C.-S., & Lo, L.-W. (2009). Near-Infrared Mesoporous Silica Nanoparticles for Optical Imaging: Characterization and In Vivo Biodistribution. *Advanced Functional Materials*, *19*(2), 215–222. https://doi.org/10.1002/adfm.200800753

Lee, S., George Thomas, R., Ju Moon, M., Ju Park, H., Park, I.-K., Lee, B.-I., & Yeon Jeong, Y. (2017). Near-Infrared Heptamethine Cyanine Based Iron Oxide Nanoparticles for Tumor Targeted Multimodal Imaging and Photothermal Therapy. *Scientific Reports*, *7*, 2108. https://doi.org/10.1038/s41598-017-01108-5

Lee, S., Lee, M. W., Cho, H. S., Song, J. W., Nam, H. S., Oh, D. J., Park, K., Oh, W.-Y., Yoo, H., & Kim, J. W. (2014). Fully Integrated High-Speed Intravascular Optical Coherence Tomography/Near-Infrared Fluorescence Structural/Molecular Imaging In Vivo Using a Clinically Available Near-Infrared Fluorescence–Emitting Indocyanine Green to Detect Inflamed Lipid-Rich Atheromata in Coronary-Sized Vessels. *Circulation: Cardiovascular Interventions*, *7*(4), 560–569. https://doi.org/10.1161/CIRCINTERVENTIONS.114.001498

Lee, S., Yun, H.-S., & Kim, S.-H. (2011). The comparative effects of mesoporous silica nanoparticles and colloidal silica on inflammation and apoptosis. *Biomaterials*, *32*(35), 9434–9443. https://doi.org/10.1016/j.biomaterials.2011.08.042

Lemine, O. M., Omri, K., Zhang, B., El Mir, L., Sajieddine, M., Alyamani, A., & Bououdina, M. (2012). Sol–gel synthesis of 8nm magnetite (Fe_3O_4) nanoparticles and their magnetic properties. *Superlattices and Microstructures*, *52*(4), 793–799. https://doi.org/10.1016/j.spmi.2012.07.009

Leslie-Pelecky, D. L., & Rieke, R. D. (1996). Magnetic Properties of Nanostructured Materials. *Chemistry of Materials*, *8*(8), 1770–1783. https://doi.org/10.1021/cm960077f

Li, S., Cheng, D., He, L., & Yuan, L. (2021). Recent Progresses in NIR-I/II Fluorescence Imaging for Surgical Navigation. *Frontiers in Bioengineering and Biotechnology*, *9*. https://www.frontiersin.org/article/10.3389/fbioe.2021.768698

Liao, J., Wei, X., Ran, B., Peng, J., Qu, Y., & Qian, Z. (2017). Polymer hybrid magnetic nanocapsules encapsulating IR820 and PTX for external magnetic field-guided tumor targeting and multifunctional theranostics. *Nanoscale*, *9*(7), 2479–2491. https://doi.org/10.1039/C7NR00033B

Lin, H., Zhou, Y., Wang, J., Wang, H., Yao, T., Chen, H., Zheng, H., Zhang, Y., Ren, E., Jiang, L., Chu, C., Chen, X., Mao, J., Wang, F., & Liu, G. (2021). Repurposing ICG enables MR/PA imaging signal amplification and iron depletion for iron-overload disorders. *Science Advances*, *7*(51), eabl5862. https://doi.org/10.1126/sciadv.abl5862

Liu, L., Li, L., Li, M., & Luo, Z. (2021). Autophagy-Dependent Ferroptosis as a Therapeutic Target in Cancer. *ChemMedChem*, *16*(19), 2942–2950. https://doi.org/10.1002/cmdc.202100334

Liu, P., Peng, Y., Ding, J., & Zhou, W. (2022). Fenton metal nanomedicines for imaging-guided combinatorial chemodynamic therapy against cancer. *Asian Journal of Pharmaceutical Sciences*, *17*(2), 177–192. https://doi.org/10.1016/j.ajps.2021.10.003

Liu, Z., Rong, P., Yu, L., Zhang, X., Yang, C., Guo, F., Zhao, Y., Zhou, K., Wang, W., & Zeng, W. (2015). Dual-Modality Noninvasive Mapping of Sentinel Lymph Node by Photoacoustic and Near-Infrared Fluorescent Imaging Using Dye-Loaded Mesoporous Silica Nanoparticles. *Molecular Pharmaceutics*, *12*(9), 3119–3128. https://doi.org/10.1021/mp500698b

Lu, A.-H., Salabas, E. L., & Schüth, F. (2007). Magnetic Nanoparticles: Synthesis, Protection, Functionalization, and Application. *Angewandte Chemie International Edition*, *46*(8), 1222–1244. https://doi.org/10.1002/anie.200602866

Lv, R., Wang, D., Xiao, L., Chen, G., Xia, J., & Prasad, P. N. (2017). Stable ICG-loaded upconversion nanoparticles: Silica core/shell theranostic nanoplatform for dual-modal upconversion and photoacoustic imaging together with photothermal therapy. *Scientific Reports*, *7*(1), 15753. https://doi.org/10.1038/s41598-017-16016-x

Ma, Y., Liu, X., Ma, Q., & Liu, Y. (2018). Near-infrared nanoparticles based on indocyanine green-conjugated albumin: A versatile platform for imaging-guided synergistic tumor chemo-phototherapy with temperature-responsive drug release. *OncoTargets and Therapy*, *11*, 8517–8528. https://doi.org/10.2147/OTT.S183887

Maeda, H., Nakamura, H., & Fang, J. (2013). The EPR effect for macromolecular drug delivery to solid tumors: Improvement of tumor uptake, lowering of systemic toxicity, and distinct tumor imaging in vivo. *Advanced Drug Delivery Reviews*, *65*(1), 71–79. https://doi.org/10.1016/j.addr.2012.10.002

Maeda, H., Tsukigawa, K., & Fang, J. (2016). A Retrospective 30 Years After Discovery of the Enhanced Permeability and Retention Effect of Solid Tumors: Next-Generation Chemotherapeutics and Photodynamic Therapy—Problems, Solutions, and Prospects. *Microcirculation*, *23*(3), 173–182. https://doi.org/10.1111/micc.12228

MagForce USA. (2022). *Stage 2B of: A Pivotal, Prospective, Three-Stage, Single-Arm Study of Focal Ablation of the Prostate With NanoTherm® Therapy System for a Limited-Volume, Clinically Localized, Intermediate-Risk Prostate Cancer* (Clinical Trial Registration No. NCT05010759). clinicaltrials.gov. https://clinicaltrials.gov/ct2/show/NCT05010759

Mahdavi, M., Namvar, F., Ahmad, M. B., & Mohamad, R. (2013). Green Biosynthesis and Characterization of Magnetic Iron Oxide (Fe_3O_4) Nanoparticles Using Seaweed (Sargassum muticum) Aqueous Extract. *Molecules*, *18*(5), 5954–5964. https://doi.org/10.3390/molecules18055954

Mahmoudi, K., Bouras, A., Bozec, D., Ivkov, R., & Hadjipanayis, C. (2018). Magnetic hyperthermia therapy for the treatment of glioblastoma: a review of the therapy's history, efficacy and application in humans. *International journal of hyperthermia, 34*(8), 1316–1328. https://doi.org/10.1080/02656736.2018.1430867

Mahmoudi, M., Sant, S., Wang, B., Laurent, S., & Sen, T. (2011). Superparamagnetic iron oxide nanoparticles (SPIONs): Development, surface modification and applications in chemotherapy. *Advanced Drug Delivery Reviews*, *63*(1), 24–46. https://doi.org/10.1016/j.addr.2010.05.006

Mahmoudi, M., Simchi, A., Imani, M., Shokrgozar, M. A., Milani, A. S., Häfeli, U. O., & Stroeve, P. (2010). A new approach for the in vitro identification of the cytotoxicity of superparamagnetic iron oxide nanoparticles. *Colloids and Surfaces. B, Biointerfaces*, *75*(1), 300–309. https://doi.org/10.1016/j.colsurfb.2009.08.044

Mahmoudi, M., Simchi, A., Milani, A. S., & Stroeve, P. (2009). Cell toxicity of superparamagnetic iron oxide nanoparticles. *Journal of Colloid and Interface Science*, *336*(2), 510–518. https://doi.org/10.1016/j.jcis.2009.04.046

Mascolo, M. C., Pei, Y., & Ring, T. A. (2013). Room Temperature Co-Precipitation Synthesis of Magnetite Nanoparticles in a Large pH Window with Different Bases. *Materials*, *6*(12), 5549–5567. https://doi.org/10.3390/ma6125549

Matsumura, Y., & Maeda, H. (1986). *A New Concept for Macromolecular Therapeutics in Cancer Chemotherapy: Mechanism of Tumoritropic Accumulation of Proteins and the Antitumor Agent Smancs*. 6.

Mazuel, F., Espinosa, A., Luciani, N., Reffay, M., Le Borgne, R., Motte, L., Desboeufs, K., Michel, A., Pellegrino, T., Lalatonne, Y., & Wilhelm, C. (2016). Massive Intracellular Biodegradation of Iron Oxide Nanoparticles Evidenced Magnetically at Single-Endosome and Tissue Levels. *ACS Nano*, *10*(8), 7627–7638. https://doi.org/10.1021/acsnano.6b02876

Mitran, R.-A., Georgescu, D., Stanica, N., Matei, C., & Berger, D. (2017). Coating Magnetite Nanoparticles with Mesostructured Silica Shell of Different Pore Size and Geometry. *Revista Romana de Materiale*, *47*(1), 437–443.

Mohammadinejad, R., Moosavi, M. A., Tavakol, S., Vardar, D. Ö., Hosseini, A., Rahmati, M., Dini, L., Hussain, S., Mandegary, A., & Klionsky, D. J. (2019). Necrotic, apoptotic and autophagic cell fates triggered by nanoparticles. *Autophagy*, *15*(1), 4–33. https://doi.org/10.1080/15548627.2018.1509171

Montiel Schneider, M. G., Martín, M. J., Otarola, J., Vakarelska, E., Simeonov, V., Lassalle, V., & Nedyalkova, M. (2022). Biomedical Applications of Iron Oxide Nanoparticles: Current Insights Progress and Perspectives. *Pharmaceutics*, *14*(1), 204. https://doi.org/10.3390/pharmaceutics14010204

Mou, Y., Wang, J., Wu, J., He, D., Zhang, C., Duan, C., & Li, B. (2019). Ferroptosis, a new form of cell death: Opportunities and challenges in cancer. *Journal of Hematology & Oncology*, *12*, 34. https://doi.org/10.1186/s13045-019-0720-y

Napierska, D., Thomassen, L. C. J., Rabolli, V., Lison, D., Gonzalez, L., Kirsch-Volders, M., Martens, J. A., & Hoet, P. H. (2009). Size-Dependent Cytotoxicity of Monodisperse

Silica Nanoparticles in Human Endothelial Cells. *Small*, *5*(7), 846–853. https://doi.org/10.1002/smll.200800461

Niu, C., Xu, Y., An, S., Zhang, M., Hu, Y., Wang, L., & Peng, Q. (2017). Near-infrared induced phase-shifted ICG/Fe_3O_4 loaded PLGA nanoparticles for photothermal tumor ablation. *Scientific Reports*, *7*, 5490. https://doi.org/10.1038/s41598-017-06122-1

Noeman, S. A., Hamooda, H. E., & Baalash, A. A. (2011). Biochemical Study of Oxidative Stress Markers in the Liver, Kidney and Heart of High Fat Diet Induced Obesity in Rats. *Diabetology & Metabolic Syndrome*, *3*, 17. https://doi.org/10.1186/1758-5996-3-17

Onda, N., Kimura, M., Yoshida, T., & Shibutani, M. (2016). Preferential tumor cellular uptake and retention of indocyanine green for in vivo tumor imaging. *International Journal of Cancer*, *139*(3), 673–682. https://doi.org/10.1002/ijc.30102

Ormond, A. B., & Freeman, H. S. (2013). Dye Sensitizers for Photodynamic Therapy. *Materials (Basel, Switzerland)*, *6*(3), 817–840. https://doi.org/10.3390/ma6030817

Paglia, D. E., & Valentine, W. N. (1967). Studies on the quantitative and qualitative characterization of erythrocyte glutathione peroxidase. *The Journal of Laboratory and Clinical Medicine*, *70*(1), 158–169. https://doi.org/10.5555/uri:pii:0022214367900765

Patel, J. (1996). *Liposomal doxorubicin: Doxil®*. *Journal of Oncology Pharmacy Practice, 2*(4), 201-210. https://doi.org/10.1177/107815529600200402

Patil, R. M., Thorat, N. D., Shete, P. B., Bedge, P. A., Gavde, S., Joshi, M. G., Tofail, S. A. M., & Bohara, R. A. (2018). Comprehensive cytotoxicity studies of superparamagnetic iron oxide nanoparticles. *Biochemistry and Biophysics Reports*, *13*, 63–72. https://doi.org/10.1016/j.bbrep.2017.12.002

Patil-Sen, Y., Torino, E., Sarno, F. D., Ponsiglione, A. M., Chhabria, V., Ahmed, W., & Mercer, T. (2020). Biocompatible superparamagnetic core-shell nanoparticles for potential use in hyperthermia-enabled drug release and as an enhanced contrast agent. *Nanotechnology*, *31*(37), 375102. https://doi.org/10.1088/1361-6528/ab91f6

Peer, D., Karp, J. M., Hong, S., Farokhzad, O. C., Margalit, R., & Langer, R. (2007). Nanocarriers as an emerging platform for cancer therapy. *Nature Nanotechnology*, *2*(12), 751–760. https://doi.org/10.1038/nnano.2007.387

Pita, R., Ehmann, F., & Papaluca, M. (2016). Nanomedicines in the EU—Regulatory Overview. *The AAPS Journal*, *18*(6), 1576–1582. https://doi.org/10.1208/s12248-016-9967-1

Polom, W., Markuszewski, M., Rho, Y. S., & Matuszewski, M. (2014). Usage of invisible near infrared light (NIR) fluorescence with indocyanine green (ICG) and methylene blue (MB) in urological oncology. Part 1. *Central European Journal of Urology*, *67*(2), 142–148. https://doi.org/10.5173/ceju.2014.02.art5

Qi, H., Yan, B., & Li, C. (2010). Preparation and magnetic properties of magnetite nanoparticles by sol-gel method. *2010 3rd International Nanoelectronics Conference (INEC)*, 888–889. https://doi.org/10.1109/INEC.2010.5425143

Q. Yin, N., Wu, P., H. Yang, T., & Wang, M. (2017). Preparation and study of a mesoporous silica-coated Fe 3 O 4 photothermal nanoprobe. *RSC Advances*, *7*(15), 9123–9129. https://doi.org/10.1039/C6RA28413B

Reddy, G. R., Bhojani, M. S., McConville, P., Moody, J., Moffat, B. A., Hall, D. E., Kim, G., Koo, Y.-E. L., Woolliscroft, M. J., Sugai, J. V., Johnson, T. D., Philbert, M. A., Kopelman, R., Rehemtulla, A., & Ross, B. D. (2006). Vascular targeted nanoparticles for imaging and treatment of brain tumors. *Clinical Cancer Research: An Official Journal of the American Association for Cancer Research*, *12*(22), 6677–6686. https://doi.org/10.1158/1078-0432.CCR-06-0946

Rosenholm, J. M., Sahlgren, C., & Lindén, M. (2010). Towards multifunctional, targeted drug delivery systems using mesoporous silica nanoparticles – opportunities & challenges. *Nanoscale*, *2*(10), 1870–1883. https://doi.org/10.1039/C0NR00156B

Rosensweig, R. E. (2002). Heating magnetic fluid with alternating magnetic field. *Journal of Magnetism and Magnetic Materials*, *252*, 370–374. https://doi.org/10.1016/S0304-8853(02)00706-0

Rurack, K., & Spieles, M. (2011). Fluorescence Quantum Yields of a Series of Red and Near-Infrared Dyes Emitting at 600−1000 nm. *Analytical Chemistry*, *83*(4), 1232–1242. https://doi.org/10.1021/ac101329h

Salvioni, L., Rizzuto, M. A., Bertolini, J. A., Pandolfi, L., Colombo, M., & Prosperi, D. (2019). Thirty Years of Cancer Nanomedicine: Success, Frustration, and Hope. *Cancers*, *11*(12), 1855. https://doi.org/10.3390/cancers11121855

Santra, S., Tapec, R., Theodoropoulou, N., Dobson, J., Hebard, A., & Tan, W. (2001). Synthesis and Characterization of Silica-Coated Iron Oxide Nanoparticles in Microemulsion: The Effect of Nonionic Surfactants. *Langmuir*, *17*(10), 2900–2906. https://doi.org/10.1021/la0008636

Sanz, B., Calatayud, M. P., Torres, T. E., Fanarraga, M. L., Ibarra, M. R., & Goya, G. F. (2017). Magnetic hyperthermia enhances cell toxicity with respect to exogenous heating. *Biomaterials*, *114*, 62–70. https://doi.org/10.1016/j.biomaterials.2016.11.008

Sato, T., Iijima, T., Seki, M., & Inagaki, N. (1987). Magnetic properties of ultrafine ferrite particles. *Journal of Magnetism and Magnetic Materials*, *65*(2), 252–256. https://doi.org/10.1016/0304-8853(87)90044-8

Sen, T., Bruce, I. J., & Mercer, T. (2010). Fabrication of novel hierarchically ordered porous magnetic nanocomposites for bio-catalysis. *Chemical Communications*, *46*(36), 6807–6809. https://doi.org/10.1039/C0CC01747G

Sen, T., Magdassi, S., Nizri, G., & Bruce, I. J. (2006). Dispersion of magnetic nanoparticles in suspension. *Micro & Nano Letters*, *1*(1), 39–42. https://doi.org/10.1049/mnl:20065033

Sen, T., Sebastianelli, A., & Bruce, I. J. (2006). Mesoporous Silica−Magnetite Nanocomposite: Fabrication and Applications in Magnetic Bioseparations. *Journal of the American Chemical Society*, *128*(22), 7130–7131. https://doi.org/10.1021/ja061393q

Sen, T., Sheppard, S. J., Mercer, T., Eizadi-sharifabad, M., Mahmoudi, M., & Elhissi, A. (2012). Simple one-pot fabrication of ultra-stable core-shell superparamagnetic nanoparticles for potential application in drug delivery. *RSC Advances*, *2*(12), 5221–5228. https://doi.org/10.1039/C2RA20199B

Sharifabad, M. E. (2016). *Study of Porous Magnetic Nanocomposites for Bio-Catalysis and Drug Delivery.* Doctoral thesis, University of Central Lancashire.

Sharma, H., Mishra, P. K., Talegaonkar, S., & Vaidya, B. (2015). Metal nanoparticles: A theranostic nanotool against cancer. *Drug Discovery Today*, *20*(9), 1143–1151. https://doi.org/10.1016/j.drudis.2015.05.009

Shen, Z., Song, J., Yung, B. C., Zhou, Z., Wu, A., & Chen, X. (2018). Emerging Strategies of Cancer Therapy Based on Ferroptosis. *Advanced Materials*, *30*(12), 1704007. https://doi.org/10.1002/adma.201704007

Sheng, Z., Hu, D., Zheng, M., Zhao, P., Liu, H., Gao, D., Gong, P., Gao, G., Zhang, P., Ma, Y., & Cai, L. (2014). Smart Human Serum Albumin-Indocyanine Green Nanoparticles Generated by Programmed Assembly for Dual-Modal Imaging-Guided Cancer Synergistic Phototherapy. *ACS Nano*, *8*(12), 12310–12322. https://doi.org/10.1021/nn5062386

Shi, J., Kantoff, P. W., Wooster, R., & Farokhzad, O. C. (2017). Cancer nanomedicine: Progress, challenges and opportunities. *Nature Reviews Cancer*, *17*(1), 20–37. https://doi.org/10.1038/nrc.2016.108

Shimada, K., Skouta, R., Kaplan, A., Yang, W. S., Hayano, M., Dixon, S. J., Brown, L. M., Valenzuela, C. A., Wolpaw, A. J., & Stockwell, B. R. (2016). Global survey of cell death mechanisms reveals metabolic regulation of ferroptosis. *Nature Chemical Biology*, *12*(7), 497–503. https://doi.org/10.1038/nchembio.2079

Slowing, I. I., Wu, C.-W., Vivero-Escoto, J. L., & Lin, V. S.-Y. (2009). Mesoporous Silica Nanoparticles for Reducing Hemolytic Activity Towards Mammalian Red Blood Cells. *Small*, *5*(1), 57–62. https://doi.org/10.1002/smll.200800926

Soares, M. P., & Hamza, I. (2016). Macrophages and Iron Metabolism. *Immunity*, *44*(3), 492–504. https://doi.org/10.1016/j.immuni.2016.02.016

Soares, S., Sousa, J., Pais, A., & Vitorino, C. (2018). Nanomedicine: Principles, Properties, and Regulatory Issues. *Frontiers in Chemistry*, *6*. https://www.frontiersin.org/article/10.3389/fchem.2018.00360

Soetaert, F., Korangath, P., Serantes, D., Fiering, S., & Ivkov, R. (2020). Cancer therapy with iron oxide nanoparticles: Agents of thermal and immune therapies. *Advanced Drug Delivery Reviews*, *163–164*, 65–83. https://doi.org/10.1016/j.addr.2020.06.025

Sonmez, M., Georgescu, M., Alexandrescu, L., Gurau, D., Ficai, A., Ficai, D., & Andronescu, E. (2015). Synthesis and applications of Fe_3O_4/SiO_2 core-shell materials. *Current Pharmaceutical Design*, *21*(37), 5324–5335. https://dx.doi.org/10.2174/1381612821666150917094031

Staniford, M. C., Lezhnina, M. M., Gruener, M., Stegemann, L., Kuczius, R., Bleicher, V., Strassert, C. A., & Kynast, U. H. (2015). Photophysical efficiency-boost of aqueous aluminium phthalocyanine by hybrid formation with nano-clays. *Chemical Communications*, *51*(70), 13534–13537. https://doi.org/10.1039/C5CC05352H

Starowicz, M., Starowicz, P., Żukrowski, J., Przewoźnik, J., Lemański, A., Kapusta, C., & Banaś, J. (2011). Electrochemical synthesis of magnetic iron oxide nanoparticles with controlled size. *Journal of Nanoparticle Research*, *13*(12), 7167–7176. https://doi.org/10.1007/s11051-011-0631-5

Stetefeld, J., McKenna, S. A., & Patel, T. R. (2016). Dynamic light scattering: A practical guide and applications in biomedical sciences. *Biophysical Reviews*, *8*(4), 409–427. https://doi.org/10.1007/s12551-016-0218-6

Stöber, W., Fink, A., & Bohn, E. (1968). Controlled growth of monodisperse silica spheres in the micron size range. *Journal of Colloid and Interface Science*, *26*(1), 62–69. https://doi.org/10.1016/0021-9797(68)90272-5

Stockwell, B. R., Friedmann Angeli, J. P., Bayir, H., Bush, A. I., Conrad, M., Dixon, S. J., Fulda, S., Gascón, S., Hatzios, S. K., Kagan, V. E., Noel, K., Jiang, X., Linkermann, A., Murphy, M. E., Overholtzer, M., Oyagi, A., Pagnussat, G. C., Park, J., Ran, Q., Zhang, D. D. (2017). Ferroptosis: A Regulated Cell Death Nexus Linking Metabolism, Redox Biology, and Disease. *Cell*, *171*(2), 273–285. https://doi.org/10.1016/j.cell.2017.09.021

Sun, K., Gao, Z., Zhang, Y., Wu, H., You, C., Wang, S., An, P., Sun, C., & Sun, B. (2018). Enhanced highly toxic reactive oxygen species levels from iron oxide core–shell mesoporous silica nanocarrier-mediated Fenton reactions for cancer therapy. *Journal of Materials Chemistry B*, *6*(37), 5876–5887. https://doi.org/10.1039/C8TB01731J

Sun, S.-N., Wei, C., Zhu, Z.-Z., Hou, Y.-L., Venkatraman, S. S., & Xu, Z.-C. (2014). Magnetic iron oxide nanoparticles: Synthesis and surface coating techniques for biomedical applications. *Chinese Physics B*, *23*(3), 037503. https://doi.org/10.1088/1674-1056/23/3/037503

Sun, Y., Chen, Z.-L., Yang, X.-X., Huang, P., Zhou, X.-P., & Du, X.-X. (2009). Magnetic chitosan nanoparticles as a drug delivery system for targeting photodynamic therapy. *Nanotechnology*, *20*(13), 135102. https://doi.org/10.1088/0957-4484/20/13/135102

Suriyanto, Ng, E. Y. K., & Kumar, S. D. (2017). Physical mechanism and modeling of heat generation and transfer in magnetic fluid hyperthermia through Néelian and Brownian relaxation: A review. *BioMedical Engineering OnLine*, *16*, 36. https://doi.org/10.1186/s12938-017-0327-x

Szatrowski, T. P., & Nathan, C. F. (1991). Production of large amounts of hydrogen peroxide by human tumor cells. *Cancer Research*, *51*(3), 794–798.

Tang, Y., & McGoron, A. J. (2009). Combined effects of laser-ICG photothermotherapy and doxorubicin chemotherapy on ovarian cancer cells. *Journal of Photochemistry and Photobiology B: Biology*, *97*(3), 138–144. https://doi.org/10.1016/j.jphotobiol.2009.09.001

Tao, Z., Toms, B. B., Goodisman, J., & Asefa, T. (2009). Mesoporosity and Functional Group Dependent Endocytosis and Cytotoxicity of Silica Nanomaterials. *Chemical Research in Toxicology*, *22*(11), 1869–1880. https://doi.org/10.1021/tx900276u

The European Commission. (2011). Commission Recommendation of 18 October 2011 on the definition of nanomaterial (2011/696/EU). *Official Journal of the European Union*, *275*. http://data.europa.eu/eli/reco/2011/696/oj/eng

Ting, C. W., Chou, Y. H., Huang, S. Y., & Chiang, W. H. (2021). Indocyanine green-carrying polymeric nanoparticles with acid-triggered detachable PEG coating and drug release for boosting cancer photothermal therapy. *Colloids and Surfaces B: Biointerfaces*, *208*, 112048. https://doi.org/10.1016/j.colsurfb.2021.112048

Tinkle, S., McNeil, S. E., Mühlebach, S., Bawa, R., Borchard, G., Barenholz, Y. C., Tamarkin, L., & Desai, N. (2014). Nanomedicines: Addressing the scientific and regulatory gap. *Annals of the New York Academy of Sciences*, *1313*, 35–56. https://doi.org/10.1111/nyas.12403

Tomizawa, Y., & Tian, J. (2012). Photodynamic Therapy for Unresectable Cholangiocarcinoma. *Digestive Diseases and Sciences*, *57*(2), 274–283. https://doi.org/10.1007/s10620-011-1957-7

Trachootham, D., Alexandre, J., & Huang, P. (2009). Targeting cancer cells by ROS-mediated mechanisms: A radical therapeutic approach? *Nature Reviews Drug Discovery*, *8*(7), 579–591. https://doi.org/10.1038/nrd2803

Tsuchida, S., & Yamada, T. (2014). Glutathione Transferases. In *Reference Module in Biomedical Sciences*. Elsevier. https://doi.org/10.1016/B978-0-12-801238-3.04351-8

Van der Meel, R., Sulheim, E., Shi, Y., Kiessling, F., Mulder, W. J. M., & Lammers, T. (2019). Smart cancer nanomedicine. *Nature Nanotechnology*, *14*(11), 1007–1017. https://doi.org/10.1038/s41565-019-0567-y

Veiseh, O., Gunn, J. W., & Zhang, M. (2010). Design and fabrication of magnetic nanoparticles for targeted drug delivery and imaging. *Advanced Drug Delivery Reviews*, *62*(3), 284–304. https://doi.org/10.1016/j.addr.2009.11.002

Verma, S. K., Thirumurugan, A., Panda, P. K., Patel, P., Nandi, A., Jha, E., Prabakaran, K., Udayabhaskar, R., Mangalaraja, R. V., Mishra, Y. K., Akbari-Fakhrabadi, A., Morel, M. J., Suar, M., & Ahuja, R. (2021). Altered electrochemical properties of iron oxide nanoparticles by carbon enhance molecular biocompatibility through discrepant atomic interaction. *Materials Today Bio*, *12*, 100131. https://doi.org/10.1016/j.mtbio.2021.100131

Veys, I., Pop, C.-F., Barbieux, R., Moreau, M., Noterman, D., De Neubourg, F., Nogaret, J.-M., Liberale, G., Larsimont, D., & Bourgeois, P. (2018). ICG fluorescence imaging as a new tool for optimization of pathological evaluation in breast cancer tumors after

neoadjuvant chemotherapy. *PLoS ONE*, *13*(5), e0197857. https://doi.org/10.1371/journal.pone.0197857

Vidal-Vidal, J., Rivas, J., & López-Quintela, M. A. (2006). Synthesis of monodisperse maghemite nanoparticles by the microemulsion method. *Colloids and Surfaces A: Physicochemical and Engineering Aspects*, *288*(1), 44–51. https://doi.org/10.1016/j.colsurfa.2006.04.027

Wang, S., Luo, J., Zhang, Z., Dong, D., Shen, Y., Fang, Y., Hu, L., Liu, M., Dai, C., Peng, S., Fang, Z., & Shang, P. (2018). Iron and magnetic: New research direction of the ferroptosis-based cancer therapy. *American Journal of Cancer Research*, *8*(10), 1933–1946.

Wang, Y., Li, X., Chen, P., Dong, Y., Liang, G., & Yu, Y. (2020). Enzyme-instructed self-aggregation of Fe_3O_4 nanoparticles for enhanced MRI T_2 imaging and photothermal therapy of tumours. *Nanoscale*, *12*(3), 1886–1893. https://doi.org/10.1039/C9NR09235H

Wang, Y., Niu, C., Fan, S., Li, Y., Li, X., Dai, Y., Shi, J., & Wang, X. (2020). Indocyanine Green Loaded Modified Mesoporous Silica Nanoparticles as an Effective Photothermal Nanoplatform. *International Journal of Molecular Sciences*, *21*(13), 4789. https://doi.org/10.3390/ijms21134789

Wang, Y., Ren, J., Liu, X., Wang, Y., Guo, Y., Guo, Y., & Lu, G. (2008). Facile synthesis of ordered magnetic mesoporous γ-Fe_2O_3/SiO_2 nanocomposites with diverse mesostructures. *Journal of Colloid and Interface Science*, *326*(1), 158–165. https://doi.org/10.1016/j.jcis.2008.07.012

Wu, M., & Huang, S. (2017). Magnetic nanoparticles in cancer diagnosis, drug delivery and treatment. *Molecular and Clinical Oncology*, *7*(5), 738–746. https://doi.org/10.3892/mco.2017.1399

Wu, W., He, Q., & Jiang, C. (2008). Magnetic Iron Oxide Nanoparticles: Synthesis and Surface Functionalization Strategies. *Nanoscale Research Letters*, *3*(11), 397–415. https://doi.org/10.1007/s11671-008-9174-9

Wu, W., Wu, Z., Yu, T., Jiang, C., & Kim, W.-S. (2015). Recent progress on magnetic iron oxide nanoparticles: Synthesis, surface functional strategies and biomedical applications. *Science and Technology of Advanced Materials*, *16*(2), 023501. https://doi.org/10.1088/1468-6996/16/2/023501

Wu, W., Xiao, X., Zhang, S., Zhou, J., Fan, L., Ren, F., & Jiang, C. (2010). Large-Scale and Controlled Synthesis of Iron Oxide Magnetic Short Nanotubes: Shape Evolution,

Growth Mechanism, and Magnetic Properties. *The Journal of Physical Chemistry C*, *114*(39), 16092–16103. https://doi.org/10.1021/jp1010154

Xue, P., Yang, R., Sun, L., Li, Q., Zhang, L., Xu, Z., & Kang, Y. (2018). Indocyanine Green-Conjugated Magnetic Prussian Blue Nanoparticles for Synchronous Photothermal/Photodynamic Tumour Therapy. *Nano-Micro Letters*, *10*(4), 74. https://doi.org/10.1007/s40820-018-0227-z

Yan, L., Amirshaghaghi, A., Huang, D., Miller, J., Stein, J. M., Busch, T. M., Cheng, Z., & Tsourkas, A. (2018). Protoporphyrin IX (PpIX)-Coated Superparamagnetic Iron Oxide Nanoparticle (SPION) Nanoclusters for Magnetic Resonance Imaging and Photodynamic Therapy. *Advanced Functional Materials*, *28*(16), 1707030. https://doi.org/10.1002/adfm.201707030

Yang, S.-J., Huang, C.-H., Wang, C.-H., Shieh, M.-J., & Chen, K.-C. (2020). The Synergistic Effect of Hyperthermia and Chemotherapy in Magnetite Nanomedicine-Based Lung Cancer Treatment. *International Journal of Nanomedicine*, *15*, 10331–10347. https://doi.org/10.2147/IJN.S281029

Yang, W. S., SriRamaratnam, R., Welsch, M. E., Shimada, K., Skouta, R., Viswanathan, V. S., Cheah, J. H., Clemons, P. A., Shamji, A. F., Clish, C. B., Brown, L. M., Girotti, A. W., Cornish, V. W., Schreiber, S. L., & Stockwell, B. R. (2014). Regulation of Ferroptotic Cancer Cell Death by GPX4. *Cell*, *156*(1), 317–331. https://doi.org/10.1016/j.cell.2013.12.010

Yin, T., Huang, P., Gao, G., Shapter, J. G., Shen, Y., Sun, R., Yue, C., Zhang, C., Liu, Y., Zhou, S., & Cui, D. (2016). Superparamagnetic Fe_3O_4-PEG2K-FA@Ce6 Nanoprobes for in Vivo Dual-mode Imaging and Targeted Photodynamic Therapy. *Scientific Reports*, *6*(1), 36187. https://doi.org/10.1038/srep36187

Yu, S., Zhang, H., Zhang, S., Zhong, M., & Fan, H. (2021). Ferrite Nanoparticles-Based Reactive Oxygen Species-Mediated Cancer Therapy. *Frontiers in Chemistry*, *9*, 651053. https://doi.org/10.3389/fchem.2021.651053

Zanganeh, S., Hutter, G., Spitler, R., Lenkov, O., Mahmoudi, M., Shaw, A., Pajarinen, J. S., Nejadnik, H., Goodman, S., Moseley, M., Coussens, L. M., & Daldrup-Link, H. E. (2016). Iron oxide nanoparticles inhibit tumour growth by inducing pro-inflammatory macrophage polarization in tumour tissues. *Nature Nanotechnology*, *11*(11), 986–994. https://doi.org/10.1038/nnano.2016.168

Zeng, Q., Ma, X., Song, Y., Chen, Q., Jiao, Q., & Zhou, L. (2022). Targeting regulated cell death in tumor nanomedicines. *Theranostics*, *12*(2), 817–841. https://doi.org/10.7150/thno.67932

Zhang, H., Li, Y.-H., Chen, Y., Wang, M.-M., Wang, X.-S., & Yin, X.-B. (2017). Fluorescence and Magnetic Resonance Dual-Modality Imaging-Guided Photothermal and Photodynamic Dual-Therapy with Magnetic Porphyrin-Metal Organic Framework Nanocomposites. *Scientific Reports*, *7*(1), 44153. https://doi.org/10.1038/srep44153

Zhang, J., Li, X., Rosenholm, J. M., & Gu, H. (2011). Synthesis and characterization of pore size-tunable magnetic mesoporous silica nanoparticles. *Journal of Colloid and Interface Science*, *361*(1), 16–24. https://doi.org/10.1016/j.jcis.2011.05.038

Zhang, R., Wu, C., Tong, L., Tang, B., & Xu, Q.-H. (2009). Multifunctional Core−Shell Nanoparticles as Highly Efficient Imaging and Photosensitizing Agents. *Langmuir*, *25*(17), 10153–10158. https://doi.org/10.1021/la902235d

Zhang, Z., Huang, C., Zhang, L., Guo, Q., Qin, Y., Fan, F., Li, B., Xiao, B., Zhu, D., & Zhang, L. (2021). PH-sensitive and bubble-generating mesoporous silica-based nanoparticles for enhanced tumor combination therapy. *Acta Pharmaceutica Sinica B*, *11*(2), 520–533. https://doi.org/10.1016/j.apsb.2020.08.013

Zou, J., Peng, Y.-G., & Tang, Y.-Y. (2014). A facile bi-phase synthesis of Fe_3O_4 @SiO_2 core–shell nanoparticles with tunable film thicknesses. *RSC Advances*, *4*(19), 9693–9700. https://doi.org/10.1039/C3RA47043A

APPENDIX I

SUPPLEMENTARY INFORMATION

S1-1: Different batches of nanoparticles and nanocomposites

Table S1-1: Different batches of IONPs and MS nanocomposites synthesised with different methods were named accordingly for the ease of presentation in the thesis.

Preferred Name	Batches	Notes
IO1	NLYPS1, NLYPS2	Hydrophilic Iron oxide nanoparticles
IO2	NLTS11, NLTS12, NLTS13, NLTS14	Hydrophilic Iron oxide nanoparticles
IO3	NLTS2, NLTS2B	Hydrophobic Iron oxide nanoparticles
MS1	MS1NLYPS1, MS2NLYPS2	Magnetic silica nanoparticles with IO1
MS2	MS3NLTS11, MS6NLTS11	Magnetic silica nanoparticles with IO2
MS3	MS8NLTS2, MS10NLTS2, MS11NLTS2	Magnetic silica nanoparticles with IO3
MS1ICG	MS1NLYPS1-ICG, MS2NLYPS2-ICG,	MS1 loaded with ICG
MS2ICG	MS3NLTS11-ICG, MS6NLTS11-ICG	MS2 loaded with ICG
MS3ICG	MS8BLTS2-ICG, MS10NLTS2-ICG, MS11NLTS2-ICG	MS3 loaded with ICG

S1-2: Particle size distribution of different nanoparticles as analysed by DLS

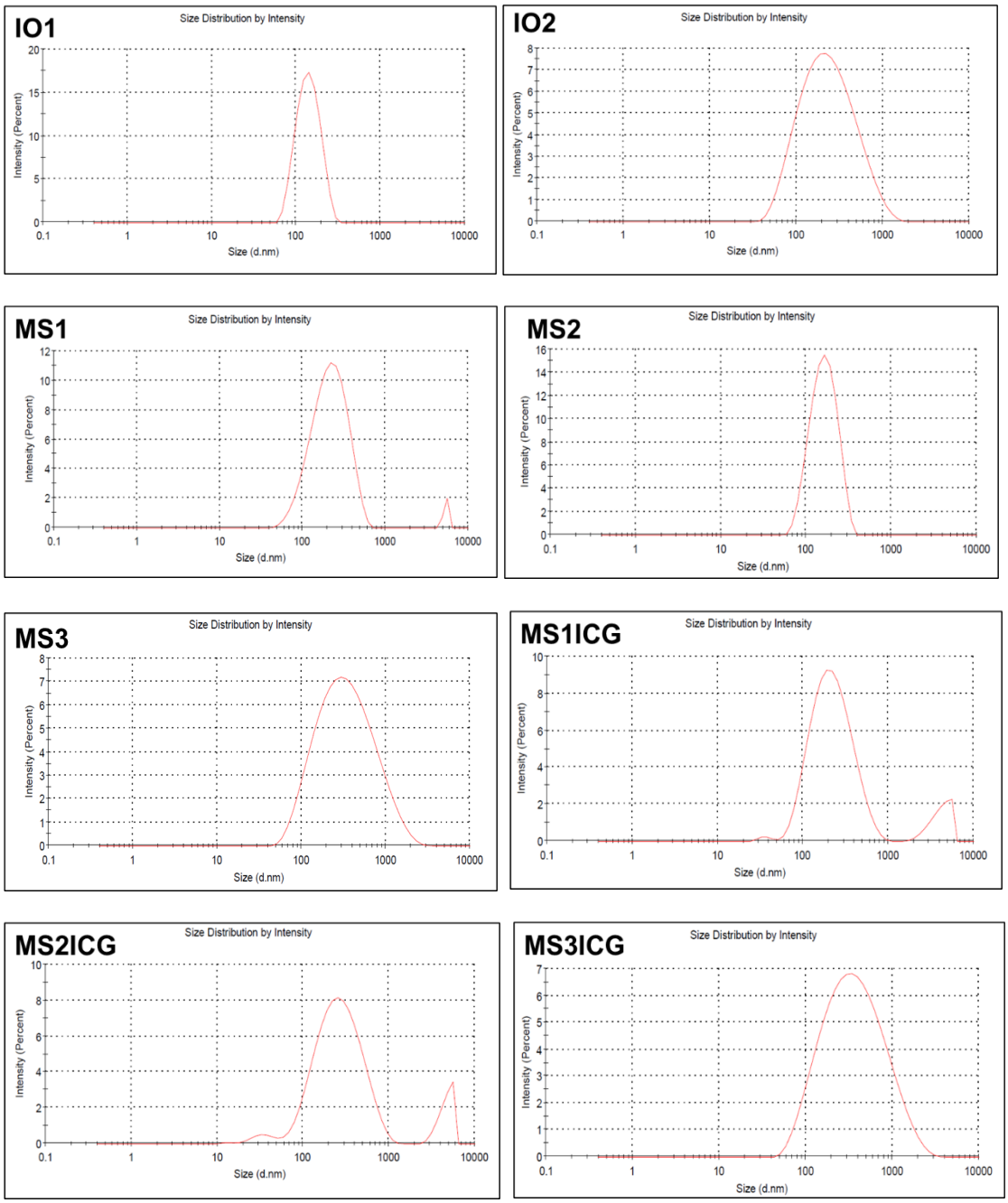

Figure S1-1: Particle size distribution of IONPs (IO1, IO2), MS nanocomposites (MS1, MS2, MS3) and MSICG nanocomposites (MS1ICG, MS2ICG, MS3ICG) calculated as mean of intensity distribution using DLS.

S1-3: Zetapotential analysis by Zetasizer.

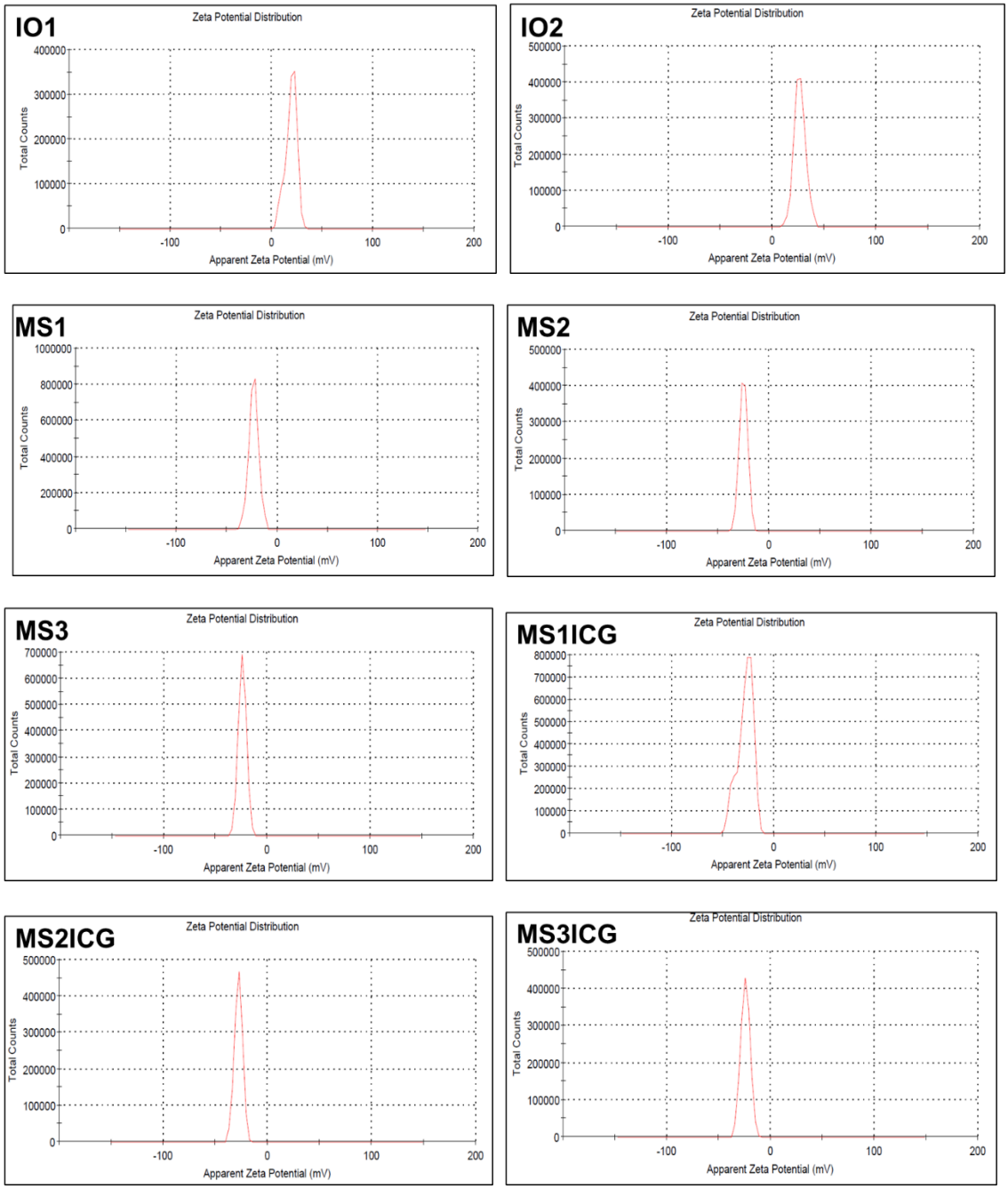

Figure S1-2: Zetapotential of IONPs (IO1, IO2), MS nanocomposites (MS1, MS2, MS3) and MSICG nanocomposites (MS1ICG, MS2ICG, MS3ICG) using Zetasizer.

S1-4: Gravimetric analysis for silica, iron oxide and iron content in the nanocomposites.

The core-shell nanocomposites were dried overnight and weighed. Then, 5 ml of concentrated HCl (32%) was added on each sample in a glass tube and left overnight to dissolve iron oxide. The following day, the solution turned yellow which was filtered using Waterman filter paper grade 42. The remaining silica on the filter paper was air dried and weighed to calculate the amount of iron oxide in the samples. The percentage of silica, iron oxide and iron in the core-shell nanocomposites were calculated as shown in the Table S2. The percentage of SiO_2: Fe_3O_4: Fe was calculated for the nanocomposites as MS1- 68%: 32%: 23%, MS2- 64%: 36%: 26% and MS3- 4.4%: 95.6%: 69.2%.

Table S1-2: The percentage of silica, iron oxide and iron in different batches of MS nanocomposites.

Samples	Silica (%)	Iron oxide (%)	Iron (%)
MS1	68	32	23
MS2	64	36	26
MS3	4.4	95.6	69.2

APPENDIX II

PUBLICATIONS

Abstracts

1. **Lamichhane N.,** Singh K K., Sen T. Iron Oxide Based Magneto Optical Nanoparticulate System for Potential Application in Cancer Therapy. *Nanomedicine: Biomolecules for Human Health (NBHH- 2021).* 27th-28th September 2021, *Virtual platform*.

2. **Lamichhane N.,** Singh K K., Shaw L., and Sen T. Magneto-Optical Nanoparticulate System for Potential Theranostic Application in Cancer Research. *Annual Postgraduate Research Conference*. 23rd-24th July 2020, University of Central Lancashire, Virtual platform.

3. **Lamichhane N**., Singh K. K., Shaw L., and Sen T. Superparamagnetic iron oxide nanoparticles containing photosensitizer for cancer theranostics application. *Functional Nanomaterials in Industrial and Clinical Applications: Academy-Industry-Clinicians meet*, 15th July 2020, University of Central Lancashire, Virtual platform. https://secondnanosymposiumatuclan.net/programme/ (see Figure S2-1)

4. **Lamichhane N.**, Singh K. K., Crosley I., Roy I., and Sen T. Magneto-Optical Nanoparticulate System for Potential Theranostic Application in Cancer Research. *Your Product in Their Hands Towards Predicting Biopharmaceutical Aggregation in Practice and Use*. 14th January 2020, University of Central Lancashire, Preston, UK (see Figure S2-2)

5. **Lamichhane N.,** Cooper B., Sharifabad E. M., Majid A., Mercer T., Crosley I., Roy I., Cassinelli N., and Sen T. Magneto-Optical Nanoparticles for Potential Theranostic Application in Cancer Research. *6th World Congress on Nanomedical Sciences*. 7th-9th January 2019, New Delhi, India. (see Figure S2-3)

Peer-review publications (published)

1. **Lamichhane N**., Sharifabad M. E., Hodgson B., Mercer T. & Sen T. 2022. Superparamagnetic iron oxide nanoparticles (SPIONs) as therapeutic and diagnostic agents. In: Nanoparticle Therapeutics: Production Technologies, Types of Nanoparticles, and Regulatory Aspects. Elsevier Science and Technology, 455-497. https://doi.org/10.1016/B978-0-12-820757-4.00003-X

2. **Lamichhane, N**., Sharma, S., Parul, P., Verma, A.K., Roy, I. & Sen, T., 2021. Iron oxide-based magneto-optical nanocomposites for in vivo biomedical applications. Biomedicines, 9(3), 288. https://doi.org/10.3390/biomedicines9030288

3. Sharma S., **Lamichhane N**., Parul, Sen T. & Roy I. 2021. Iron oxide nanoparticles conjugated with organic optical probes for in vivo diagnostic and therapeutic applications. Nanomedicine, 16(11), 943-962. https://doi.org/10.2217/nnm-2020-0442

Peer-review publications (in preparation)

1. **Lamichhane N**., Yadav M., Biswas L., Mercer T., Verma K. A., Sen T. Magneto-Optical Nanocomposites Induced Oxidative Stress and Assessment of Regulated Cell Death Pathways Upon Laser Irradiation *In-Vitro*. Biomedicine, 2022 (under preparation)

2. **Lamichhane N**., Yadav M., Biswas L., Sultana A., Prasad S., Mercer T., Singh K. K., Verma K. A., Sen T. Multifunctional Iron oxide- Indocyanine green Nanocomposites for Light-Activated Cancer therapeutics. Nanomedicine, 2022 (under preparation)

Poster presented at conferences:

Figure S2-1: Superparamagnetic iron oxide nanoparticles containing photosensitizer for cancer theranostics application in *Functional Nanomaterials in Industrial and Clinical Applications: Academy-Industry-Clinicians meet* 15th July 2020, University of Central Lancashire, Virtual platform.

SUPERPARAMAGNETIC IRON OXIDE NANOPARTICLES CONTAINING PHOTOSENSITIZER FOR CANCER THERANOSTICS APPLICATION

Nisha Lamichhane[1]*, Kamalinder K Singh[2], Lisa Shaw[2] and Tapas Sen[1]

[1]Nano-biomaterials Research Group, School of Physical Sciences and Computing, [2]School of Pharmacy and Biomedical Sciences,

[1,2]University of Central Lancashire, Preston, PR1 2HE, United Kingdom;

*Corresponding Author's Email: nlamichhane2@uclan.ac.uk

P-2-12

ABSTRACT

With the increasing mortality rate in line with incidence, the diagnostic procedures and treatments on liver cancer needs to be advanced. [1] In this context, a new paradigm in cancer theranostics is achieved by using multifunctional biocompatible nanoparticulate system.

Herein, we report synthesis and characterisation of mesoporous silica-superparamagnetic iron oxide nanoparticles loaded with optical Indocyanine Green (ICG) as a photosensitizer for multifunctional nanoparticulate system (MSN-SPIONs-ICG). The ability to heat the suspension of MSN-SPIONs-ICG under AMF was observed to the set hyperthermia temperature of 42 °C. Similarly, a temperature change of around 6 °C of NIR laser irradiation (808nm, 120mW) was observed on ICG loaded nanocomposites. Furthermore, the formation of singlet oxygen after irradiation of laser light was confirmed using the decay profile of 9,10-anthracenediyl-bis (methylene) dimalonic acid (ABMDMA) dye.

With the initial encouraging results, we plan to use commercial liver cancer cell lines (HepG2) to perform the *in-vitro* hyperthermia and PTT/PDT studies.

INTRODUCTION

Superparamagnetic iron oxide nanoparticles (SPIONs) are preferred magnetic nanoparticles offering excellent magnetic properties with low toxicity, being used as a magnetic resonance imaging contrast agent [2]. In addition, the heating ability of SPIONs under alternating magnetic field (AMF) for hyperthermia therapy shapes the modality for cancer treatment. Furthermore, the use of Indocyanine Green (ICG) in intra-operative fluorescence imaging for liver cancer has been universally accepted[3] while it's photosensitising properties for Photodynamic and Photothermal therapies have not been investigated much. Designing the multifunctional magneto-optical nanoparticulate system comprising SPIONs and ICG will facilitate the imaging and other therapeutic properties rendering theranostic application.

AIMS AND OBJECTIVES

In our study, we intend to utilise the advantage of multifunctional nanoparticles' properties such as diagnostic (imaging) and therapeutics (MIIT/PTT/PDT) for cancer theranostic application.

The objectives are to synthesise and characterise the nanocomposites in a single platform and explore the functionalities such as MHT: localised heating under Alternating Magnetic Field (AMF), Optical imaging: Near-Infrared fluorophores (NIRF) for imaging and PTT/PDT: the irradiation of NIR laser light of specific wavelengths compatible for application in liver cancer theranostics.

CHARACTERISATION

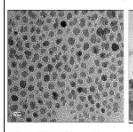

Figure 4: TEM image of hydrophobic SPIONs

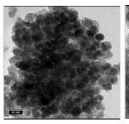

Figure 5: TEM image of mesoporous silica- hydrophobic SPIONs

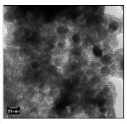

Figure 6: TEM image of mesoporous silica- hydrophobic SPIONs (M1)

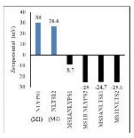

Figure 7: Zeta potential

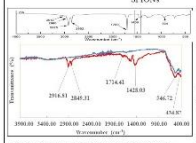

Figure 8: FT-IR data of hydrophobic (red) and hydrophilic (blue) SPIONs. Inset: Oleic acid

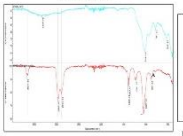

Figure 9: FT-IR data of mesoporous silica# hydrophilic SPIONs (MS1BNLYPS2) (M1) (A) after acidic wash and (B) before washing

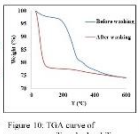

Figure 10: TGA curve of mesoporous silica- hydrophilic SPIONs before and after washing

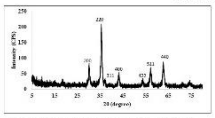

Figure 11: XRD pattern of hydrophilic SPIONs (M1)

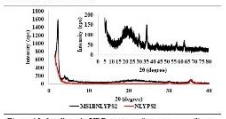

Figure 12: Small angle XRD pattern of mesoporous silica-hydrophilic SPIONs (Black) and hydrophilic SPIONs (Red) (M1) Inset: XRD pattern of mesoporous silica- hydrophilic SPIONs (M1)

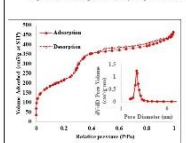

Figure 13: N_2 adsorption-desorption isotherm of MS-hydrophilic SPIONs (M1). Inset: Pore size distribution curve with peak centred at 2.9 nm

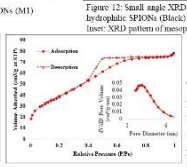

Figure 14: N_2 adsorption-desorption isotherm of MS-hydrophilic SPIONs. Inset: Pore size distribution curve with peak centred at 3.4 nm

Table 1: ICG loading capacity

Sample	Batch number	ICG Fed (nmol/mg)	ICG loaded (nmol/mg)	DLC (%)	EE (%)
MS-hydrophilic SPIONs (M1)-ICG	MS1ANLYPS1-ICG2	69.62	47.77	3.7	68.6
MS-hydrophilic SPIONs (M1)-ICG	MS1BNLYPS2-ICG1	46.1	7.72	0.6	16.8
MS-hydrophilic SPIONs (M2)-ICG	MS3ANLTS11-ICG2	46.1	10.78	0.84	23.4
MS- hydrophobic SPIONs-ICG	MS11NLTS2B-ICG2	46.1	14.83	1.1	32.2

The synthesised mesoporous silica-SPIONs are spherical in morphology (TEM), negatively charged (Zeta potential), molecular confirmation (FT-IR), crystalline (XRD) and mesoporous (BET). ICG was encapsulated within the mesopores with higher encapsulation efficiency.

EXPERIMENTAL METHODOLOGY

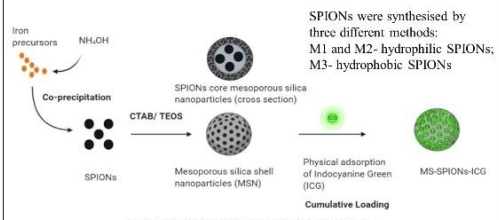

Figure 1: Synthesis of mesoporous silica-SPIONs-ICG nanocomposite.
Iron precursors: ($FeCl_2.4H_2O$: iron (II) chloride tetrahydrate ; $FeCl_3.6H_2O$: iron (III) chloride hexahydrate; CTAB: hexadecyl-trimethyl ammonium bromide, NH_4OH: Ammonium hydroxide, NaOH: Sodium hydroxide, TEOS: tetraethyl orthosilicate; ICG: Indocyanine Green)

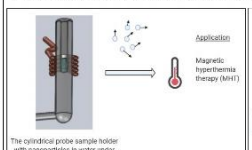

Figure 2: Magnetic Hyperthermia Therapy using SPIONs nanocomposites under AMF

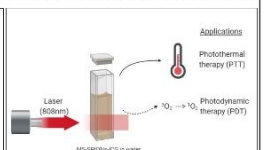

Figure 3: Photothermal therapy and Photodynamic therapy using SPIONs containing ICG under laser irradiation.

RESULT AND DISCUSSION

Hyperthermia study under AMF

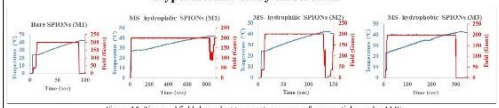

Figure 15: Time and field dependent temperature curves of nanoparticles under AMF

Photo-thermal efficiency study

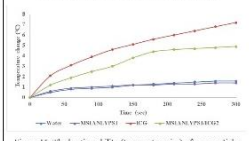

Figure 16: The heating ability (temperature rise) of nanoparticles (M1) by 808nm laser irradiation (power density of 120 mW cm^{-2}) for a period of 5 minutes was recorded for free ICG, water MS1ANLYPS1/ICG2 and MS1ANLYPS1.

Singlet oxygen generation study

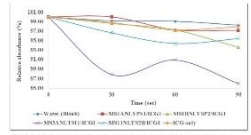

Figure 17: Relative UV absorbance of ABMDMA at 400nm in different solutions: water, free ICG, MS1ANLYPS1/ICG3 (M1), MS1BNLYPS2/ICG1 (M1), MS3ANLTS11/ICG1 (M2), and MS11NLTS2B/ICG1 (M3) with ICG concentration of 20μM within 90 seconds under 808nm laser irradiation (120 mW cm^{-2})

The bare SPIONs and MS-SPIONs showed efficient heating efficiency to target temperature (42°C) under AMF in few minutes. The ICG loaded nanoparticles were able to generate singlet oxygen which was observed through photo-bleaching of 9,10-anthracenediyl-bis (methylene) dimalonic acid (ABMDMA). It also showed hyperthermia and photostability upon laser irradiation.

CONCLUSION AND FUTURE WORK

We have presented an optimum synthesis protocol of mesoporous silica- SPIONs- ICG conjugated nanoparticulate systems and their full characterisation. The ICG loaded nanoparticles showed efficient photothermal and photodynamic properties. In future, the optimised nanoparticles will be tested for *in-vitro* cell viability and toxicity studies on commercial liver cancer cell lines, in the presence of external stimuli such as Alternative Magnetic Field (AMF) and laser irradiation.

REFERENCES

1. Oke, J.L., *et al*., 2018. Scientific reports, 8(1), 1-8.
2. Mahmoudi, M., *et al*., 2011. Advanced drug delivery reviews, 63(1-2), 24-46.
3. Boni, L., *et al*., 2015. Surgical endoscopy, 29(7), 2046-2055.

ACKNOWLEDGEMENT:

Figure S2-2: Magneto-Optical Nanoparticulate System for Potential Theranostic Application in Cancer Research. *Your Product in Their Hands Towards Predicting Biopharmaceutical Aggregation in Practice and Use.* 14th January 2020, University of Central Lancashire, Preston, UK

MAGNETO-OPTICAL NANOPARTICULATE SYSTEM FOR POTENTIAL THERANOSTIC APPLICATION IN LIVER CANCER

Nisha Lamichhane[1]*, Kamalinder K Singh[2], Lisa Shaw[2], Iain Crosley[3], Indrajit Roy[4] and Tapas Sen[1]

[1]Nano-biomaterials Research Group, School of Physical Sciences and Computing, University of Central Lancashire, Preston, PR1 2HE, United Kingdom; [2]School of Pharmacy and Biomedical Sciences, University of Central Lancashire, Preston, PR1 2HE, United Kingdom; [3]Hosokawa Micron Ltd., Runcorn, WA7 3DS, UK; [4]Department of Chemistry, Delhi University, Delhi-110007, India

*Corresponding Author's Email: nlamichhane2@uclan.ac.uk

INTRODUCTION

Despite advances in diagnostic procedures and treatments, cancer is the most serious threat for human health. In case of liver cancer, the mortality rate is still increasing with around 51% over the past decade.[1] Using the concept of 'smart' multifunctional nanoparticles, additional modalities can be employed to strategically improve the cancer theranostics.[2] Currently, we are attempting to use the advantage of multifunctionality such as (i) Magnetic targeting: localisation to target cells with the influence of an external magnetic field in therapy; (ii) Magnetic fluid hyperthermia: localised heating under Alternating Magnetic Field (AMF) in therapy; (iii) Optical imaging: Near-Infrared fluorophores (NIRF) for imaging in diagnosis; and (iv) Photothermal therapy (PTT) and photodynamic therapy (PDT) by the irradiation of laser light of specific wavelength compatible for application in liver cancer.

EXPERIMENTAL METHODOLOGY

A. Synthesis of superparamagnetic iron oxide nanoparticles (SPIONs)

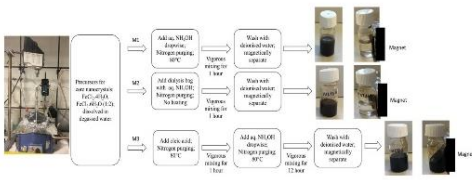

B. Synthesis of mesoporous silica-SPIONs nanoparticulate system

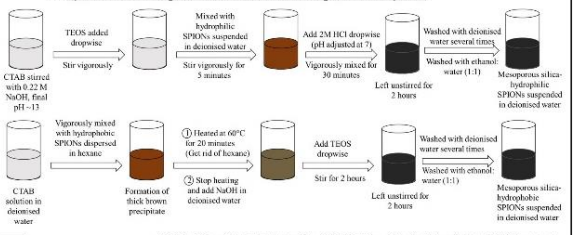

C. Loading ICG in mesoporous silica- Fe_3O_4 nanoparticulate system

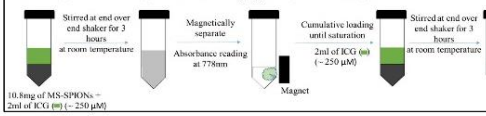

($FeCl_2.4H_2O$: iron (II) chloride tetrahydrate ; $FeCl_3.6H_2O$: iron (III) chloride hexahydrate; CTAB: hexadecyl-trimethyl ammonium bromide, NH_4OH: Ammonium hydroxide; NaOH: Sodium hydroxide; HCl: Hydrochloric acid; TEOS: tetraethyl orthosilicate; ICG: Indocyanine Green)

SPIONs were synthesised by three different methods: M1 and M2- hydrophilic SPIONs; M3- hydrophobic SPIONs. Mesoporous silica coated SPIONs were then synthesised and later ICG was loaded onto it through physical adsorption.

CHARACTERISATION

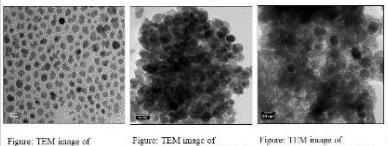

Figure: TEM image of hydrophobic SPIONs

Figure: TEM image of mesoporous silica- hydrophobic SPIONs

Figure: TEM image of mesoporous silica- hydrophilic SPIONs (M1)

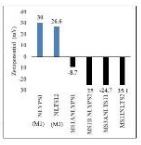

Figure: Zeta potential

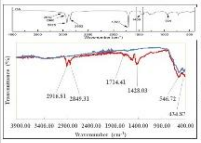

Figure: FT-IR data of hydrophobic (red) and hydrophilic (blue) SPIONs. Inset: Oleic acid

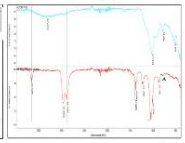

Figure: FT-IR data of mesoporous silica- hydrophilic SPIONs (MS1HNLYPS2) (M1) (A) after acidic wash and (B) before washing

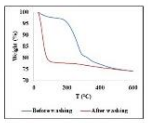

Figure: TGA curve of mesoporous silica- hydrophilic SPIONs before and after washing

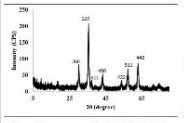

Figure: XRD pattern of hydrophilic SPIONs (M1)

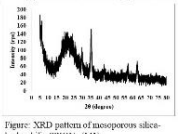

Figure: XRD pattern of mesoporous silica-hydrophilic SPIONs (M1)

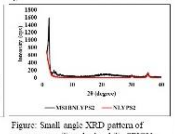

Figure: Small angle XRD pattern of mesoporous silica- hydrophilic SPIONs (Black) and hydrophilic SPIONs (Red) (M1)

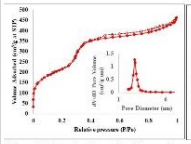

Figure: N_2 adsorption-desorption isotherm of MS-hydrophilic SPIONs (M1). Inset: Pore size distribution curve with peak centred at 2.9 nm

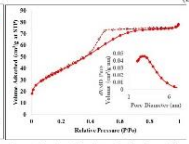

Figure: N_2 adsorption-desorption isotherm of MS-hydrophobic SPIONs. Inset: Pore size distribution curve with peak centred at 3.35 nm

Table: ICG loading capacity

Sample	Batch number	ICG Fed (mmol/mg)	ICG loaded (mmol/mg)	DLC (%)	EE (%)
MS-hydrophilic SPIONs(M1)- ICG	MS1ANLYPS1-ICG2	69.62	47.77	3.7	68.6
MS-hydrophilic SPIONs (M1)-ICG	MS1HNLYPS2-ICG1	46.1	7.72	0.6	16.8
MS-hydrophilic SPIONs(M2)-ICG	MS1ANLTS1H-ICG2	46.1	10.78	0.84	23.4
MS- hydrophobic SPIONs-ICG	MS1HNLTS2H-ICG2	46.1	14.83	1.1	32.2

The synthesised mesoporous silica-SPIONs are spherical in morphology (TEM), negatively charged (Zeta potential), molecular confirmation (FT-IR), crystalline (XRD) and mesoporous (BET). ICG was encapsulated within the mesopores with higher encapsulation efficiency.

RESULT AND DISCUSSION

Hyperthermia study under AMF

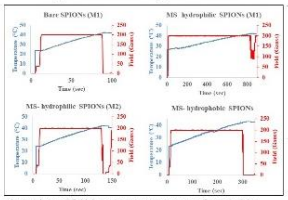

Figure: Time and field dependent temperature curve of nanoparticles under AMF

Singlet oxygen generation study

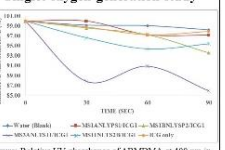

Figure: Relative UV absorbance of ABMDMA at 400 nm in different solutions: water, free ICG, MS1ANLYPS1/ICG1 (M1), MS1HNLYPS2/ICG1 (M1), MS3ANLTS1H/ICG1 (M2), and MS1HNLTS2H/ICG1 with ICG concentration of 20µM within 90 seconds under 808nm laser irradiation (120 mW cm^{-2})

Photothermal efficiency study

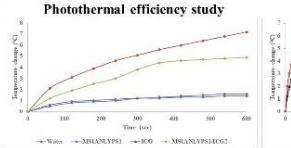

Figure: The heating ability (temperature rise) of nanoparticles (M1) by 808nm laser irradiation (power density of 120 mW cm^{-2}) for a period of 6 minutes was recorded for free ICG, MS1ANLYPS1/ICG2, MS1ANLYPS1 and water

Photostability study

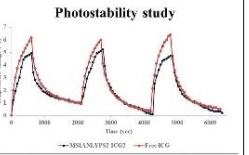

Figure: Photostability test of free ICG and MS1ANLYPS1-ICG (M1) with three cycles of laser on/off upon 808nm laser irradiation at 120 mW cm^{-2} for 10 minutes

The bare SPIONs and MS-SPIONs showed efficient heating temperature of 42°C under AMF. The ICG loaded nanoparticles were able to generate singlet oxygen which was observed through photobleaching of 9,10-anthracenediyl-bis (methylene) dimalonic acid (ABMDMA). It showed rise in temperature and photostability upon laser irradiation.

CONCLUSION AND FUTURE WORK

We have successfully synthesised mesoporous silica- SPIONs- ICG conjugated nanoparticulate systems and characterised the materials. The ICG loaded nanoparticles showed efficient photothermal and photodynamic properties. In future, the optimised nanoparticles will be tested for *in-vitro* cell viability and toxicity studies on commercial liver cancer cell lines. *In-vitro* ROS generation and hyperthermia studies will also be performed.

REFERENCES

1.Cancer Research UK, https://www.cancerresearchuk.org/health-professional/cancer-statistics/statistics-by-cancer-type/liver-cancer#heading-One [Accessed 4 January 2020]

2.Chowdhury, A. D., Ganganboina, A. B., Tsai, Y. C., Chiu, H. C. & Doong, R. A., 2018. Multifunctional GQDs-Concanavalin A Fe_3O_4 nanocomposites for cancer cells detection and targeted drug delivery. Analytica Chimica Acta, 1027, 109-120.

ACKNOWLEDGEMENT:

UKIERI UK-India Education and Research Initiative

HOSOKAWA MICRON LTD

uclan University of Central Lancashire

Figure S2-3: Magneto-Optical Nanoparticles for Potential Theranostic Application in Cancer Research. *6th World Congress on Nanomedical Sciences*. 7th-9th January 2019, New Delhi, India.